PNNL-26993

Pacific Northwest
NATIONAL LABORATORY

Proudly Operated by Battelle *Since 1965*

Blind Testing of PARENT Open Techniques

Results

February 2018

RM Meyer
AE Holmes

Prepared for the U.S. Nuclear Regulatory Commission
under a Related Services Agreement with the U.S. Department of Energy
CONTRACT DE-AC05-76RL01830

U.S. DEPARTMENT OF
ENERGY

PACIFIC NORTHWEST NATIONAL LABORATORY
operated by
BATTELLE
for the
UNITED STATES DEPARTMENT OF ENERGY
under Contract DE-AC05-76RL01830

PNNL-26993

Blind Testing of PARENT Open Techniques

Results

RM Meyer
AE Holmes

February 2018

Prepared for
the U.S. Nuclear Regulatory Commission
under a Related Services Agreement
with the U.S. Department of Energy
Contract DE-AC05-76RL01830

Pacific Northwest National Laboratory
Richland, Washington 99352

Summary

This report documents the results from a blind round-robin test conducted with techniques that were applied in the open testing portion of the Program for Assessing the Reliability of Emerging Nondestructive Technologies (PARENT) (Meyer et al. 2017). Techniques applied in PARENT open testing were novel and attempted to advance upon established techniques (i.e., those regularly used in the field) by employing novel data/signal processing methods and/or novel physical modalities. Open testing has limitations with respect to assessing detection performance and could introduce a bias in sizing due to the knowledge of the location of flaws. Thus, the present test was performed in an attempt to assess detection performance and to obtain a more confident assessment of sizing capability for techniques that demonstrated high potential in PARENT open testing.

PARENT open test techniques were evaluated in this study by performing a quantitative statistical analysis of detection performance and sizing performance. These results are compared to the performance exhibited by applicable established techniques evaluated in PARENT blind testing as a benchmark. Data was collected from examinations of a small-bore dissimilar metal weld test block by ten techniques (implemented by eight teams). This analysis showed that several of the novel PARENT open test techniques exhibit detection performances that are as good as the established techniques. Notably, two of the techniques that did so were eddy current techniques (ECT.16 and AECT.33). The other techniques to exhibit high detection performance included SHPA.06, SAFT.17, and PA-TP.29 (applied to surface-breaking flaws). Several of the PARENT open test techniques exhibited a very high false call rate (e.g., PA-ATOFD.29 [applied to interior flaws], PA-TP.29 [applied to interior flaws], and HHUT.29). This can likely be attributed to the experience of the teams performing these inspections because open test teams, in general, were researchers and not individuals trained to perform examinations commercially. There was a clear distinction in depth sizing performance demonstrated by the emerging techniques and established techniques. In this case, excluding all techniques with number of observations (NOBS) less than 5, the best-performing emerging technique exhibited a depth sizing root-mean-square error (RMSE) twice as large as the worst-performing established technique. With respect to length sizing performance, excluding all techniques with NOBS less than five, two of the emerging techniques (SHPA.06 and ECT.16) performed better than all of the established techniques based on RMSE values. However, the rest of the emerging techniques exhibited worse performance than any of the established techniques.

A qualitative analysis of nondestructive examination response images (B-scan images) was also performed in an attempt to observe potential correlations between response image features and performance, particularly based on depth sizing error observed in indication plots. Technique SAFT.17 was capable of profiling the depth of indications. For cases in which an indication was a false call or the indication demonstrated gross sizing error, the depth profile appeared very irregular and uneven for examinations performed from the carbon steel side of the weld. Smoother depth profiles were observed for detections with limited sizing error. For technique SHPA.06, mostly accurate depth sizing is observed with the exception of two indications. The cause of the sizing error appears to be background noise caused by material defects or inherent material heterogeneity for one indication; for the other indication, it is possible that the true crack tip signal is overwhelmed by saturation in the B-scan caused by wedge reflections or transducer ringdown. PA-TP.29 B-scan images exhibit a higher background signal and less visual clarity than the B-scan images produced by PA-ATOFD.29. This is inconsistent with the quantitative detection analysis results, which show that detection performance (higher probability of detection and lower FCR – see Table 4.1) for PA-TP.29 is significantly better than for PA-ATOFD.29. Although the background level can be qualitatively inferred from the response images, quantitative representation of the signal-to-noise ratio (SNR) may not be inferred from the images and it is possible that SNR is actually greater for PA-TP.29 than for PA-ATOFD.29 despite the appearance of higher background level.

Acknowledgments

The authors express appreciation to Bruce Lin and Iouri Prokofiev of the U.S. Nuclear Regulatory Commission for their leadership of the PARENT extension efforts. Several people and organizations in Japan, South Korea, Finland, Switzerland, Sweden, and the United States contributed to the PARENT program and these efforts are acknowledged in NUREG/CR-7235 and NUREG/CR-7236. For the scope of effort described in this report, additional acknowledgement is extended to the following participating organizations for their efforts and contributions, which included providing test teams and techniques, providing the test block, administration, and review and critique of this report:

- Organizations from Japan
  - Institute of Nuclear Safety System, Incorporated (INSS)
  - Tohoku University
  - Japan Power Engineering and Inspection Corporation (JAPEIC)

- Organizations from Korea
  - Korea Institute of Nuclear Safety (KINS)
  - Korea Research Institute of Standards and Science (KRISS)
  - Sungkyunkwan University (SKKU)
  - Hanyangg University (HYU)

- Organizations from Europe
  - Swedish Radiation Safety Authority (SSM)
  - Swedish Qualification Center (SQC)
  - Swiss Federal Nuclear Safety Inspectorate (ENSI)
  - Swiss Association for Technical Inspections, Nuclear Inspectorate (SVTI)
  - VTT Technical Research Centre of Finland

- Organization from the United States
  - U.S. Nuclear Regulatory Commission (NRC)

The authors would also like to thank Ms. Kay Hass for typing and editing versions and revisions of this document.

Acronyms and Abbreviations

2D	two dimensional
3D	three dimensional
AECT	advanced eddy current testing
ASME	American Society of Mechanical Engineers
CAN	contact acoustic nonlinearity
ECT	eddy current testing
EDM	electro-discharge machine
FCP	false call probability
FCR	false call rate
HHUT	higher harmonic ultrasonic technique
I.D.	inner diameter
MFC	mechanical fatigue crack
NDE	nondestructive examination
NOBS	number of observations
O.D.	outer diameter
OCECT	orthogonal coil array eddy current technique
PA-ATOFD	phased-array asymmetrical beam time-of-flight diffraction
PARENT	Program for Assessing the Reliability of Emerging Nondestructive Technologies
PA-TP	phased-array twin probe
PA-TRT	time reversal technique for focusing of PAUT
PAUT	phased-array ultrasonic testing
PE	pulse echo
POD	probability of detection
RMSE	root-mean-square error
SAFT	synthetic aperture focusing technique
SAW	surface acoustic waves
SBDMW	small-bore dissimilar metal weld
SC	solidification crack
SCC	stress corrosion crack
SDH	side-drilled hole
SHPA	subharmonic phased array
SNR	signal-to-noise ratio
SPACE	subharmonic phased array for crack evaluation
TOFD	time-of-flight diffraction
TR	transmit receive
TRT	time reversal technique

UIRT	ultrasound infrared thermography
UT	ultrasonic testing

Contents

Figures

Tables

1.0 Introduction

This report documents results from a blind round-robin test conducted with techniques that were applied in the open testing portion of the Program for Assessing the Reliability of Emerging Nondestructive Technologies (PARENT) (Meyer et al. 2017). Open testing is useful for performing a basic capability assessment of novel and emerging nondestructive examination (NDE) technologies, but the testing format does not facilitate a realistic measure of detection performance. In addition, bias may exist in sizing results. Conducting a blind test of novel and emerging NDE techniques that exhibited high performance in open testing enables measurement of detection performance for such techniques and a more confident estimate of sizing capabilities.

The techniques applied in open testing in PARENT were novel and are not implemented in the field. In this study, as in PARENT, the open techniques are implemented by teams that do not perform inspections on a routine basis. In comparison, the techniques applied in PARENT blind testing are established in the industry and were implemented by commercial inspection vendors (Meyer and Heasler 2017). As a result, the blind test of PARENT open techniques was limited in scope because of infrastructure limitations (i.e., lack of equipment to handle and scan large test blocks) of some of the open test teams.

Although NDE performance depends on several factors, an implicit assumption (and focus) of this effort is that technology is a significant factor in performance and that the best performance that can be expected is fundamentally limited by the technology. Many of the open techniques applied in the open testing portion of PARENT incorporated novel signal/data processing methods and/or novel physical modalities for inspection. It is reasoned that these novel enhancements should improve metrics associated with signal quality (i.e., signal-to-noise ratio [SNR]) in comparison to established techniques.

This test followed the same protocol for testing applied in PARENT blind testing and interested readers are encouraged to refer to Section 4.0 of NUREG/CR-7235 (Meyer and Heasler 2017) for a description of the protocol for reporting and analyzing data. In this effort, a quantitative statistical analysis of detection performance plus length and depth sizing performance is included. The results from the quantitative statistical analysis are compared to the results obtained for relevant techniques applied in PARENT blind testing as a way to judge performance relative to established techniques. In addition, a qualitative review of some of the response images (B-scan images) is also performed. The review of response images mostly focuses on crack tip response detection and trying to draw conclusions regarding depth sizing performance from crack tip response images.

Section 2.0 of this report includes a description of the test block used in this blind test evaluation of PARENT open techniques and defines the objective area for examination. Descriptions of the open techniques used in the test are included in Section 3.0. Descriptions are also documented in PNNL-23387 (Meyer 2014); however, because only a subset of those techniques were implemented in this effort, their descriptions are also provided here for convenience. Section 4.0 includes the results from the quantitative statistical detection performance and sizing analyses and Section 5.0 includes a review of some response images. Finally, conclusions are summarized in Section 6.0.

2.0 Description of Test Block

This section briefly describes the test block that was partially examined in the blind test assessment of open techniques from PARENT. Most of the open test participants are associated with universities or other research organizations and are not commercial providers of inspection services. As a consequence, their laboratories are equipped with limited rigging capabilities that preclude testing on test pieces that are too large; thus, a small-bore dissimilar metal weld (SBDMW) test block was selected for this test (as opposed to a large-bore dissimilar metal weld test block).

The test block is an SBDMW test block with full circumference and the coordinate system defined for acquiring and reporting data is provided in Figure 2.1. The zero point is defined as that location on the test block where X=0, Y=0, and Z=0. Figure 2.1 also provides the definitions for the directional vectors X+, Y+, and Z+ in relation to the zero point and with respect to the material construction of the test block. The location for Z=0, Y=0 is at the outer diameter (O.D.) surface of the test block, at the center of the weld, and is located a distance "D" from the face edge of the carbon steel pipe. The X=0 location is indicated by a punch marking on the test block outer surface. A summary of dimensions for the test block is provided in Table 2.1. For the purpose of this test, the target examination area (referred to as the "objective area") was restricted to a region from X=0 to X=1000 mm. This restriction was applied because many of the teams did not possess equipment for performing automated scanning and had to collect data by scanning manually.

Artificial flaws were fabricated into the test block using a process known as weld solidification cracking. Weld solidification cracks (SCs) may be used to simulate service-type defects such as interdendritic stress corrosion cracking or primary water stress corrosion cracking. The region where the cracks are fabricated is excised and filled with a "poisoned" weld metal that is designed to crack upon cooling. In this case, the SCs are tightened either through a welding process or through application of a mechanical pressure during fabrication to result in cracks with narrower width. Care must be taken when SCs are to be used to determine the capability of NDE methods because the region of flaw fabrication may be too obvious for the examination, similar to flaws that are implanted, especially in base metal. For this reason, SCs are recommended for simulating flaws in weld regions.

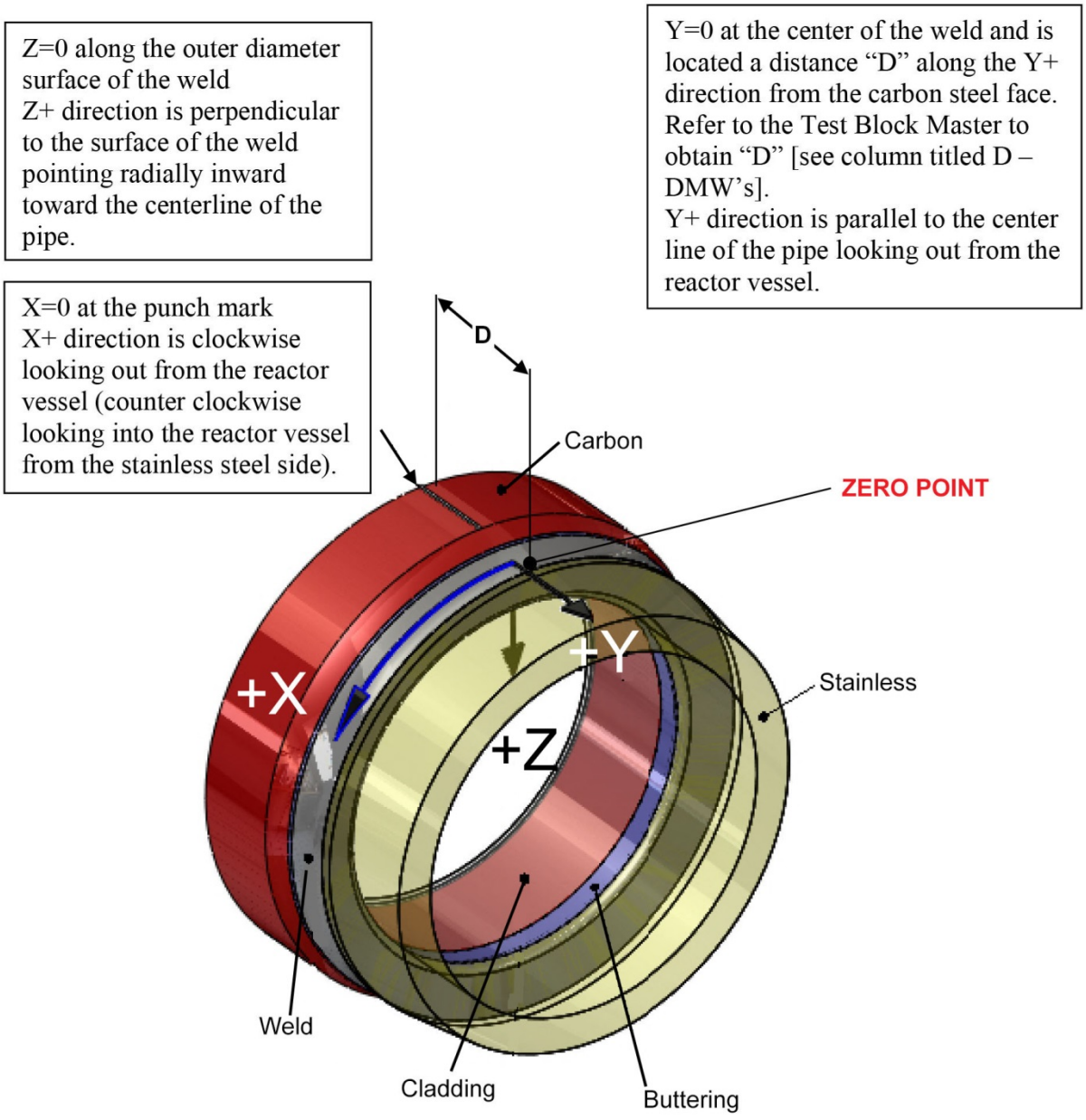

Figure 2.1. Coordinate System Definition for the SBDMW Test Block

Table 2.1. Summary of Dimensions for the Test Block

Test Block Identification Number	Inner Diameter, mm	Outer Diameter, mm	Thickness, mm	D, mm	Circumferential Extent, degrees
P40	736.0	815.0	39.5	170.0	360.0

3.0 Description of Techniques

This section provides a description of the open techniques implemented in this study. While descriptions of all PARENT open test techniques are documented in PNNL-23387 (Meyer 2014), this section focuses only on describing those open techniques applied in the blind testing assessment that is the subject of this report. The original content that test teams provided is included in the appendices of PNNL-23387. Where applicable, reference to this material is made in the sections below. In total, ten open techniques were applied in this blind test assessment by eight teams. All teams applied a single technique with the exception of team 29, which applied three techniques: phased array asymmetric time-of-flight diffraction (PA-ATOFD), phased array twin probe (PA-TP), and higher harmonic ultrasonic testing (HHUT). Descriptions of all of the techniques applied in this study are provided in the remaining subsections.

3.1 Subharmonic Phased Array (Team 6)

The subharmonic phased array (SHPA) technique, or subharmonic phased array for crack evaluation (SPACE), was implemented by team 6 and is an advanced ultrasonic testing technique that is based on the observation of nonlinear acoustic responses from material damage and phased-array imaging techniques. More specifically, for crack evaluation, SHPA is based on the periodic contact (clapping) of the faces of tight cracks during the compressional period of an applied elastic wave, also referred to as contact acoustic nonlinearity (CAN). In this case, the clapping can occur if the amplitude of the elastic displacement is greater than the crack face separation (see Figure 3.1). In comparison to observations of higher harmonic generations, observations of subharmonic responses exhibit better selectivity to closed cracks (Ohara et al. 2008).

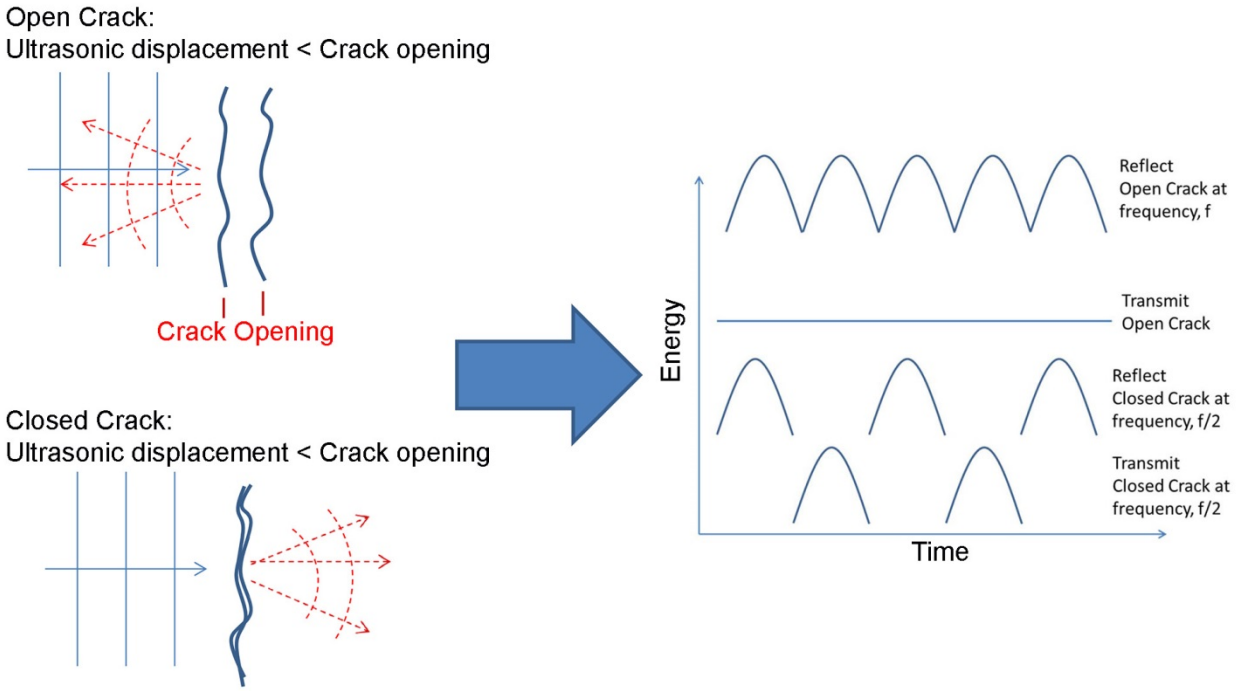

Figure 3.1. Illustration of the Crack Face "Clapping" Phenomena that is the Basis for Subharmonic Generation when Elastic Waves are Applied to Tight Cracks

SHPA provides array images at the fundamental frequency f and subharmonic array images at the subharmonic frequency f/2, visualizing the open and closed parts of cracks, respectively. SHPA was implemented in a surface acoustic waves (SAW) mode to assess flaw detection and length sizing capability and in a bulk wave mode to assess flaw depth sizing capability (see Figure 3.2). As the figure shows, SAW mode requires mounting the transducer on the same surface as the flaw's surface-breaking feature, while bulk wave mode is implemented similar to the way conventional ultrasonic testing (UT) and phased-array UT (PAUT) would typically be performed in the field with the transducer mounted on the component O.D. surface.

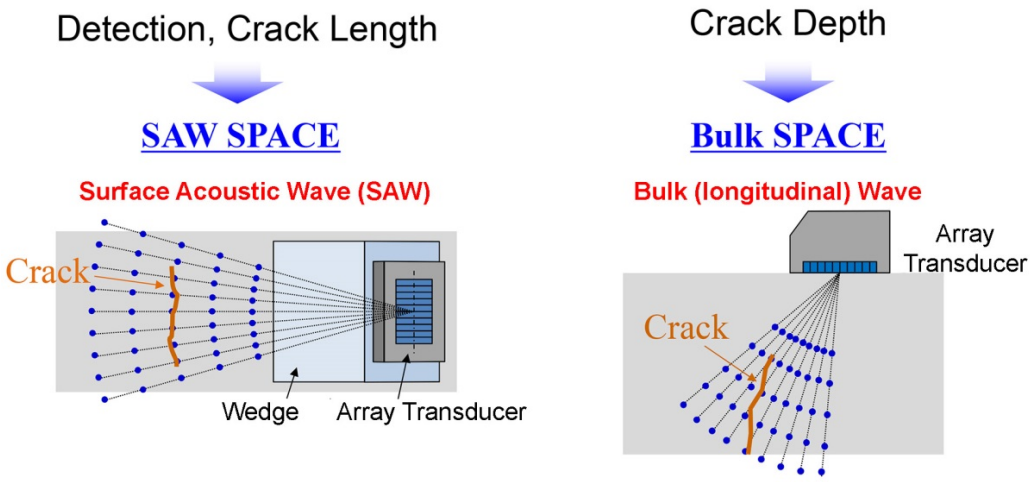

Figure 3.2. Illustration of SPACE Implementation in SAW Mode to Assess Detection and Length Sizing Capability and in Bulk Wave Mode to Assess Depth Sizing Capability

SHPA was implemented using a single phased-array transducer for transmitting and receiving and using short burst waves for excitations. For both SAW and bulk wave modes, a 5 MHz matrix array transducer with 32 elements at 0.5 mm pitch spacing was used. A 2 MHz (1 MHz subharmonic), 3-cycle burst excitation was applied to the transducer for SAW mode operation while a 7 MHz (3.5 MHz subharmonic), 3-cycle burst excitation was applied for bulk wave mode. Input parameters for both SAW and bulk wave mode implementations are provided in Table 3.1. An illustration of SHPA data analysis for length and depth sizing of flaws is provided in Figure 3.3.

A PowerPoint overview describing how the SHPA technique was implemented for PARENT can be found in Appendix C.1.2, and a more detailed description of how SHPA was implemented in PARENT can be found in Appendix C.5.3 of NUREG/CR-7236 (Meyer et al. 2017).

Table 3.1. Summary of Input Condition Parameters for the SHPA SAW and Bulk Wave Modes

	SAW Mode	Bulk Wave Mode
Excitation Frequency (MHz)	2 MHz	7 MHz
Subharmonic Generation (MHz)	1 MHz	3.5 MHz
Excitation Burst Cycles	3	3
Steering Angles	Skew: −14° to 15° (1° step)	Refraction: 12° to 71° (1° step)
Application	Detection and length sizing	Depth sizing

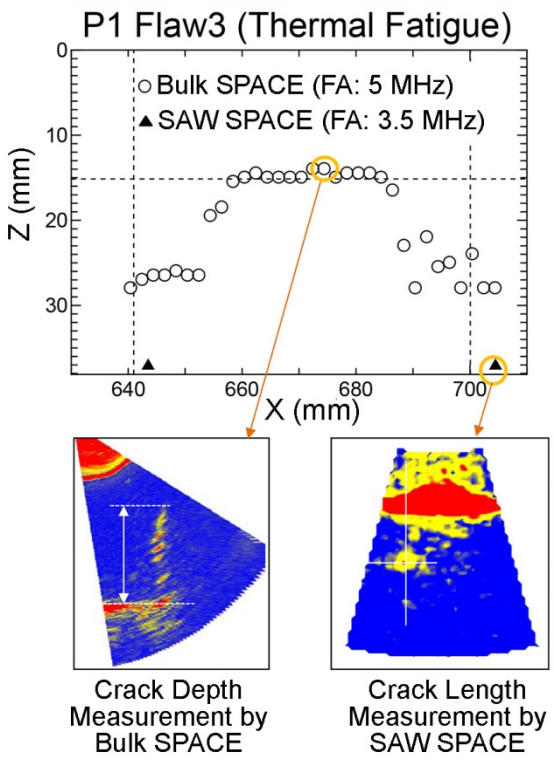

Figure 3.3. Illustration of SHPA Data Analysis for Length and Depth Sizing of Flaws

3.2 Phased-Array Asymmetrical Beam Time-of-Flight Diffraction (Team 29)

The PA-ATOFD technique is implemented using a pair of two-dimensional (2D) matrix array probes, with one probe serving as the transmitter and the other probe serving as the receiver (Ishida and Kitasaka 2013). Each probe is mounted on opposite sides of the flaw under investigation, similar to a regular time-of-flight diffraction (TOFD) configuration. However, the PA-ATOFD technique is based on the direct insonification of the crack tip as opposed to listening for the crack tip response when the base of the crack is insonified. With PA-ATOFD, the scan angle and focal depth of the transmitting and receiving probes may be arbitrarily adjusted, as indicated in Figure 3.4, to obtain the tip echo of the flaw from multiple scan angles. This enables improved discrimination of tip-echo signals from sources of noise through synthesis of the data from multiple scan angles and depths of focus as illustrated in Figure 3.5 by a method referred to as the multi-angle synthesis method. A procedure is applied to correct measured depth values of indications to estimate "true" depth for both the PA-ATOFD and phased-array twin probe (PA-TP) and is described for both techniques in Section 3.3.

A PowerPoint overview of how the PA-ATOFD technique was implemented in PARENT can be found in Appendix C.1.2, and a more detailed description of how PA-ATOFD was implemented in PARENT can be found in Appendix C.5.1 of NUREG/CR-7236 (Meyer et al. 2017).

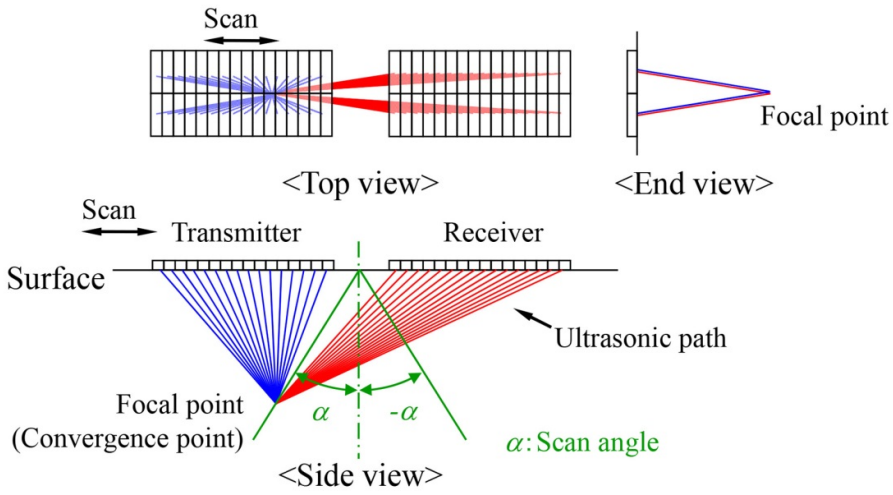

Figure 3.4. Schematic Illustration of the PA-ATOFD Technique

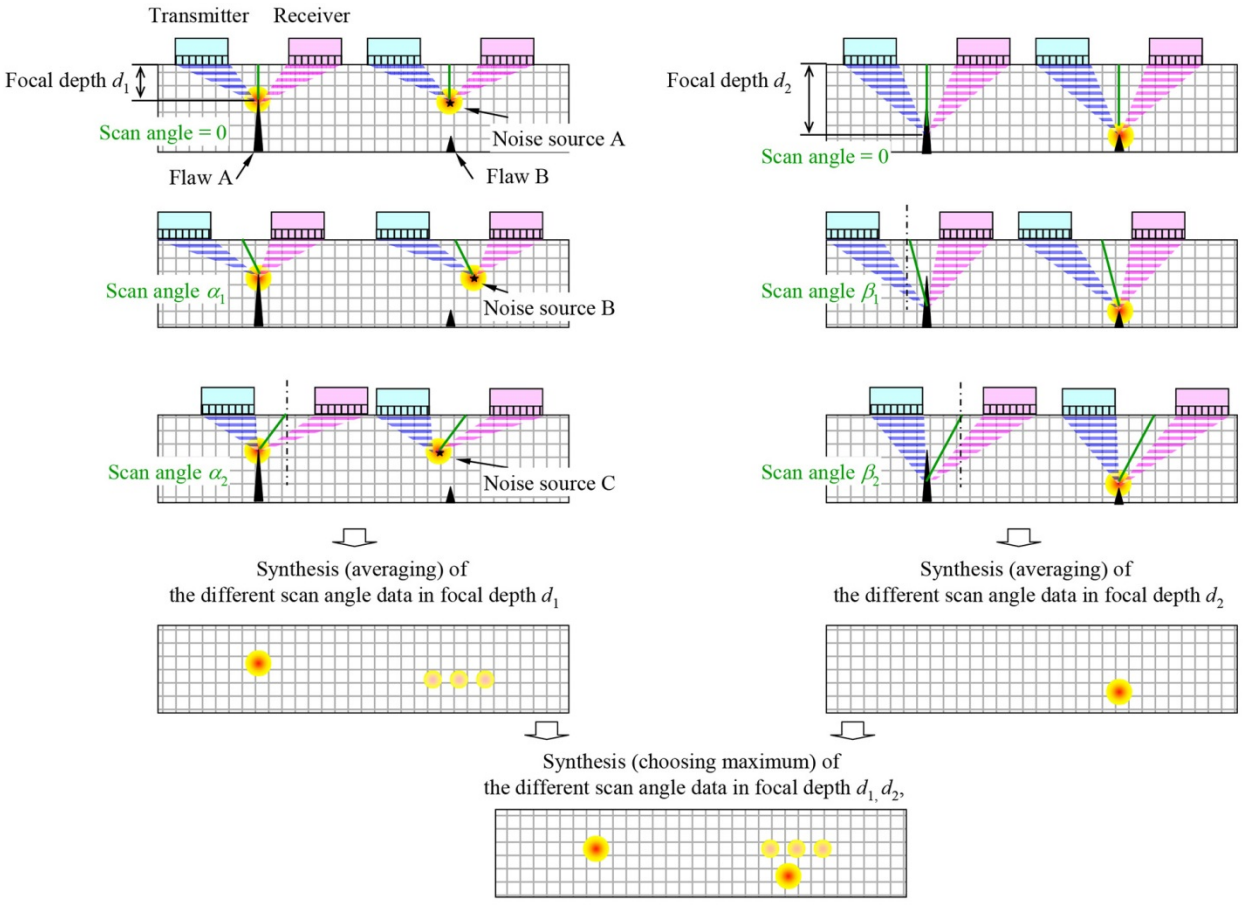

Figure 3.5. Data from Multiple Scan Angles and Depths of Focus are Synthesized in PA-ATOFD to Help Discriminate Crack Tip Signals from Noise

3.3 Phased Array Twin Probe (Team 29)

The PA-TP technique is very similar to the PA-ATOFD technique except that both the transmitter and receiver are oriented in the direction perpendicular to the scan direction as opposed to parallel to the scan direction for the PA-ATOFD technique. An illustration of the PA-TP technique is provided in Figure 3.6. With PA-TP, the scan angle and focal depth of the transmitting and receiving probes may be arbitrarily adjusted to enable improved discrimination of tip signals from sources of noise through synthesis (by multi-angle synthesis method) of the data from multiple scan angles and depths of focus as illustrated in Figure 3.7. The selection of the PA-ATOFD or PA-TP method will depend significantly on access conditions.

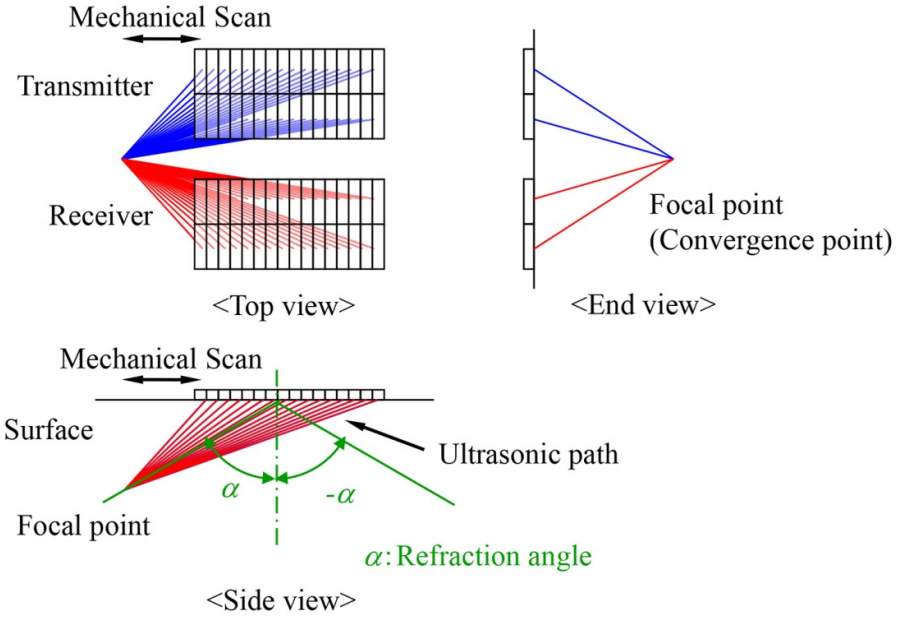

Figure 3.6. Schematic Illustration of the PA-TP Technique

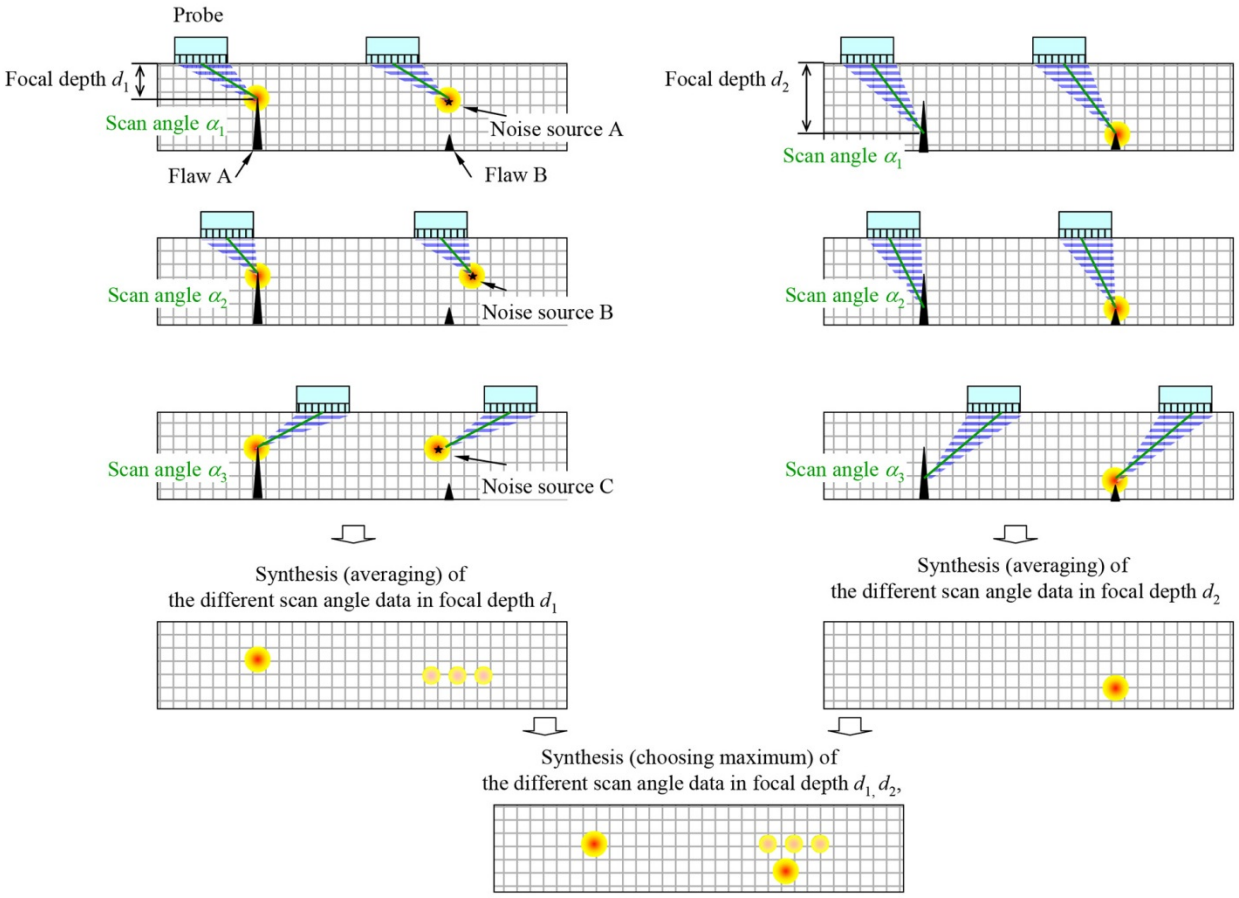

Figure 3.7. Data from Multiple Scan Angles and Depths of Focus are Synthesized in PA-TP to Help Discriminate Crack Tip Signals from Noise

In order to estimate the actual depth of a flaw, the measured depth from a B-scan image (example shown in Figure 3.8) is corrected by using a side-drilled-hole (SDH) reference block. The depth values recorded in the data sheets are the corrected depth values.

The procedure for determining the corrected depth values is as follows:

1. Depth correction for the PA-ATOFD and PA-TP techniques in the axial and circumferential scan directions was performed by using SDHs (t/4 and t/2 depth; t is the block thickness) in a large-bore reference block with a thickness of 77.5 mm (Figure 3.9).
2. Figure 3.10 shows the response images from the SDHs by the multi-angle synthesis method for the four measurements mentioned above.
3. The measured depth is estimated from the location of the peak amplitude in the response from the SDH. The differences in the measured depths and the true depths for the t/2 and t/4 SDHs are calculated and averaged together to estimate a correction that should be applied for determining flaw depth (Table 3.2).
4. Flaw depth is calculated by applying the correction to the measured value. This corrected flaw depth value is what was reported in datasheets.

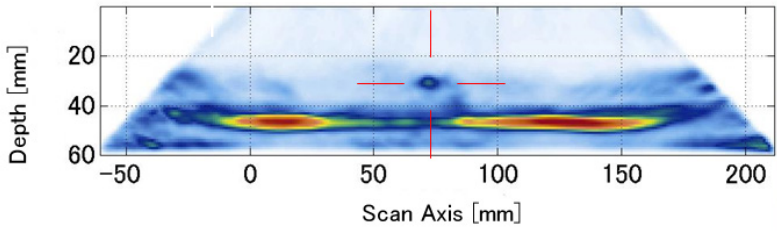

Figure 3.8. Example of a B-scan Response Image for PA-ATOFD and PA-TP Techniques. The red cursor highlights a response that is suspected to represent the tip of a crack.

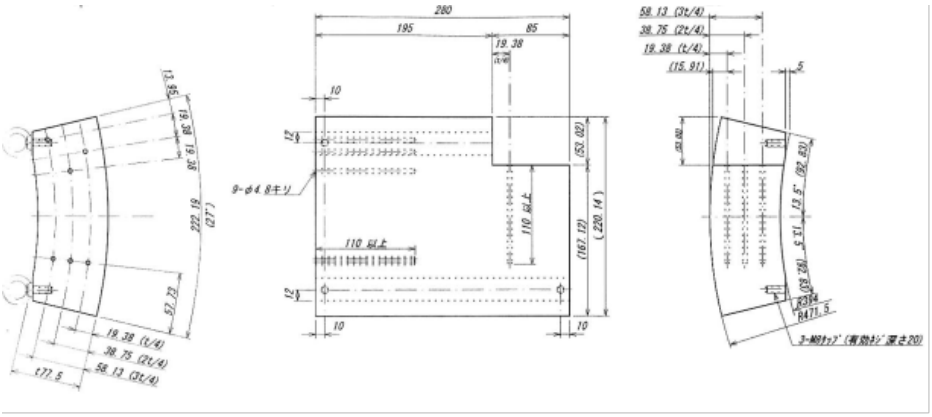

Figure 3.9. Large Bore Reference Block

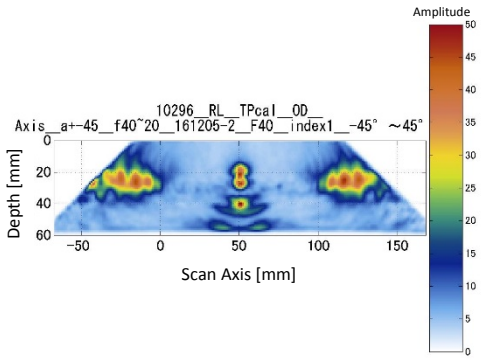

PA-TP, Axis

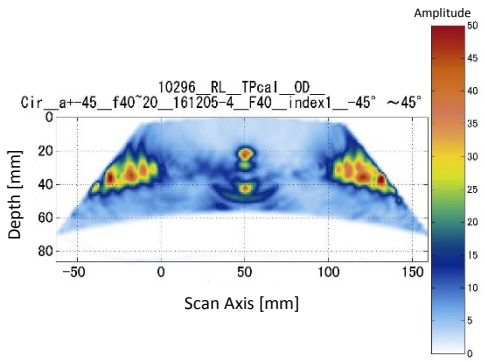

PA-TP, Cir.

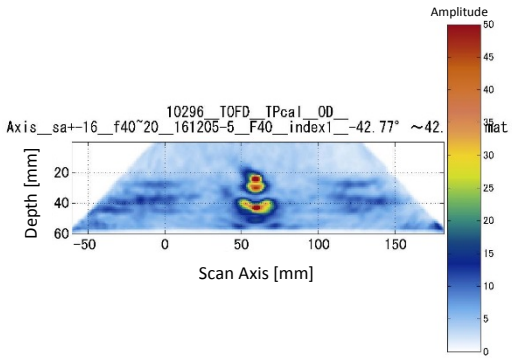

PA-ATOFD, Axis

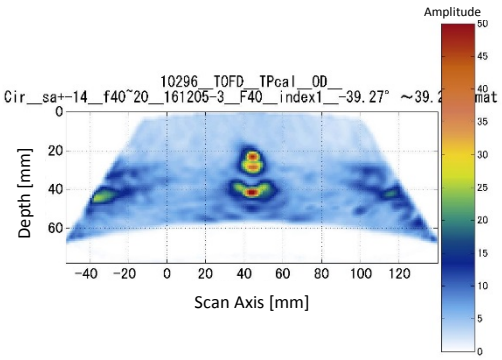

PA-ATOFD, Cir.

Figure 3.10. Images of Synthesis of Indication from the SDH by the Multi-Angle Synthesis Method

Table 3.2. Correction Applied to Measurements of Indication Depth

	PA-TP, Axial		PA-TP, Circumferential	
SDH (real depth)	t/4 (19.375)	t/2 (38.75)	t/4 (19.375)	t/2 (38.75)
measurements	21	40	23	42
Difference from the real depth of the SDH	1.625	1.25	3.625	3.25
Average difference	1.4375		3.4375	
	PA-ATOFD, Axial		PA-ATOFD, Circumferential	
SDH (real depth)	t/4 (19.375)	t/2 (38.75)	t/4 (19.375)	t/2 (38.75)
measurements	24	43	23	41
Difference from the real depth of the SDH	4.625	4.25	3.625	2.25
Average difference	4.4375		2.9375	

A PowerPoint overview of how the PA-TP technique was implemented in PARENT can be found in Appendix C.1.2, and a more detailed description of how PA-TP was implemented in PARENT can be found in Appendix C.5.1 of NUREG/CR-7236 (Meyer et al. 2017).

3.4 Adaptive Phased-Array UT Focusing (Team 22)

The time reversal technique for focusing of PAUT (PA-TRT) is a means for transmitting electronically focused ultrasonic energy through even nonhomogeneous media (Fink 1992; Fink 1999). PA-TRT is an iterative technique in which the reflection of ultrasonic energy from a target is interpreted as the emission of a weak ultrasonic signal from the target, which is detected by an array transducer. Under this interpretation, the target acts as a localized source and the sound field spreads as it propagates away from the target towards the array transducer. After digitization and recording of the signals at the transducer, they are time reversed and re-transmitted to generate a sound field that becomes more focused as it travels from the array transducer back to the target (see Figure 3.11). As the process is repeated, the focusing of the sound field improves. Formally, the basis for PA-TRT lies in the reciprocity property of the wave equation.

A significant advantage of PA-TRT is its ability to adaptively focus in nonhomogeneous media. In contrast to synthetic aperture focusing techniques (SAFT), knowledge of the actual path that ultrasonic signals travel through the test material is not required. The techniques should be capable of performing both inner diameter (I.D.) and O.D. inspections.

A PowerPoint overview of how PA-TRT was implemented in PARENT can be found in Appendix C.1.1 and a more detailed description of how PA-TRT was implemented in PARENT can be found in Appendix C.3.6 of NUREG/CR-7236 (Meyer et al. 2017).

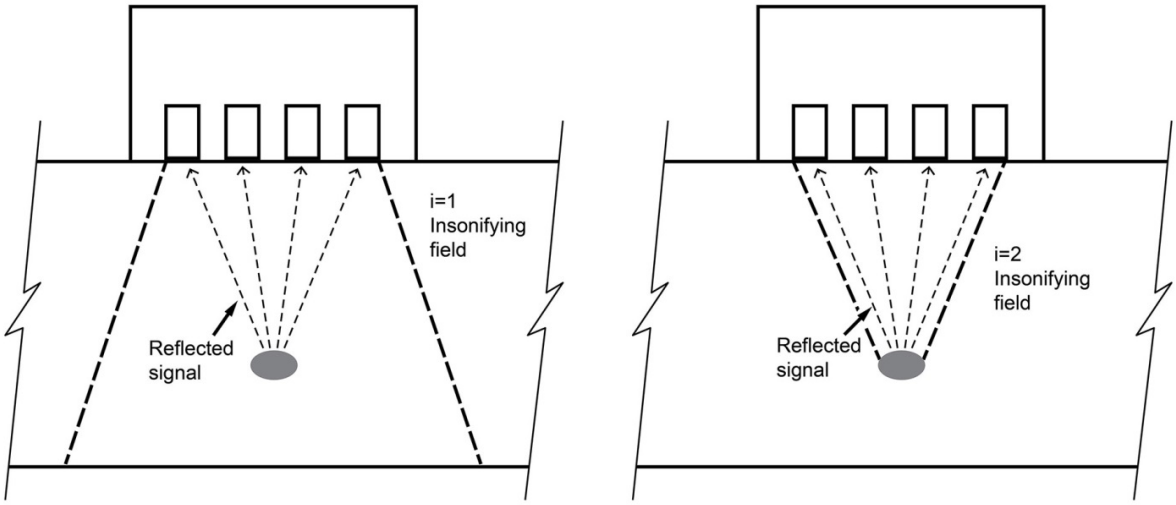

Figure 3.11. Illustration of the PAUT Time Reversal Technique (PA-TRT) Concept for Focusing Ultrasonic Energy

3.5 Higher Harmonic Ultrasonic Technique (Teams 29 and 30)

The HHUT for crack detection is also based on the phenomenon of CAN, as illustrated in Figure 3.1. Higher harmonics are generated, in addition to subharmonics, because of the nonlinearity induced in signals as they interact with the crack faces (illustrated in Figure 3.12). As a result, the acoustic waveform becomes distorted and the higher harmonic frequency components are generated in the transmitted wave or in the reflected wave from the crack.

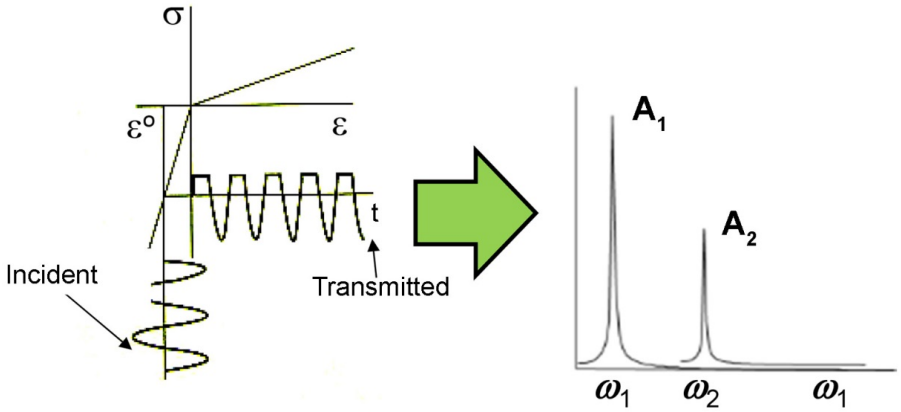

Figure 3.12. Illustration of Higher Harmonic Generation Because of the CAN Phenomenon

Thus, it would be possible to detect closed cracks by monitoring the magnitude of the higher harmonic frequency component generated in the transmitted or the reflected wave. Usually, the relative nonlinear parameter (β′) defined by the ratio of the second-order harmonic frequency magnitude to the power of the fundamental frequency magnitude is used as the monitoring parameter (Jhang 2000), although the generation of higher-order harmonics can provide useful monitoring parameters as well. Overviews of how HHUT was implemented in PARENT can be found in the Appendices B.1.1 and B.1.2 of NUREG/CR-7236 (Meyer et al. 2017). More detailed descriptions of how HHUT was implemented in PARENT can be found in Appendices C.3.7 and C.5.5 of NUREG/CR-7236.

HHUT can be implemented in pulse-echo (PE) or transmit-receive (TR) modes as shown in Figure 3.13. The technique could be implemented on the component I.D. or O.D. To ensure sufficient interaction with the crack faces, the transducers should be mounted at an angle with respect to the crack faces or perpendicular to them. The advantage of this technique compared to conventional UT is its sensitivity to closed cracks. However, compared to the subharmonic techniques described previously, higher harmonics are not as selective for closed cracks, although this may not necessarily be viewed as a drawback for all applications. A disadvantage of HHUT is that physical understanding of the technique is incomplete. As a consequence, quantitative characterization of flaws by HHUT will be difficult with a single measurement and may require relative comparison to responses obtained from already well-characterized flaws.

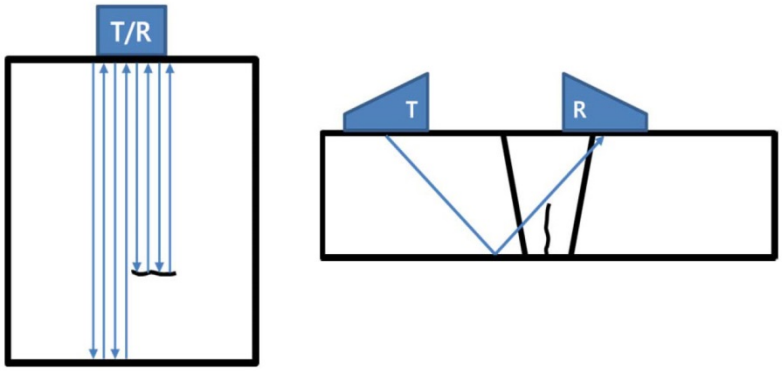

Figure 3.13. Illustration of HHUT Implementation in PE (*left*) and TR (*right*) Modes

3.6 Three-Dimensional Synthetic Aperture Focusing Technique (Team 17)

SAFT is a signal processing technique to correct for distortions in scanning images as a result of transducer focusing distortion, to obtain images with improved resolution. Similar to PAUT, SAFT enables electronic control over transducer focus and can greatly improve inspection performance compared to conventional UT. However, with SAFT, this control is implemented through post-processing of collected data. The basis for SAFT is easiest to illustrate for the 2D scenario as shown in Figure 3.14.

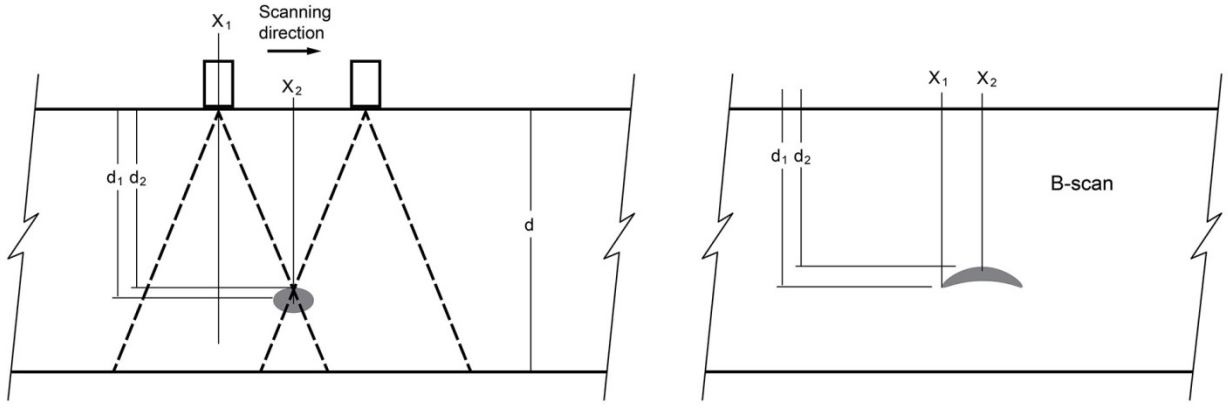

Figure 3.14. 2D Illustration of SAFT Correction for Focusing Distortion in Ultrasonic Inspections (*left*); B-scan Illustrating Distortion Caused by Beam Focusing Effects (*right*)

In this figure, an unfocused transducer located at x_1 transmits a signal and receives an echo from the defect located at x_2. As the transducer is scanned along x over the location of the defect, the B-scan image is created illustrating the distortion of the actual defect as a result of poor focusing. This distortion can be corrected with knowledge of the incident beam width and path traveled by ultrasound through the test piece (Elbern and Guimaraes 1999),

$$d_2 = \left[d_1^2 - \left(x_1 - x_2 \right)^2 \right]^{1/2} \tag{3.1}$$

SAFT can also be implemented with a transducer array in which each element in the transducer can be individually excited in sequence while all elements "listen" for echo signals. Using a matrix-array transducer allows SAFT imaging to be performed in three dimensions (3D) (see Figure 3.15). An obvious advantage of implementing SAFT with array transducers is that it enables flaws to be characterized much faster and reduces the amount of mechanical scanning required for the transducer. Data from 3D-SAFT can be presented in the form of a variety of images including A-scans, B-scans, C-scans, and D-scans. Thus, analysis procedures are similar to those for PAUT. A PowerPoint overview of how the 3D-SAFT was implemented in PARENT can be found in Appendix C.1.2, while a more detailed description of how the 3D-SAFT technique was implemented in PARENT can be found in Appendix C.5.2 of NUREG/CR-7236 (Meyer et al. 2017).

3D-SAFT is a powerful technique in that it enables near arbitrary focusing and rapid characterization of defects through post processing of data. Similar to PAUT, 3D-SAFT requires the use of sophisticated probes and data recording and processing equipment.

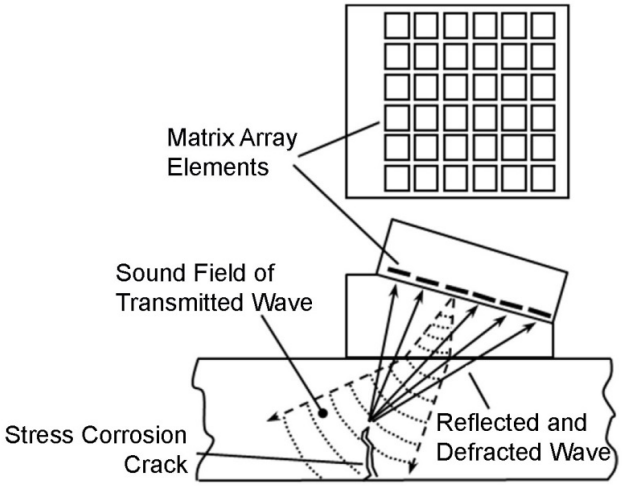

Figure 3.15. Implementation of 3D SAFT Using a Matrix-Array Transducer. Individual elements are excited in sequence, while all elements "listen" for echoes.

3.7 Advanced Eddy Current Testing Technique (Team 33)

In practice, an eddy current probe consists of one or more coils with the axis alignment most often perpendicular or parallel to the inspection surface normal. An alternating current source is applied to the one or more coils, generating magnetic fields. These magnetic fields induce eddy currents in the conducting materials when the probe is positioned nearby (see Figure 3.16). Flaws and defects in the test material impede the flow of eddy currents manifesting as a change in the measurable eddy current coil impedance. An important parameter for eddy current testing is the skin depth,

$$\delta = \sqrt{\frac{1}{\pi f \sigma \mu}} \tag{3.2}$$

which provides a measure of the depth to which eddy current fields can penetrate in a test material. As can be seen from Eq. (3.2), this quantity depends on the coil frequency, f, and electrical conductivity, σ, of the test material (μ is the magnetic permeability). Thus, in metal components, the depth of penetration is usually small and the eddy current technique is often limited to surface examinations. Multi-coil techniques include separate coils for the generation of eddy current fields in the test material and for detection of the fields at the surface, as illustrated in Figure 3.17. These types of probes may also be referred to as reflection probes, driver-pickup, exciter-pickup, or send-receive probes. This contrasts with conventional eddy current testing (ECT) in which the same coil is used for both field generation and for signal reception. A PowerPoint overview of how the second technique (referred to as the advanced ECT technique [AECT]) was implemented can be found in Appendix C.1.2, and a more detailed description of how AECT was implemented in PARENT can be found in Appendix C.5.7 of NUREG/CR-7236 (Braatz et al. 2014).

The advantage of eddy current techniques over ultrasonic techniques is that they are usually more sensitive to small defects and the probes do not require fluid coupling to the test material surface. As noted, a significant disadvantage of eddy current techniques is that they are often relegated to surface inspections and are not very useful for characterizing the depth of flaws beyond 1 or 2 mm. In addition, the increased sensitivity of ECT can make it more prone to false calls from the pick-up of signals from superficial surface imperfections (such as scratches) and ECT techniques can be sensitive to lift-off variations and variations in material conductivity and/or magnetic permeability.

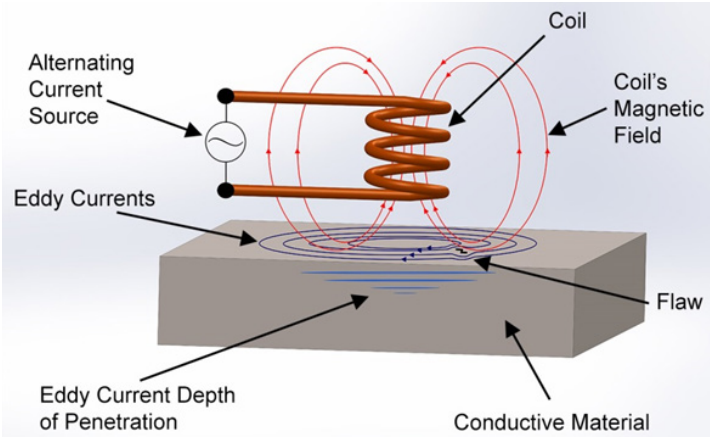

Figure 3.16. Depiction of a Single-Coil Eddy Current Probe with an Alternating Current Excitation, Induced Magnetic Fields, and Induced Eddy Currents. Disturbance of eddy current flow can be caused by existence of a defect.

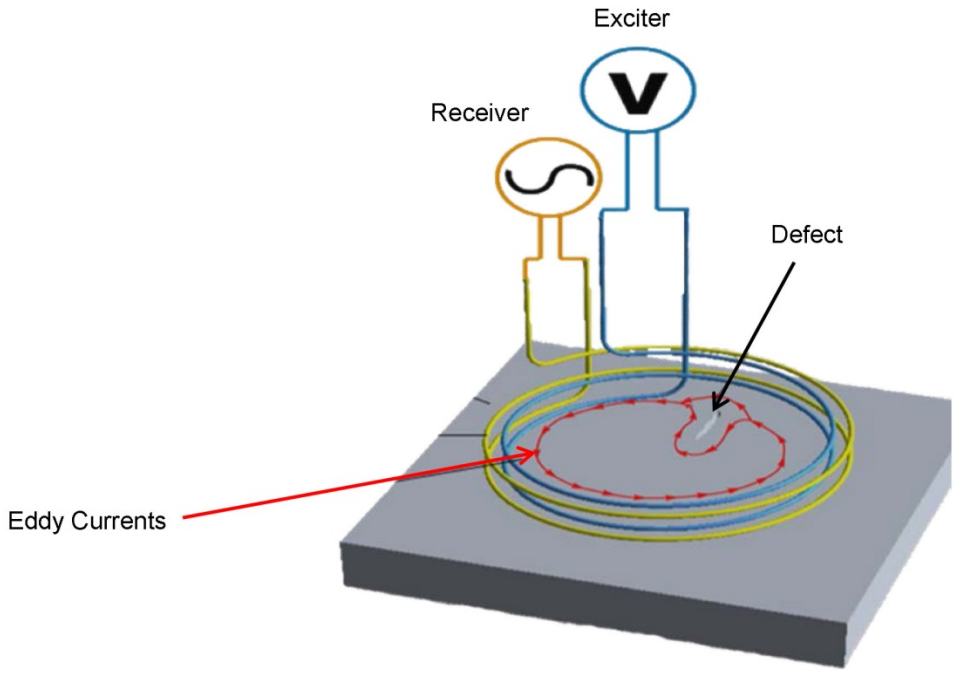

Figure 3.17. Schematic Illustration of an Eddy Current Probe with Separate Coils for Field Excitation and for Signal Detection

3.8 Orthogonal Coil Array Eddy Current Technique (Team 16)

The orthogonal coil array eddy current technique (OCECT) was implemented using a commercial eddy current probe with an array of orthogonal coil pairs. The single orthogonal coil pair configuration has also been referred to as "plus-point" because when viewed from the test piece the intersecting orthogonal coils look similar to a plus sign (Figure 3.18). The OCECT is a differential eddy current technique meaning that the output of one coil is referenced to the output of the other coil. Differential eddy current probes are typically less sensitive to lift-off and surface irregularities. One advantage of OCECT is that it has directional sensitivity to flaws, making it possible to distinguish between axial and circumferential defects. The orthogonal coil configuration helps minimize the influence of flaw orientation with respect to the probe performance as defects that are parallel to the current flow can be missed. Rotation of the OCECT probe can also be performed to further minimize the influence of flaw orientation. A PowerPoint overview of how OCECT was implemented in PARENT can be found in Appendix C.1.2, and a more detailed description of its implementation can be found in Appendix C.5.6 of NUREG/CR-7236 (Meyer et al. 2017).

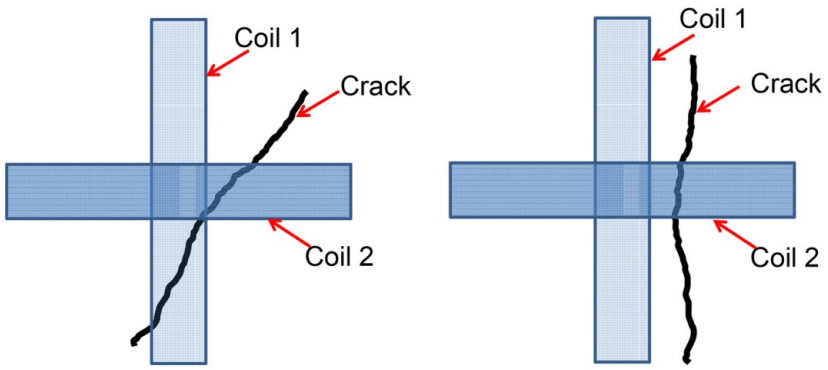

Figure 3.18. Illustration of Orthogonal Coil Pair and Relative Orientation to Surface Crack Profiles. Rotation can be employed in the use of this probe configuration to minimize the influence of relative crack orientation on response.

3.9 Ultrasound Infrared Thermography (Team 20)

Ultrasound infrared thermography (UIRT) is based on the detection of thermal energy generated when elastic energy is absorbed by a defect and converted to thermal energy through thermos elastic effects. An illustration of the general concept is provided in Figure 3.19. The result is an infrared image in the test specimen to which standard image analysis techniques may be applied to characterize defects based on temperature differences (see Figure 3.20). The main UIRT techniques include pulsed, phase lock-in, or a combination of both (Dillenz et al. 2000; Maldague 2001). A PowerPoint overview of how UIR was implemented in PARENT can be found in Appendix C.1.1, while a more detailed description is provided in Appendix C.3.4 of NUREG/CR-7236 (Meyer et al. 2017).

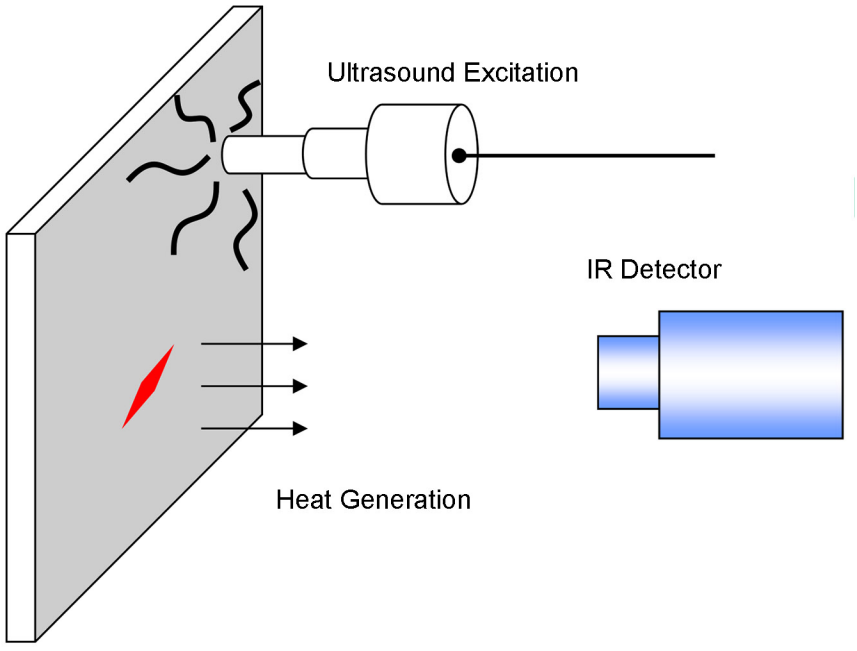

Figure 3.19. Illustration of the UIRT Concept

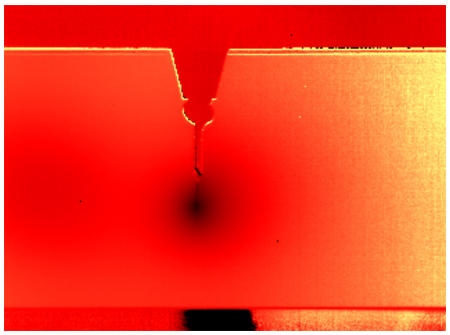

Figure 3.20. UIRT Image of a Test Specimen with Crack

With lock-in phase UIRT, amplitude and phase information about the thermal waves emitted from the specimen is preserved for several frequencies. The advantage of this is that it enables characterizing the depth of a source of thermal emissions within the test component. With pulsed phase lock-in thermography, broadband thermal signals arriving at each pixel of an infrared (IR) detector camera are analyzed using Fast Fourier Transform (FFT) analysis. The advantage of UIRT is that it potentially enables more rapid examination of large areas based on camera images in contrast to techniques that would require a point-by-point raster scan. The technique could be used to perform both OD and ID inspections. The potential disadvantage of the technique is that it requires a low thermal noise background so that flaws could be imaged reliably.

4.0 Detection and Sizing Analysis Results

This section summarizes detection and sizing analysis results obtained for the open techniques applied to the blind test over the objective area of test block P40. In addition, detection and sizing analysis data is also summarized for procedures that were applied to P40 during the PARENT blind test by reanalyzing that data over the objective area defined for this test. In this way, the performances of technologies applied in the open test (emerging technologies) can be compared to the performances of technologies applied in the blind test (established technologies) of PARENT. Indication plots for the emerging technologies and the established technologies are provided in Appendices A and B, respectively. The rest of the section provides a summary of overall detection and false call performances for emerging and established technologies and summaries of depth and length sizing errors for emerging and established technologies. Probability of detection (POD) curves and depth and length sizing regression plots are provided in Appendices C, D, and E, respectively.

A summary of overall detection and false call rate performance is provided in Table 4.1 and Table 4.2 for the emerging and established technologies, respectively. In these tables, NOBS refers to the number of observations, which is the number of flaws within the inspection region for these tables. POD is the probability of detection (%), FCP is the false call probability (%), and FCR is the false call rate (#/m). Overall, there are a few emerging technologies that appear to have performed as well as the best-performing established technologies (all except UT.134, UT.126, and PAUT.126). These include techniques ECT.16, SAFT.17, AECT.17, and SHPA.6. Technique PA-TP.29 (surface) also demonstrated high POD but the FCR was approximately twice as large or greater as FCR observed for the best-performing established technologies. Several of the emerging technologies exhibited high POD with exceptionally large FCRs. These include PA-ATOFD.29 (interior), PA-TP.29 (interior), and HHUT.29. For these techniques, teams reported indications discovered in the test block interior (not surface-breaking) even though the objective of the test was aimed at detection of surface-breaking flaws and interior flaws or defects were not included in the true-state description. This suggests that the sensitivity threshold for these techniques may have been set too low for this test resulting in high noise. It is conceivable that the FCRs could be improved considerably if the personnel implementing these techniques had more training and if better procedures were developed for implementation of the techniques.

Summaries of POD as a function of flaw depth and length do not provide insight additional to that provided by the overall POD and FCR summaries in Table 4.1 and Table 4.2, and are included in Appendix C.

Summaries of depth sizing errors for emerging and established technologies are provided in Table 4.3 and Table 4.4, respectively. In these tables, NOBS refers to the number of observations, which is equal to the number of detected flaws. Bias and root-mean-square error (RMSE) are sizing error statistics that are defined by Equations (4.5) and (4.7) in NUREG/CR-7235 (Meyer and Heasler 2017). These tables indicate a clear disparity in depth sizing performance between emerging and established technologies. If results for open techniques and blind procedures for which NOBS is less than five are excluded, then the best depth sizing observed for the emerging technologies is by technique PA-TP.29 (surface) with an RMSE of 9.2 mm. For the established technologies excluding UT.134, UT.126, and PAUT.126, the depth sizing RMSE is 4.8 mm or less.

Table 4.1. Overall Detection and False Call Summary for Open Techniques (Emerging)

	NOBS	POD	FCP	FCR	Access
ECT.16	6	100	0	0.0	I.D.
SAFT.17	5	100	4	1.4	O.D.
UIRT.20	6	17	0	0.0	O.D.
PA-ATOFD.29 (interior)	6	83	46	24.5	O.D.
PA-ATOFD.29 (surface)	6	50	17	7.7	O.D.
PA-TP.29 (interior)	6	100	60	36.8	O.D.
PA-TP.29 (surface)	6	100	7	3.1	O.D.
HHUT.29	6	83	67	44.5	O.D.
HHUT.30	2	50	3	1.1	O.D.
AECT.33	6	100	4	1.5	I.D.
SHPA.6	6	100	0	0.0	O.D.

Table 4.2. Overall Detection and False Call Summary for Blind Techniques (Established)

	NOBS	POD	FCP	FCR	Access
PAUT.108	6	83	4	1.5	O.D.
UT.108	6	83	4	1.5	O.D.
PAUT.115	6	100	0	0.0	O.D.
UT.TOFD.117	6	100	0	0.0	O.D.
PAUT.126	6	50	0	0.0	O.D.
UT.126	6	17	7	3.1	O.D.
PAUT.128	6	100	0	0.0	O.D.
UT.134	6	67	4	1.5	O.D.

Table 4.3. Summary of Depth Sizing Error for Open Techniques (Emerging)

	NOBS	Bias	RMSE
SAFT.17	5	5.5	12.5
PA-ATOFD.29 (interior)	5	−6.7	11.4
PA-ATOFD.29 (surface)	3	1.0	2.5
PA-TP.29 (interior)	6	−5.3	9.8
PA-TP.29 (surface)	6	−1.8	9.2
HHUT.29	5	−19.8	21.4
SHPA.6	6	1.6	8.2

Table 4.4. Summary of Depth Sizing Error for Blind Techniques (Established)

	NOBS	Bias	RMSE
PAUT.108	5	−2.1	2.5
UT.108	5	−3.1	3.8
PAUT.115	6	−0.6	1.5
UT.TOFD.117	6	−1.7	4.8
PAUT.126	3	−7.8	9.0
UT.126	1	−19.0	19.0
PAUT.128	6	−1.7	4.8
UT.134	4	−17.4	18.8

Summaries of length sizing errors for emerging and established technologies are provided in Table 4.5 and Table 4.6, respectively. NOBS, Bias, and RMSE have the same definitions for length and depth sizing. If results for open techniques and blind procedures for which NOBS is less than five are excluded, then these tables indicate that two of the open techniques (ECT.16 and SHPA.6) demonstrate better length sizing performance than all of the blind procedures. Otherwise, however, the established technologies appear to outperform the emerging technologies as the range of RMSEs for established technologies is 6.7 mm to 13.4 mm. For emerging technologies (excluding ECT.16 and SHPA.6), the range of RMSEs is 13.6 mm to 30.2 mm.

Table 4.5. Summary of Length Sizing Error for Open Techniques (Emerging)

	NOBS	Bias	RMSE
ECT.16	6	−1.6	5.9
SAFT.17	5	22.2	29.4
UIRT.20	1	−30.0	30.0
PA-ATOFD.29 (interior)	4	−14.4	16.5
PA-ATOFD.29 (surface)	3	22.4	27.6
PA-TP.29 (interior)	6	−9.8	17.5
PA-TP.29 (surface)	6	−3.2	14.2
HHUT.29	5	−28.3	30.2
HHUT.30	1	−5.9	5.9
AECT.33	6	−7.9	13.6
SHPA.6	6	−2.2	6.3

Table 4.6. Summary of Length Sizing Error for Blind Techniques (Established)

	NOBS	Bias	RMSE
PAUT.108	5	−2.4	6.7
UT.108	5	1.8	7.4
PAUT.115	6	6.2	9.8
UT.TOFD.117	6	−0.5	8.1
PAUT.126	3	−3.0	16.8
UT.126	1	10.0	10.0
PAUT.128	6	11.8	13.4
UT.134	4	−5.8	11.7

5.0 Review of Response Images

In addition to quantitative statistical analysis of detection and sizing, a qualitative review of response images for open techniques (emerging technologies) was performed and is described in this section. Response images (usually B-scan images) are compared to indication plots for individual indications in an attempt to gain understanding of the relationship between response image features (such as background noise) and reported performance. For some of the techniques, comparisons are also made of response images from several different flaw types by comparing response images obtained in this study with response images collected from the PARENT open test. The above analysis is performed for techniques SAFT.17, SHPA.06, and PA-TRT.22 and described below.

5.1 SAFT.17 Response Images

Response images obtained from technique SAFT.17 in the blind test are shown in Figure 5.1 to Figure 5.4. Indication plots are also included as a reference so the response images can be compared to the reported dimensions for flaws. Figure 5.1 and Figure 5.3 include B-scan images for indications obtained from the carbon steel side and stainless steel side of the weld, respectively (refer to Figure 2.1). The cursors in the B-scan images indicate the location of hypothesized crack apexes. All of the response images are for indications that are classified as hits, with the exception of indication 02. Thus, all of the response images can be associated with actual flaws except for the response images for indication 02, which is a false call.

Depth profiles for the indications within the objective area are provided in Figure 5.2 and Figure 5.4, respectively. These figures can be compared to the indication plots displaying X–Z coordinates. It is notable that indication 02 is not associated with a flaw and that indication 04 grossly oversizes its associated flaw. Otherwise, indications 01 and 06 size their associated flaws accurately while indications 03 and 05 exhibit some modest undersizing and oversizing, respectively. If the indication depth profiles obtained from the carbon steel side of the weld are reviewed (Figure 5.2), it appears that the profiles for indications 02 and 04 are very uneven. The depth profiles for indications 01, 03, 05, and 06 are relatively smooth by comparison. One might speculate, based on these profiles, that indications 02 and 04 are not capturing genuine crack tips. However, in viewing the depth profiles obtained from the stainless steel side of the weld (Figure 5.4), all of the profiles appear much more uneven in comparison to the profiles obtained from the carbon steel side (Figure 5.2). Perhaps this is a SNR phenomena caused by increased attenuation of the ultrasound in the stainless steel in comparison to carbon steel, but the exact cause is not known.

Finally, comparison of SAFT.17 responses from several types of simulated flaws can be made qualitatively from Figure 5.5. This figure shows depth profiles for indications obtained by SAFT.17 in PARENT open testing from an electro-discharge machine (EDM) notch, a mechanical fatigue crack, and a stress corrosion crack (SCC) in test blocks P42, P30, and P32, respectively. The figure also displays depth profiles for indications associated with three solidification cracks in the blind test of SAFT.17. Specifically, the depth profiles for indications 01, 04, and 06 from the carbon steel side of the weld are included. The depth profiles for the EDM notch and the mechanical fatigue crack (MFC) appear relatively smooth and flat for most of the flaw profile. The depth profile for the SCC is highly uneven, by comparison, as it exhibits strong variation in depth across the length of the indication. The depth profiles for the SCs are not as smooth and flat as the EDM notch and MFC profiles, and they are not as uneven as the depth profiles for the SCC flaw. The one possible exception is indication 04, which exhibits unevenness comparable to an SCC flaw. It is worth noting that indication 04 grossly oversized its associated flaw.

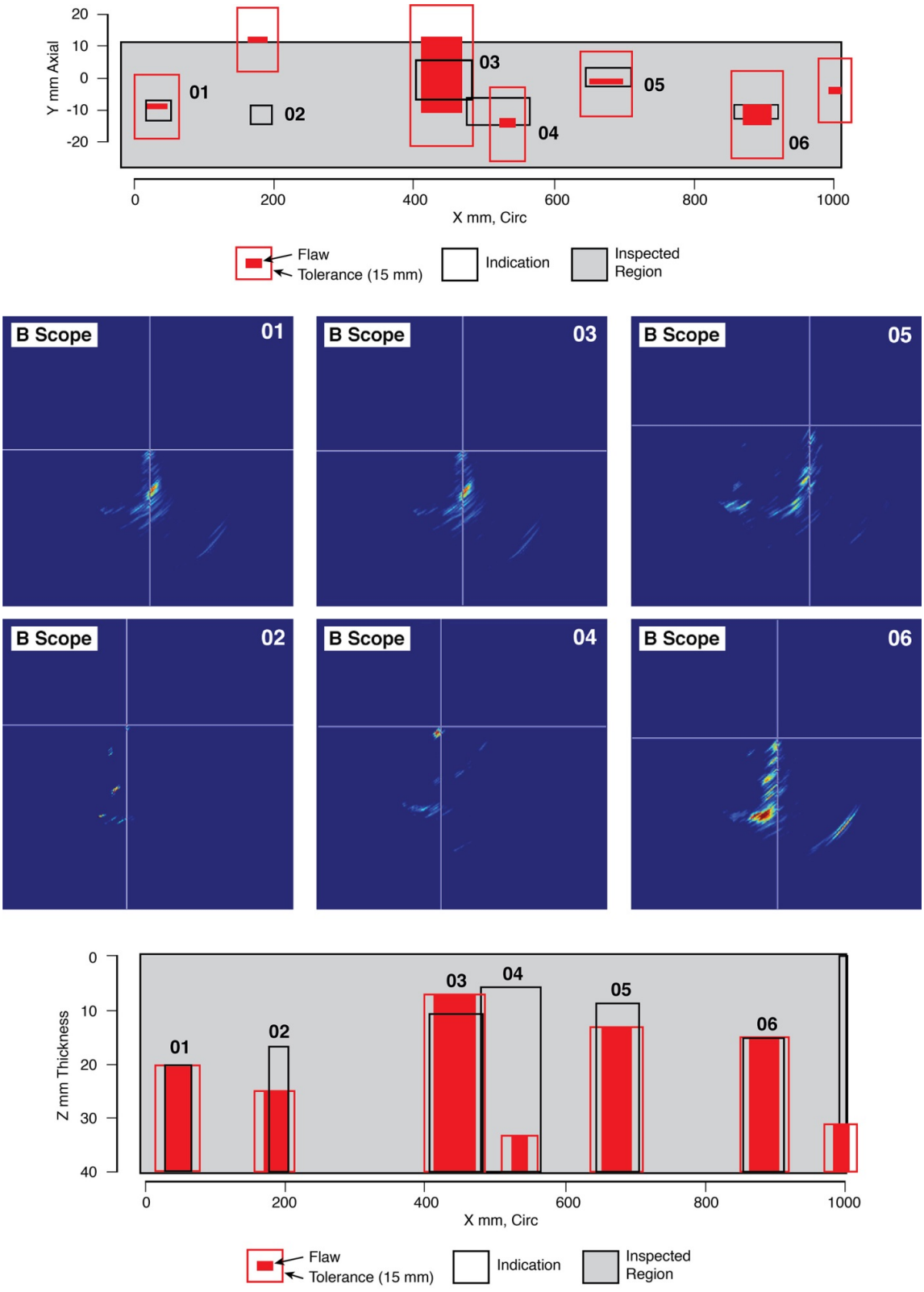

Figure 5.1. B-scan Images Obtained from Indications within the Objective Area on P40 for Technique SAFT.17 from the Carbon Steel Side of the Weld. The cursor in the B-scan images indicates the location of the hypothesized crack apex.

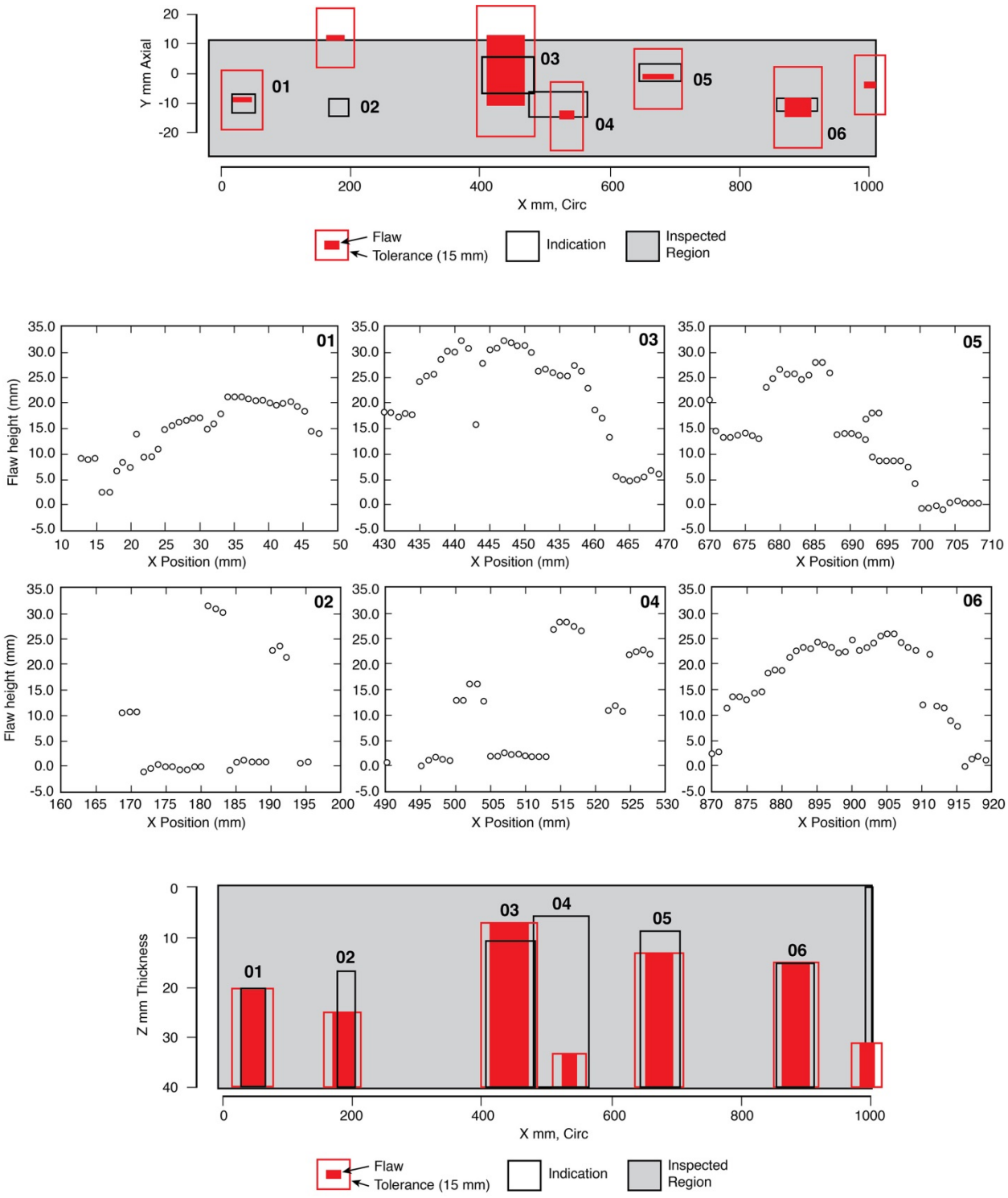

Figure 5.2. Depth Profiles for Indications within the Objective Area on P40 Obtained with Technique SAFT.17 from the Carbon Steel Side of the Weld

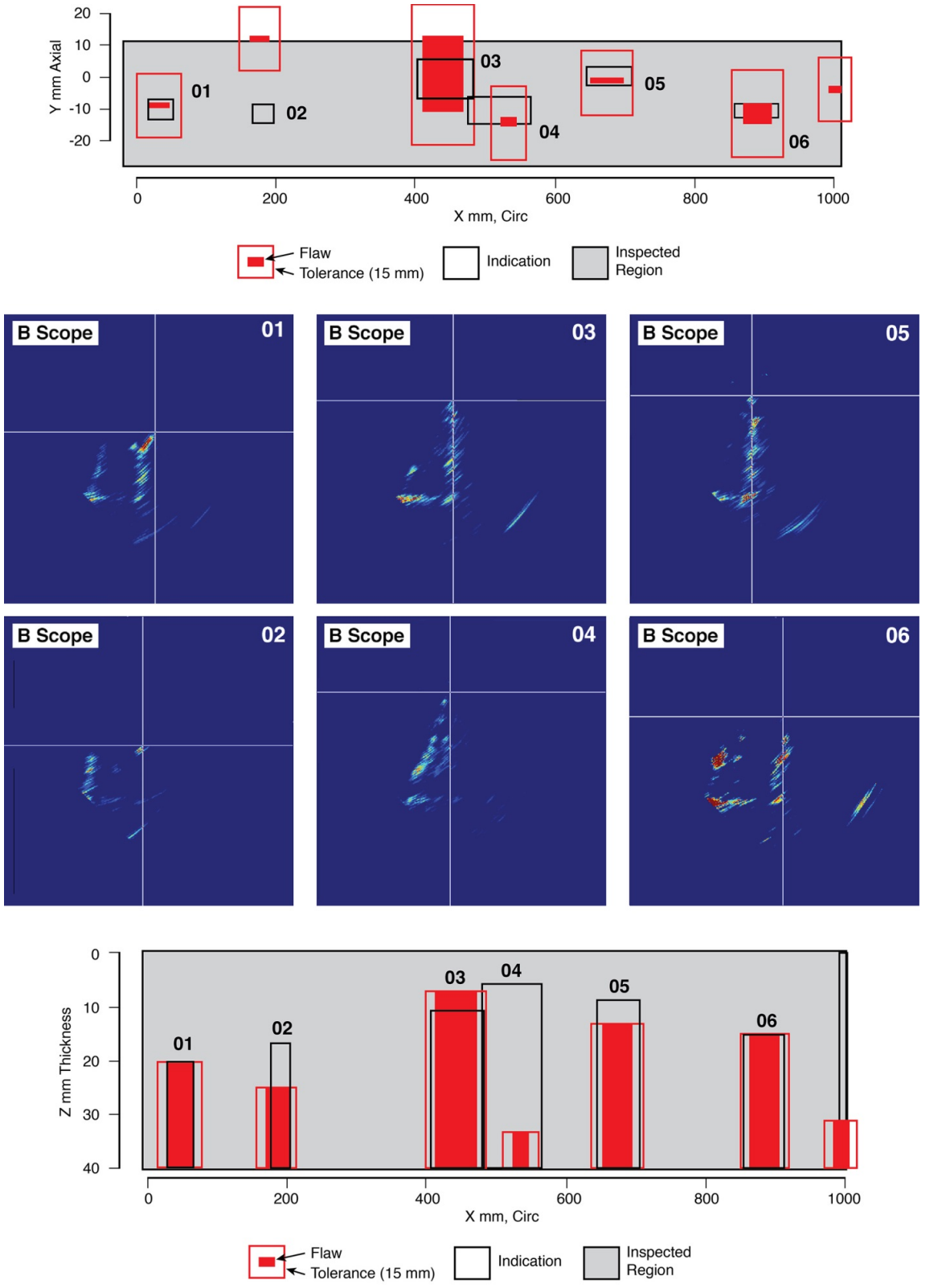

Figure 5.3. B-scan Images Obtained from Indications within the Objective Area on P40 for Technique SAFT.17 from the Stainless Steel Side of the Weld. The cursor in the B-scan images indicates the location of the hypothesized crack apex.

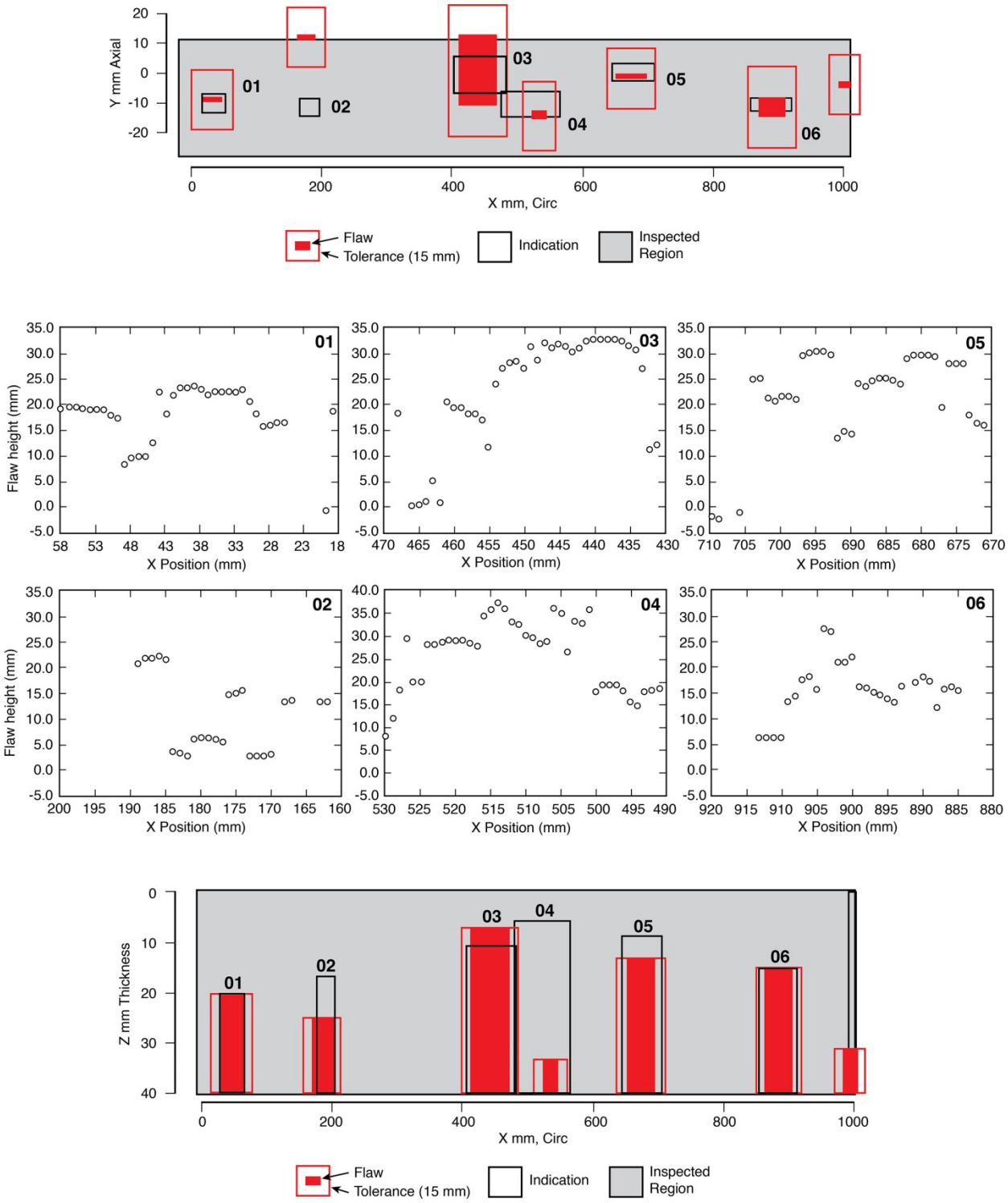

Figure 5.4. Depth Profiles for Indications within the Objective Area on P40 Obtained with Technique SAFT.17 from the Stainless Steel Side of the Weld

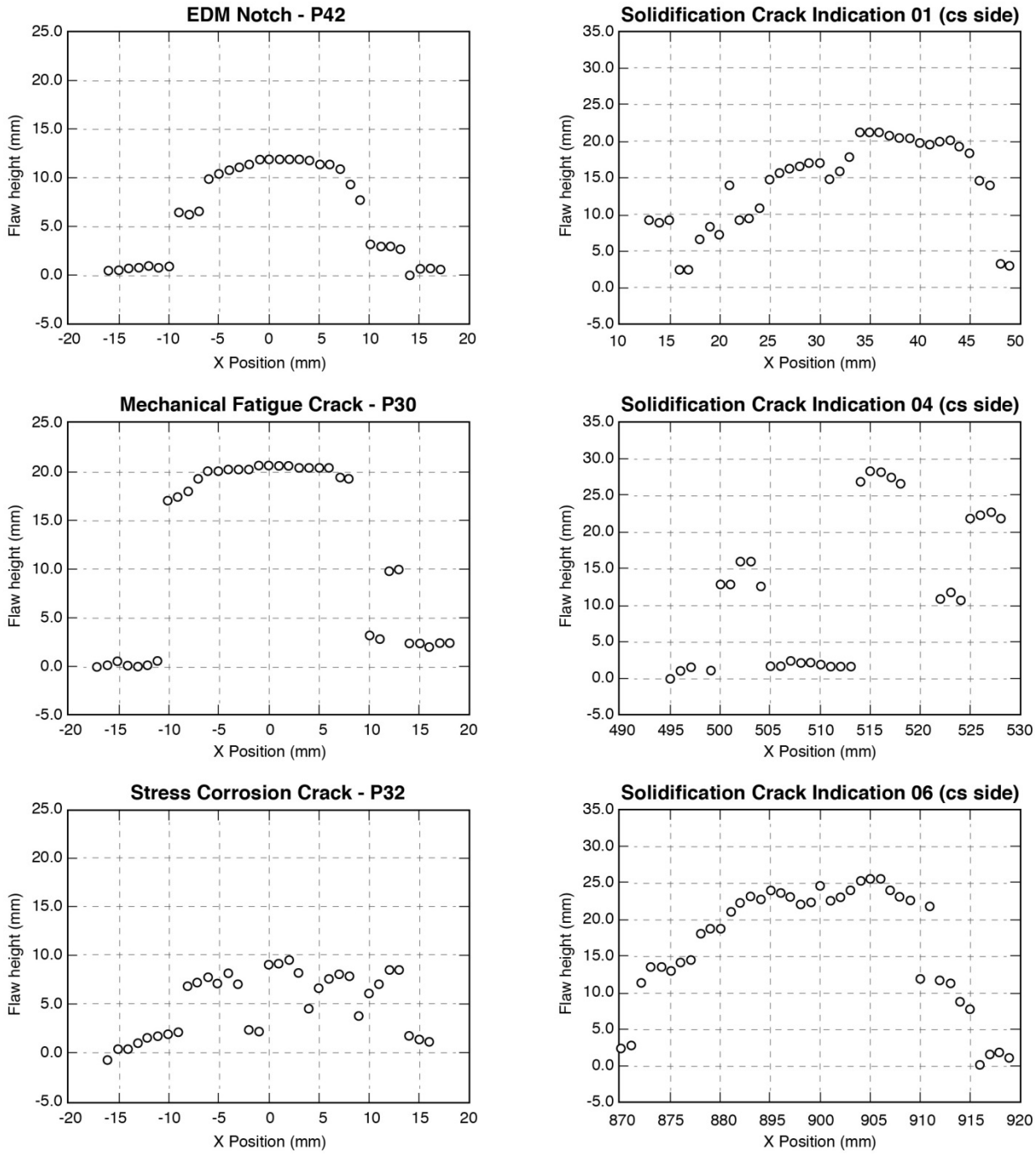

Figure 5.5. (*left side*): Depth Profiles of Indications Obtained by SAFT.17 from an EDM Notch in PARENT Open Testing from Test Block P42, a MFC in PARENT Open Testing from Test Block P30, and from a SCC in PARENT Open Testing from Test Block P32. (*right side*): Depth Profiles of Indications Associated with Solidification Cracks Obtained by SAFT.17 from Indication 01 from the Carbon Steel Side (*top*), Indication 04 from the Carbon Steel Side (*middle*), and Indication 06 from the Carbon Steel Side (*bottom*).

5.2 SHPA.06 Response Images

Response images obtained from the blind testing of technique SHPA.06 are provided in Figure 5.6. Indication plots for the SHPA.06 examination of the objective area are also included in Figure 5.6 for convenience. It can be noted from the indication plots that all of the indications are classified as hits and can be associated with actual flaws. A review of the bottom indication plot (X–Z coordinate view) shows that most of the indications depth size their associated flaws pretty accurately. The exceptions include indications 03 and 04. Indication 03 significantly undersizes its associated flaw while indication 04 grossly oversizes its associated flaw. These results are also consistent with the results for SAFT.17. For indication 04, it appears that there are significant sources of noise causing the gross depth sizing error. Presumably, the sources of this noise include other material anomalies that produce reflections similar in appearance to crack tip signals. The indication 03 result is interesting because the actual depth of the flaw (based on the indication plot) indicates that the tip signal would be located in or near the top portion of the B-scan which displays saturated intensity and the tip could be buried by this noise. The intensity of the B-scan is saturated in this region possibly due to transducer ringdown effects (SHPA.06 uses a single transducer in PE mode) and/or wedge reflections. This could be an important contribution to undersizing error for especially deep flaws, in general, and suggests that single transducer PE methods are ill-suited for depth sizing especially deep flaws.

Figure 5.7 includes B-scan image responses from SAFT.17 applied in PARENT open testing to the flat bar test blocks P28 (SCC flaw), P29 (SCC flaw), P30 (MFC flaw), and P32 (SCC flaw). Indication plots are also included in Figure 5.7 so that the response images can be compared with the reported depth sizing performance. It is apparent from the indication plots that the MFC flaw was depth sized more accurately than any of the SCC flaws. A review of the B-scans indicates that the B-scan for the MFC flaw appears to have less noise, or a lower SNR, than the B-scans for the SCC flaws. This would be consistent given the relatively more complex flaw morphologies that are associated with SCC flaws. The branching and irregular shape of the flaws can produce multiple tip signals, and the uneven surface of the crack face could also result in irregular scattering that may interfere with tip responses.

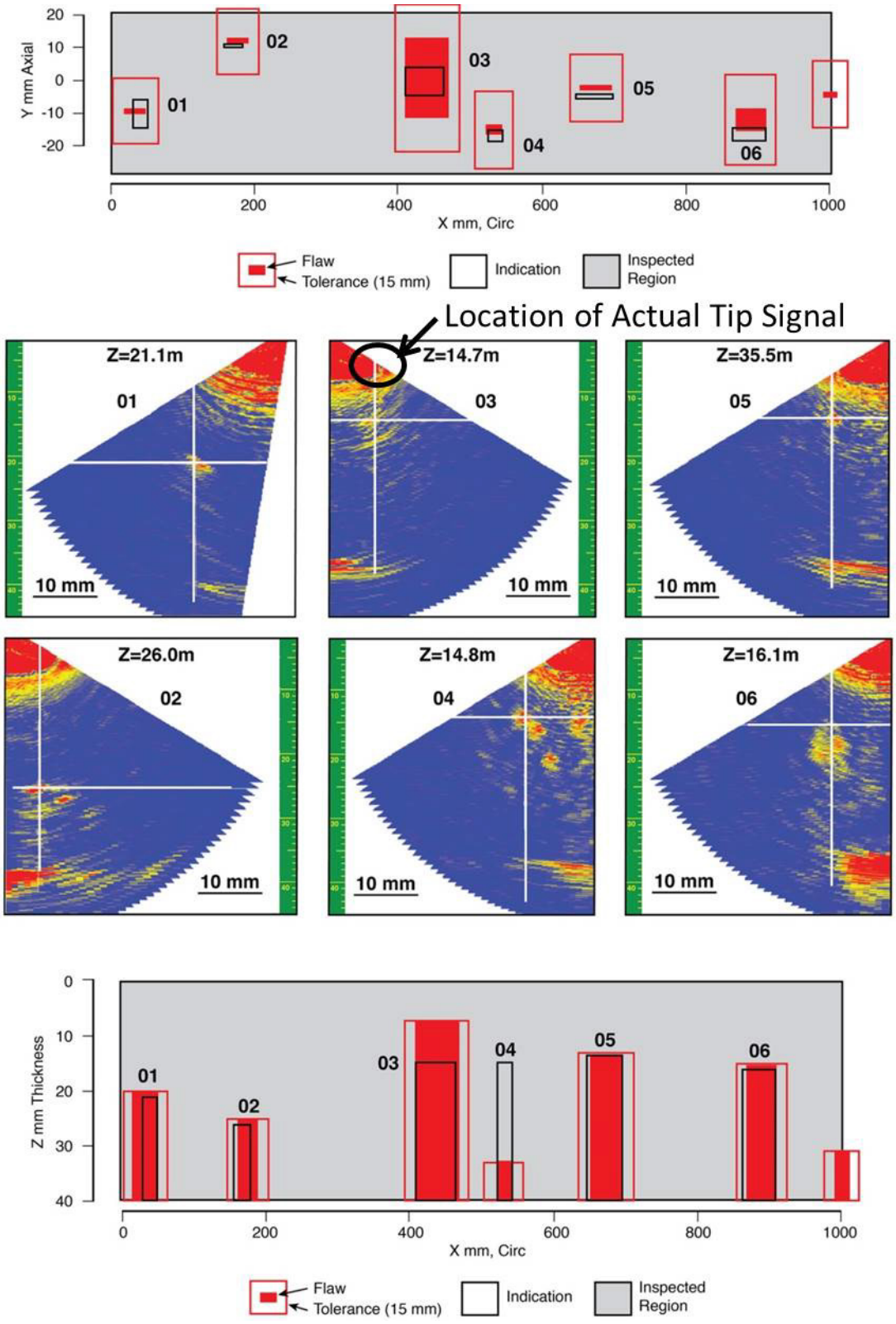

Figure 5.6. B-scan Images Obtained from Indications Reported within the Objective Area on P40 for Technique SHPA.06. The cursor in each image indicates the location of a hypothesized crack apex.

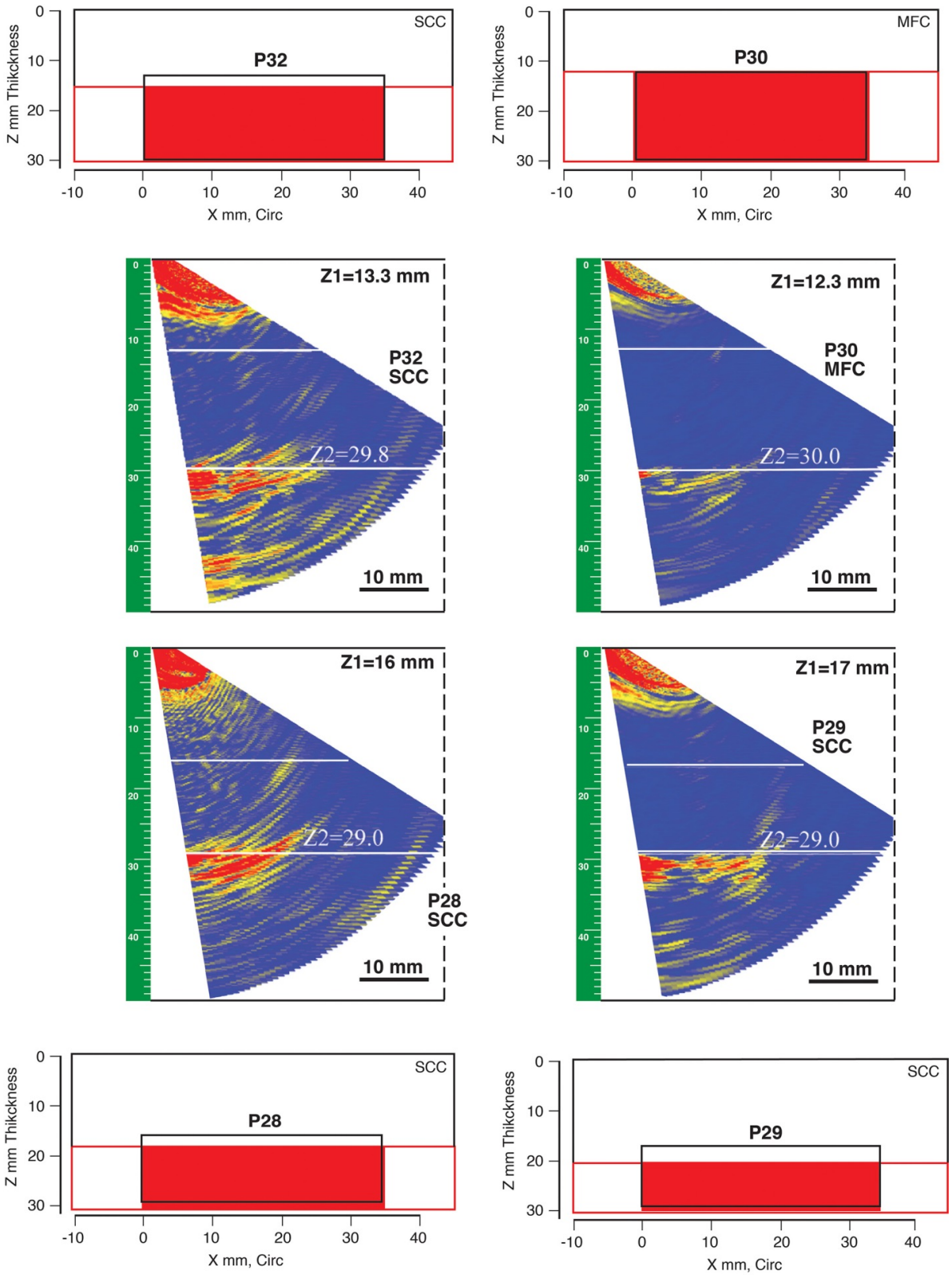

Figure 5.7. B-scan Images Obtained from Indications Reported for Different Simulated Flaw Types in the Flat Bar Test Specimens Used in PARENT Open Testing

5.3 PA-TRT.22 Response Images

Team 22 inspected the incorrect portion of the test block in blind testing so the results obtained by technique PA-TRT are not compared to results obtained by other emerging techniques or by established techniques. However, the indication plot for the PA-TRT technique applied to the incorrect area is provided in Figure 5.8. Figure 5.8 also shows how implementation of adaptive focusing (time reversal technique) significantly enhanced the amplitude of corner reflection signals in comparison to conventional PAUT focusing. Figure 5.9 provides an example comparison of A-scans obtained for indication 05 and the enhancement for a specific corner reflection signal. The figure also shows how the adaptive focusing is achieved by modification of the time delay law in comparison to the time delay law that would be used for conventional PAUT focusing. This illustrates, in principle, that further gains in NDE performance may be accessible through technological innovations. This assumes that improved SNR performance should translate to a significant improvement in POD.

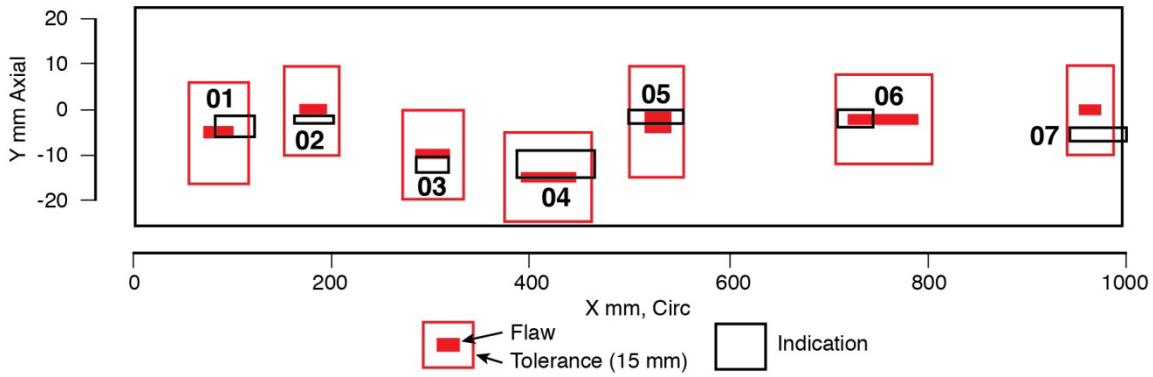

Peak - to - Peak Amplitude (Corner Reflection Signal)

Defect No:	1	2	3	4	5	6	7
Conventional	184	74	48	66	90	87	60
Adaptive	286	361	250	251	366	288	182
Ratio, Adaptive of Concentional (%)	155.43	487.84	520.83	380.3	406.67	331.03	303.33

Figure 5.8. Depiction of the Indication Plot for Technique PA-TRT.22 and the Enhancement that the Adaptive Focusing Technique (time-reversal technique) Provides with Respect to SNR in Comparison to a Conventional PAUT Technique

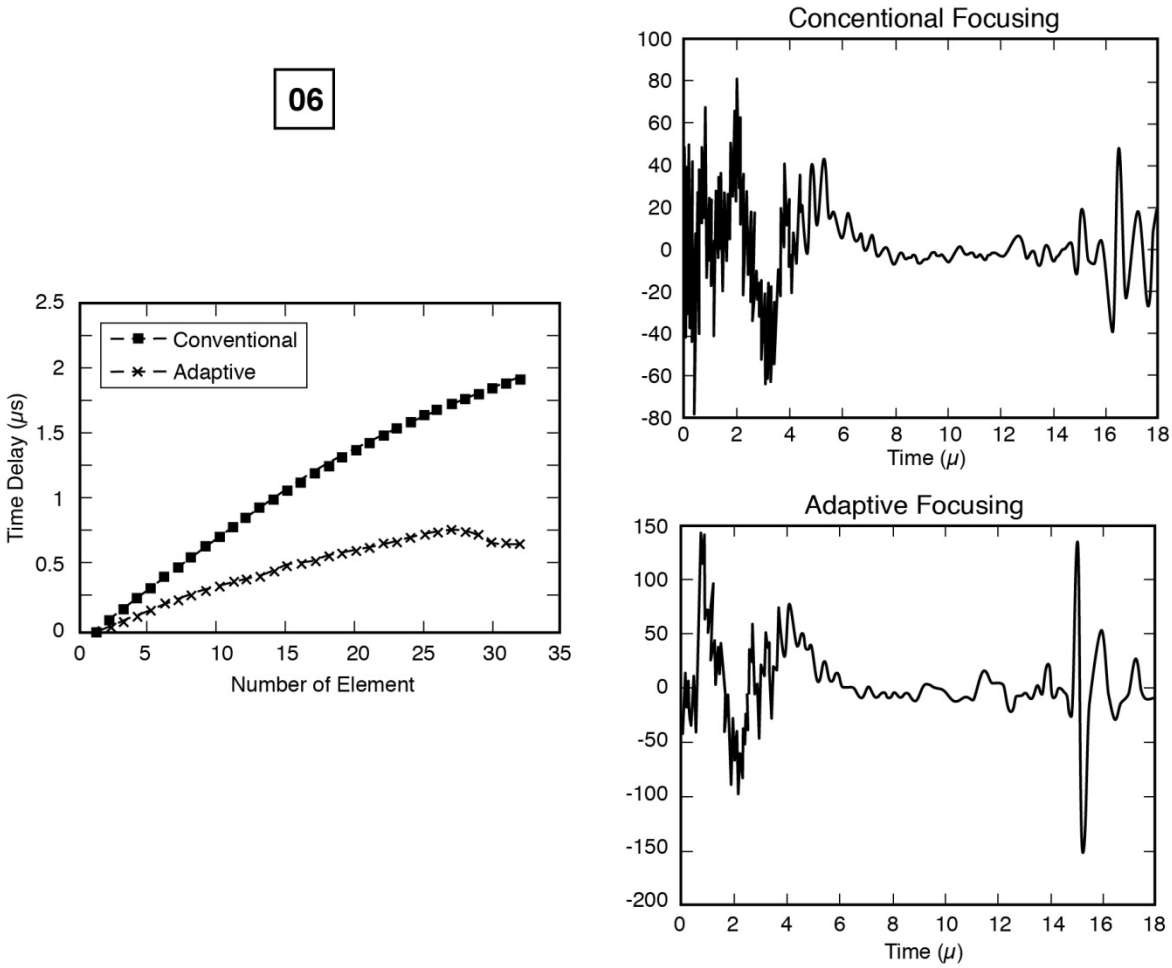

Figure 5.9. Example A-scans Provided for Indication 06 Indicating the Enhancement of the Corner Reflection Signal for the Adaptive Focusing Technique (time reversal technique) in Comparison to a Conventional PAUT Technique. This figure also displays how the time delay law is modified for implementation of adaptive focusing in comparison to implementation of conventional PAUT focusing.

5.4 PA-TP.29 (Surface) Response Images

Indication plots obtained from the examination of the objective area by technique PA-TP.29 are provided in Figure 5.10 for both X–Y and X–Z views. The plots are divided over regions from 0 mm–500 mm and from 500 mm–1000 mm. Response images (B-scan images) from axial scans for several of the indications are provided in Figure 5.11, Figure 5.12, and Figure 5.13, respectively. The red cursor in the images indicates the response from a crack tip. The top of the images represents the surface of the test block that the probes access. The cracks initiate from the opposite surface of the test block, which is visible in the B-scan images as the linear reflection just below the 40 mm depth in each of the response images. A correction is applied to the depth of the flaw measured from the B-scan images using the procedure outlined in Section 3.3.

Figure 5.11 displays B-scan response images for indications 01, 02, and 03 where indications 01 and 02 appear to be associated with actual flaws while indication 03 is a false call. From the indication plots, it is apparent that the flaws associated with indications 01 and 02 are depth sized with moderate error.

Indication 01 slightly undersizes its associated flaw and a review of the B-scan image for Figure 5.11 shows that another feature is located adjacent to the feature identified as the flaw tip. Its conceivable this other feature is actually associated with the flaw and would result in estimating a deeper flaw size which may be closer to the actual flaw depth. For indication 03, a feature in the B-scan image was considered to be a crack tip response. The shape and amplitude of the feature appear similar to the features identified as crack tips in the B-scan images for indications 01 and 02; however, no flaw is actually associated with this response.

Figure 5.12 displays B-scan response images for indications 07, 04, and 08. All indications are associated with actual flaws and indications 07 and 04 are associated with the same flaw. A review of the indication plot in Figure 5.10 shows gross sizing error for all of these indications (gross undersizing for indications 07 and 04; gross oversizing for indication 08). Figure 5.13 displays B-scan response images for indications 09, 10, and 12 which are all associated with actual flaws. Significant sizing error (undersizing) is apparent for all of these indications from Figure 5.10. The response from indication 09, in particular, appears very weak.

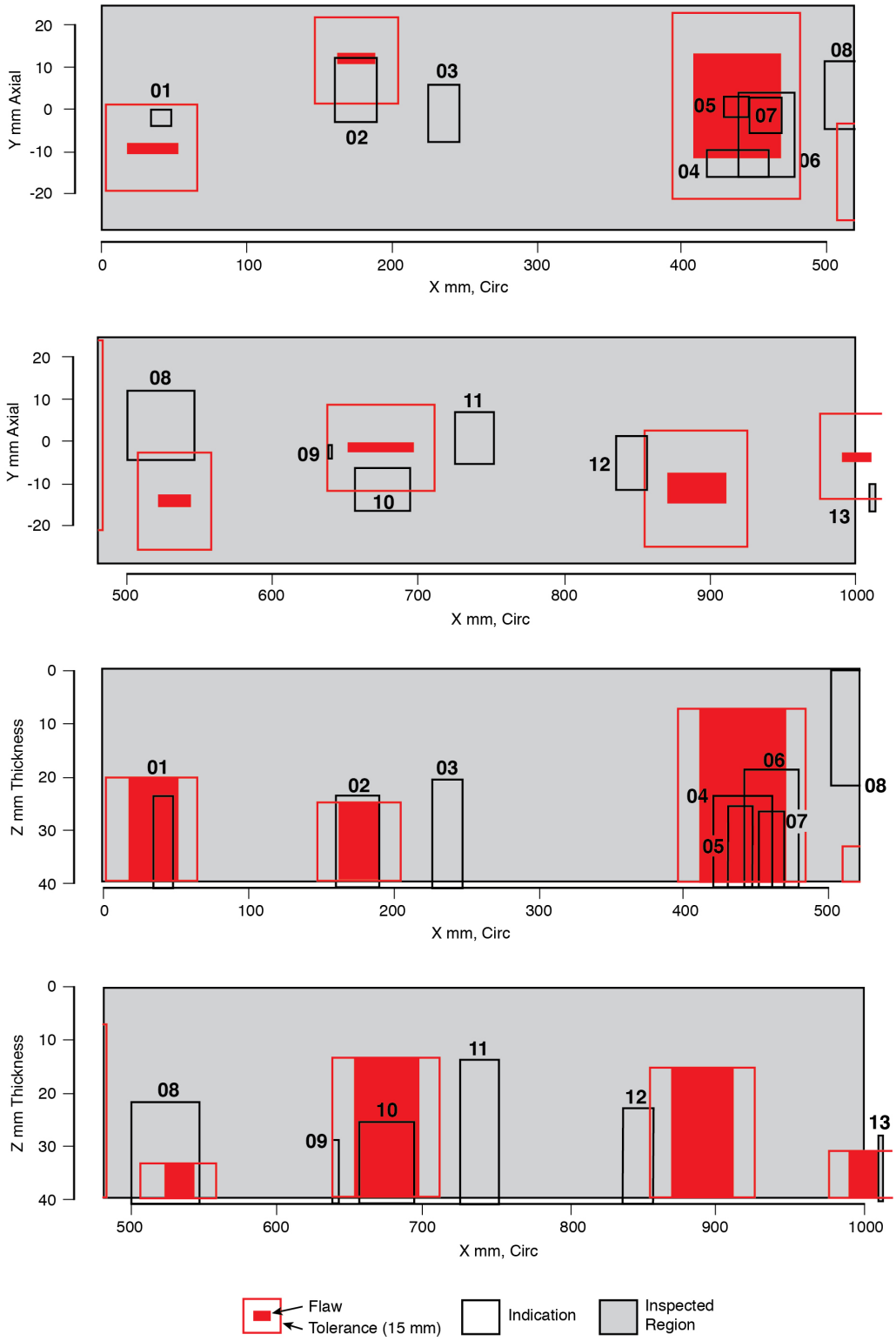

Figure 5.10. Indication Plots for the Examination of the Objective Area by PA-TP.29 [both (X–Y) and (X–Z) orientations]

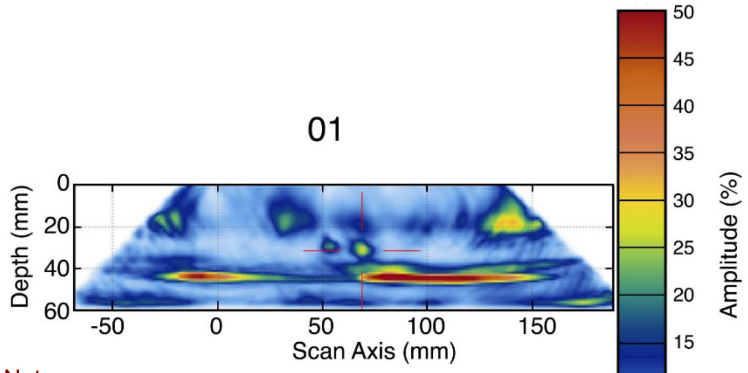

Note:
The vertical axis of this image shows the raw value measured by this technique. So, the depth of cursor does not show the true depth of flaw indication. This measured raw data value of indication is compensated to the true depth using the image data for SDH reference test block.

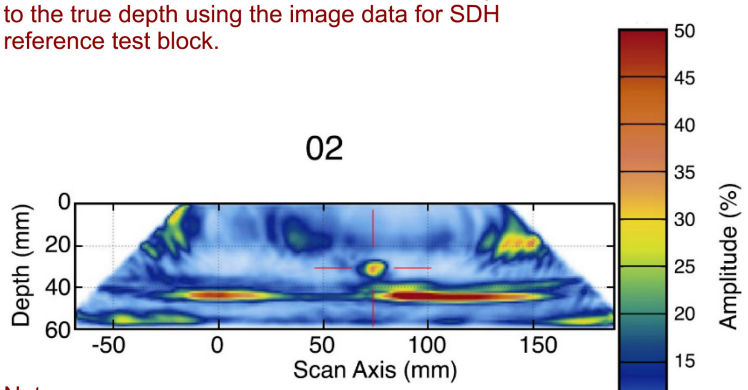

Note:
The vertical axis of this image shows the raw value measured by this technique. So, the depth of cursor does not show the true depth of flaw indication. This measured raw data value of indication is compensated to the true depth using the image data for SDH reference test block.

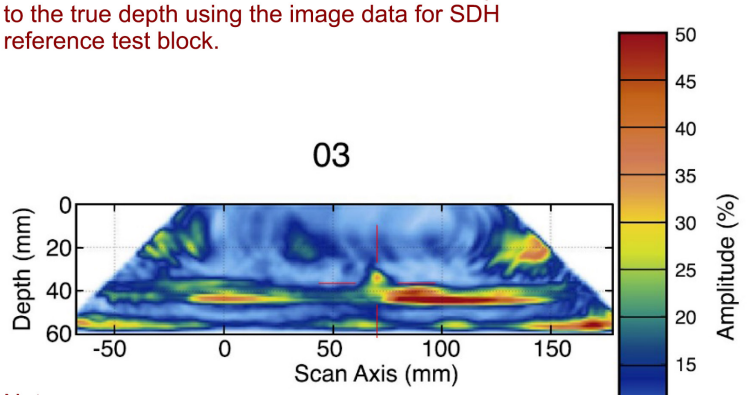

Note:
The vertical axis of this image shows the raw value measured by this technique. So, the depth of cursor does not show the true depth of flaw indication. This measured raw data value of indication is compensated to the true depth using the image data for SDH reference test block.

Figure 5.11. B-scan Image Responses for Indications 01, 02, and 03 (see Figure 5.10) from Application of PA-TP.29 to the Examination of the Objective Area

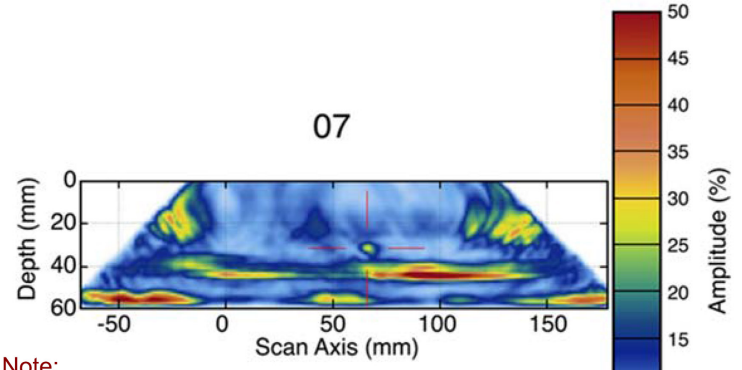

Note:
The vertical axis of this image shows the raw value measured by this technique. So, the depth of cursor does not show the true depth of flaw indication. This measured raw data value of indication is compensated to the true depth using the image data for SDH reference test block.

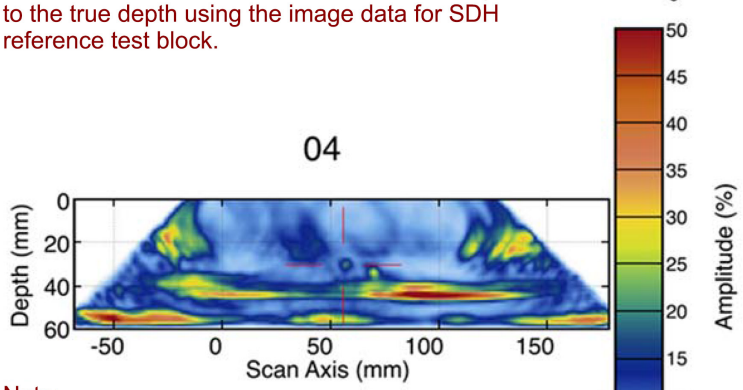

Note:
The vertical axis of this image shows the raw value measured by this technique. So, the depth of cursor does not show the true depth of flaw indication. This measured raw data value of indication is compensated to the true depth using the image data for SDH reference test block.

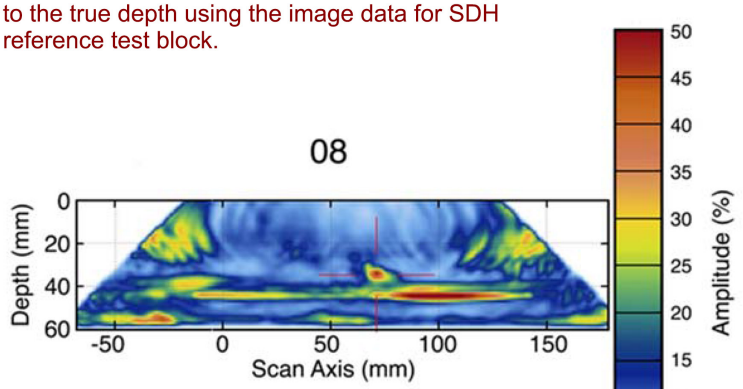

Note:
The vertical axis of this image shows the raw value measured by this technique. So, the depth of cursor does not show the true depth of flaw indication. This measured raw data value of indication is compensated to the true depth using the image data for SDH reference test block.

Figure 5.12. B-scan Image Responses for Indications 07, 04, and 08 (see Figure 5.10) from Application of PA-TP.29 to the Examination of the Objective Area

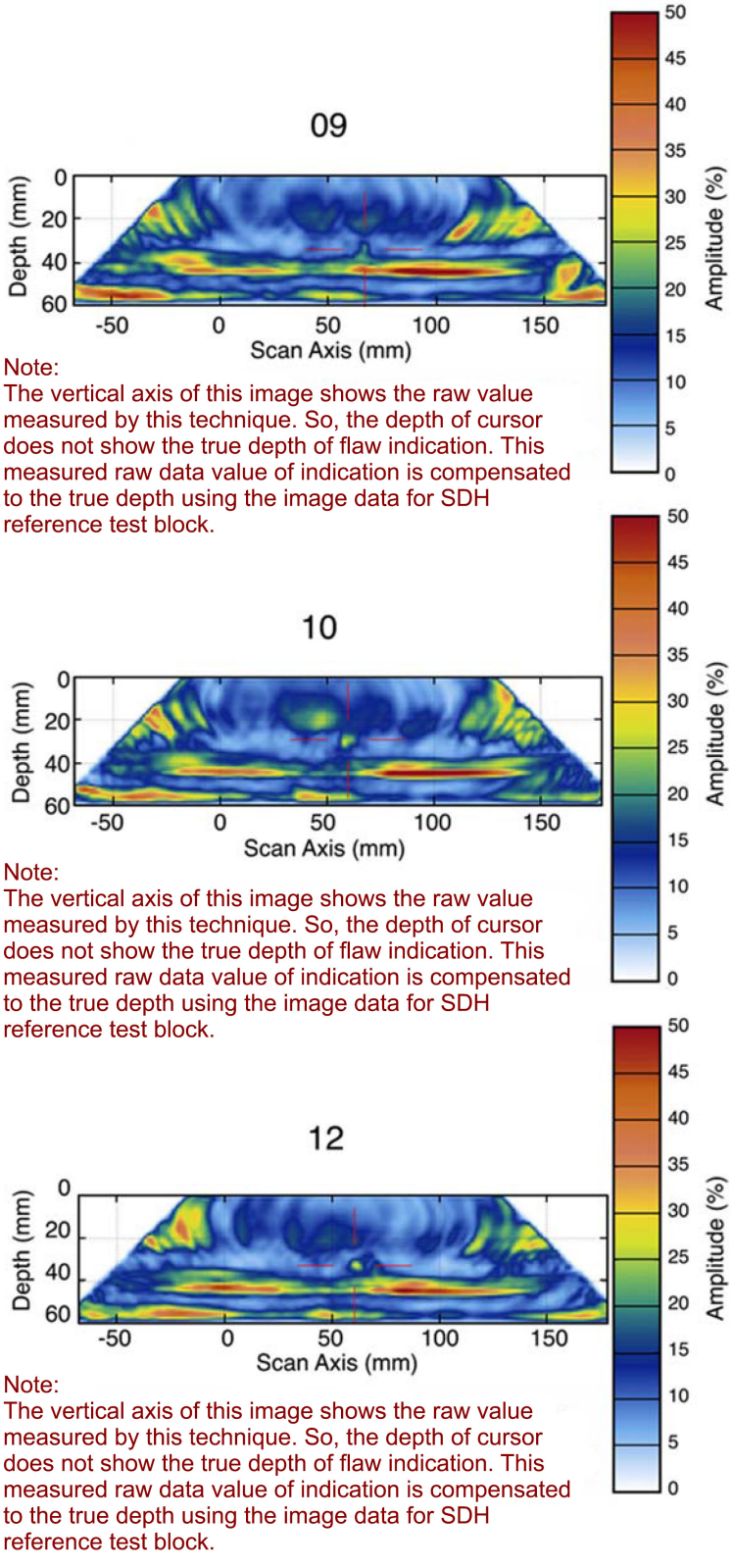

Figure 5.13. B-scan Image Responses for Indications 09, 10, and 12 (see Figure 5.10) from Application of PA-TP.29 to the Examination of the Objective Area

5.5 PA-ATOFD.29 (Surface) Response Images

Indication plots obtained from the examination of the objective area by technique PA-ATOFD.29 are provided in Figure 5.14 for both X–Y and X–Z views. The plots are divided over regions from 0 mm–500 mm and from 500 mm–1000 mm. Response images (B-scan images) from axial scans for several of the indications are provided in Figure 5.15, Figure 5.16, and Figure 5.17, respectively. A correction is applied to the depth of the flaw measured from the B-scan images using the procedure outlined in Section 3.3. A comparison of the B-scan images in Figure 5.15, Figure 5.16, and Figure 5.17 to the B-scan images in Figure 5.11, Figure 5.12, and Figure 5.13 show that the B-scan images for the PA-ATOFD.29 have less background noise than for PA-TP.29. Table 4.1 shows that the detection performance (POD and FCR) were superior for the technique PA-TP.29 (surface) in comparison to the technique PA-ATOFD.29 (surface).

Figure 5.15 displays B-scan response images for indications 02, 03, and 05 where indications 02 and 05 appear to be associated with actual flaws while indication 03 is a false call. From the indication plots, it is apparent that the flaws associated with indications 02 and 05 are depth sized with moderate error. Indication 02 undersizes its associated flaw and indication 05 oversizes its associated flaw. For indication 03, a very weak feature in the B-scan image was considered to be a crack tip response.

Figure 5.16 displays B-scan response images for indications 07, 08, and 12. Indications 07 and 08 are false calls while indication 12 is associated with an actual flaw. The indication plot in Figure 5.14 shows that it estimates the depth of the associated flaw accurately. The responses for indications 07 and 08 are much weaker than the response for indication 12.

Figure 5.17 displays B-scan response images for indications 13 and 14, which are both associated with actual flaws. Moderate undersizing is exhibited for indication 13 while gross oversizing is exhibited for indication 14. The responses appear to be fairly weak for both indications.

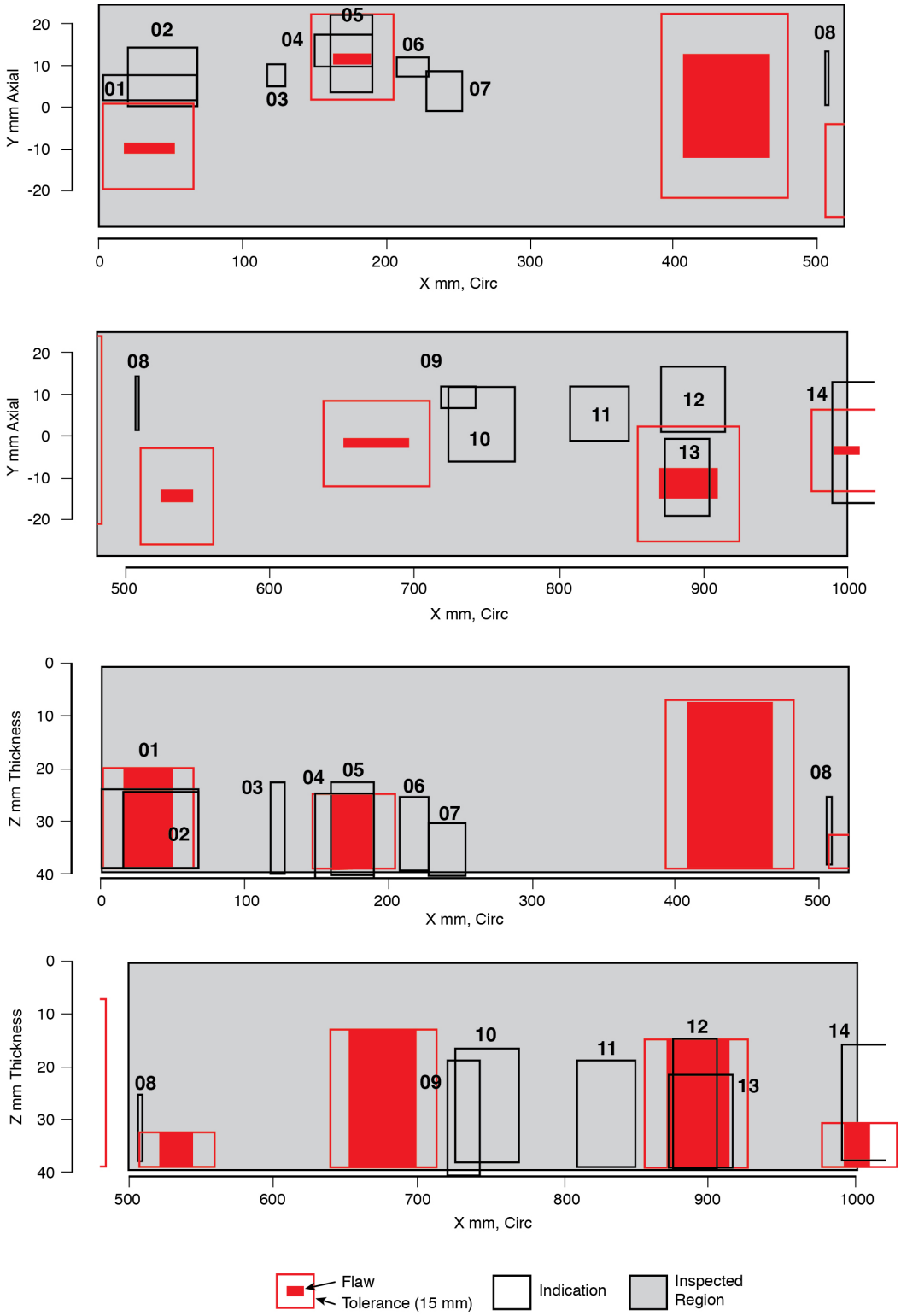

Figure 5.14. Indication Plots for the Examination of the Objective Area by PA-ATOFD.29 [both (X–Y) and (X–Z) orientations]

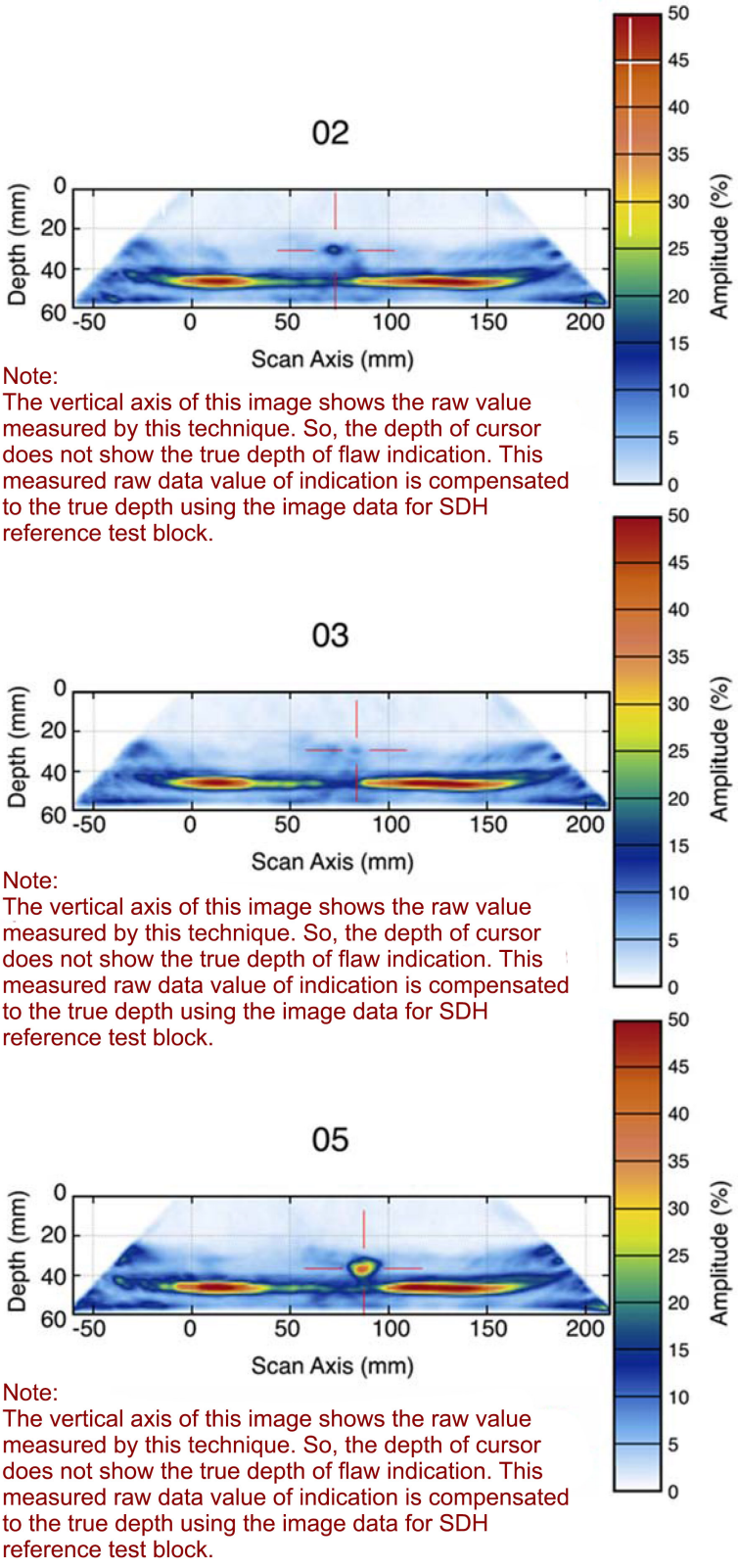

Figure 5.15. B-scan Image Responses for Indications 02, 03, and 05 (see Figure 5.14) from Application of PA-ATOFD.29 to the Examination of the Objective Area

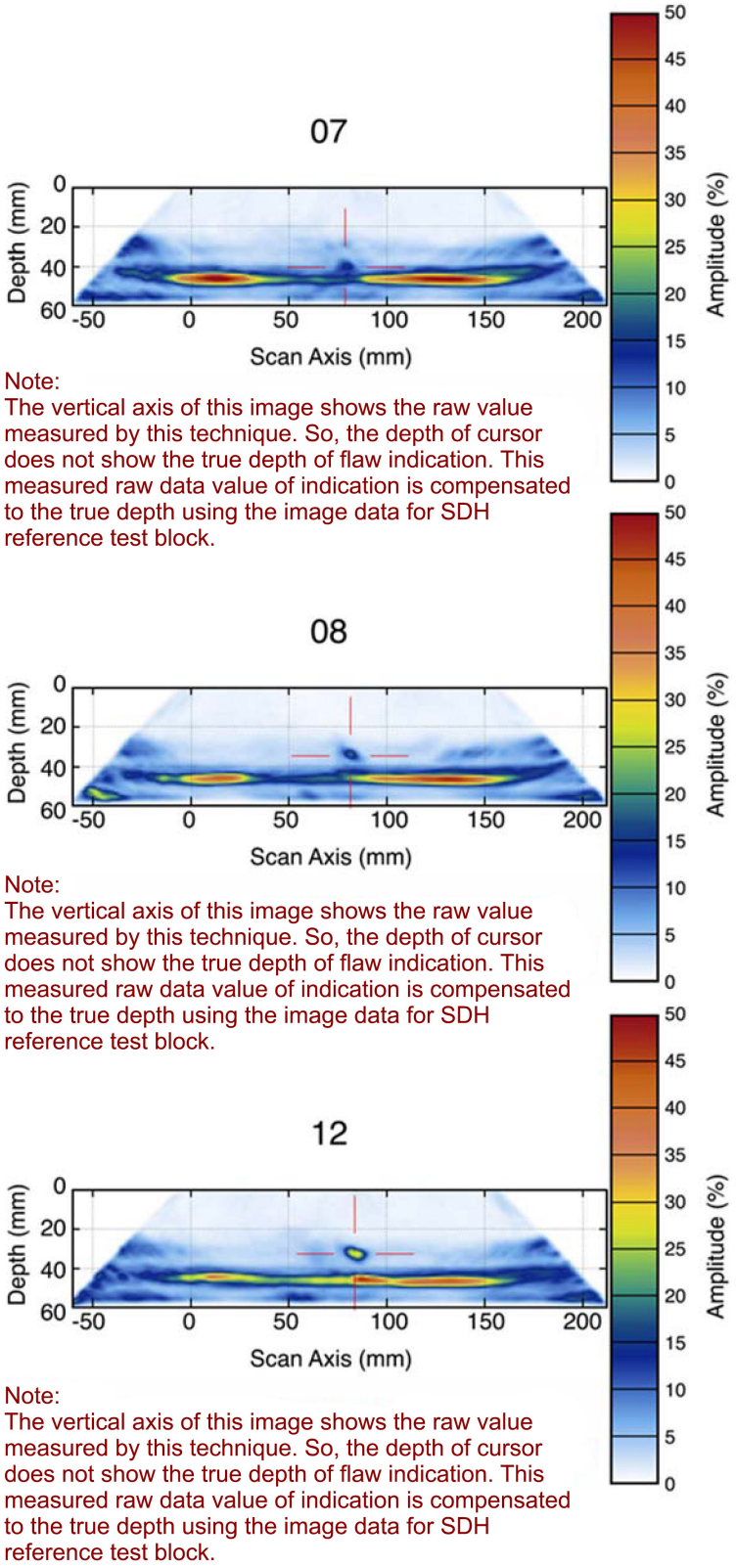

Figure 5.16. B-scan Image Responses for Indications 07, 08, and 12 (see Figure 5.14) from Application of PA-ATOFD.29 to the Examination of the Objective Area

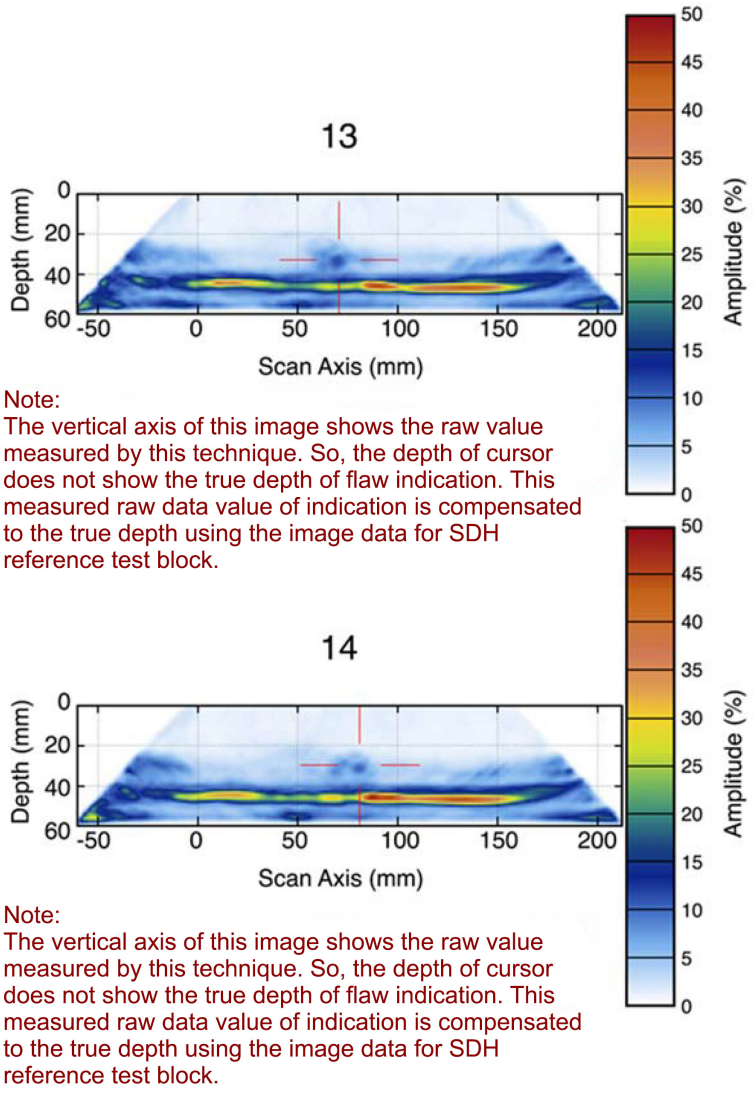

Figure 5.17. B-scan Image Responses for Indications 13 and 14 (see Figure 5.14) from Application of PA-ATOFD.29 to the Examination of the Objective Area

6.0 Conclusions

This report documents the results from a blind round-robin test conducted with techniques that were applied in the open testing portion of PARENT (Meyer et al. 2017). Techniques applied in PARENT open testing were novel and attempted to advance upon established techniques (i.e., those regularly used in the field) by employing novel data/signal processing methods and/or novel physical modalities. Open testing has limitations with respect to assessing detection performance and could introduce a bias in sizing due to the knowledge of the location of flaws. Thus, the present test was performed in an attempt to assess detection performance and to obtain a more confident assessment of sizing capability for techniques that demonstrated high potential in PARENT open testing.

PARENT open test techniques were evaluated in this study with a quantitative statistical analysis of detection performance and sizing performance. These results are compared to the performance exhibited by applicable established techniques evaluated in PARENT blind testing as a benchmark. This analysis showed that several of the novel PARENT open test techniques exhibit detection performances that are as good as the established techniques. Notably, two of the techniques that did so were eddy current techniques (ECT.16 and AECT.33). The other techniques to exhibit high detection performance included SHPA.06, SAFT.17, and PA-TP.29 (applied to surface-breaking flaws). Several of the PARENT open test techniques exhibited a very high false call rate (e.g., PA-ATOFD.29 [applied to the interior flaws], PA-TP.29 [applied to the interior flaws], and HHUT.29). This can probably be attributed to the experience of the teams performing these inspections because open test teams, in general, were researchers and not individuals trained to perform examinations commercially. There was a clear distinction in depth sizing performance demonstrated by the emerging techniques and established techniques. In this case, excluding all techniques with NOBS less than 5, the best performing emerging technique exhibited a depth sizing RMSE twice as large as the worst performing established technique. With respect to length sizing performance, excluding all techniques with NOBS less than 5, two of the emerging techniques (SHPA.06 and ECT.16) performed better than any of the established techniques based on RMSE values. However, no other emerging techniques performed better than any established technique.

A qualitative analysis of NDE response images (B-scan images) was also performed in an attempt to observe potential correlations between response image features and performance, particularly based on depth sizing error observed in indication plots. Technique SAFT.17 was capable of profiling the depth of indications. For cases in which an indication was a false call or the indication demonstrated gross sizing error, the depth profile appeared very irregular and uneven for examinations performed from the carbon steel side of the weld. Smoother depth profiles were observed for detections with limited sizing error. For technique SHPA.06, mostly accurate depth sizing is observed with the exception of two indications. The cause of the sizing error appears to be background noise caused by material defects or inherent material heterogeneity for one indication; for the other indication, it is possible that the true crack tip signal is overwhelmed by saturation in the B-scan caused by wedge reflections and transducer ringdown. PA-TP.29 B-scan images exhibit a higher background signal and less visual clarity than the B-scan images produced by PA-ATOFD.29. This is inconsistent with the quantitative detection analysis results, which show that detection performance (higher POD and lower FCR – see Table 4.1) for PA-TP.29 is significantly better than for PA-ATOFD.29. Although the background level can be qualitatively inferred from the response images, quantitative representation of the signal-to-noise ratio (SNR) may not be inferred from the images and it is possible that SNR is actually greater for PA-TP.29 than for PA-ATOFD.29 despite the appearance of higher background level.

7.0 References

Braatz BG, PG Heasler and RM Meyer. 2014. *PARENT Quick Blind Round-Robin Test Report*. PNNL-22677, Pacific Northwest National Laboratory, Richland, Washington. ADAMS Accession No. ML14276A052.

Dillenz A, D Wu, K Breitruck and G Busse. 2000. "Lock-in Thermography for Depth Resolved Defect Characterisation." In *15th World Conference on Nondestructive Testing*. October 15-21, 2000, Rome, Italy. The Italian Society for Nondestructive Testing and Monitoring Diagnostics. Available at Available at http://www.ndt.net/article/wcndt00/papers/idn738/idn738.htm.

Elbern AW and L Guimaraes. 1999. "Synthetic Aperture Focusing Technique for Image Resaturation." In *International Symposium on NDT Contribution to the Infrastructure Safety Systems (NDTISS'99)*. November 22-26, 1999, Torres, Brazil. UFSM, Santa Maria, RS, Brazil.

Fink M. 1992. "Time Reversal of Ultrasonic Fields. I. Basic Principles." *IEEE Transactions on Ultrasonics, Ferroelectrics and Frequency Control* 39(5):555-566. DOI: 10.1109/58.156174.

Fink M. 1999. "Time-Reversed Acoustics." *Scientific American* November:91-97.

Ishida H and J Kitasaka. 2013. "Development of a Phased Array TOFD UT Method to Measure the Depth of SCCs in Dissimilar Metal Weld." In *9th International Conference on NDE in Relation to Structural Integrity for Nuclear and Pressurized Components*, pp. 754-762. May 22-24, 2012, Seattle, Washington. NDT.net, Rheintalstr, Germany. Available at http://www.ndt.net/article/jrc-nde2012/papers/120.pdf.

Jhang K-Y. 2000. "Applications of Nonlinear Ultrasonics to the NDE of Material Degradation." *IEEE Transactions on Ultrasonics, Ferroelectrics and Frequency Control* 47(3):540-548. DOI: 10.1109/58.842040.

Maldague X. 2001. *Theory and Practice of Infrared Technology for Nondestructive Testing*, John Wiley and Sons, New York.

Meyer RM. 2014. *NDE Techniques Used in PARENT Open Round Robin Testing*. PNNL-23387, Pacific Northwest National Laboratory, Richland, Washington.

Meyer RM and PG Heasler. 2017. *Results of Blind Testing for the Program to Assess the Reliability of Emerging Nondestructive Techniques*. NUREG/CR-7235, PNNL-24196, U.S. Nuclear Regulatory Commission, Washington, D.C. ADAMS Accession No. ML17159A466.

Meyer RM, AE Holmes and PG Heasler. 2017. *Results of Open Testing for the Program to Assess the Reliability of Emerging Nondestructive Techniques*. NUREG/CR-7236, PNNL-24708, U.S. Nuclear Regulatory Commission, Washington, D.C. ADAMS Accession No. ML17223A700 and ML17223A704.

Ohara Y, S Yamamoto, T Mihara and K Yamanaka. 2008. "Ultrasonic Evaluation of Closed Cracks Using Subharmonic Phased Array." *Japanese Journal of Applied Physics* 47(5):3908-3915. DOI: 10.1143/JJAP.47.3908.

Appendix A

Indication Plots for Emerging Technologies

Appendix A

Indication Plots for Emerging Technologies

This section summarizes the results of the blind test assessment of open techniques from PARENT by displaying indication plots for each examination. The objective area for the test was limited to a region from X=0 mm to X=1000 mm in accordance to the coordinate system defined in Figure 2.1. However, a few teams examined all or most of the weld region in the test block. The indication plots for these examinations are displayed following the indication plots for examination of the objective area.

A.1 Inspections of the Objective Area

The indication plots for examinations of the objective area are organized by technique and team number. Indication plots are provided for the X–Y view which depict hits, misses, and false calls based on overlap between indications and flaws. Indication plots are provided for the X–Z view only for techniques that are capable of depth sizing. The overlap between indications in the X–Z view is not considered in the determination of hits, misses, and false calls. However, this view can illustrate how well the depth of each flaw is estimated. The flaw on the border of the objective area (at X=1000 mm) is excluded from the analysis; therefore, detections of this flaw are not credited and misses of this flaw are not penalized.

A.1.1 SHPA Inspection of Objective Area by Team 6

The indication plots for the SHPA technique applied to the objective area by team 6 are provided in Figure A.1 and Figure A.2. Figure A.1 indicates that six out of six flaws within the objective area are detected and that there are no false calls. Figure A.2 indicates that depth sizing accuracy is pretty good except for two of the flaws near the middle of the region (between X=400 mm and X=600 mm). In this case, one flaw is undersized significantly and the other flaw is oversized significantly.

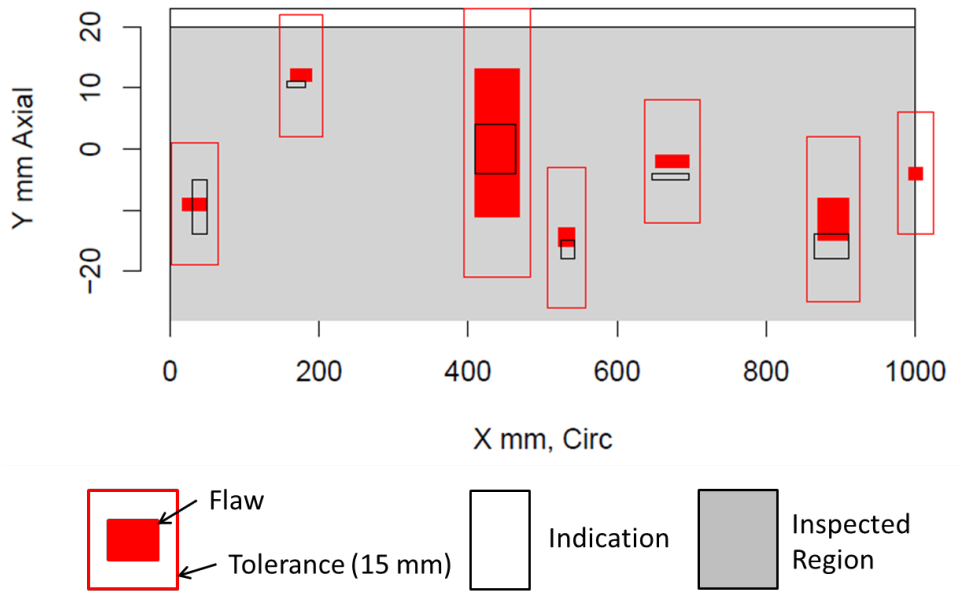

Figure A.1. Indication Plot (X–Y view) for Inspection of the Objective Area by the SHPA Technique Employed by Team 6

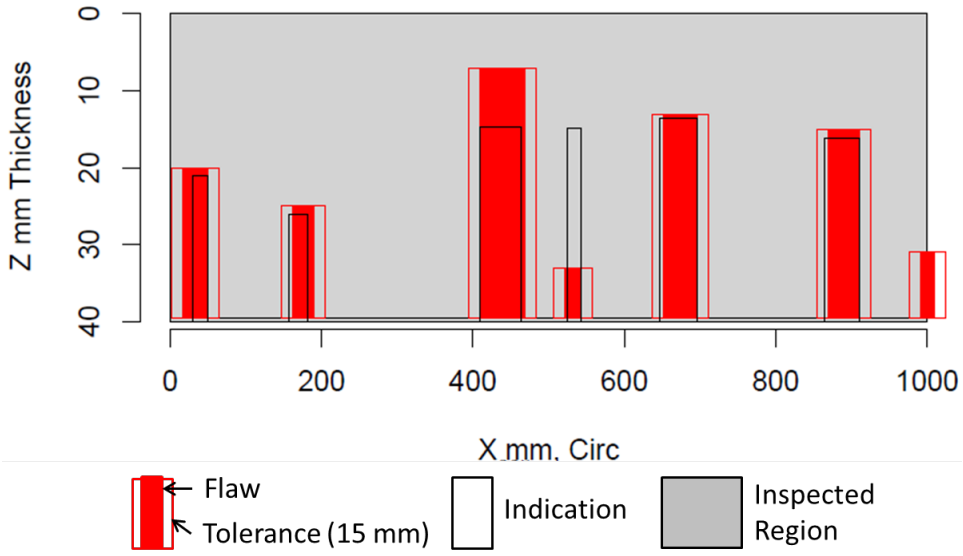

Figure A.2. Indication Plot (X–Z view) for Inspection of the Objective Area by the SHPA Technique Employed by Team 6

A.1.2 ECT Inspection of Objective Area by Team 16

The indication plot for the ECT technique applied to the objective area by team 16 is provided in Figure A.3. This plot indicates that six out of six flaws within the objective area are detected and that there are no false calls.

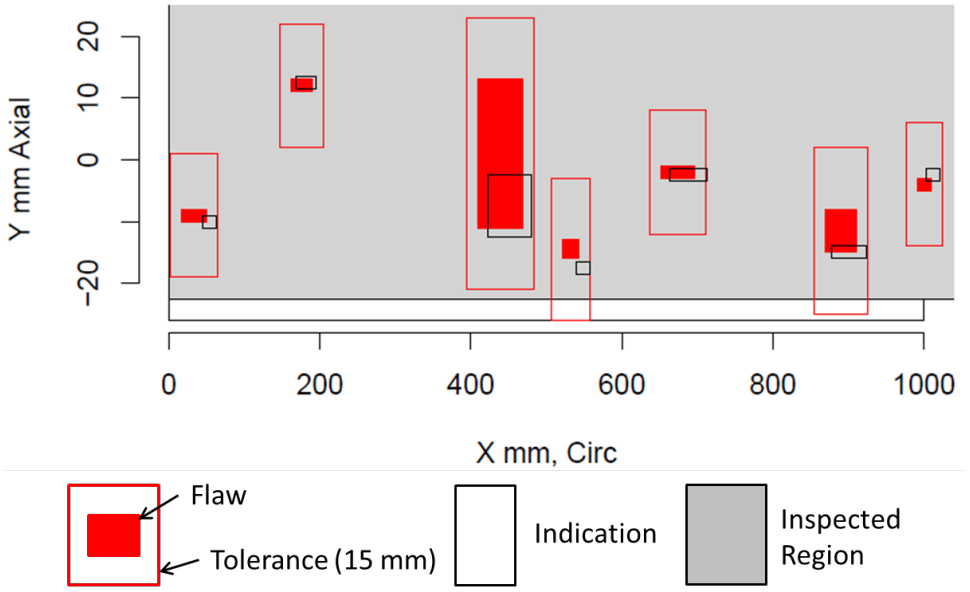

Figure A.3. Indication Plot (X–Y view) for Inspection of the Objective Area by the ECT Technique Employed by Team 16

A.1.3 SAFT Inspection of Objective Area by Team 17

The indication plots for the SAFT technique applied to the objective area by team 17 are provided in Figure A.4 and Figure A.5. Figure A.4 indicates that five out of five flaws within the objective area are detected and that there is one false call. In this case, only five flaws are evaluated because the region inspected by team 17 did not include the flaw located near X=200 mm. Figure A.5 indicates that the detected flaws are sized accurately with the exception of the flaw near X=500 mm, which is oversized considerably.

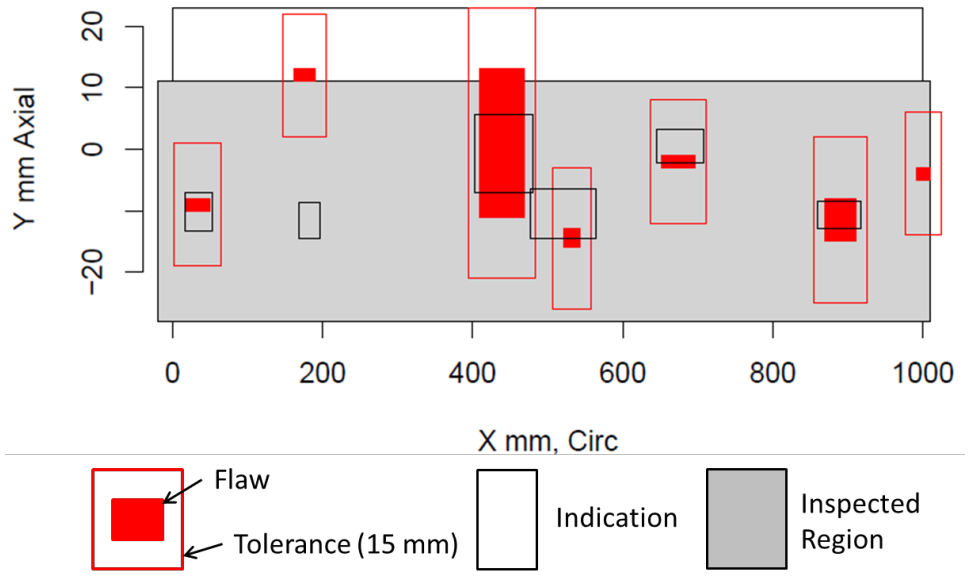

Figure A.4. Indication Plot (X–Y view) for Inspection of the Objective Area by the SAFT Technique Employed by Team 1

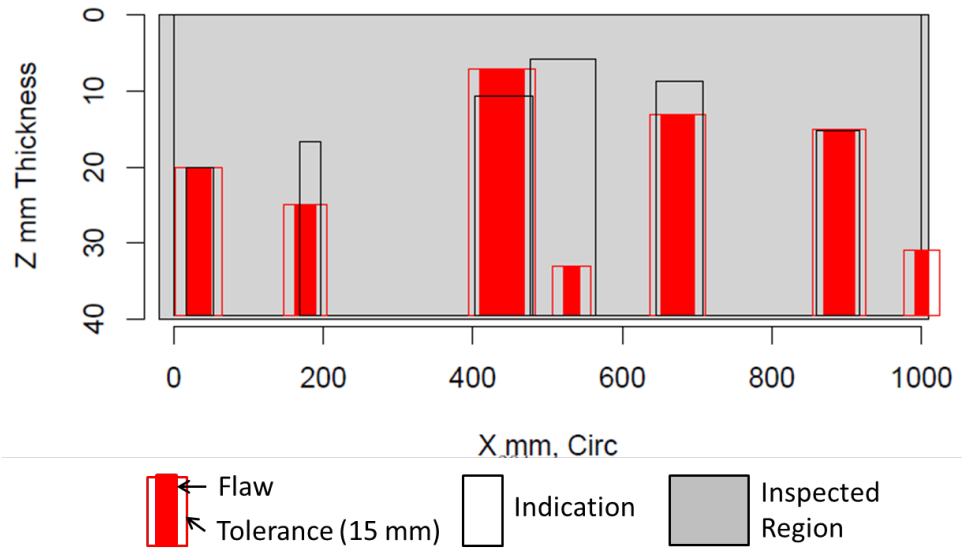

Figure A.5. Indication Plot (X–Z view) for Inspection of the Objective Area by the SAFT Technique Employed by Team 17

A.1.4 Ultrasound Infrared Inspection of Objective Area by Team 20

The indication plot for the ultrasound infrared thermography (UIRT) technique applied to the objective area by team 20 is provided in Figure A.6. This plot indicates that only one out of six flaws within the objective area is detected and that there are no false calls.

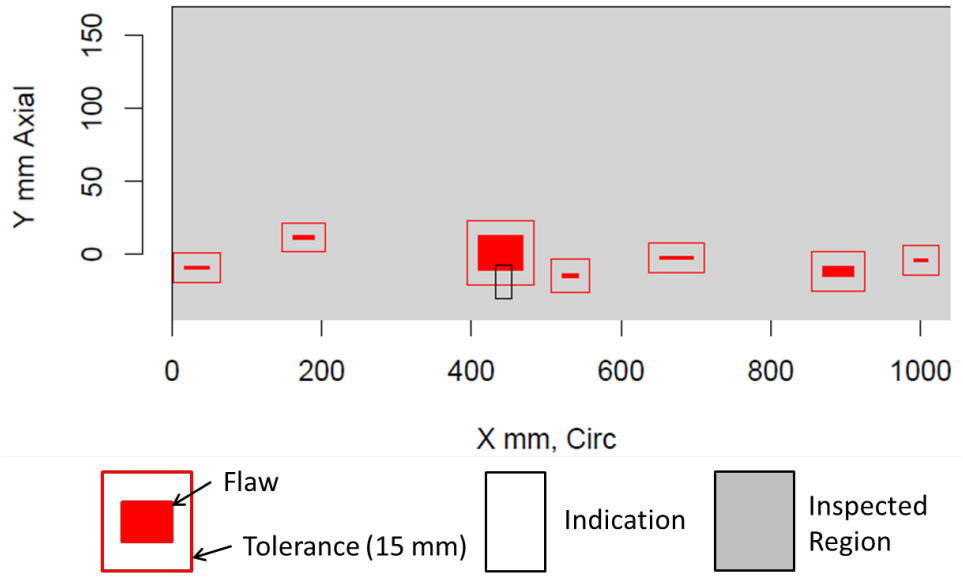

Figure A.6. Indication Plot (X–Y view) for Inspection of the Objective Area by the UIRT Technique Employed by Team 20

A.1.5 HHUT Inspection of Objective Area by Team 29

The indication plots for the HHUT technique applied to the objective area by team 29 are provided in Figure A.7 and Figure A.8. The objective area is split into two sections (i.e., 0 mm to 500 mm and 500 mm to 1000 mm) due to the large number of indications reported. No attempt was made at combining indications because they were all volumetric (see Figure A.8). The plots in Figure A.7 indicate that five out of six flaws are detected; however, there are a large number of false calls and the pattern of indications suggests that detections could be the result of chance.

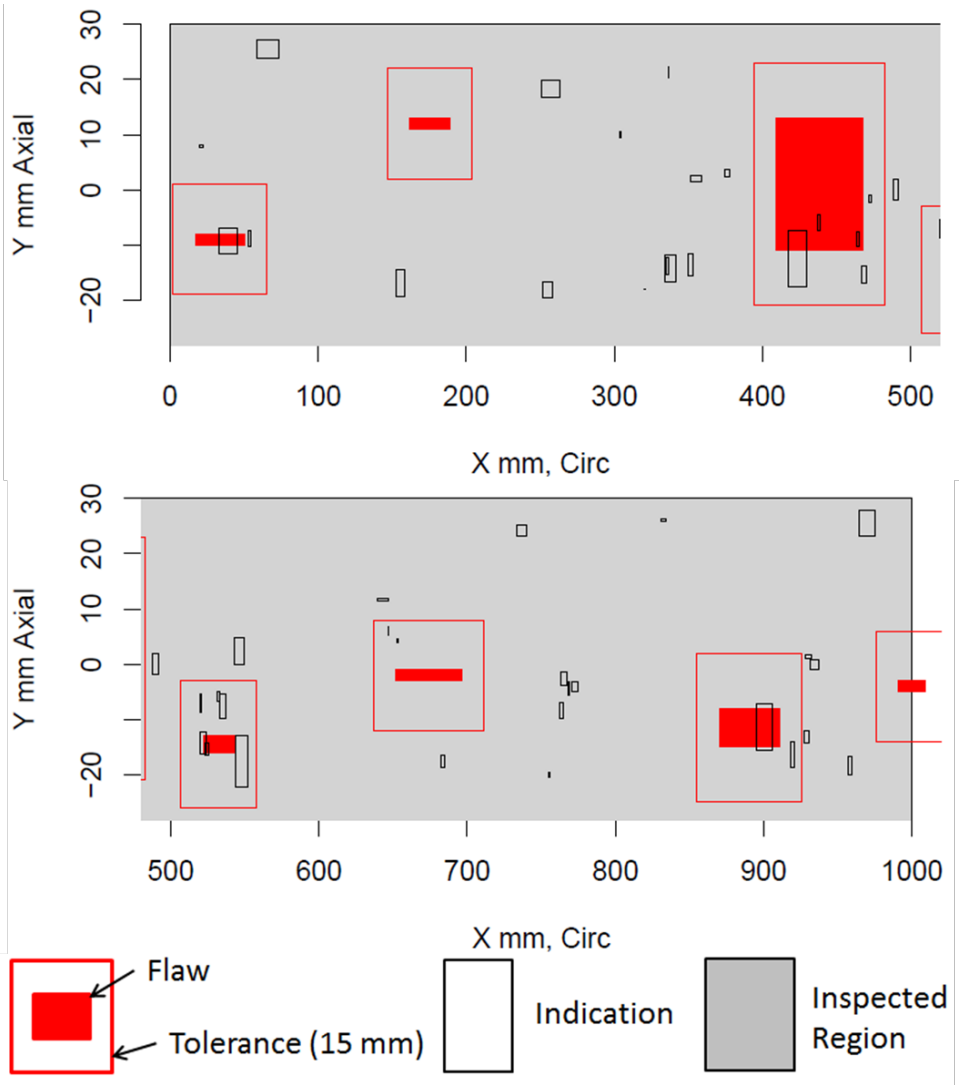

Figure A.7. Indication Plot (X–Y view) for Inspection of the Objective Area by the HHUT Technique Employed by Team 29

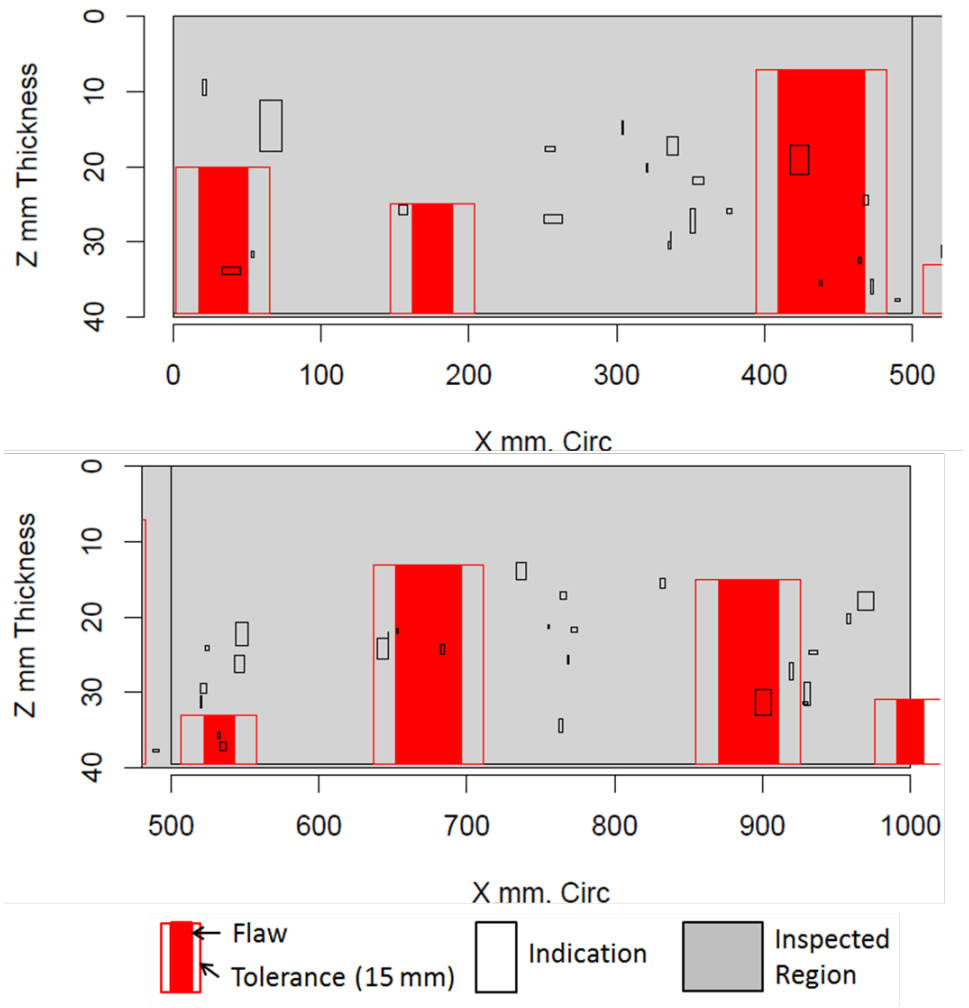

Figure A.8. Indication Plot (X–Z view) for Inspection of the Objective Area by the HHUT Technique Employed by Team 29

A.1.6 PA-ATOFD Inspection of Objective Area by Team 29

The indication plots for the PA-ATOFD technique applied to the objective area by team 29 are provided in Figure A.9 and Figure A.10. The objective area is split into two sections (i.e., 0 mm to 500 mm and 500 mm to 1000 mm) due to the large number of indications originally reported. The indication plots displayed result from application of the American Society of Mechanical Engineers (ASME) Section XI IWA-3400 rules for linear surface flaws to account for multiple flaws that are in close proximity. The plots in Figure A.9 indicate that three out of six flaws are detected and that there are a substantial number of false calls (i.e., five).

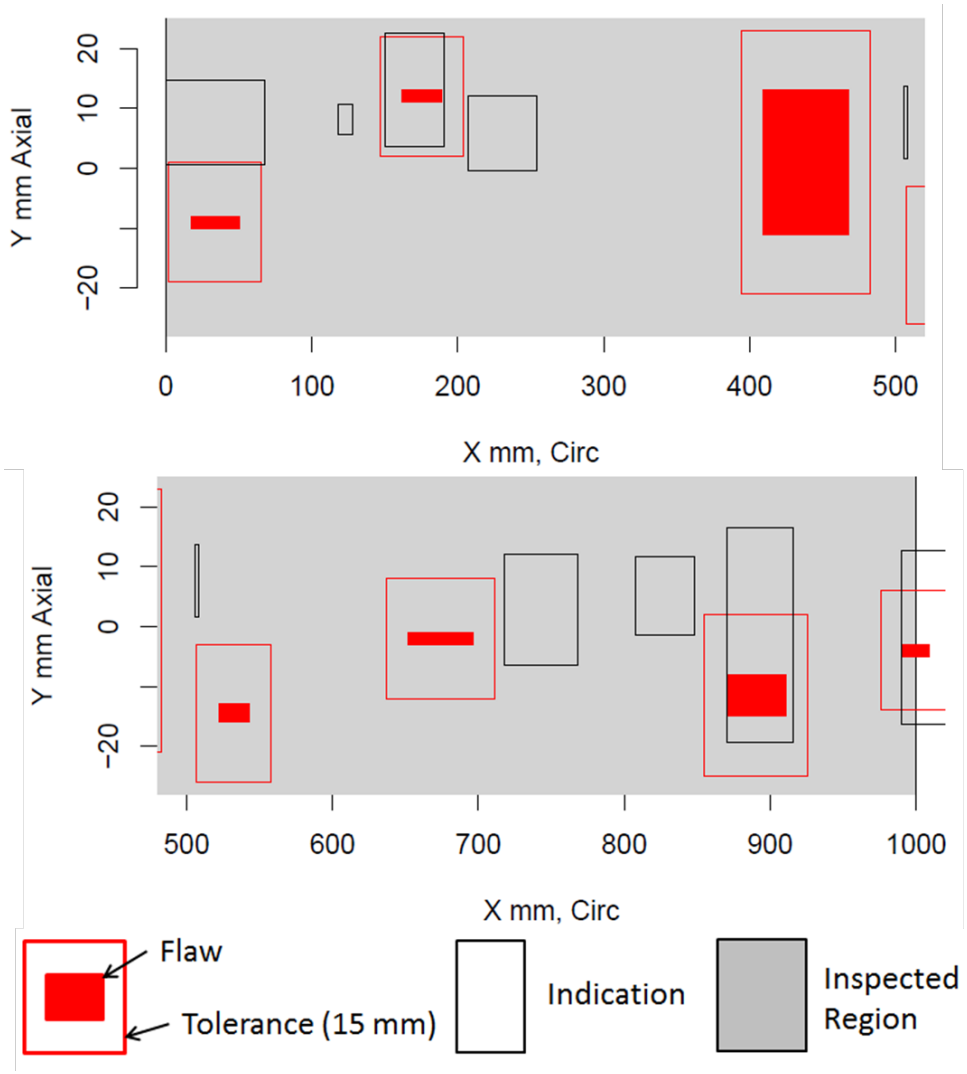

Figure A.9. Indication Plot (X–Y view) for Inspection of Surface-Breaking Defects in the Objective Area by the PA-ATOFD Technique Employed by Team 29

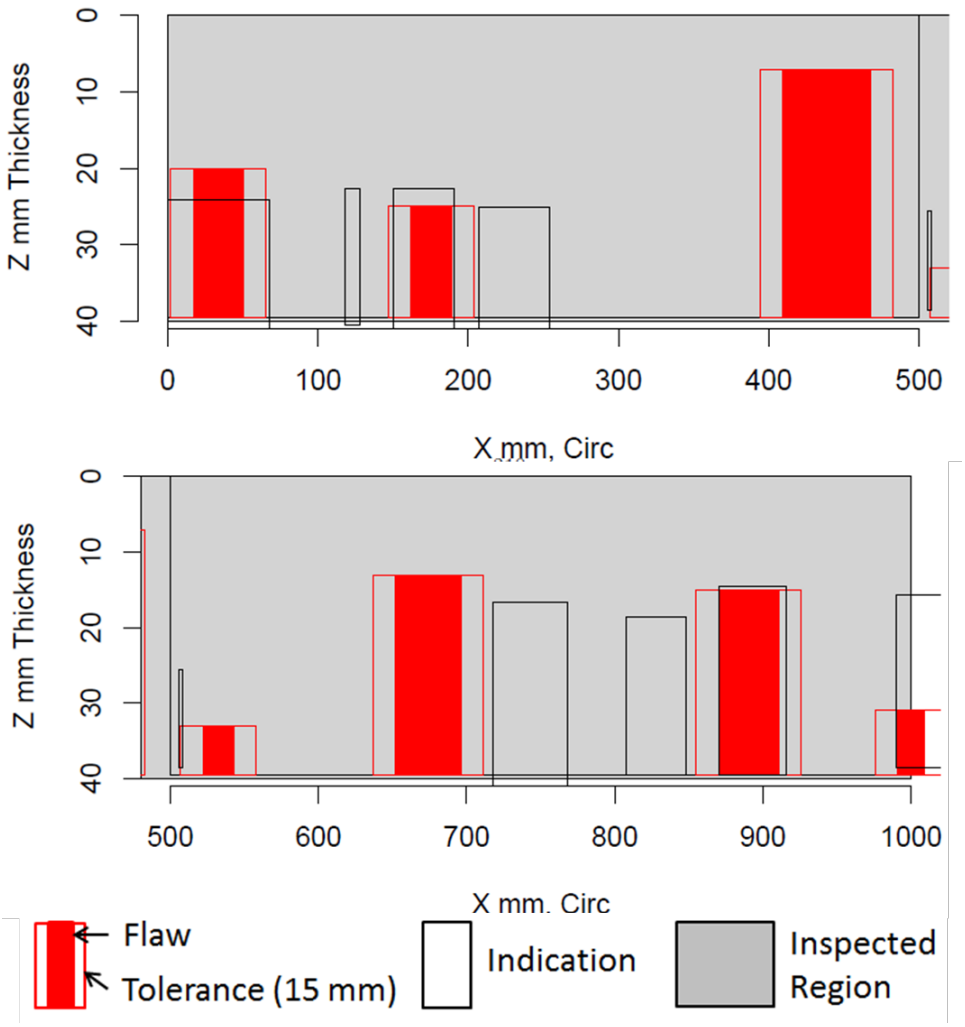

Figure A.10. Indication Plot (X–Z view) for Inspection of Surface-Breaking Defects in the Objective Area by the PA-ATOFD Technique Employed by Team 29

Figure A.11 and Figure A.12 display indication plots for the PA-ATOFD technique applied by team 29 to examine the interior of the test block over the objective area. The objective area is split into two sections (i.e., 0 mm to 500 mm and 500 mm to 1000 mm) due to the large number of indications originally reported. The indications do not signal surface-breaking defects, as Figure A.12 shows. The ASME Section XI IWA-3400 rules for linear surface flaws to account for multiple flaws that are in close proximity are not applied because the indications are not surface-breaking. Figure A.11 shows that five out of six flaws are detected, but there are several false calls.

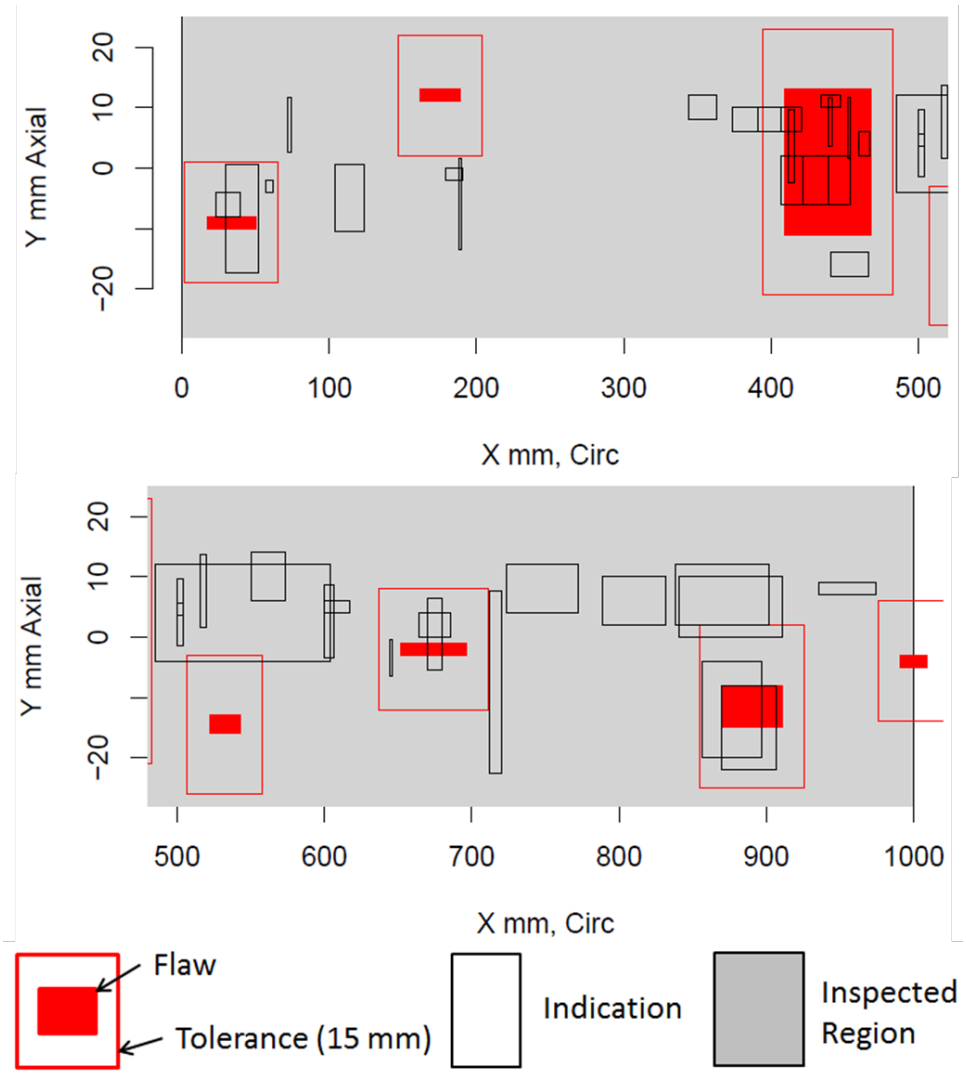

Figure A.11. Indication Plot (X–Y view) for Inspection of Interior Defects in the Objective Area by the PA-ATOFD Technique Employed by Team 29

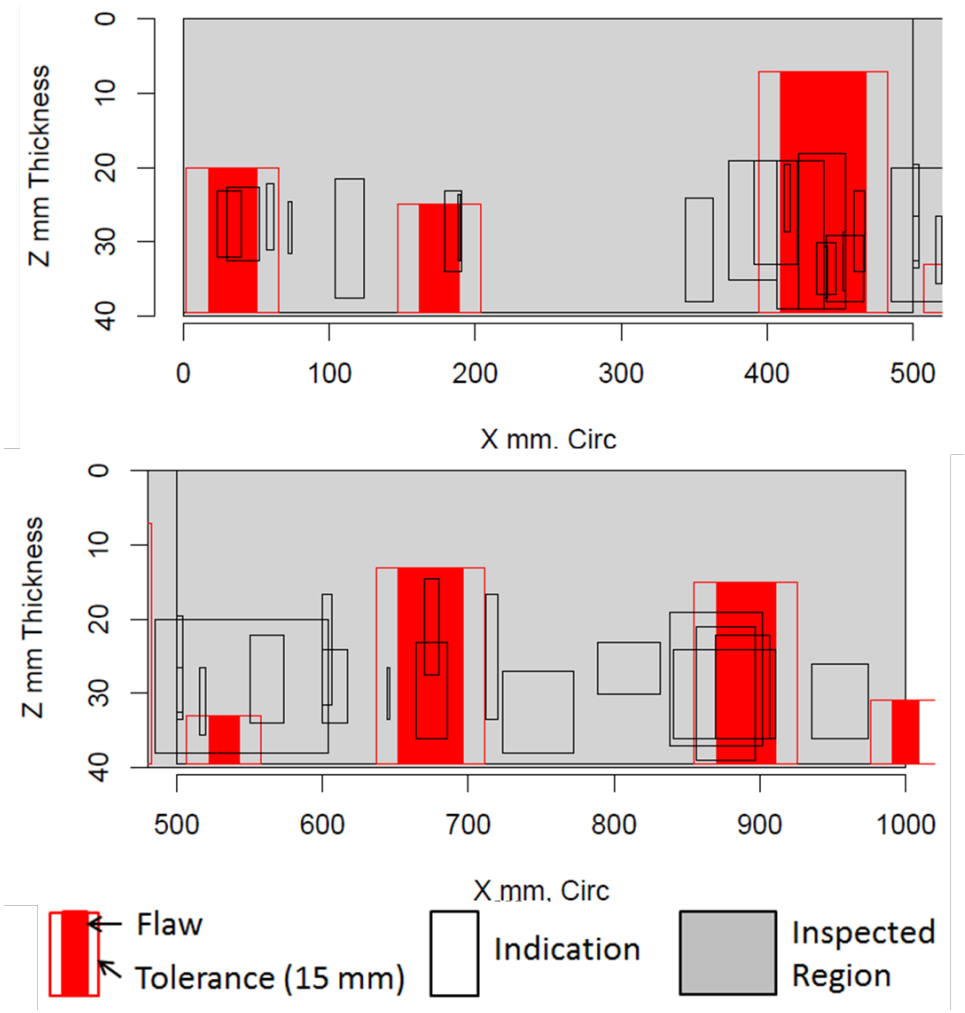

Figure A.12. Indication Plot (X–Z view) for Inspection of Interior Defects in the Objective Area by the PA-ATOFD Technique Employed by Team 29

A.1.7 PA-TP Inspection of Objective Area by Team 29

The indication plots for the PA-TP technique applied to the objective area by team 29 are provided in Figure A.13 and Figure A.14. The objective area is split into two sections (i.e., 0 mm to 500 mm and 500 mm to 1000 mm) due to the large number of indications originally reported. The indication plots displayed result from application of the ASME Section XI IWA-3400 rules for linear surface flaws to account for multiple flaws that are in close proximity. The plots in Figure A.13 indicate that six out of six flaws are detected and that there are two false calls.

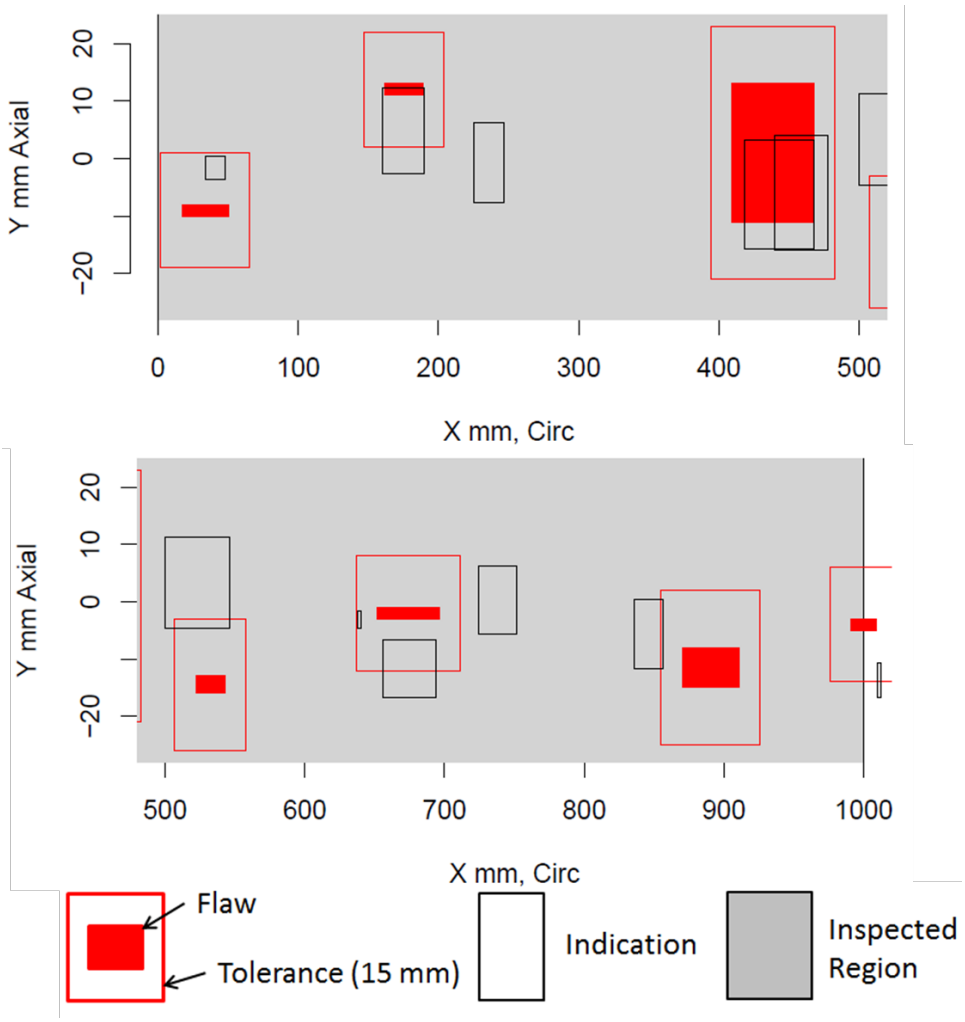

Figure A.13. Indication Plot (X–Y view) for Inspection of Surface Breaking Defects in the Objective Area by the PA-TP Technique Employed by Team 29

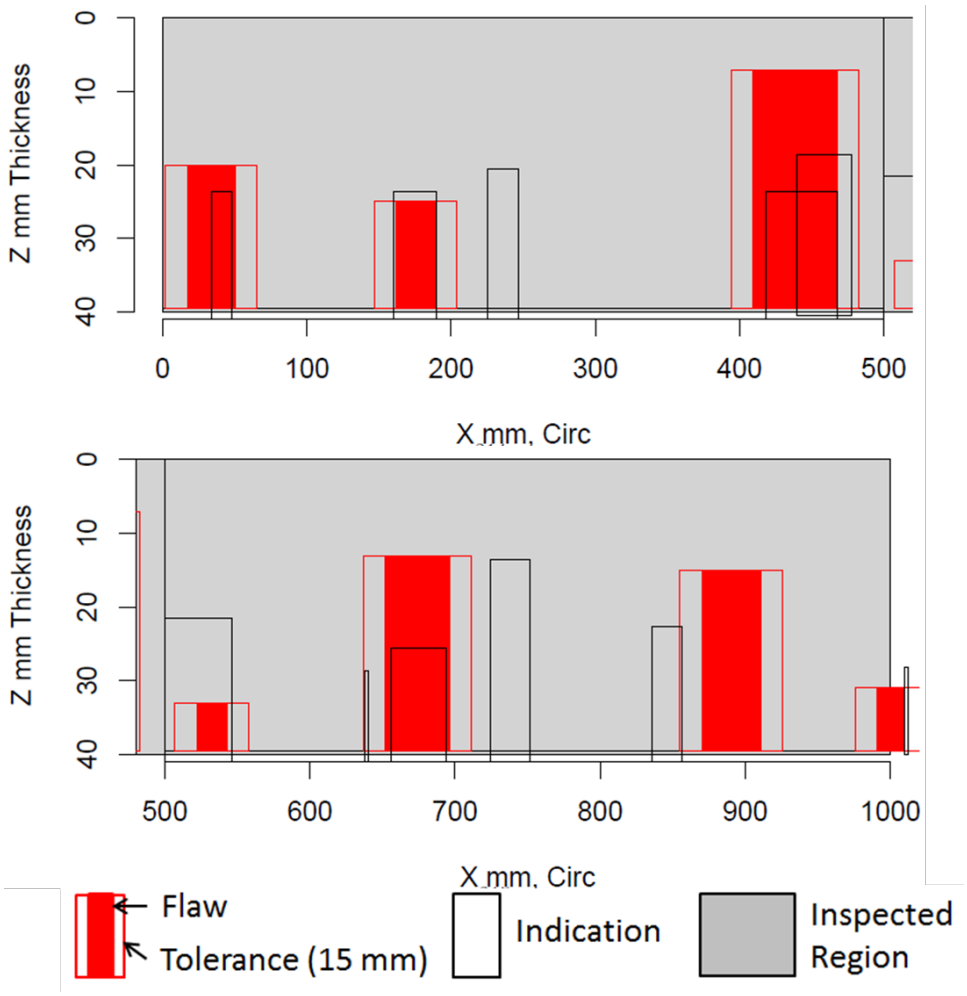

Figure A.14. Indication Plot (X–Z view) for Inspection of Surface Breaking Defects in the Objective Area by the PA-TP Technique Employed by Team 29

Figure A.15 and Figure A.16 display indication plots for the PA-TP technique applied by team 29 to examine the interior of the test block over the objective area. The objective area is split into two sections (i.e., 0 mm to 500 mm and 500 mm to 1000 mm) due to the large number of indications originally reported. The indications do not signal surface-breaking defects, as Figure A.16 shows. The ASME Section XI IWA-3400 rules for linear surface flaws to account for multiple flaws that are in close proximity are not applied because the indications are not surface-breaking. Figure A.15 shows that six out of six flaws are detected, but there are several false calls.

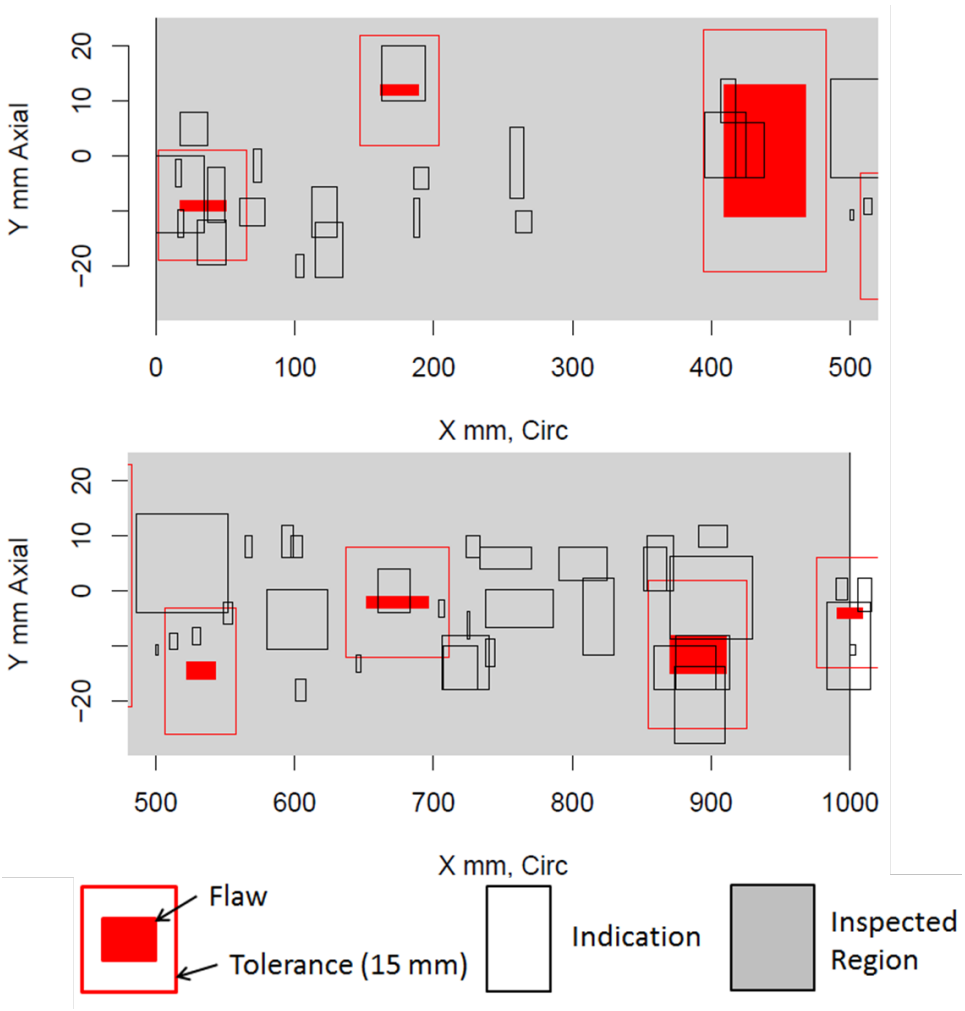

Figure A.15. Indication Plot (X–Y view) for Inspection of Interior Defects in the Objective Area by the PA-TP Technique Employed by Team 29

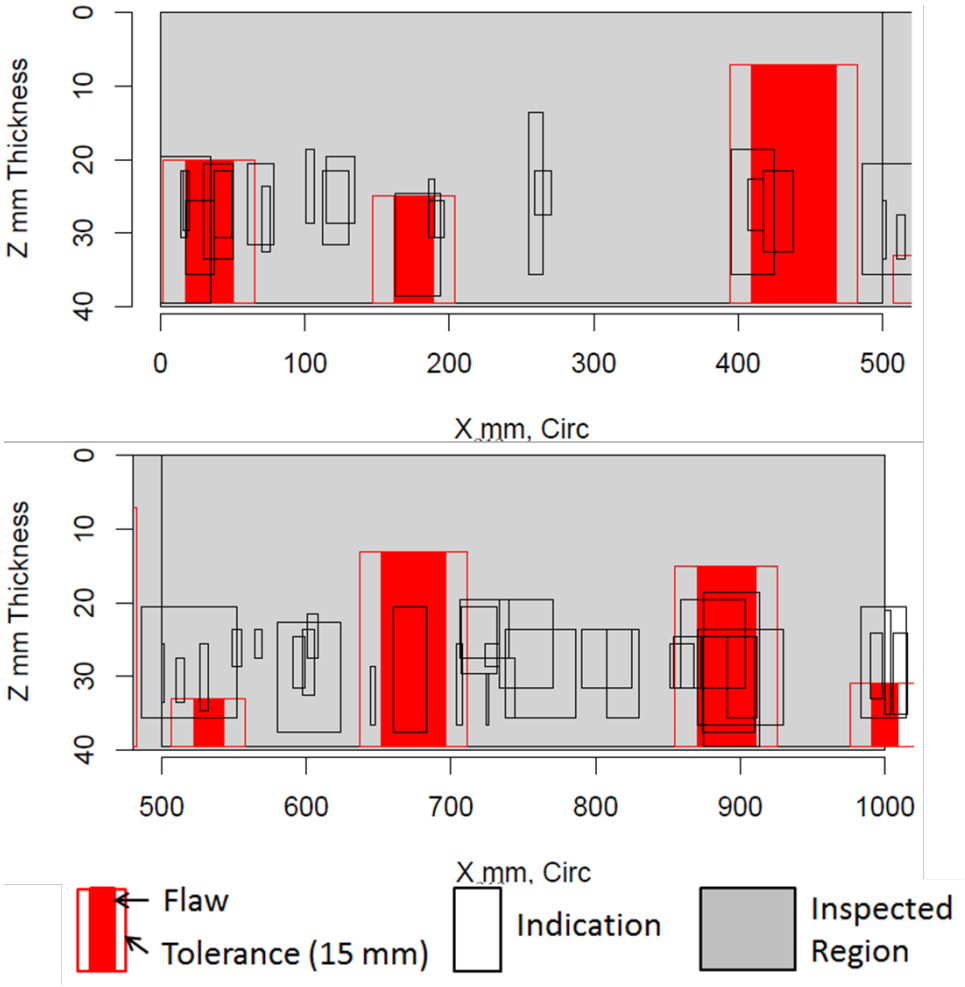

Figure A.16. Indication Plot (X–Z view) for Inspection of Interior Defects in the Objective Area by the PA-TP Technique Employed by Team 29

A.1.8 HHUT Inspection of Objective Area by Team 30

The indication plots for the SAFT technique applied to the objective area by team 17 are provided in Figure A.17 and Figure A.18. Figure A.17 shows that only the +Y side of the weld was inspected, thus, only two flaws within the objective area were actually included in the inspected region. Of these two flaws, one flaw is detected and the other flaw is missed. There is also one false call.

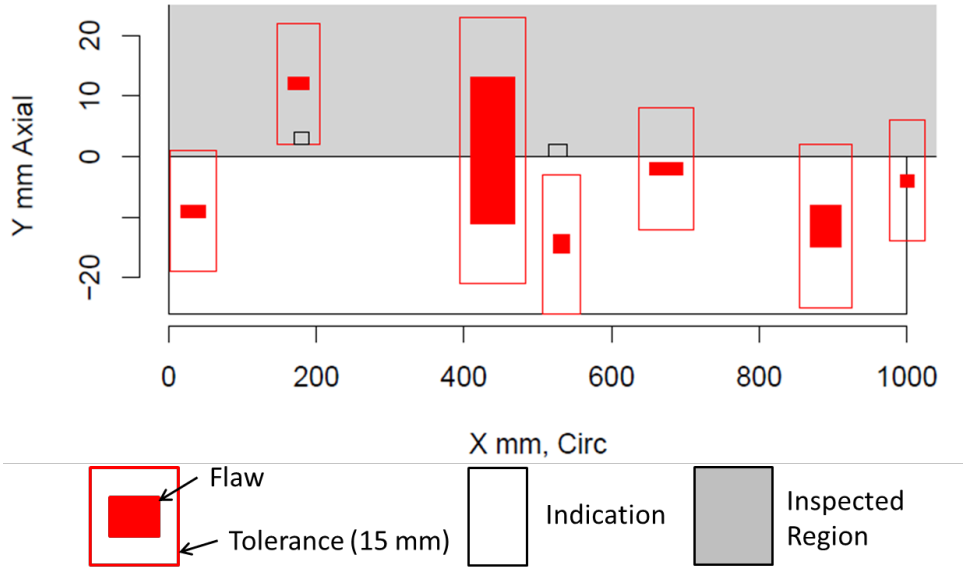

Figure A.17. Indication Plot (X–Y view) for Inspection of the Objective Area by the HHUT Technique Employed by Team 30

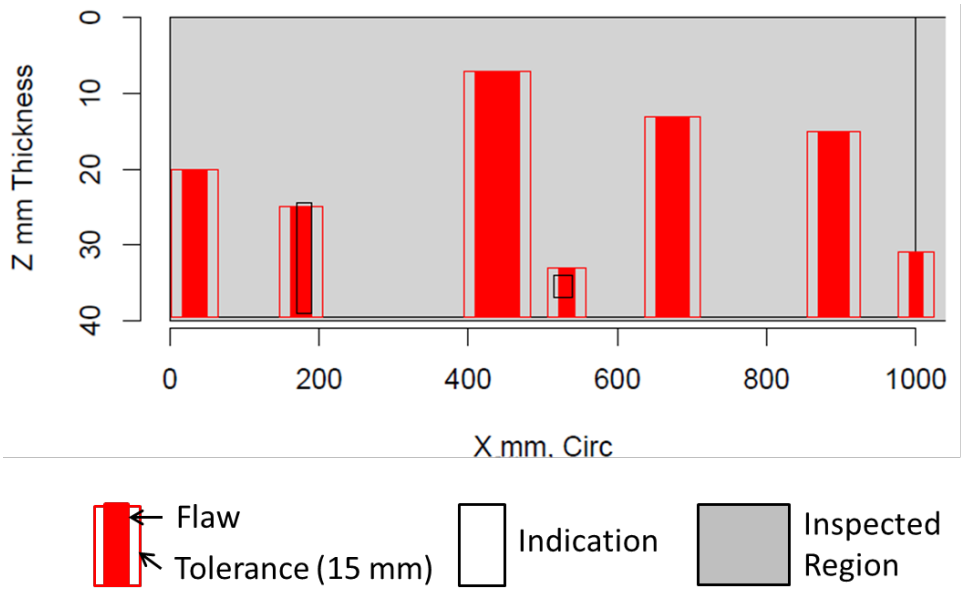

Figure A.18. Indication Plot (X–Z view) for Inspection of the Objective Area by the HHUT Technique Employed by Team 30

A.1.9 AECT Inspection of Objective Area by Team 33

The indication plot for the AECT technique applied to the objective area by team 33 is provided in Figure A.19. This plot indicates that six out of six flaws within the objective area are detected and that there is one false calls.

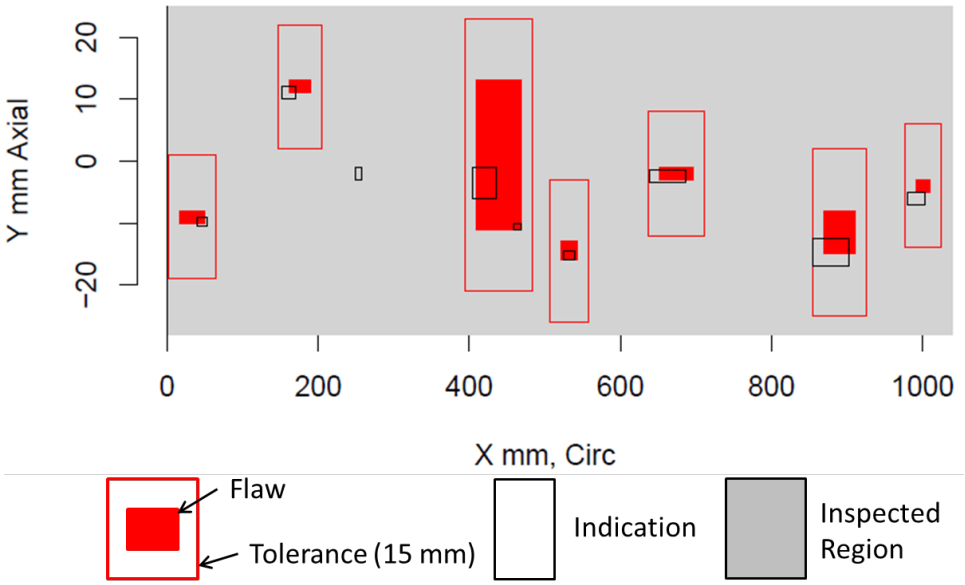

Figure A.19. Indication Plot (X–Y view) for Inspection of the Objective Area by the AECT Technique Employed by Team 33

A.2 Inspections of the Entire Weld

A few teams examined all, or most, of the weld region in the test block. Data obtained from examining regions outside of the objective area are not included in the data analysis; however, the indication plots are included in this section.

A.2.1 ECT Inspection of Entire Weld by Team 16

The indication plot for the ECT technique applied to the entire weld region by team 16 is provided in Figure A.20. This plot indicates that all flaws are detected and that there are no false calls.

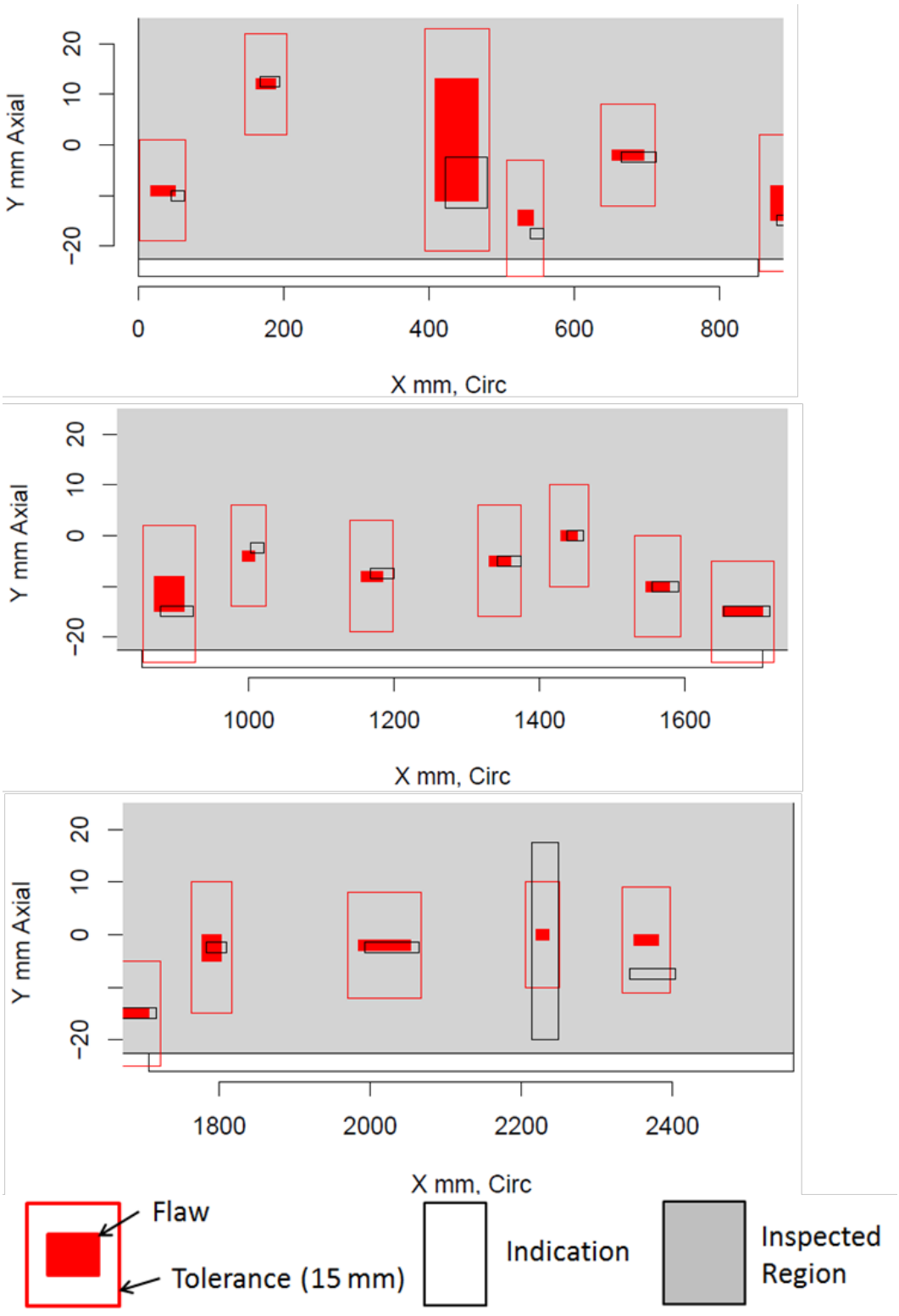

Figure A.20. Indication Plot (X–Y view) for Inspection of the Entire Weld Area by the ECT Technique Employed by Team 16

A.2.2 UIRT Inspection of Entire Weld by Team 20

The indication plot for the UIRT technique applied to the entire weld region by team 20 is provided in Figure A.21. This plot indicates that only three flaws are detected (15 flaws are missed) and that there are no false calls.

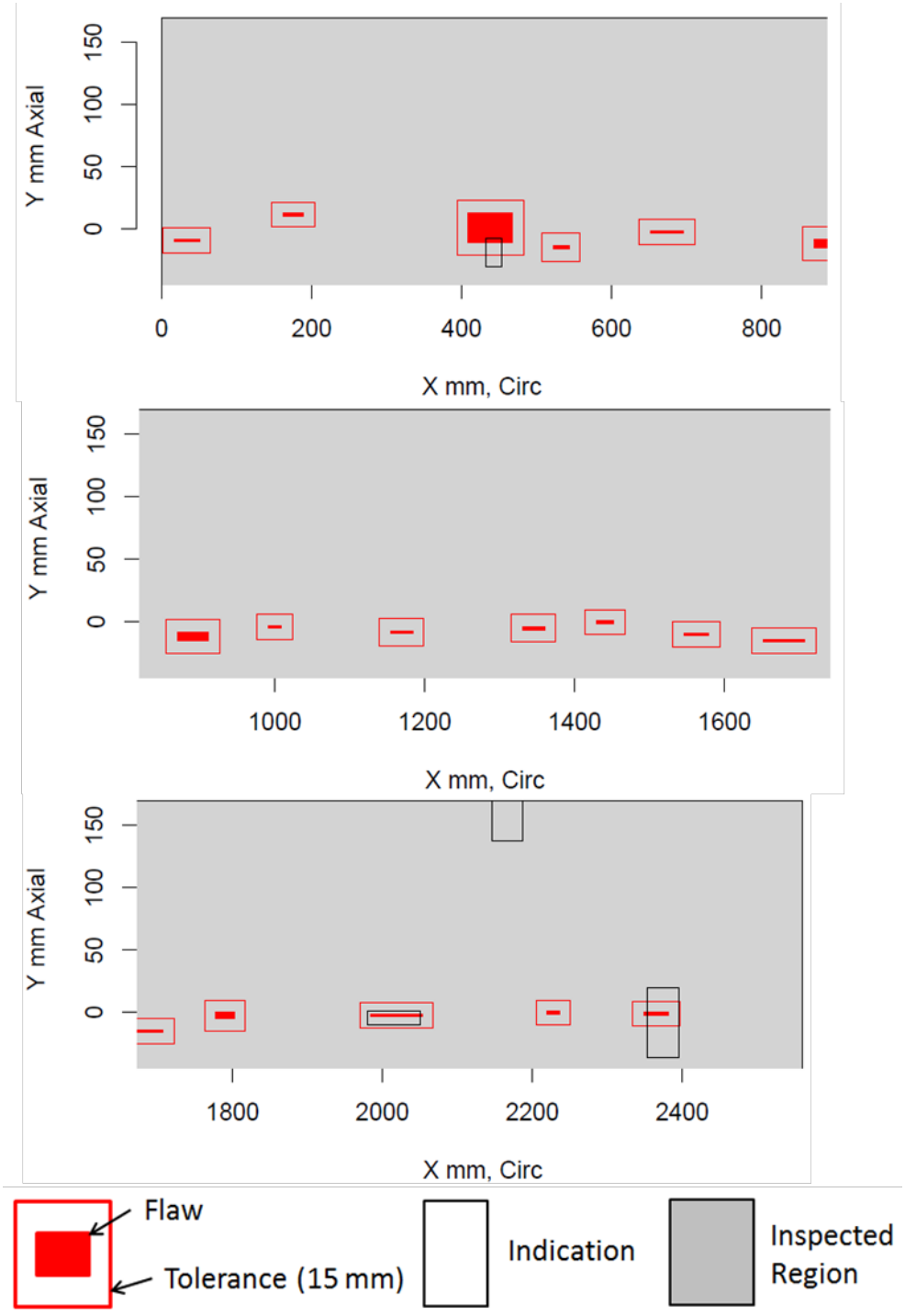

Figure A.21. Indication Plot (X–Y view) for Inspection of the Entire Weld Area by the UIRT Technique Employed by Team 20

A.2.3 AECT Inspection of Entire Weld by Team 33

The indication plot for the AECT technique applied to most of the weld region by team 33 is provided in Figure A.22. This plot indicates that all flaws within the inspected region are detected and that there is one false call.

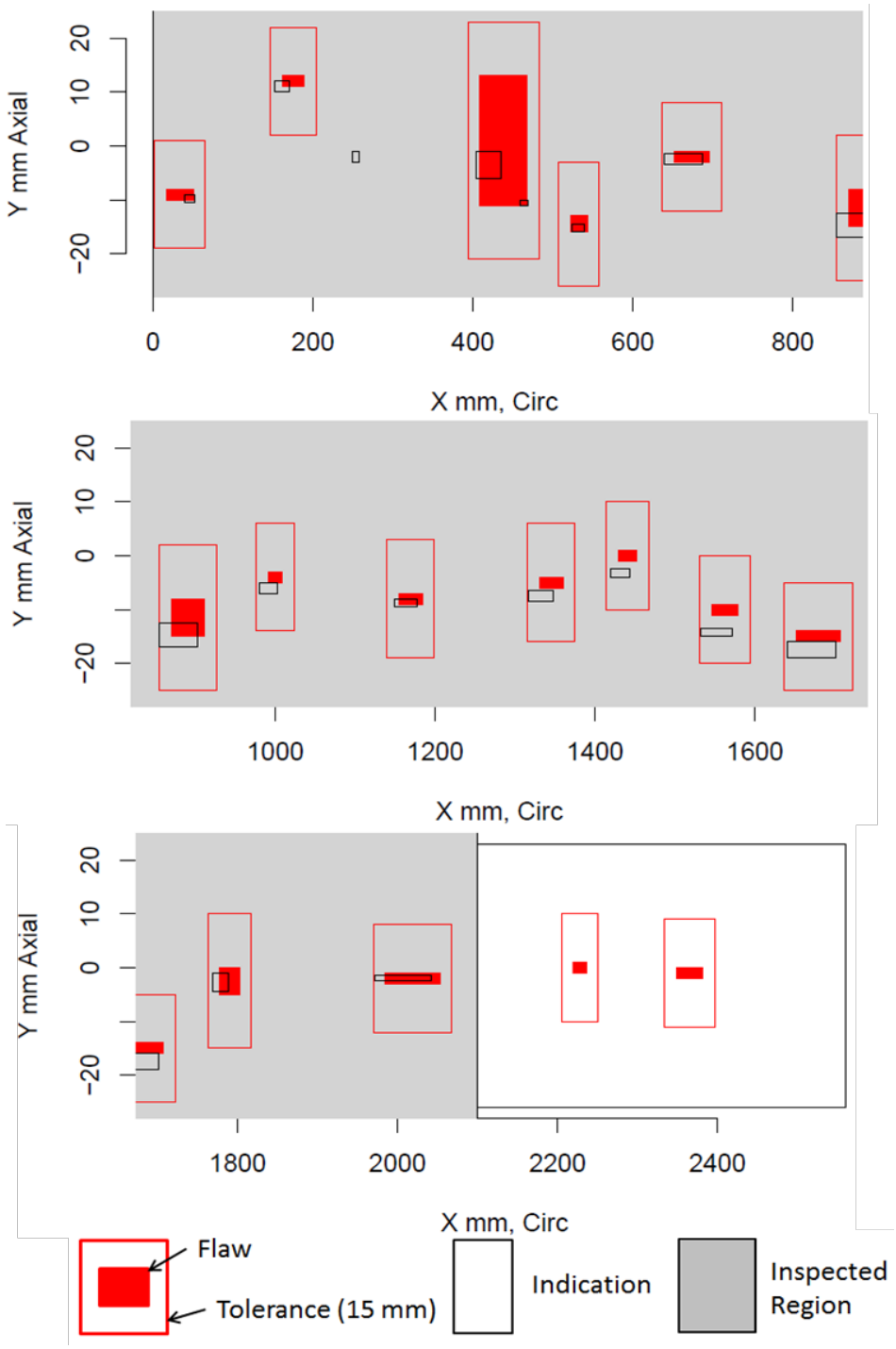

Figure A.22. Indication Plot (X–Y view) for Inspection of the Entire Weld Area by the AECT Technique Employed by Team 33

A.3 PA-TRT Inspection by Team 22

Team 22 inspected the incorrect portion of the test block so the results obtained by technique PA-TRT are not compared to results obtained by other emerging techniques or by established techniques. However, the indication plot for the PA-TRT technique applied to the incorrect area is provided in Figure A.23. This plot indicates that for the area inspected, six out of six flaws are detected and that there are no false calls.

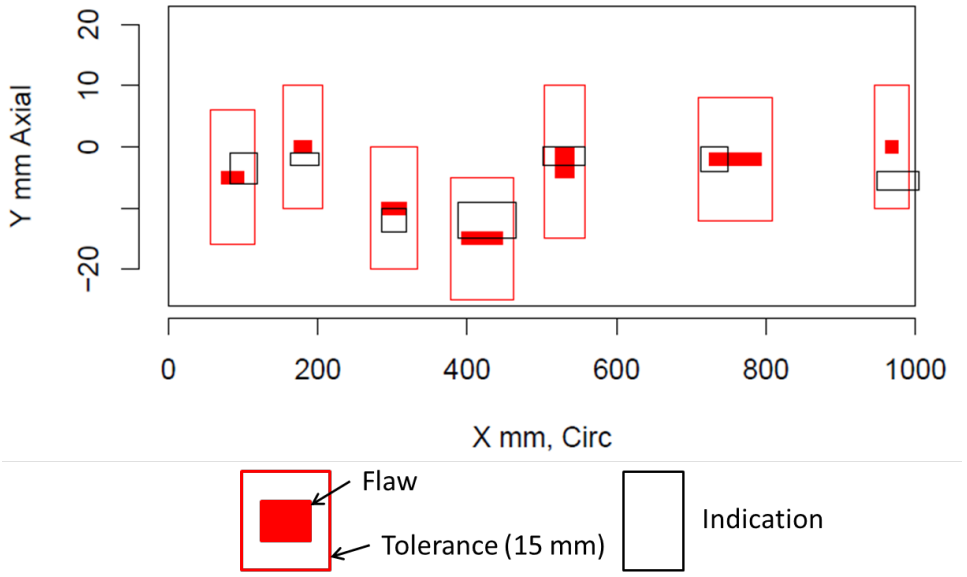

Figure A.23. Indication Plot (X–Y view) for Inspection of an Incorrect Area by the PA-TRT Technique Employed by Team 22

Appendix B

Indication Plots for Established Technologies

Appendix B

Indication Plots for Established Technologies

This section summarizes the results obtained from analysis of data obtained from established technologies in PARENT blind testing, which is documented in NUREG/CR-7325 (Meyer and Heasler 2017), over the objective area used in the blind test of open techniques by displaying indication plots for each examination. The objective area for the test was limited to a region of ΔX=1000 mm in accordance to the coordinate system defined in Figure 2.1. The origin of the coordinate system was shifted between PARENT blind testing described in NUREG/CR-7325 and the blind testing of open techniques. Thus, the range of the X-axis in the plots below is from X= 300 mm to X=2300 mm.

B.1 Procedure PAUT.108 Results from Objective Area

The indication plots for procedure PAUT.108 applied to the objective area are provided in Figure B.1 and Figure B.2. Figure B.1 indicates that five out of six flaws within the objective area are detected and that there is one false call. Figure B.2 indicates that all of the detected flaws are slightly undersized, with the exception of one flaw.

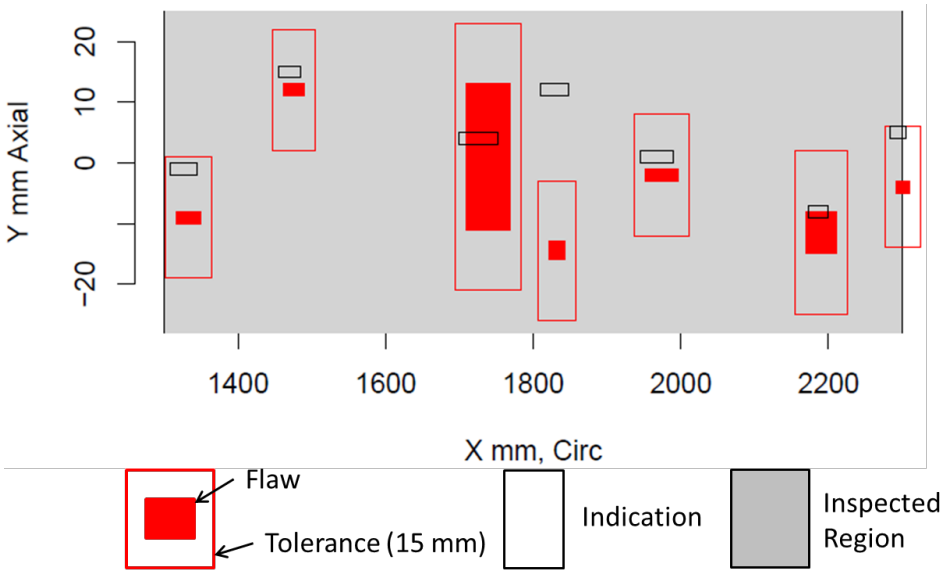

Figure B.1. Indication Plot (X–Y view) for Inspection of the Objective Area by the PAUT Technique Employed by Team 108

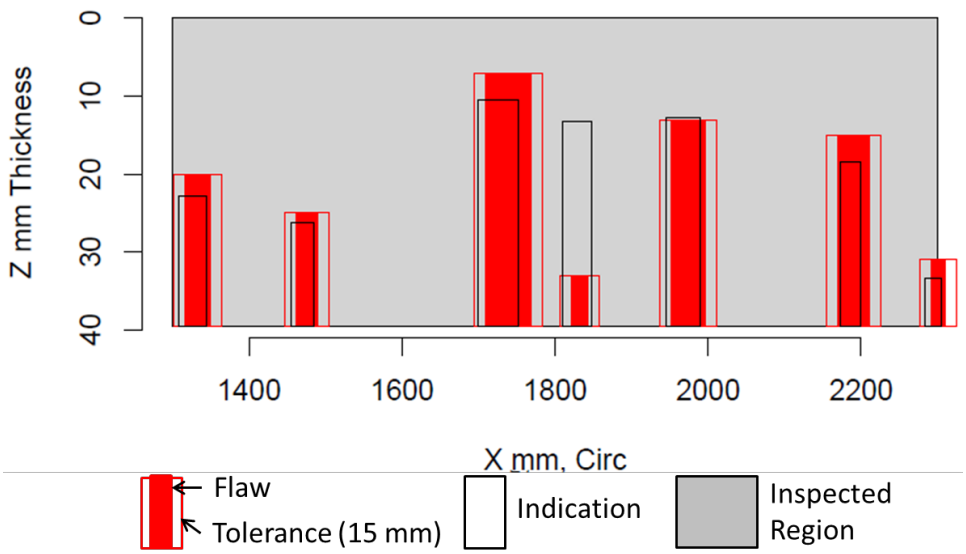

Figure B.2. Indication Plot (X–Z view) for Inspection of the Objective Area by the PAUT Technique Employed by Team 108

B.2 Procedure PAUT.115 Results from Objective Area

The indication plots for procedure PAUT.115 applied to the objective area are provided in Figure B.3 and Figure B.4. Figure B.3 indicates that six out of six flaws within the objective area are detected and that there are no false calls. Figure B.4 indicates pretty accurate depth sizing for all of the detected flaws.

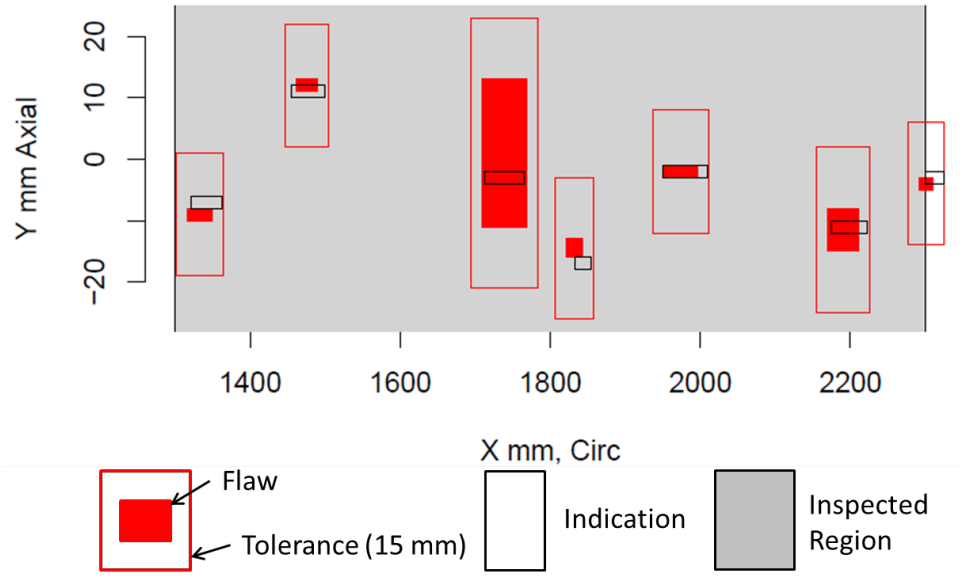

Figure B.3. Indication Plot (X–Y view) for Inspection of the Objective Area by the PAUT Technique Employed by Team 115

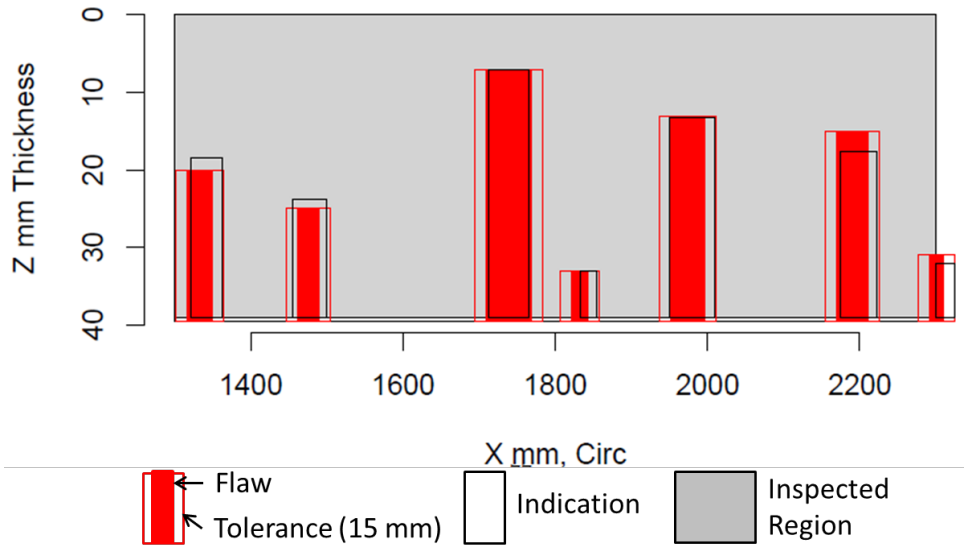

Figure B.4. Indication Plot (X–Z view) for Inspection of the Objective Area by the PAUT Technique Employed by Team 115

B.3 Procedure PAUT.126 Results from Objective Area

The indication plots for procedure PAUT.126 applied to the objective area are provided in Figure B.5 and Figure B.6. Figure B.5 indicates that three out of six flaws within the objective area are detected and that there are no false calls. Figure B.6 indicates that all of the detected flaws are undersized.

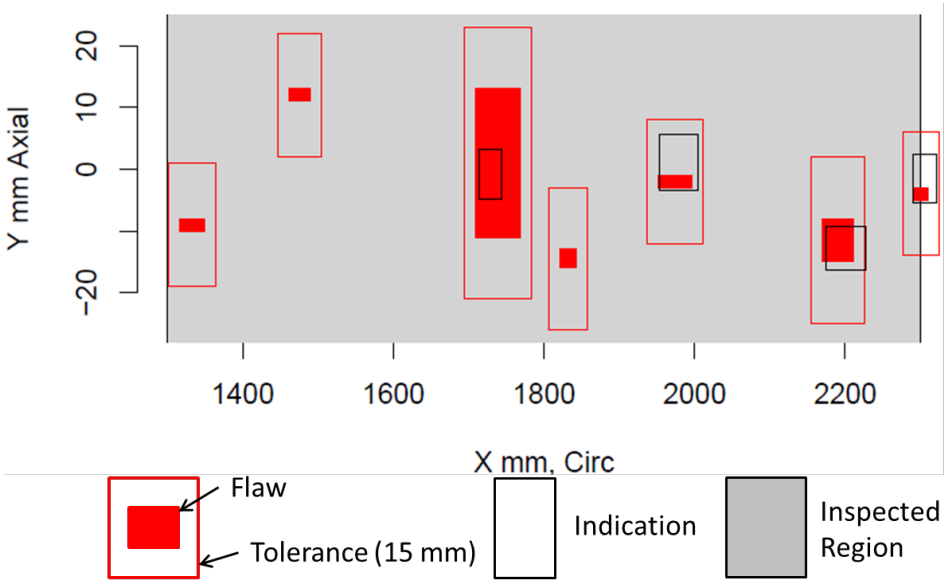

Figure B.5. Indication Plot (X–Y view) for Inspection of the Objective Area by the PAUT Technique Employed by Team 126

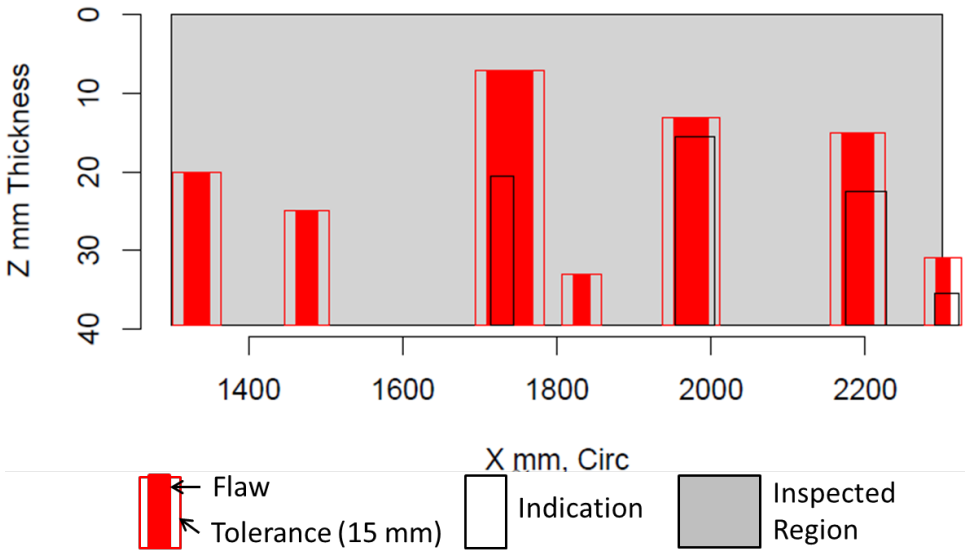

Figure B.6. Indication Plot (X–Z view) for Inspection of the Objective Area by the PAUT Technique Employed by Team 126

B.4 Procedure PAUT.128 Results from Objective Area

The indication plots for procedure PAUT.128 applied to the objective area are provided in Figure B.7 and Figure B.8. Figure B.7 indicates that six out of six flaws within the objective area are detected and that there are no false calls. Figure B.8 shows mixed sizing results. Two of the detected flaws appear to be sized pretty accurately. Some significant oversizing and undersizing is observed for the remainder of the detected flaws.

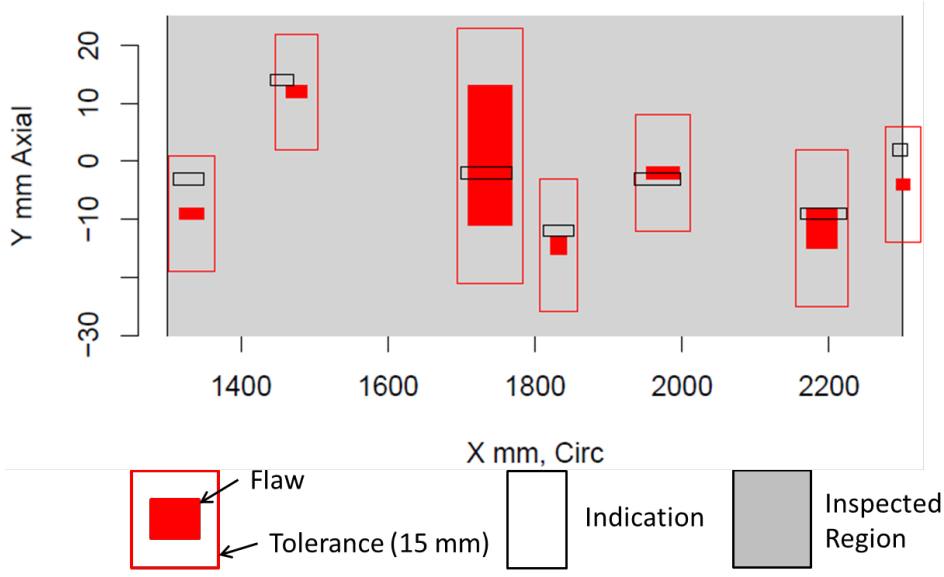

Figure B.7. Indication Plot (X–Y view) for Inspection of the Objective Area by the PAUT Technique Employed by Team 128

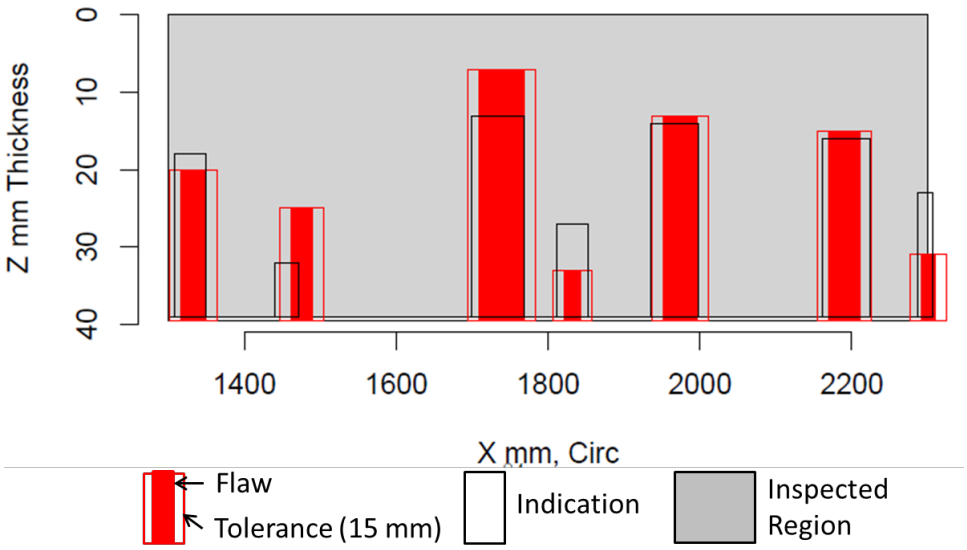

Figure B.8. Indication Plot (X–Z view) for Inspection of the Objective Area by the PAUT Technique Employed by Team 128

B.5 Procedure UT.108 Results from Objective Area

The indication plots for procedure UT.108 applied to the objective area are provided in Figure B.9 and Figure B.10. Figure B.9 indicates that five out of six flaws within the objective area are detected and that there is one false calls. Figure B.10 indicates that most of the detected flaws are slightly undersized, with the exception of one flaw. It also appears that UT.108 was unable to properly determine that one of the flaws was surface breaking.

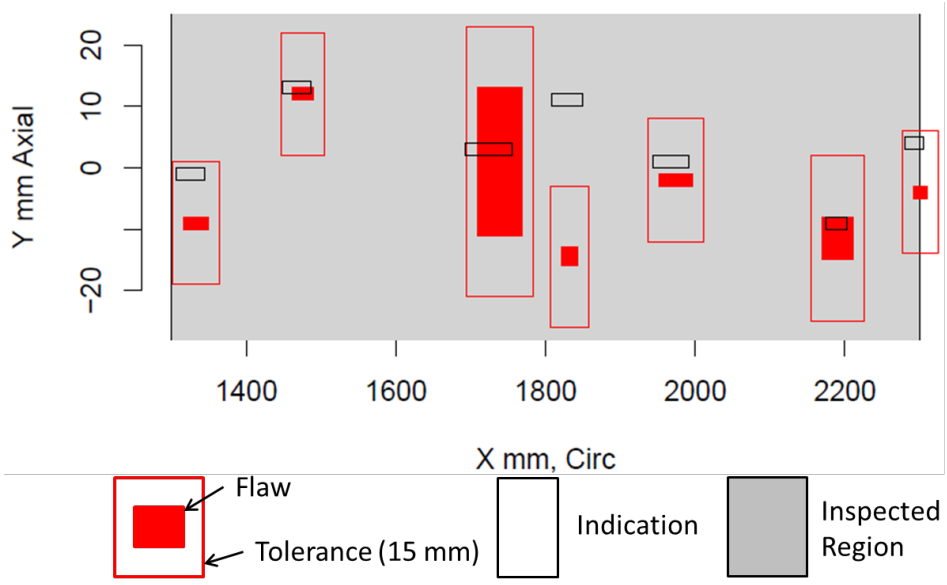

Figure B.9. Indication Plot (X–Y view) for Inspection of the Objective Area by the UT Technique Employed by Team 108

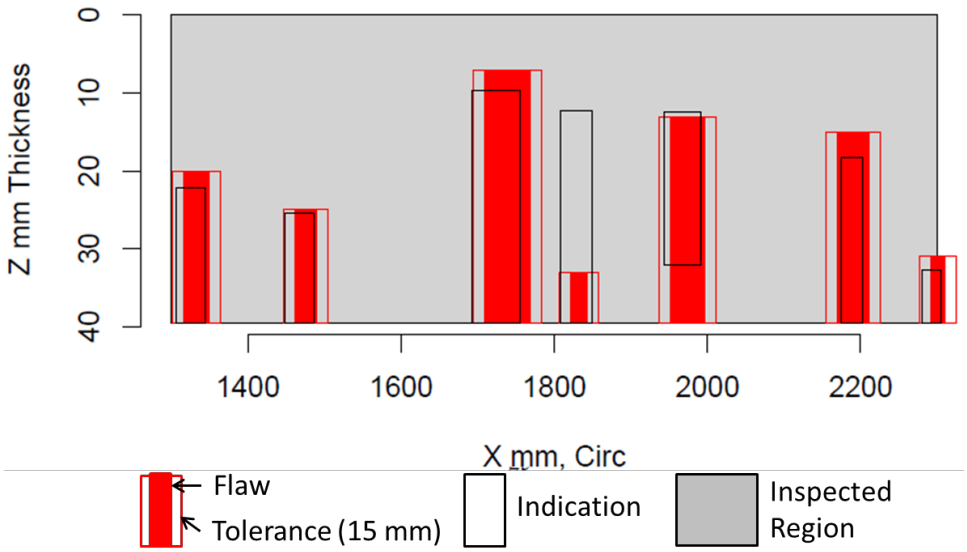

Figure B.10. Indication Plot (X–Z view) for Inspection of the Objective Area by the UT Technique Employed by Team 108

B.6 Procedure UT.126 Results from Objective Area

The indication plots for procedure UT.126 applied to the objective area are provided in Figure B.11 and Figure B.12. Figure B.11 appears to indicate that three out of six flaws within the objective area are detected. However, only one of the flaws is actually detected since two of the indications are on the border of the tolerance boundary and have no overlapping area between the indications and the area defined by tolerance boundaries. The indications appear to overlap with the areas defined by tolerance boundaries in Figure B.11 because the dimension of the indications is exaggerated for visual aid. Thus, they are classified as false calls. Figure B.12 indicates that the one detected flaw is significantly undersized.

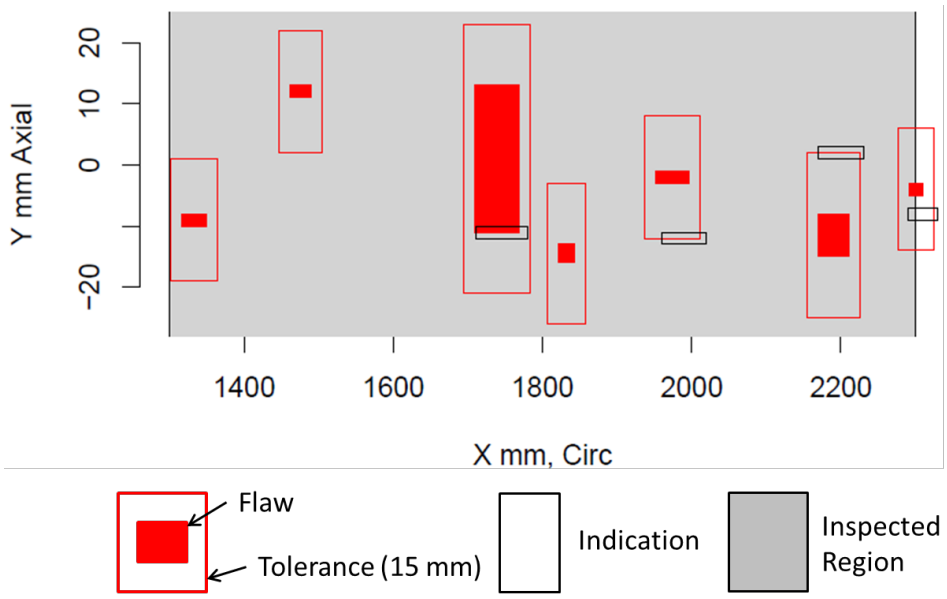

Figure B.11. Indication Plot (X–Y view) for Inspection of the Objective Area by the UT Technique Employed by Team 126

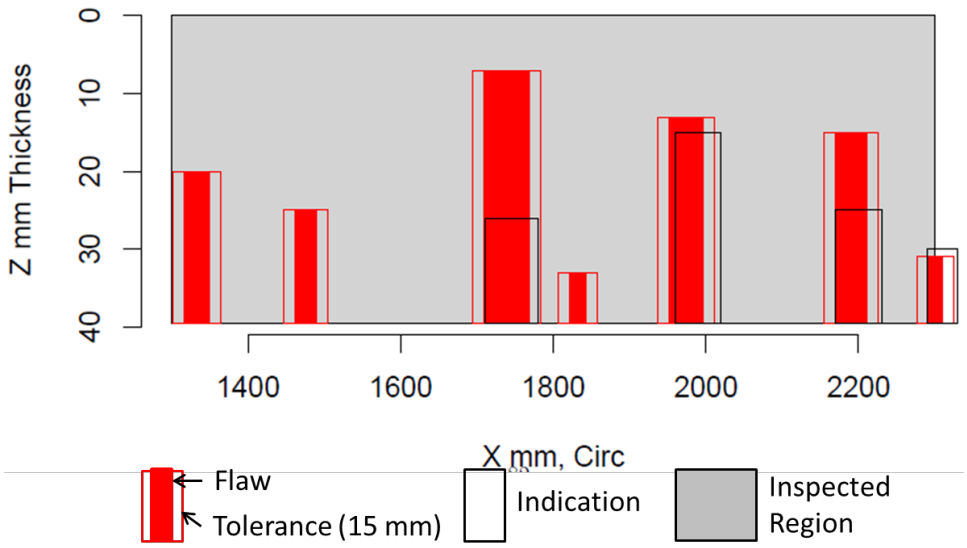

Figure B.12. Indication Plot (X–Z view) for Inspection of the Objective Area by the UT Technique Employed by Team 126

B.7 Procedure UT.134 Results from Objective Area

The indication plots for procedure UT.134 applied to the objective area are provided in Figure B.13 and Figure B.14. Figure B.13 indicates that four out of six flaws within the objective area are detected and that there is one false call. Figure B.14 indicates that all of the detected flaws are significantly undersized and that there was a failure to characterized one of the detected flaws as surface-breaking.

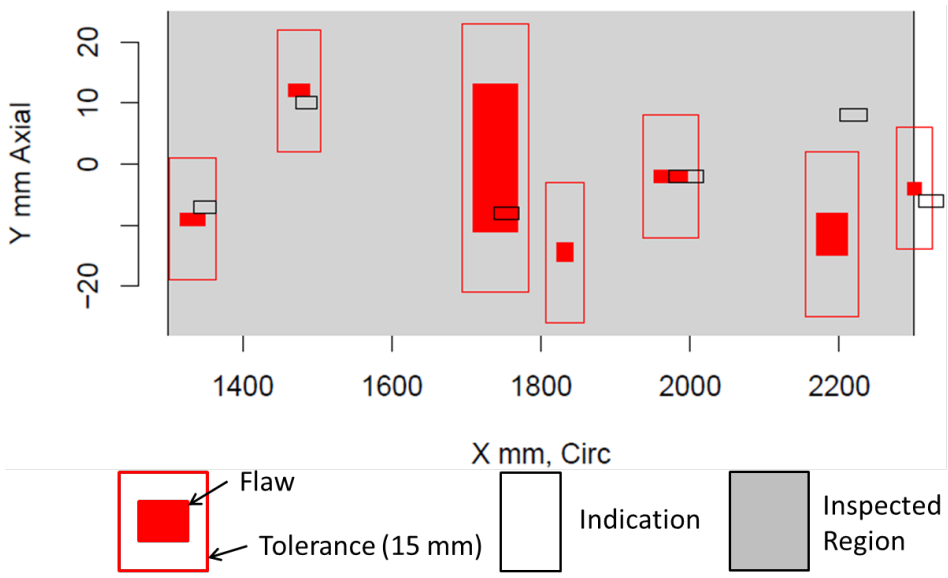

Figure B.13. Indication Plot (X–Y view) for Inspection of the Objective Area by the UT Technique Employed by Team 134

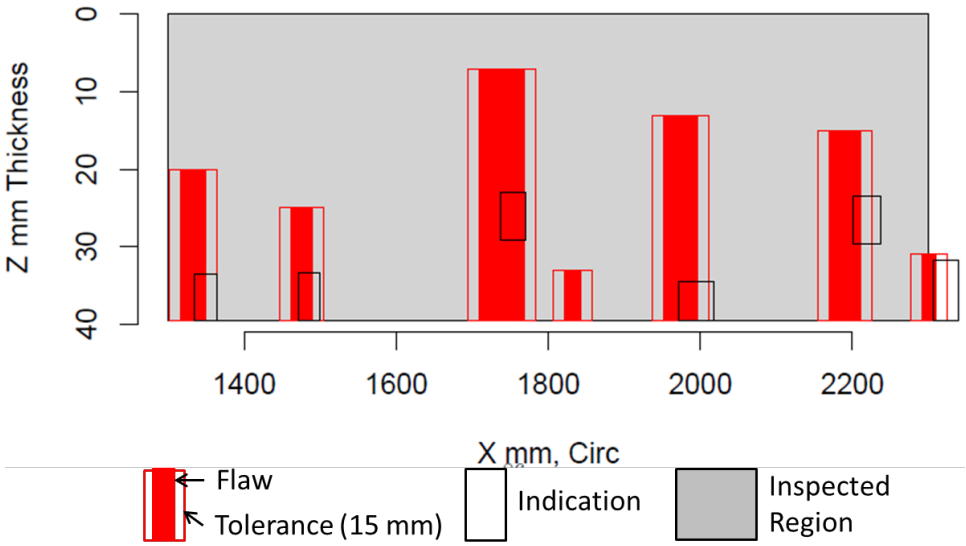

Figure B.14. Indication Plot (X–Z view) for Inspection of the Objective Area by the UT Technique Employed by Team 134

B.8 Procedure UT.TOFD.117 Results from Objective Area

The indication plots for procedure UT.TOFD.117 applied to the objective area are provided in Figure B.15 and Figure B.16. Figure B.15 indicates that six out of six flaws within the objective area are detected and that there are no false calls. Figure B.16 indicates pretty accurate depth sizing for all of the detected flaws.

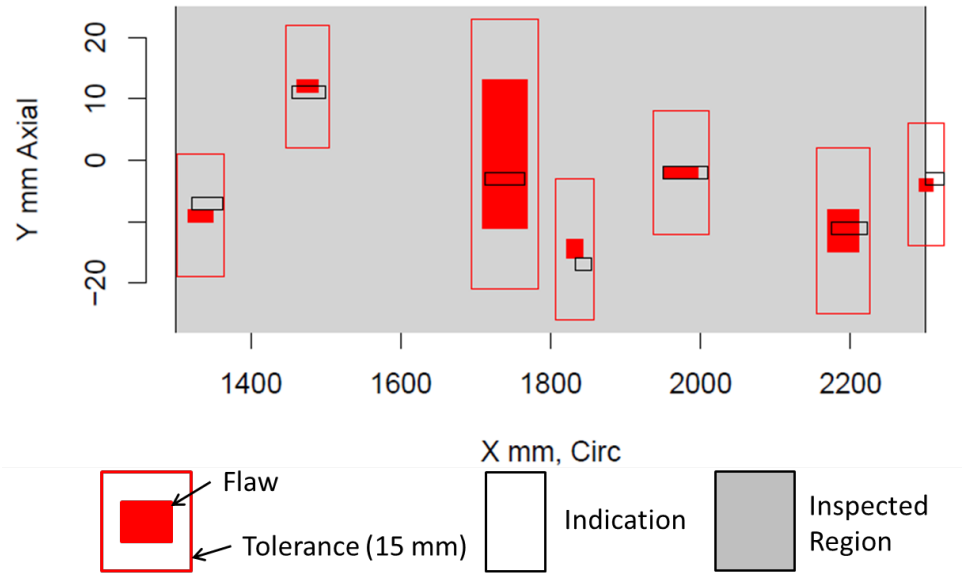

Figure B.15. Indication Plot (X–Y view) for Inspection of the Objective Area by the UT.TOFD Technique Employed by Team 117

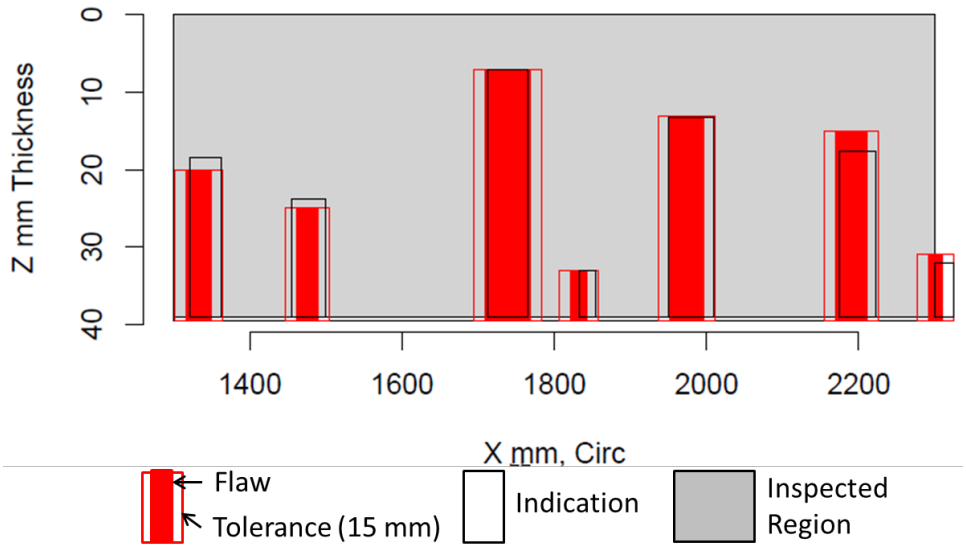

Figure B.16. Indication Plot (X–Z view) for Inspection of the Objective Area by the UT.TOFD Technique Employed by Team 117

Appendix C

Probability of Detection Results

Appendix C

Probability of Detection Results

C.1 Tabulated POD as a Function of Flaw Depth for Open Techniques (Emerging) and Blind Procedures (Established)

Table C.1. Summary of POD versus Depth for Open Techniques (Emerging)

	NOBS	FCR	0 mm	5 mm	10 mm	15 mm	30 mm
ECT.16	6	0.00	5	15	37	66	99
SAFT.17	5	1.44	8	18	35	58	96
UIRT.20	6	0.00	1	2	4	8	40
PA-ATOFD.29 (interior)	6	24.55	61	66	70	74	83
PA-ATOFD.29 (surface)	6	7.67	22	26	31	36	52
PA-TP.29 (interior)	6	36.82	92	91	91	90	89
PA-TP.29 (surface)	6	3.07	12	26	47	70	97
HHUT.29	6	44.49	97	96	94	91	77
HHUT.30	2	1.13	5	8	11	16	39
AECT.33	6	1.53	9	21	43	68	98
SHPA.6	6	0.00	5	15	37	66	99

Table C.2. Summary of POD versus Depth for Blind Procedures (Established)

	NOBS	FCR	0 mm	5 mm	10 mm	15 mm	30 mm
PAUT.108	6	1.53	6	15	33	57	96
UT.108	6	1.53	6	15	33	57	96
PAUT.115	6	0.00	5	15	37	66	99
UT.TOFD.117	6	0.00	5	15	37	66	99
PAUT.126	6	0.00	1	4	9	20	81
UT.126	6	3.07	8	10	14	18	36
PAUT.128	6	0.00	5	15	37	66	99
UT.134	6	1.53	7	13	22	37	82

C.2 Tabulated POD as a Function of Flaw Length for Open Techniques (Emerging) and Blind Procedures (Established)

Table C.3. Summary of POD versus Length for Open Techniques (Emerging)

	NOBS	FCR	0 mm	5 mm	10 mm	15 mm	30 mm
ECT.16	6	0.00	4	9	18	32	84
SAFT.17	5	1.44	7	12	21	33	77
UIRT.20	6	0.00	1	1	2	3	12
PA-ATOFD.29 (interior)	6	24.55	61	64	67	69	76
PA-ATOFD.29 (surface)	6	7.67	22	25	27	30	39
PA-TP.29 (interior)	6	36.82	92	91	91	91	90
PA-TP.29 (surface)	6	3.07	11	19	30	44	83
HHUT.29	6	44.49	97	96	95	94	88
HHUT.30	2	1.13	5	7	9	11	20
AECT.33	6	1.53	8	14	25	40	84
SHPA.6	6	0.00	4	9	18	32	84

Table C.4. Summary of POD versus Length for Blind Procedures (Established)

	NOBS	FCR	0 mm	5 mm	10 mm	15 mm	30 mm
PAUT.108	6	1.53	6	11	18	28	70
UT.108	6	1.53	6	11	18	28	70
PAUT.115	6	0.00	4	9	18	32	84
UT.TOFD.117	6	0.00	4	9	18	32	84
PAUT.126	6	0.00	1	3	5	8	34
UT.126	6	3.07	8	9	11	13	22
PAUT.128	6	0.00	4	9	18	32	84
UT.134	6	1.53	7	10	14	21	49

C.3 POD Plots as a Function of Flaw Depth for Open Techniques (Emerging)

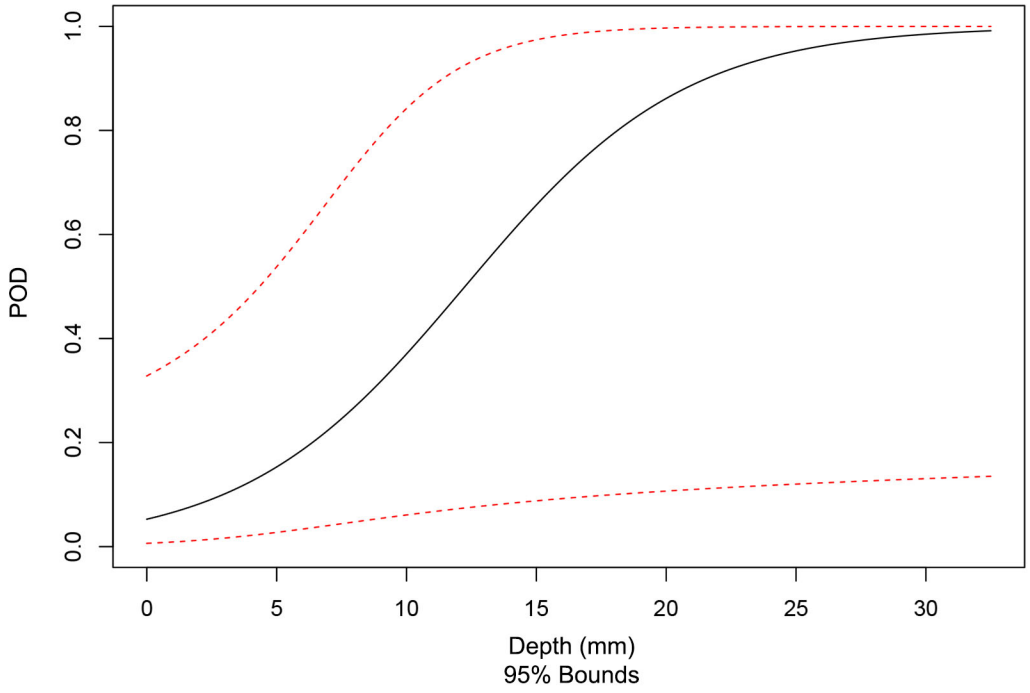

Figure C.1. Plot of POD as a Function of Flaw Depth for the SHPA Technique Employed by Team 6

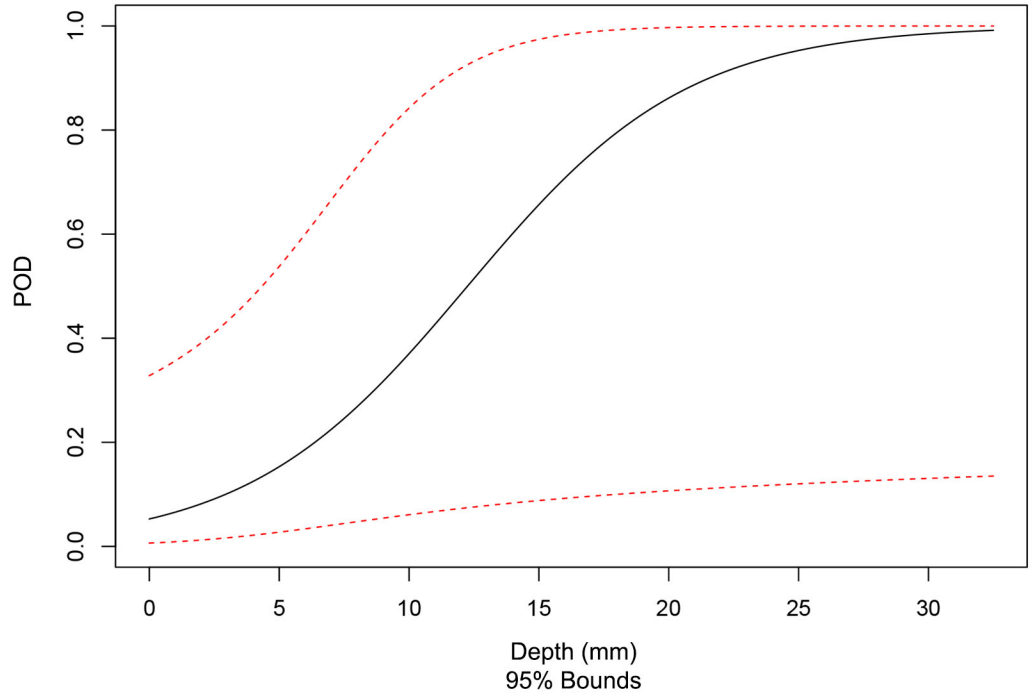

Figure C.2. Plot of POD as a Function of Flaw Depth for the ECT Technique Employed by Team 16

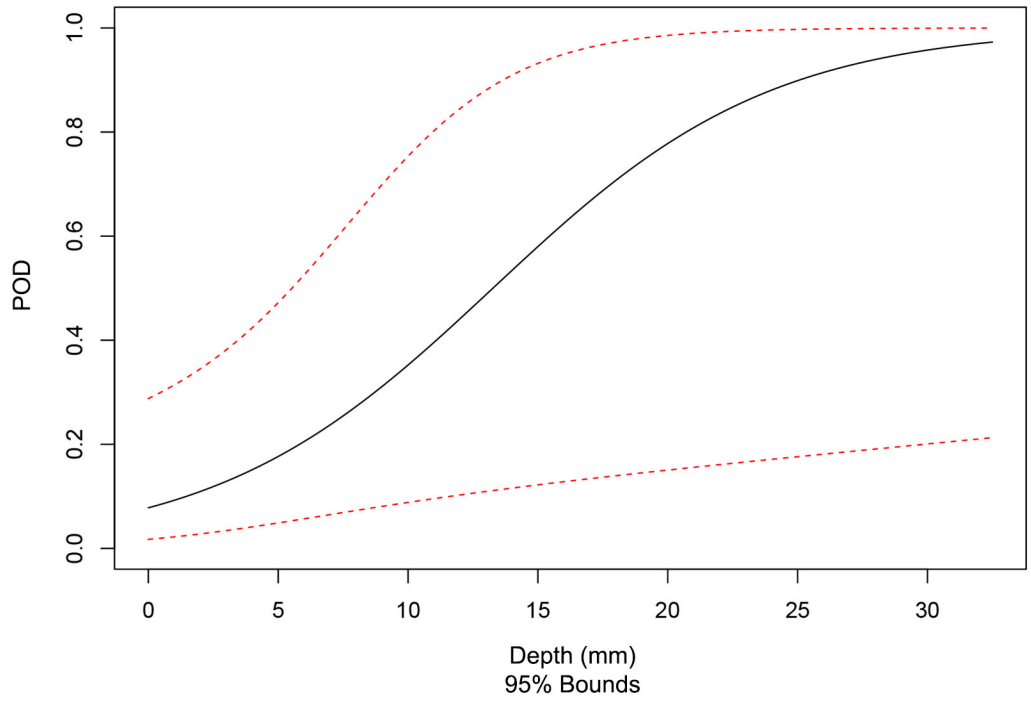

Figure C.3. Plot of POD as a Function of Flaw Depth for the SAFT Technique Employed by Team 17

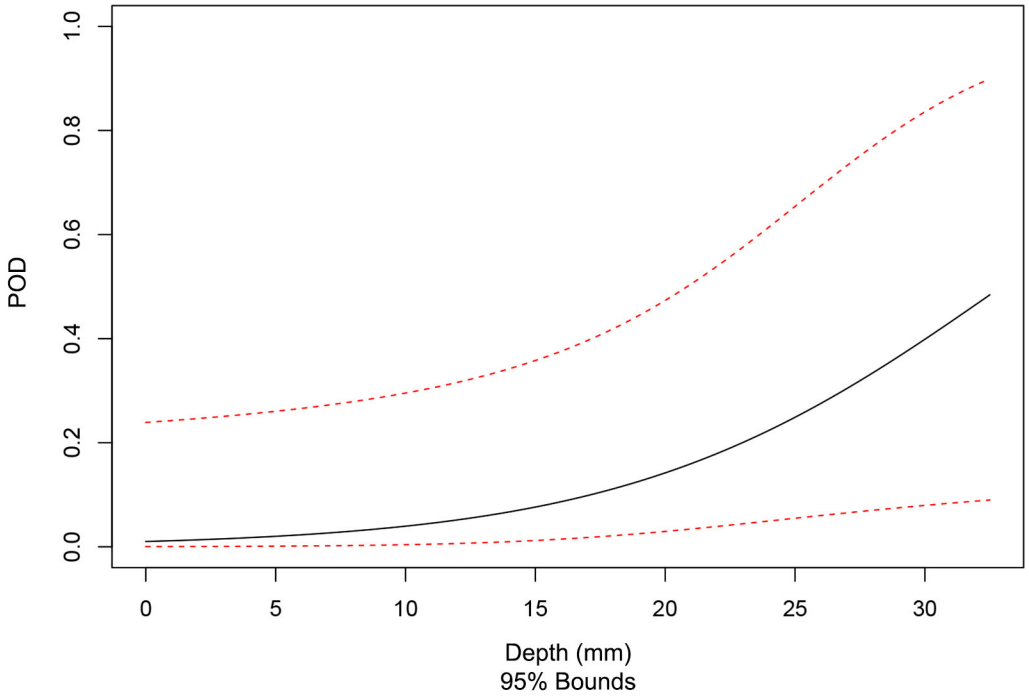

Figure C.4. Plot of POD as a Function of Flaw Depth for the UIRT Technique Employed by Team 20

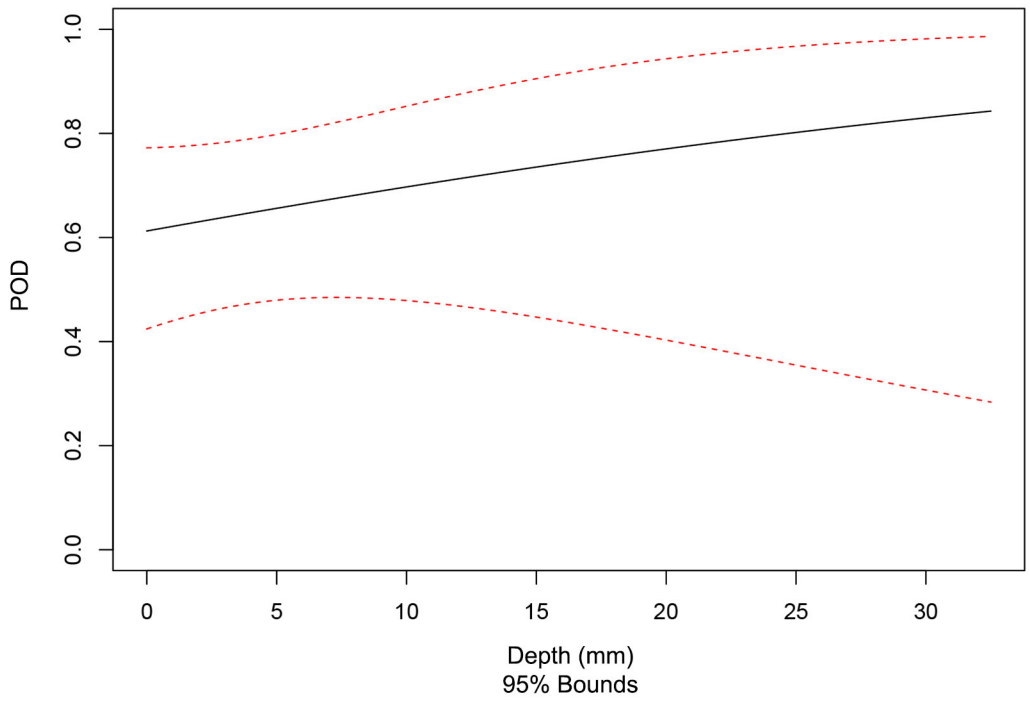

Figure C.5. Plot of POD as a Function of Flaw Depth for the PA-ATOFD (Interior) Technique Employed by Team 29

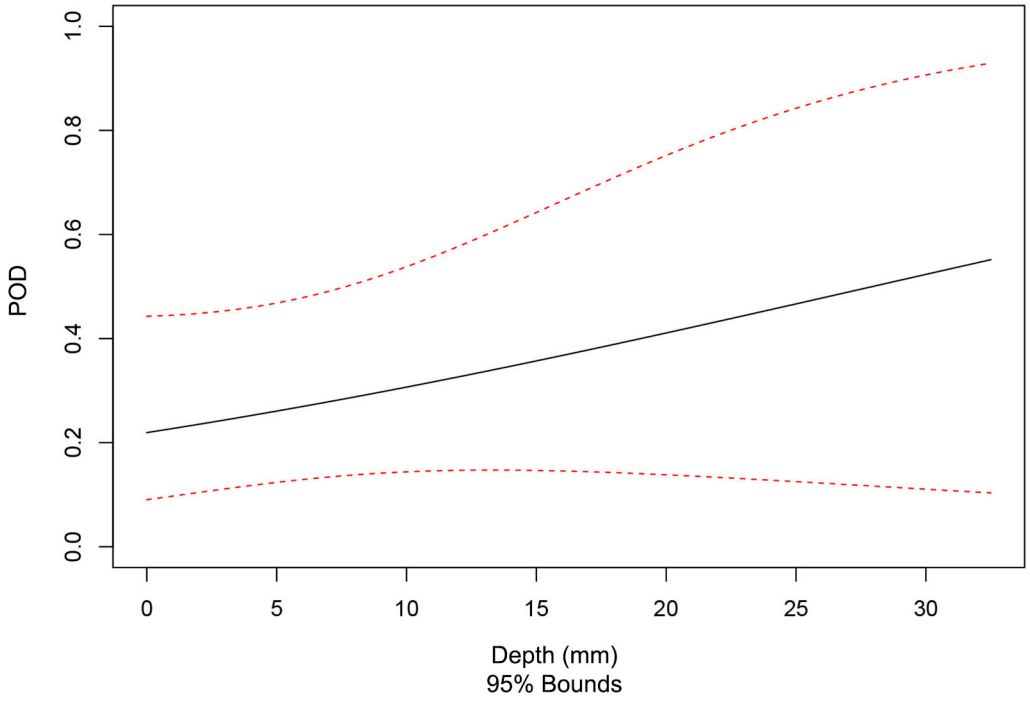

Figure C.6. Plot of POD as a Function of Flaw Depth for the PA-ATOFD (Surface-Breaking) Technique Employed by Team 29

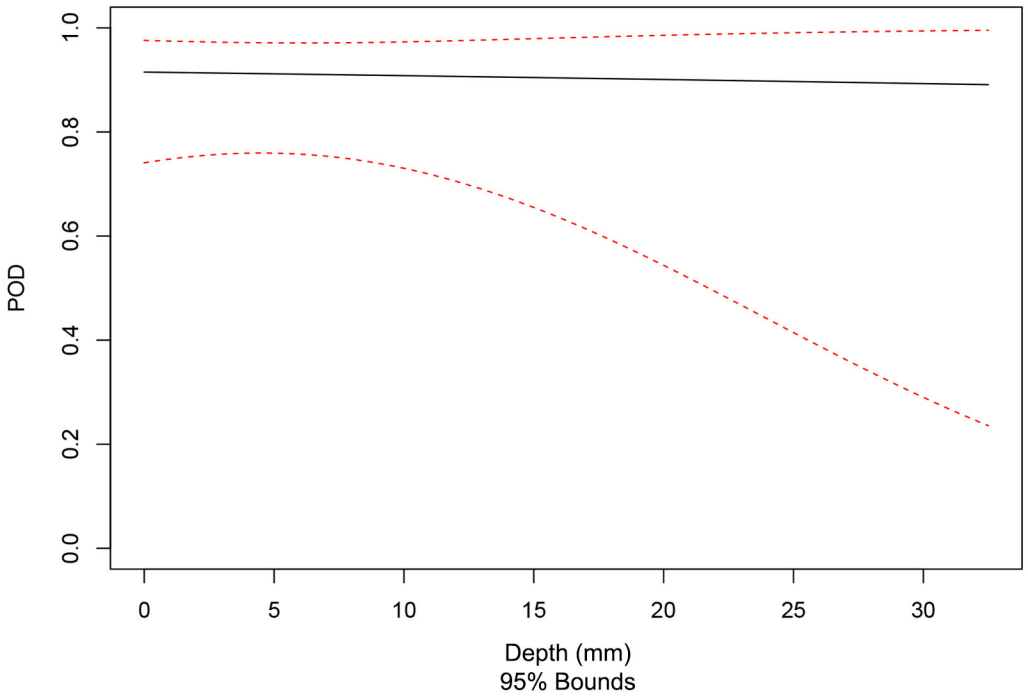

Figure C.7. Plot of POD as a Function of Flaw Depth for the PA-TP (Interior) Technique Employed by Team 29

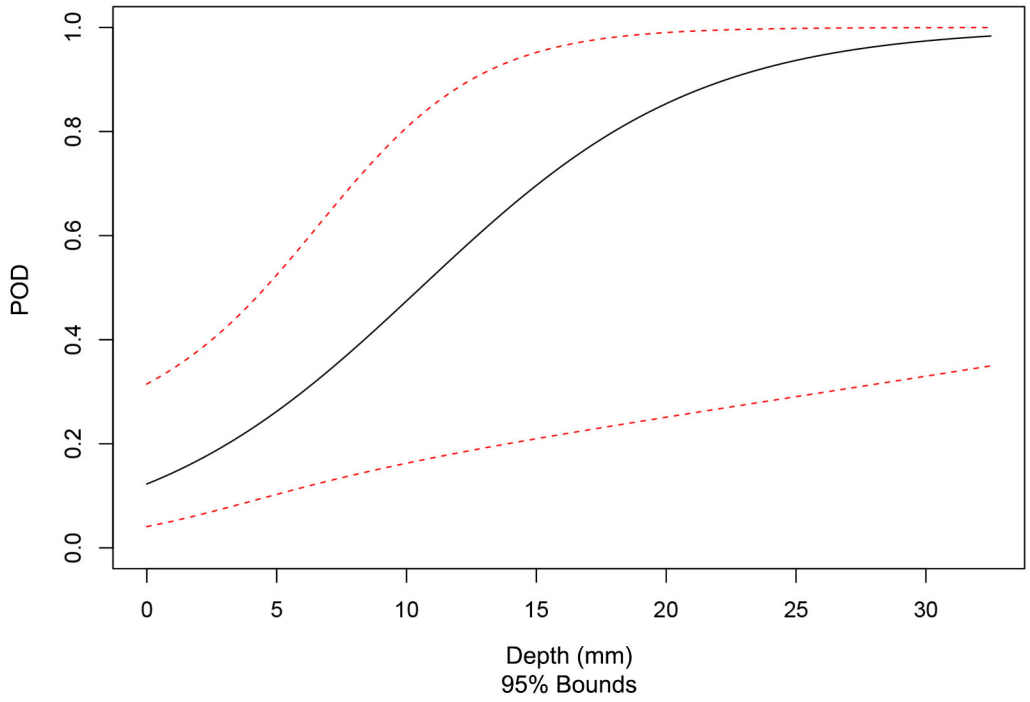

Figure C.8. Plot of POD as a Function of Flaw Depth for the PA-TP (Surface-Breaking) Technique Employed by Team 29

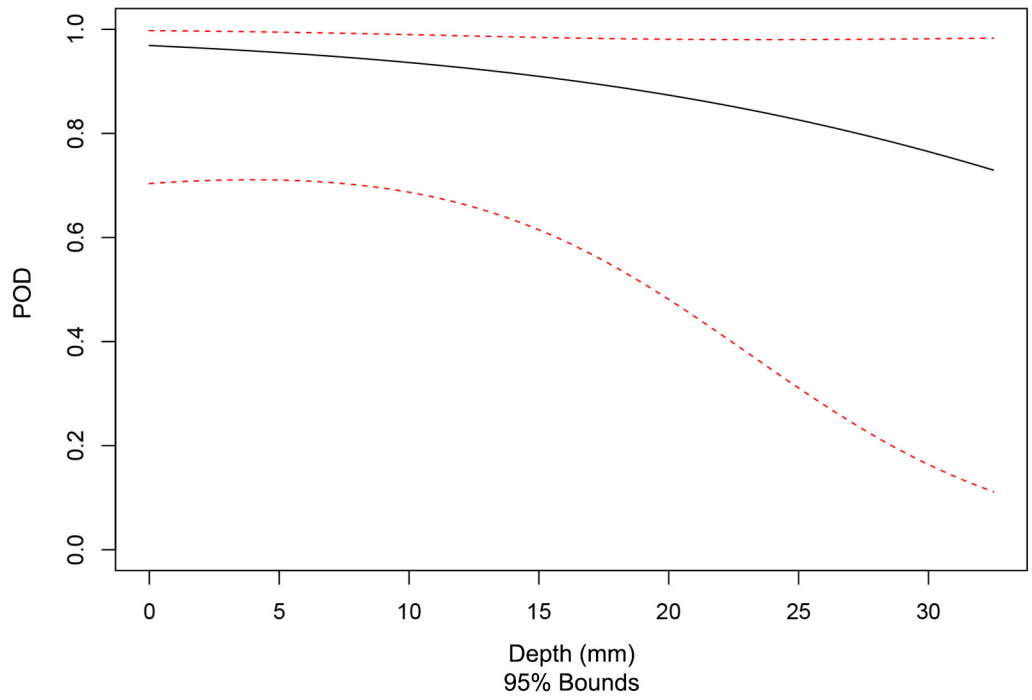

Figure C.9. Plot of POD as a Function of Flaw Depth for the HHUT Technique Employed by Team 29

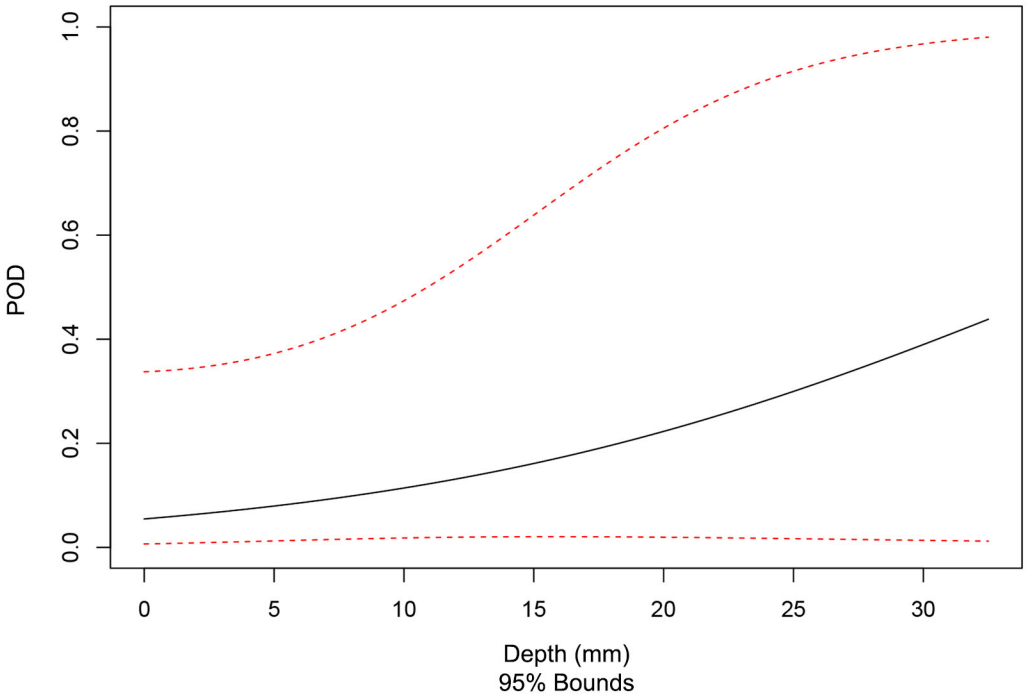

Figure C.10. Plot of POD as a Function of Flaw Depth for the HHUT Technique Employed by Team 30

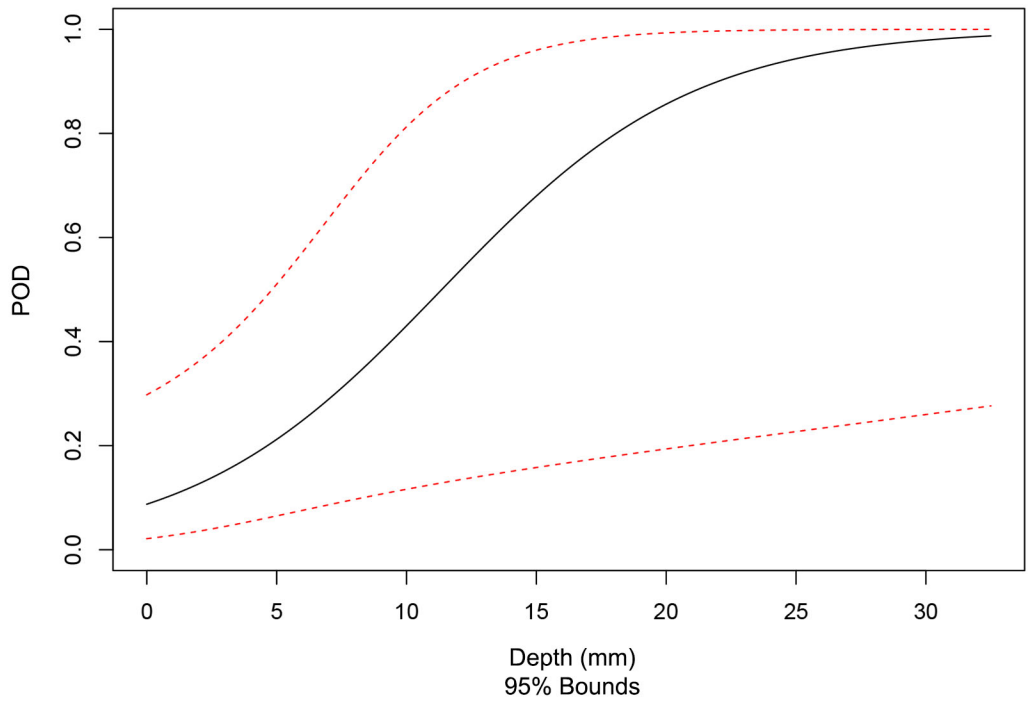

Figure C.11. Plot of POD as a Function of Flaw Depth for the AECT Technique Employed by Team 33

C.4 POD Plots as a Function of Flaw Depth for Blind Procedures (Established)

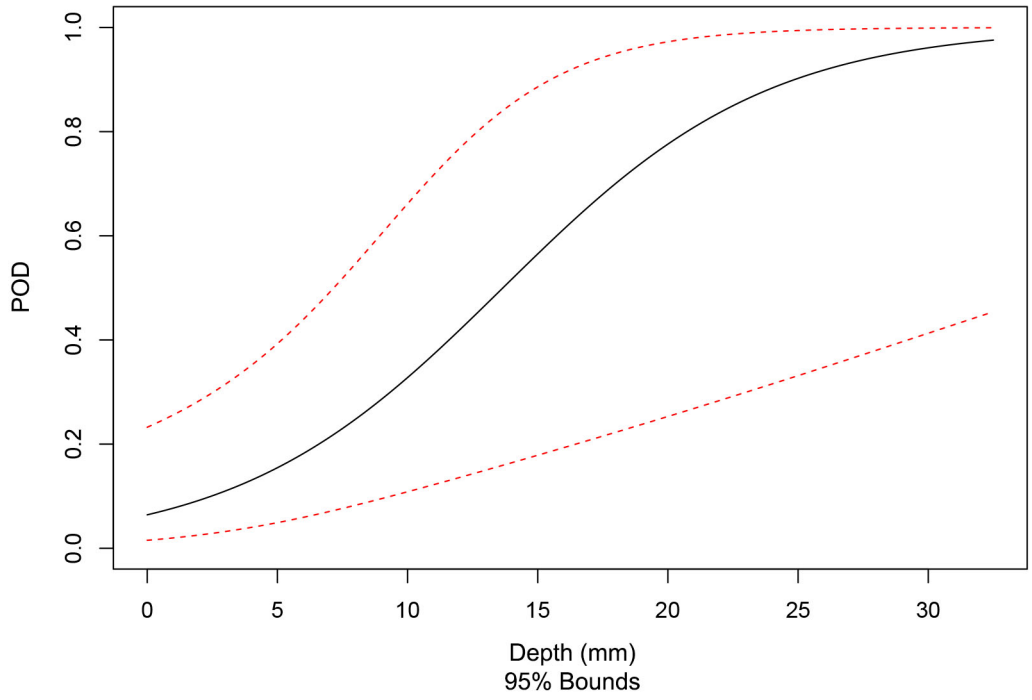

Figure C.12. Plot of POD as a Function of Flaw Depth for the PAUT Procedure Employed by Team 108

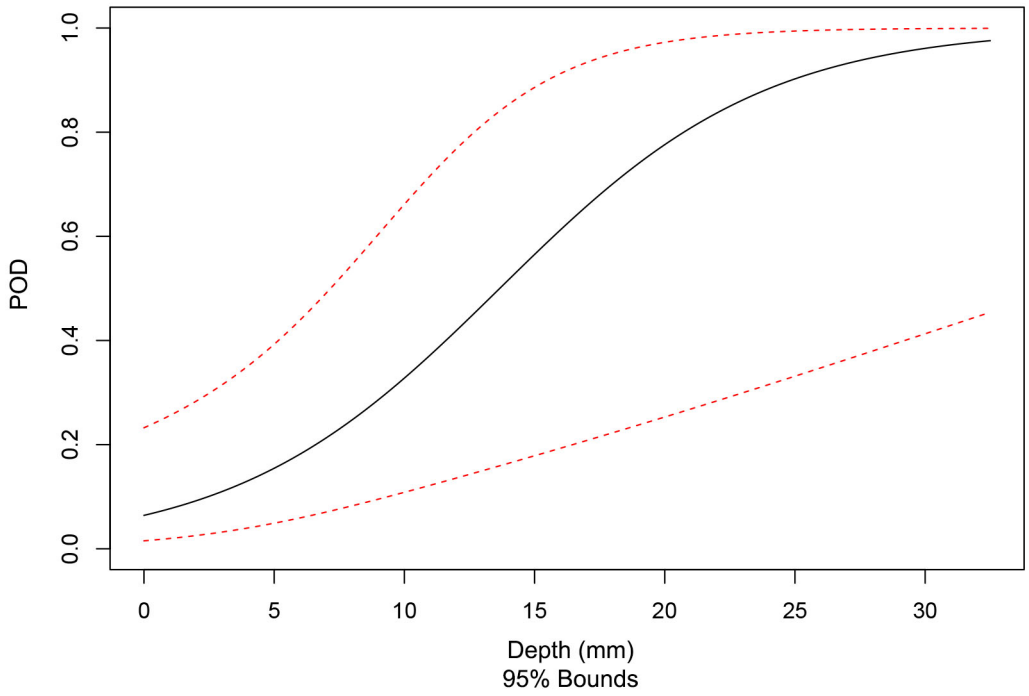

Figure C.13. Plot of POD as a Function of Flaw Depth for the UT Procedure Employed by Team 108

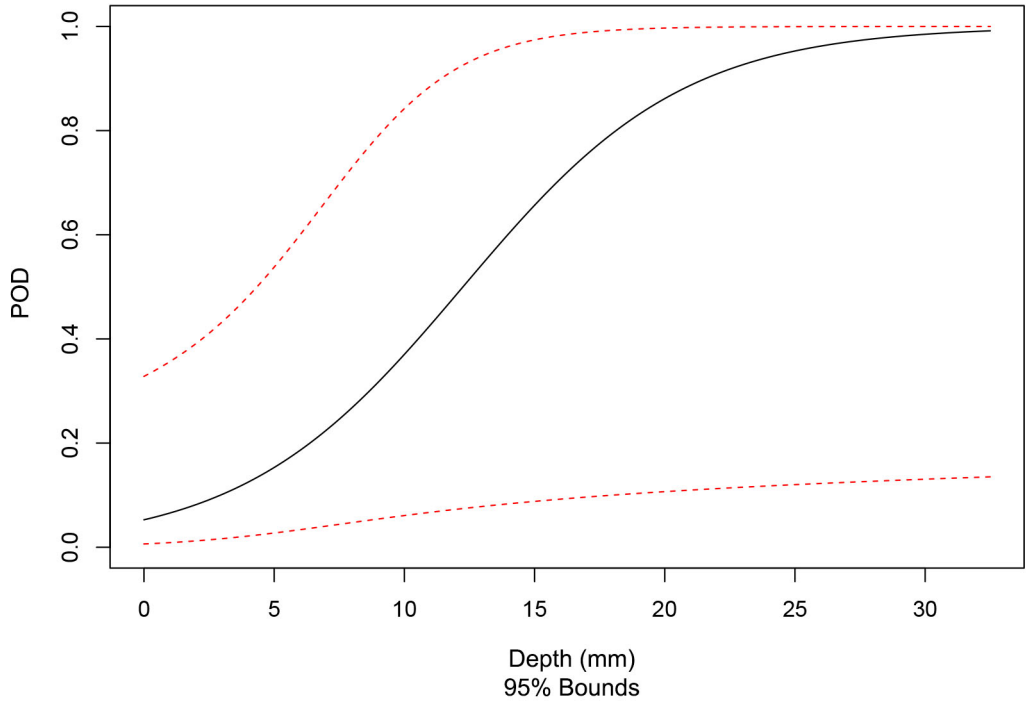

Figure C.14. Plot of POD as a Function of Flaw Depth for the PAUT Procedure Employed by Team 115

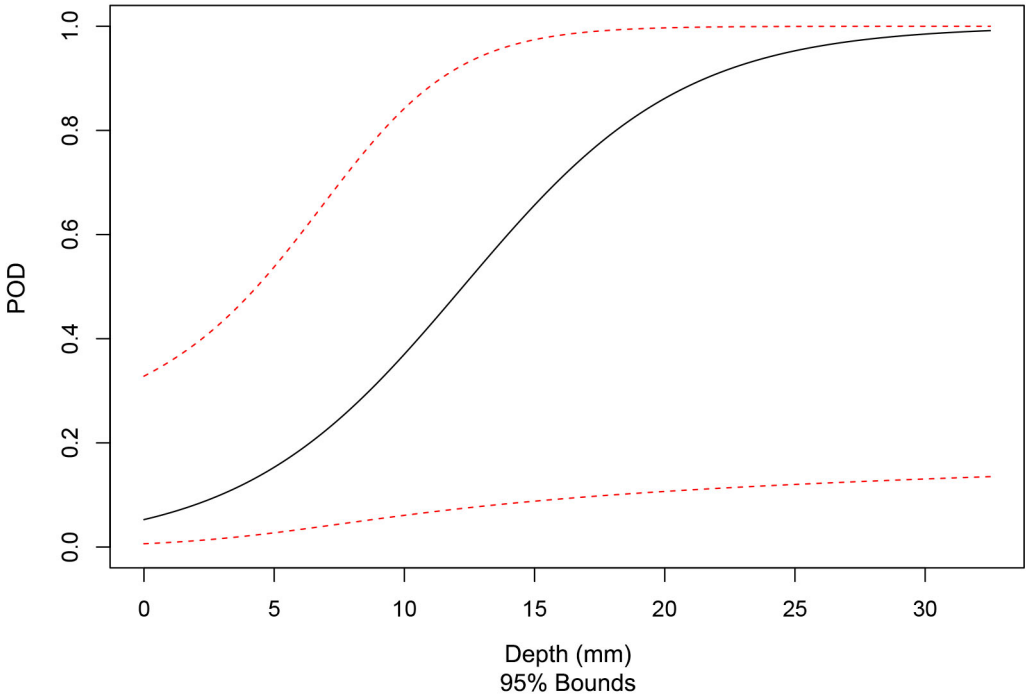

Figure C.15. Plot of POD as a Function of Flaw Depth for the UT.TOFD Procedure Employed by Team 117

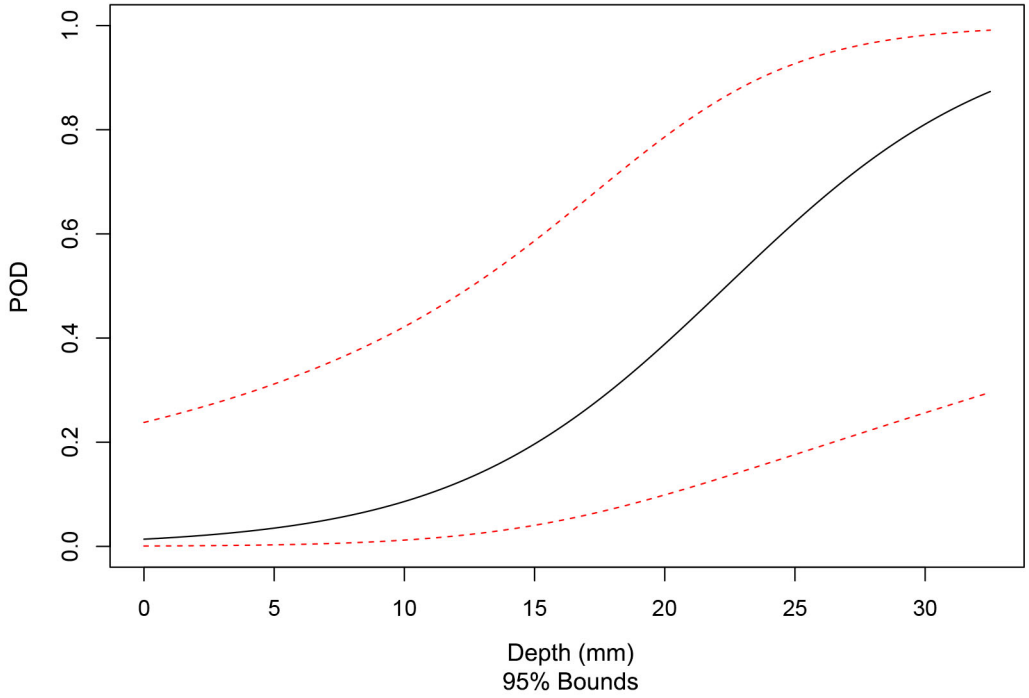

Figure C.16. Plot of POD as a Function of Flaw Depth for the PAUT Procedure Employed by Team 126

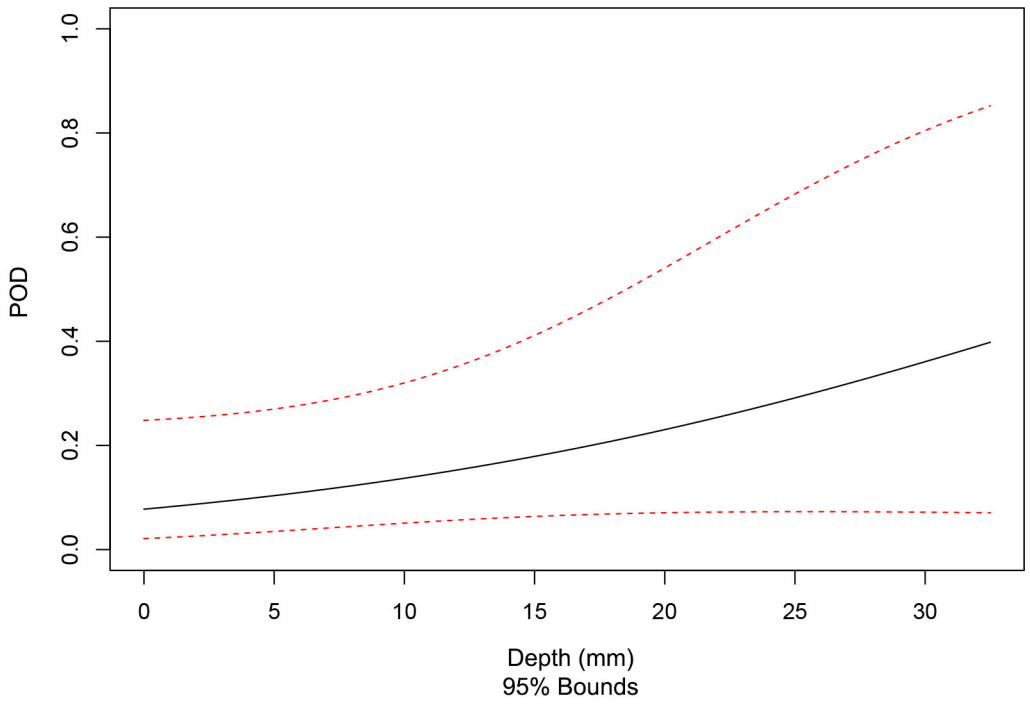

Figure C.17. Plot of POD as a Function of Flaw Depth for the UT Procedure Employed by Team 126

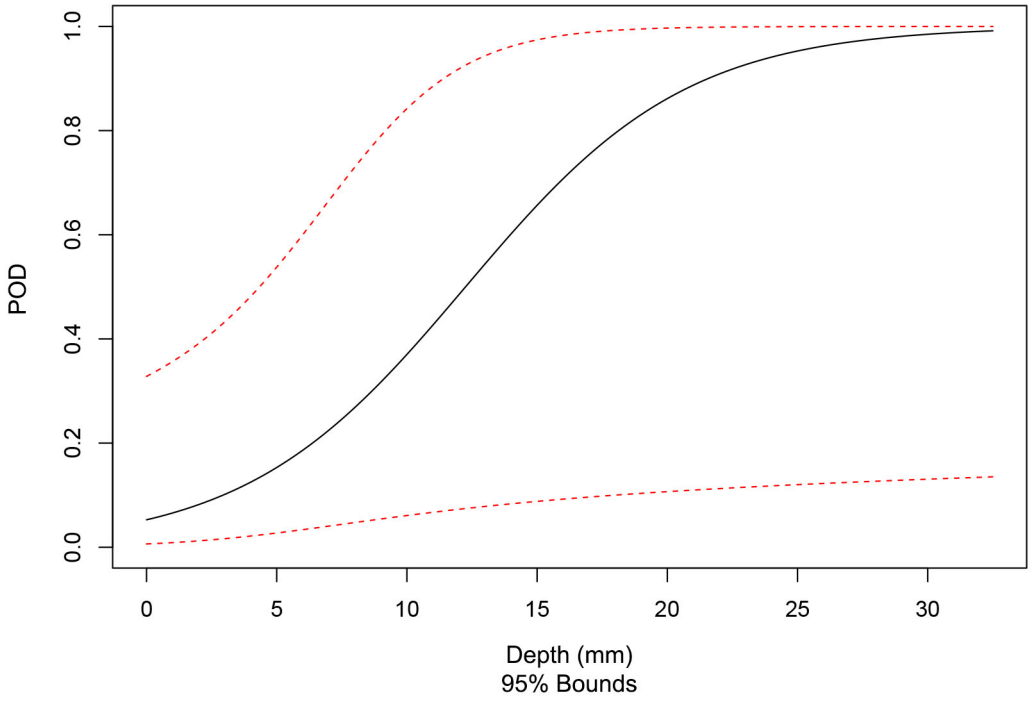

Figure C.18. Plot of POD as a Function of Flaw Depth for the PAUT Procedure Employed by Team 128

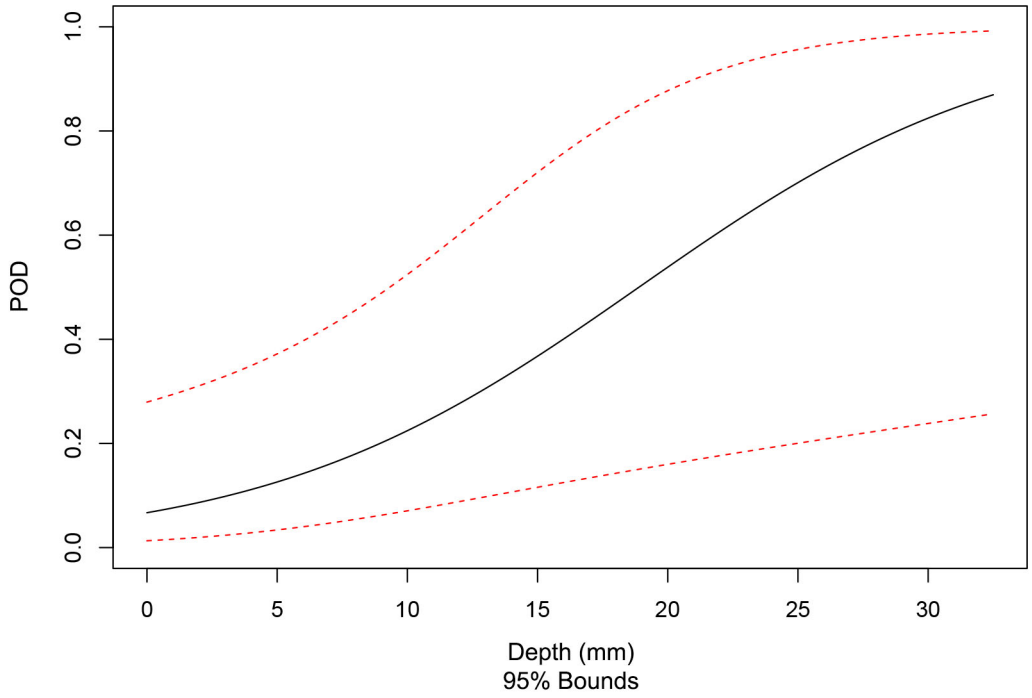

Figure C.19. Plot of POD as a Function of Flaw Depth for the UT Procedure Employed by Team 134

C.5 POD Plots as a Function of Flaw Length for Open Techniques (Emerging)

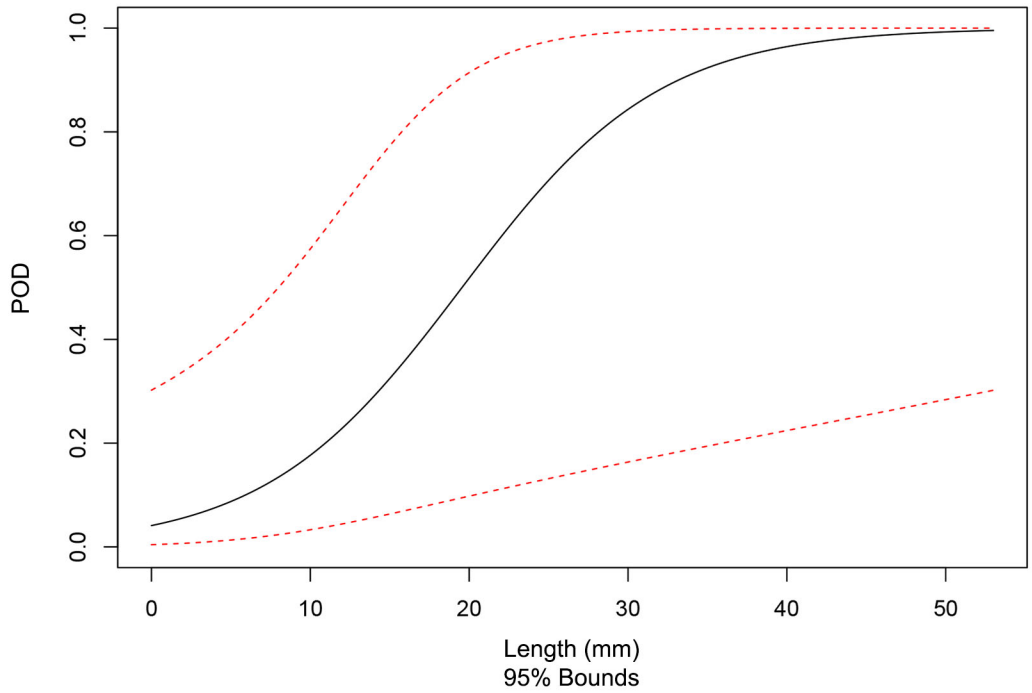

Figure C.20. Plot of POD as a Function of Flaw Length for the SHPA Technique Employed by Team 6

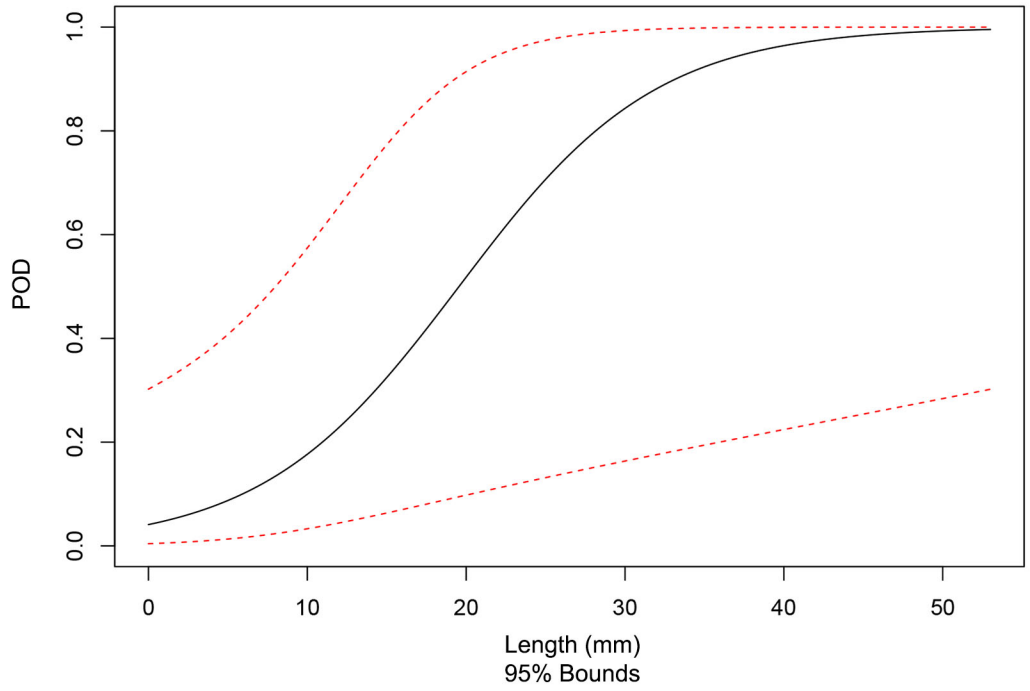

Figure C.21. Plot of POD as a Function of Flaw Length for the ECT Technique Employed by Team 16

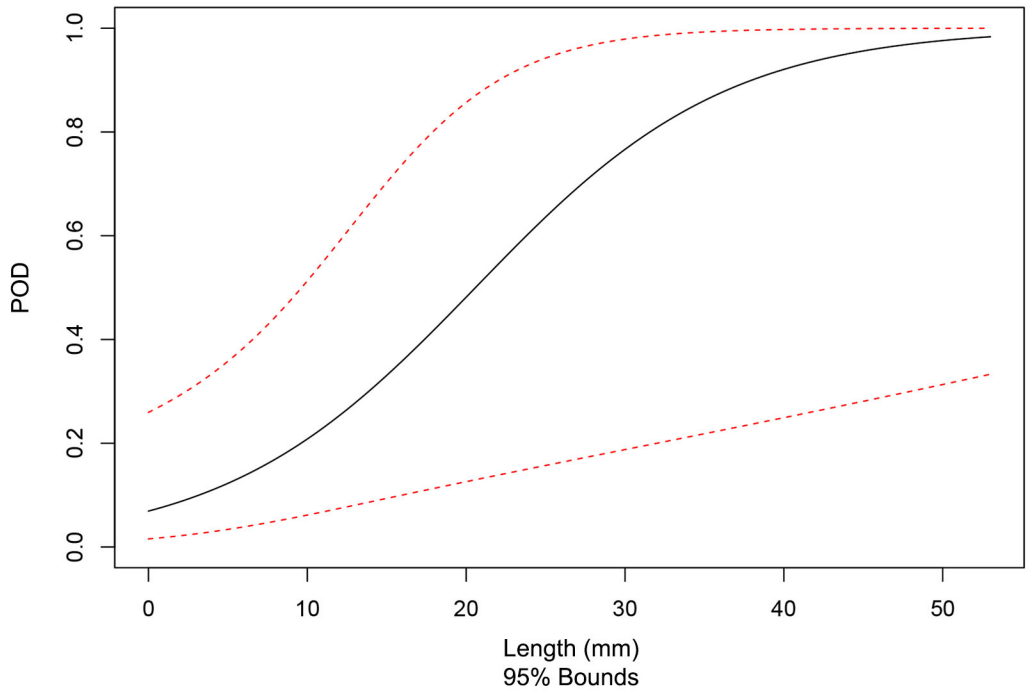

Figure C.22. Plot of POD as a Function of Flaw Length for the SAFT Technique Employed by Team 17

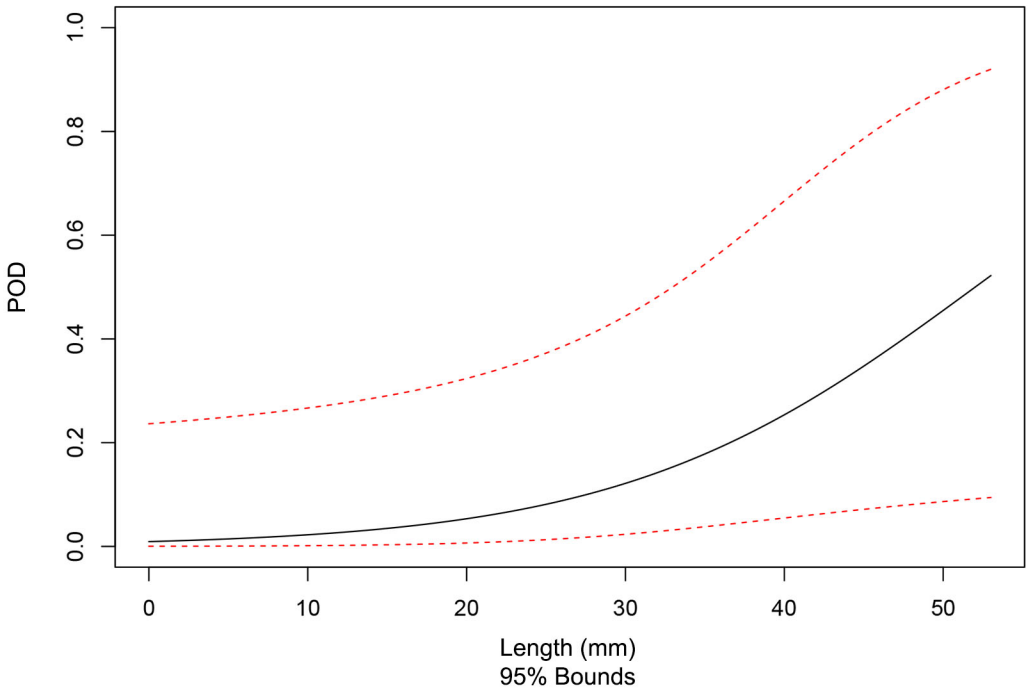

Figure C.23. Plot of POD as a Function of Flaw Length for the UIRT Technique Employed by Team 20

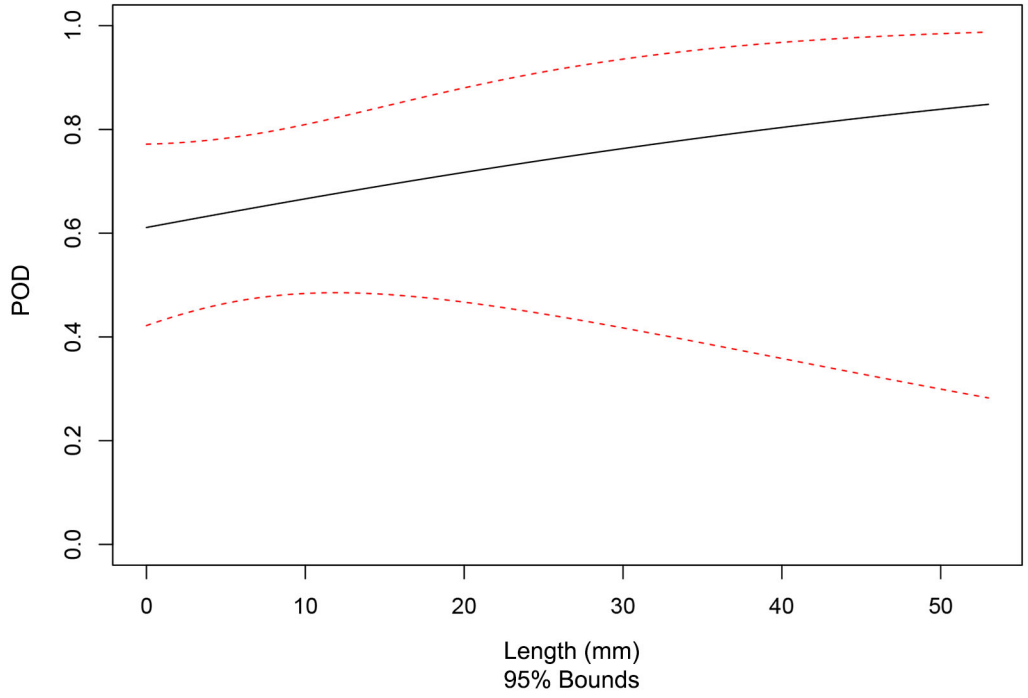

Figure C.24. Plot of POD as a Function of Flaw Length for the PA-ATOFD (Interior) Technique Employed by Team 29

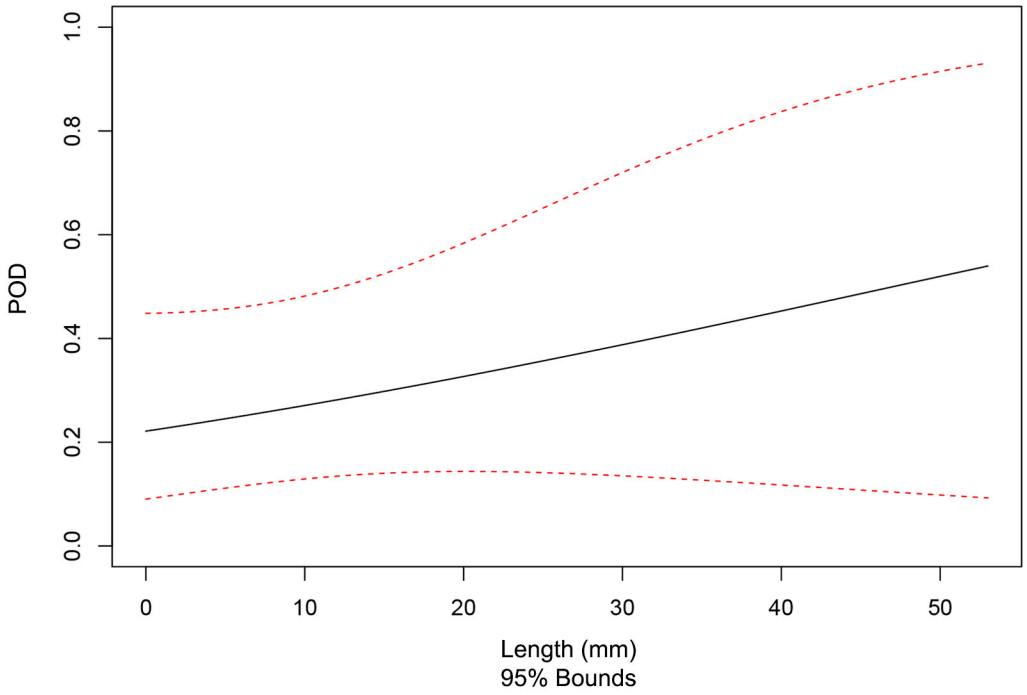

Figure C.25. Plot of POD as a Function of Flaw Length for the PA-ATOFD (Surface-Breaking) Technique Employed by Team 29

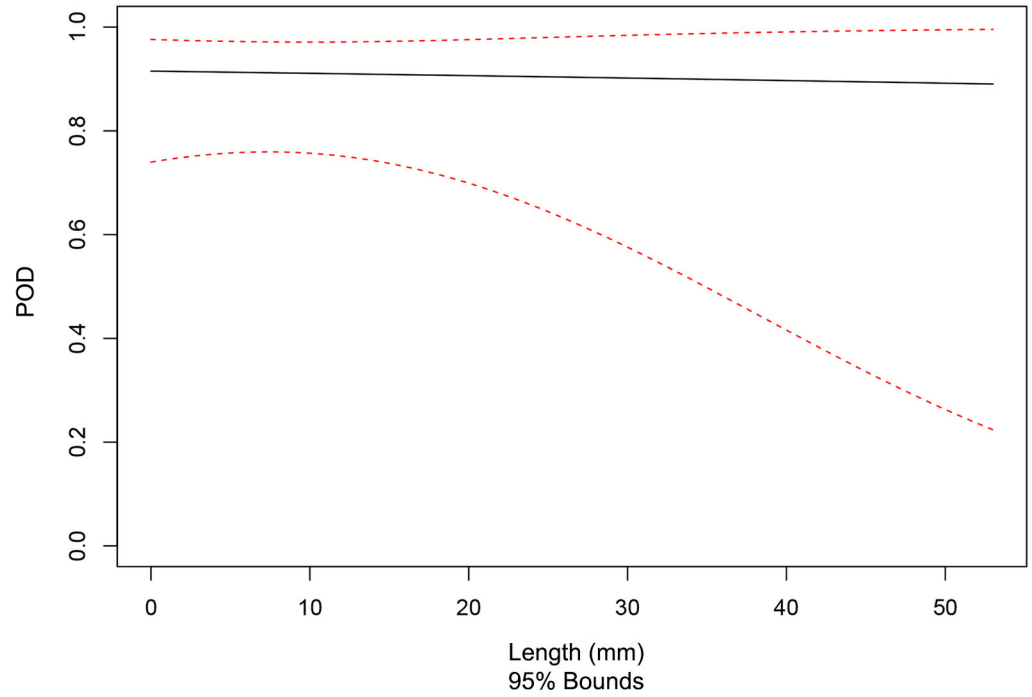

Figure C.26. Plot of POD as a Function of Flaw Length for the PA-TP (Interior) Technique Employed by Team 29

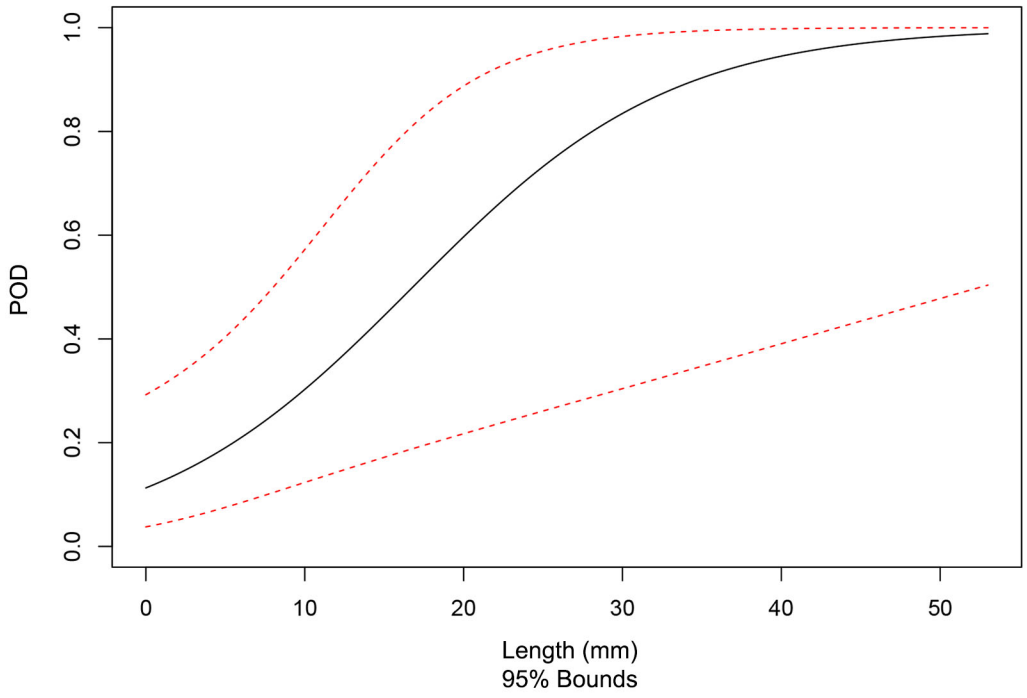

Figure C.27. Plot of POD as a Function of Flaw Length for the PA-TP (Surface-Breaking) Technique Employed by Team 29

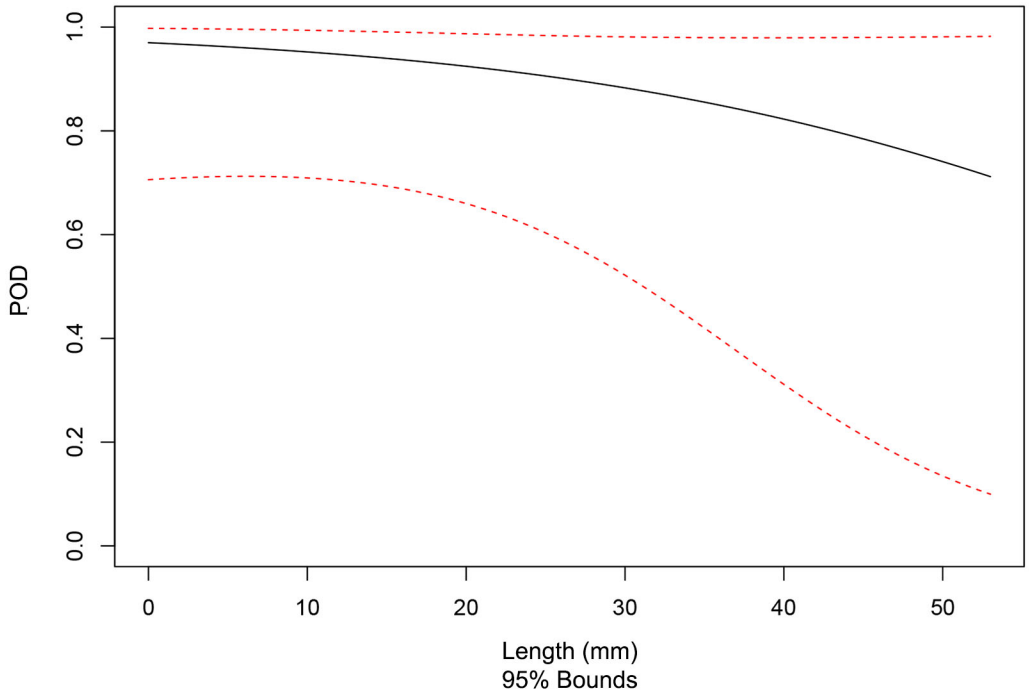

Figure C.28. Plot of POD as a Function of Flaw Length for the HHUT Technique Employed by Team 29

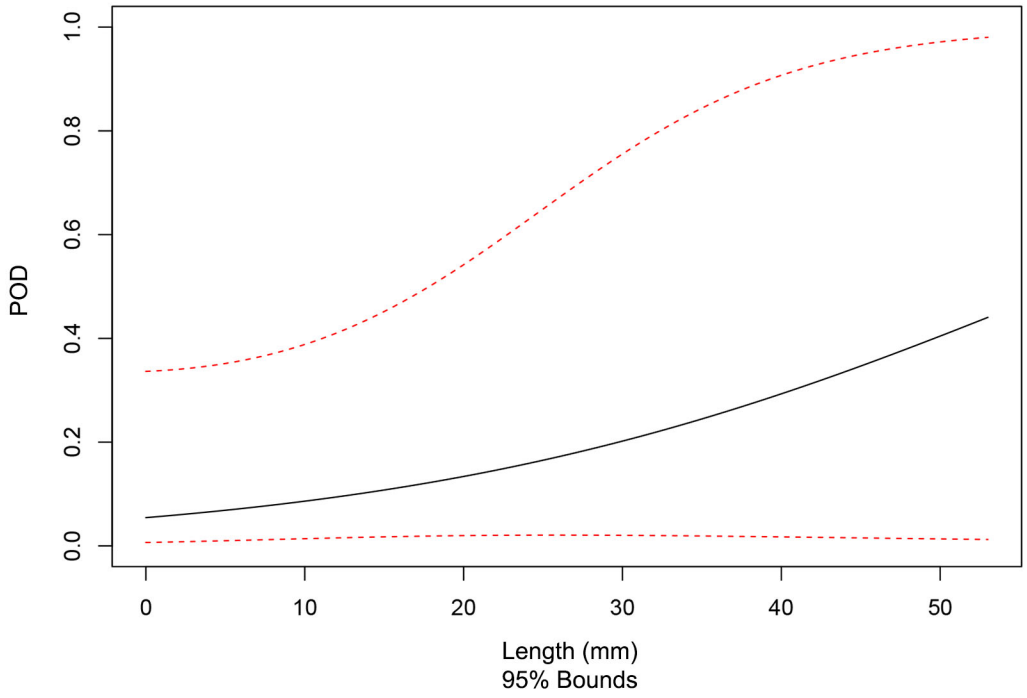

Figure C.29. Plot of POD as a Function of Flaw Length for the HHUT Technique Employed by Team 30

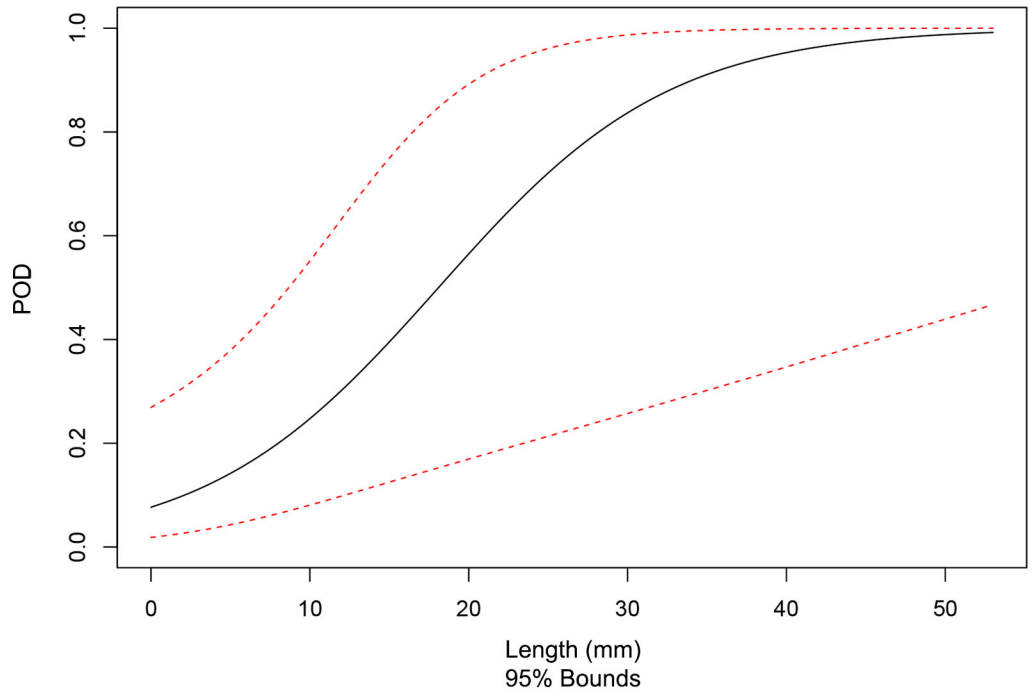

Figure C.30. Plot of POD as a Function of Flaw Length for the AECT Technique Employed by Team 33

C.6 POD Plots as a Function of Flaw Length for Blind Procedures (Established)

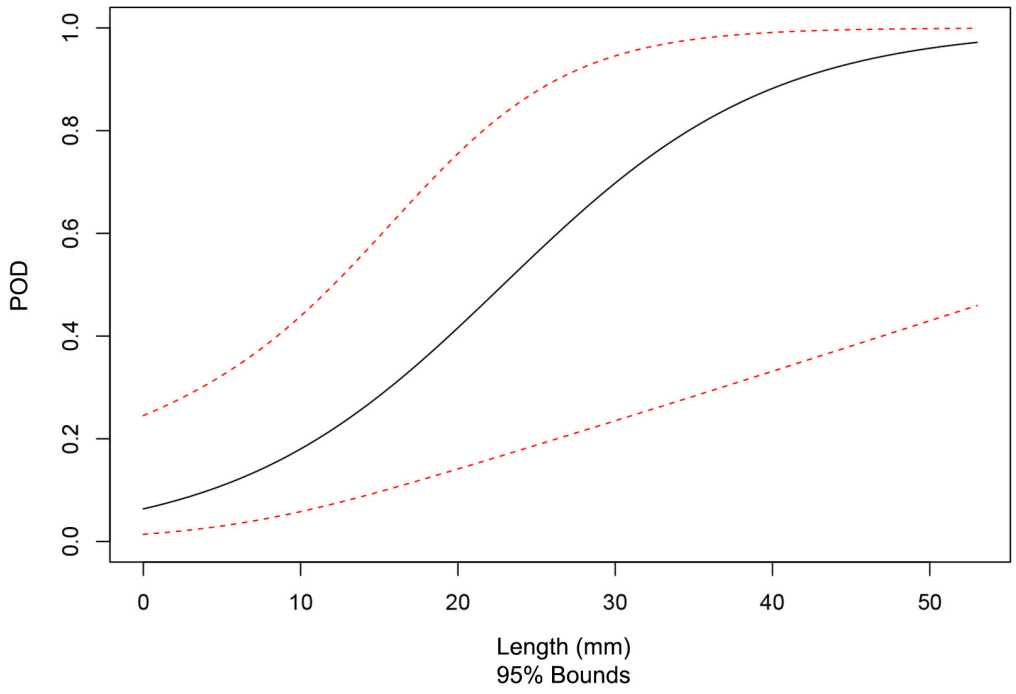

Figure C.31. Plot of POD as a Function of Flaw Length for the PAUT Procedure Employed by Team 108

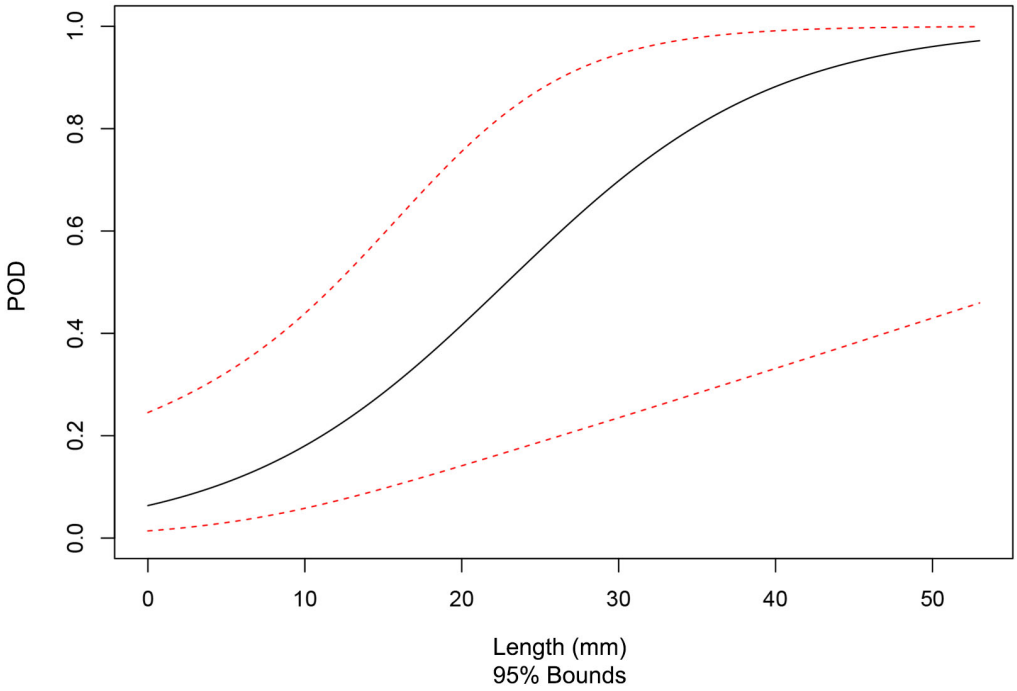

Figure C.32. Plot of POD as a Function of Flaw Length for the UT Procedure Employed by Team 108

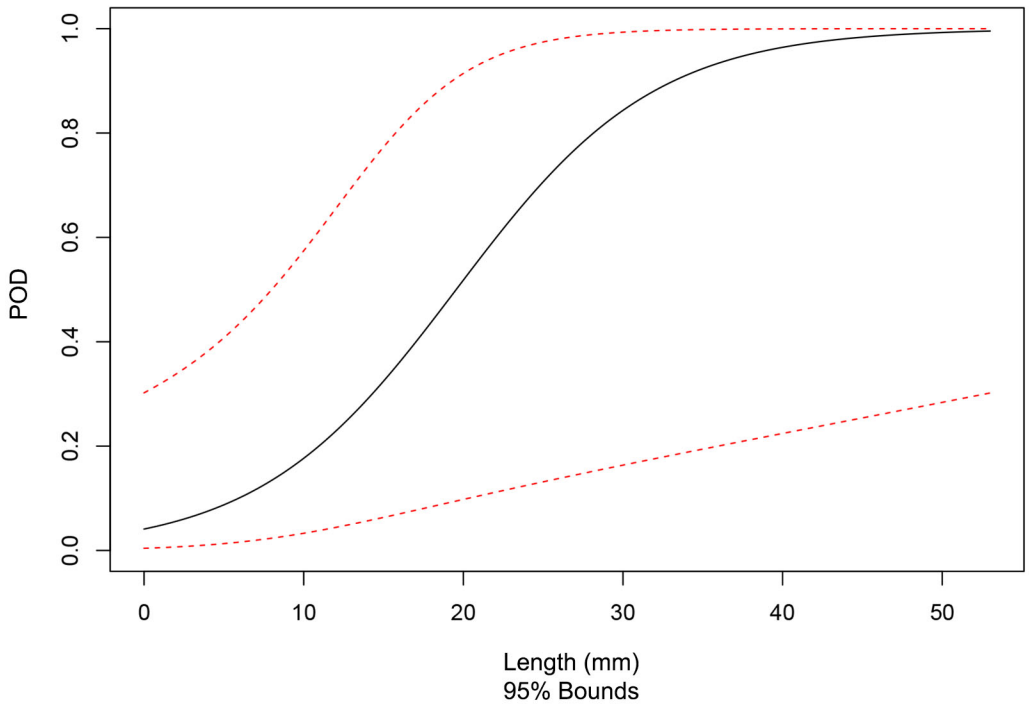

Figure C.33. Plot of POD as a Function of Flaw Length for the PAUT Procedure Employed by Team 115

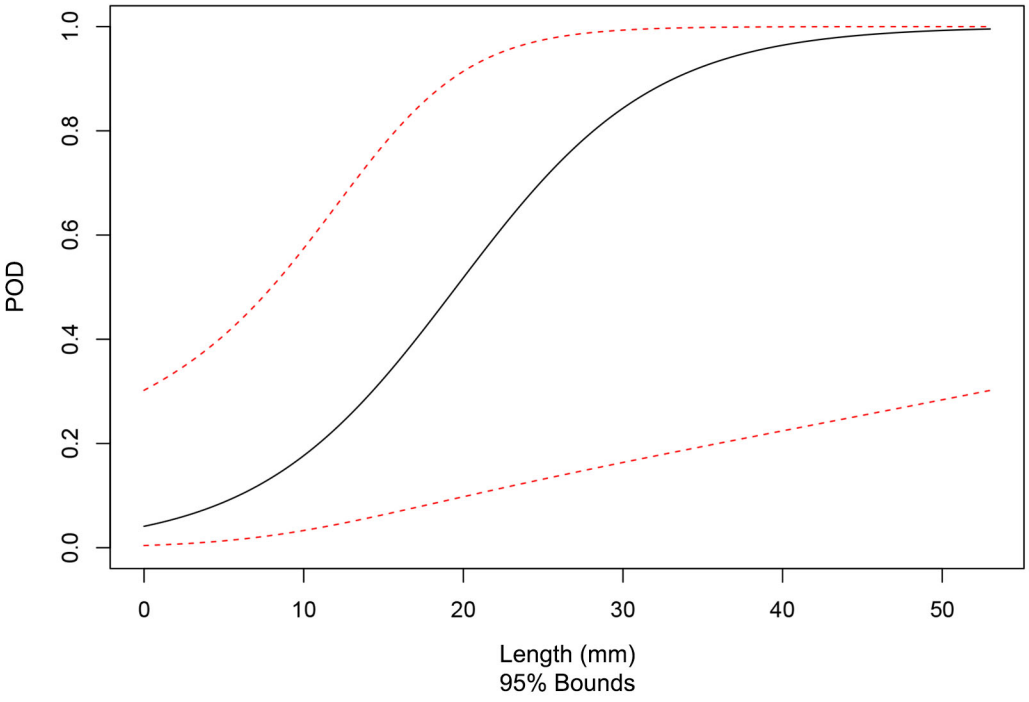

Figure C.34. Plot of POD as a Function of Flaw Length for the UT.TOFD Procedure Employed by Team 117

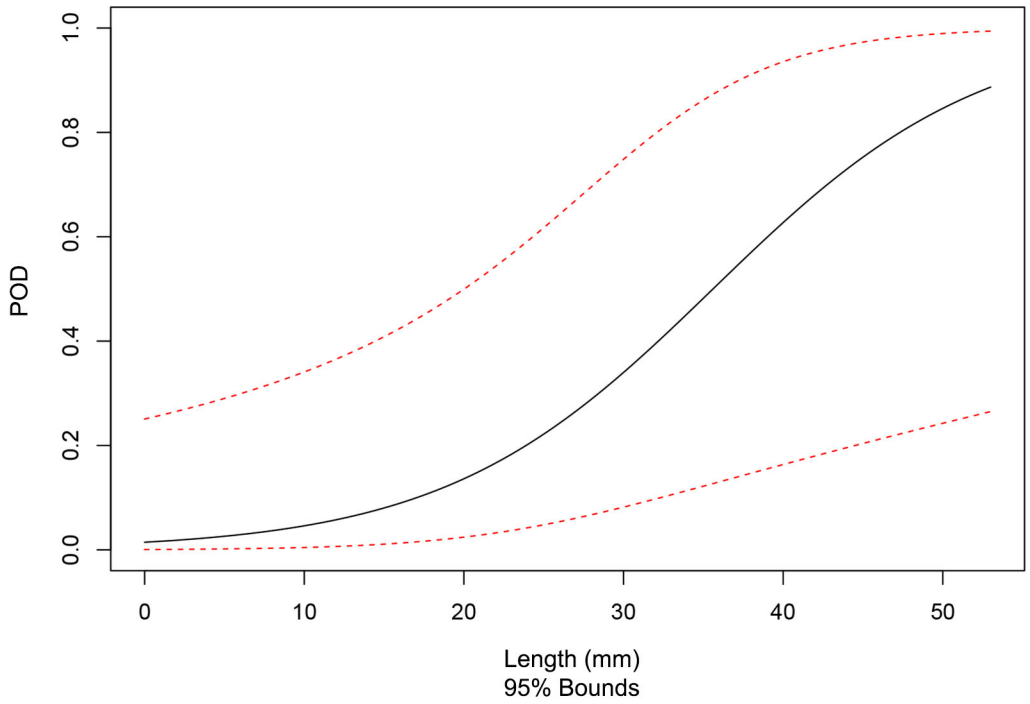

Figure C.35. Plot of POD as a Function of Flaw Length for the PAUT Procedure Employed by Team 126

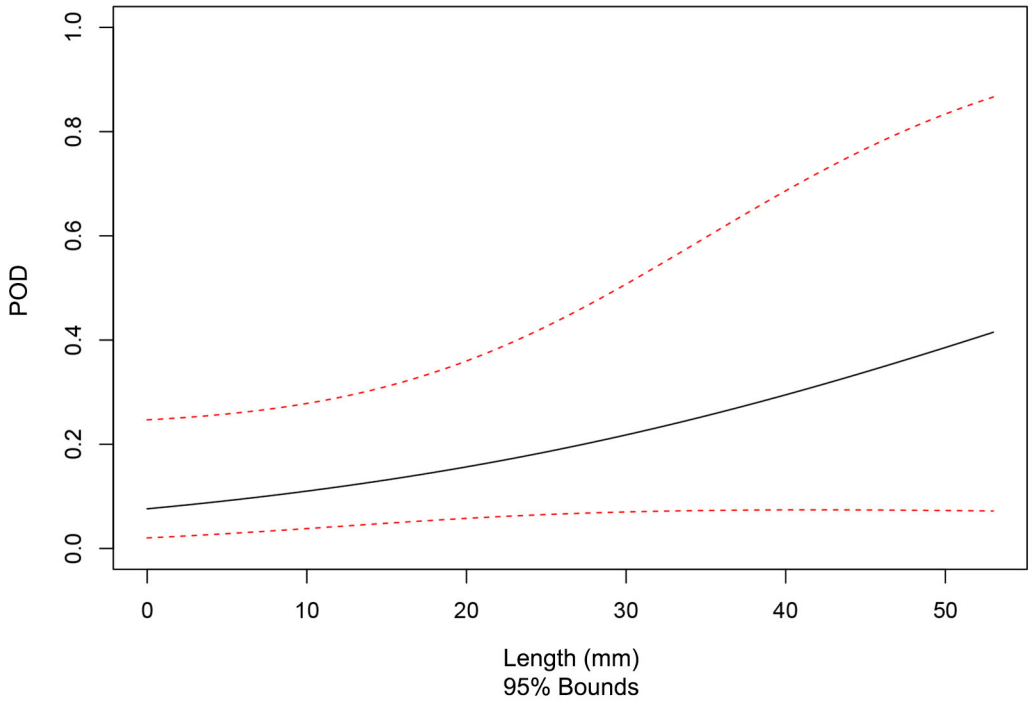

Figure C.36. Plot of POD as a Function of Flaw Length for the UT Procedure Employed by Team 126

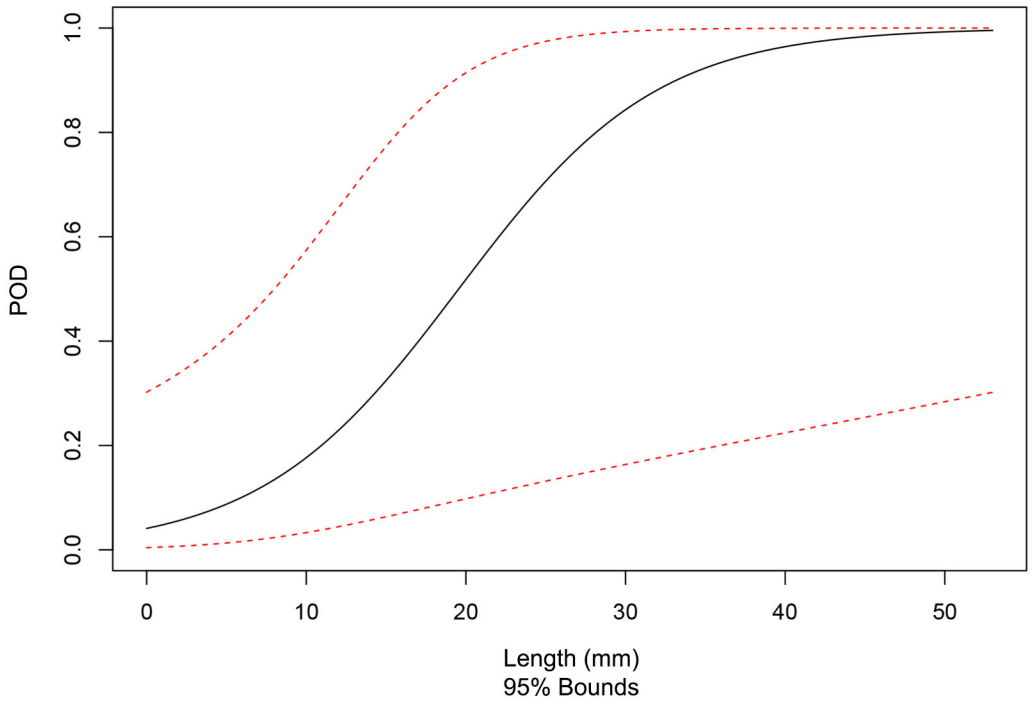

Figure C.37. Plot of POD as a Function of Flaw Length for the PAUT Procedure Employed by Team 128

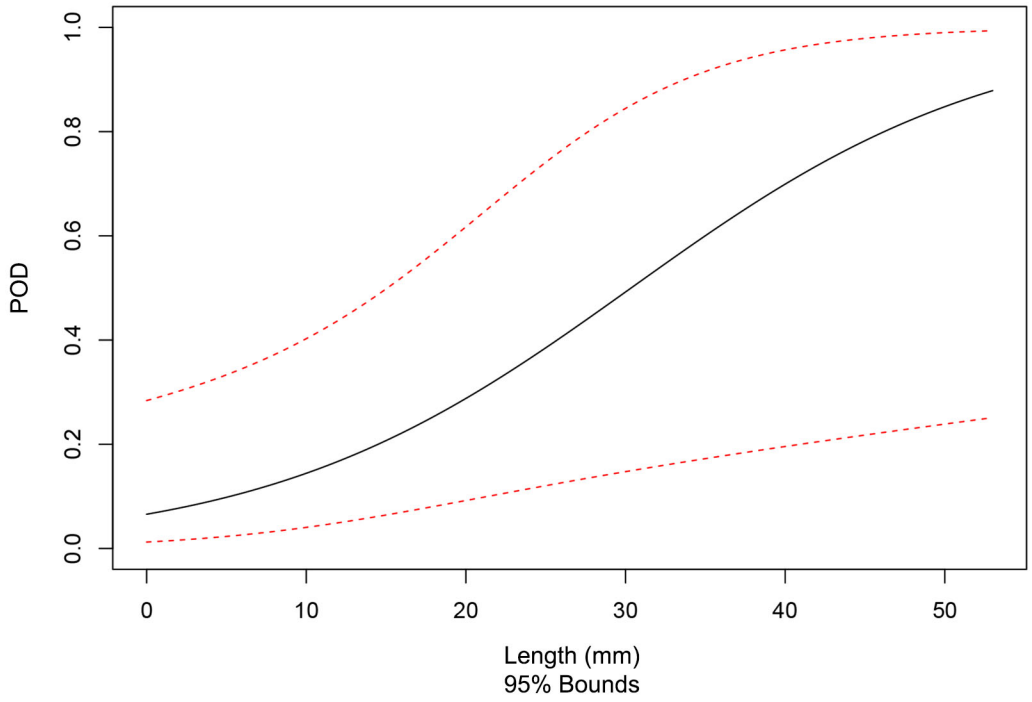

Figure C.38. Plot of POD as a Function of Flaw Length for the UT Procedure Employed by Team 134

Appendix D

Depth Sizing Regression Plots

Appendix D

Depth Sizing Regression Plots

D.1 Depth Sizing Regression Plots for Open Techniques (Emerging)

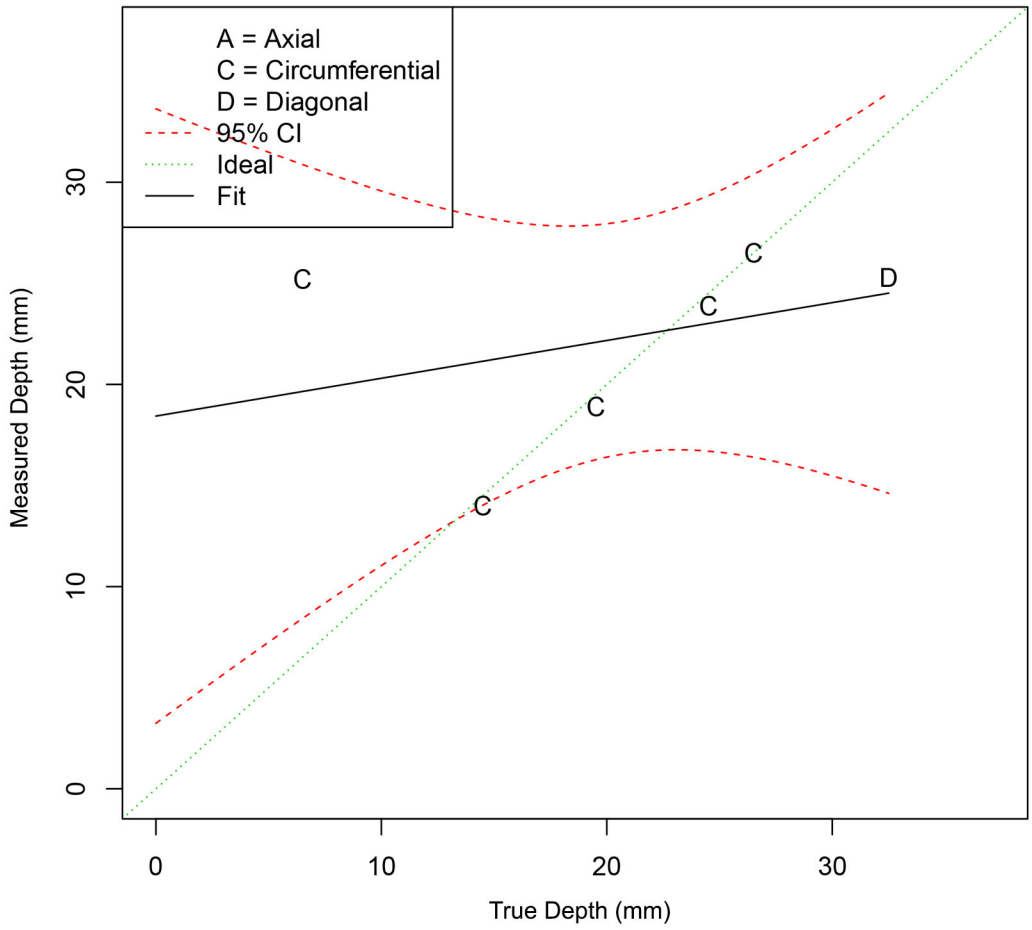

Figure D.1. Depth Sizing Regression Plot for the SHPA Technique Employed by Team 6

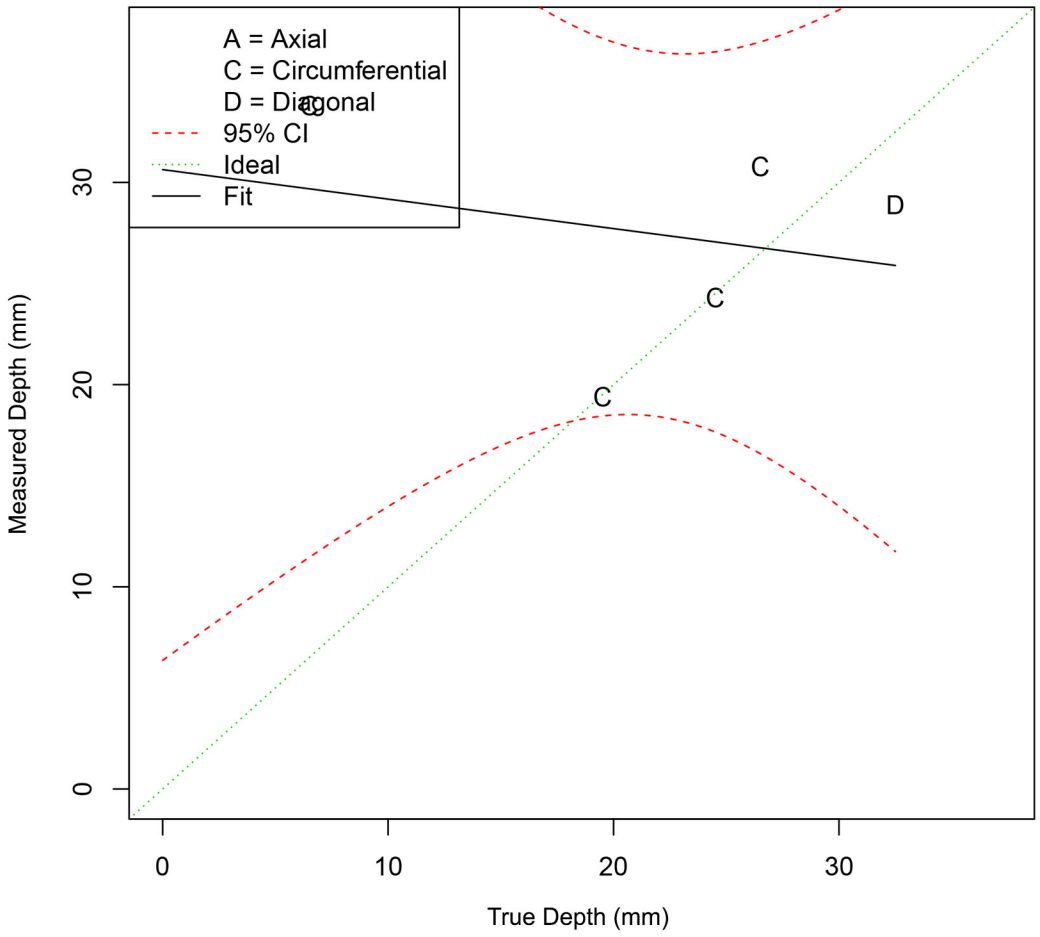

Figure D.2. Depth Sizing Regression Plot for the SAFT Technique Employed by Team 17

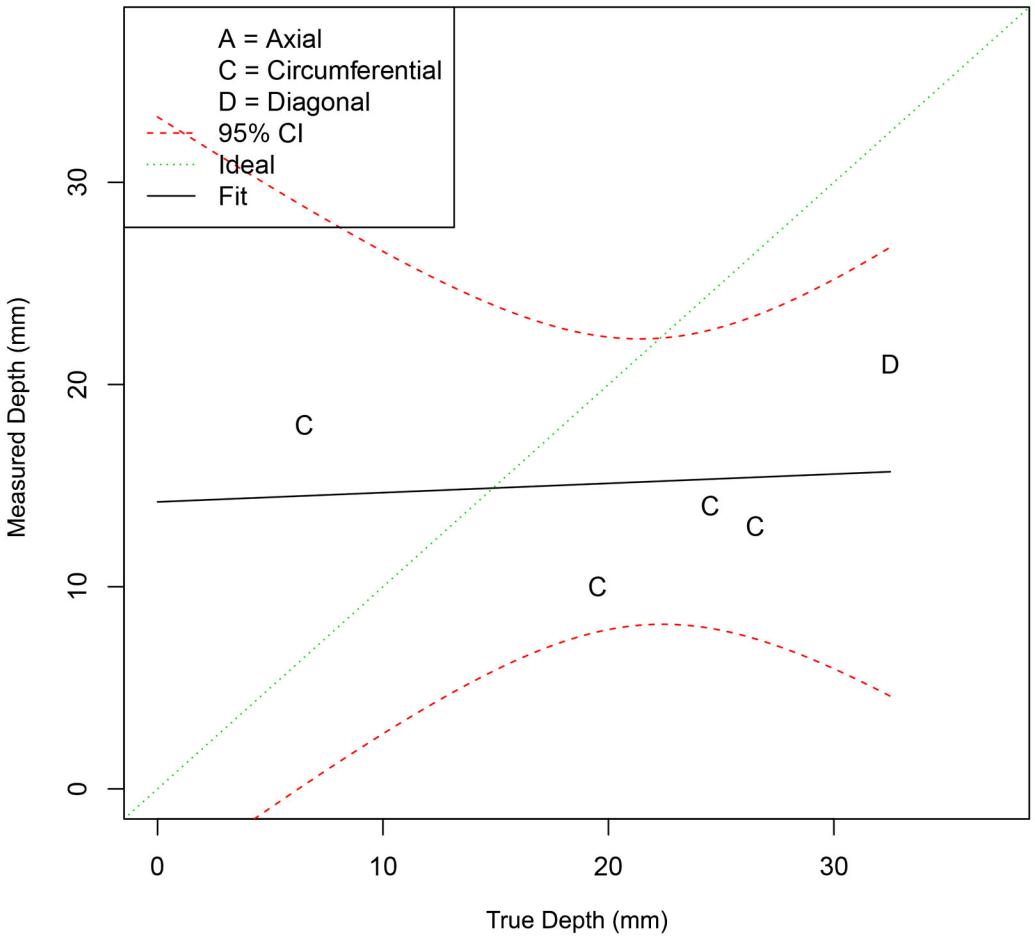

Figure D.3. Depth Sizing Regression Plot for the PA-ATOFD (Interior) Technique Employed by Team 29

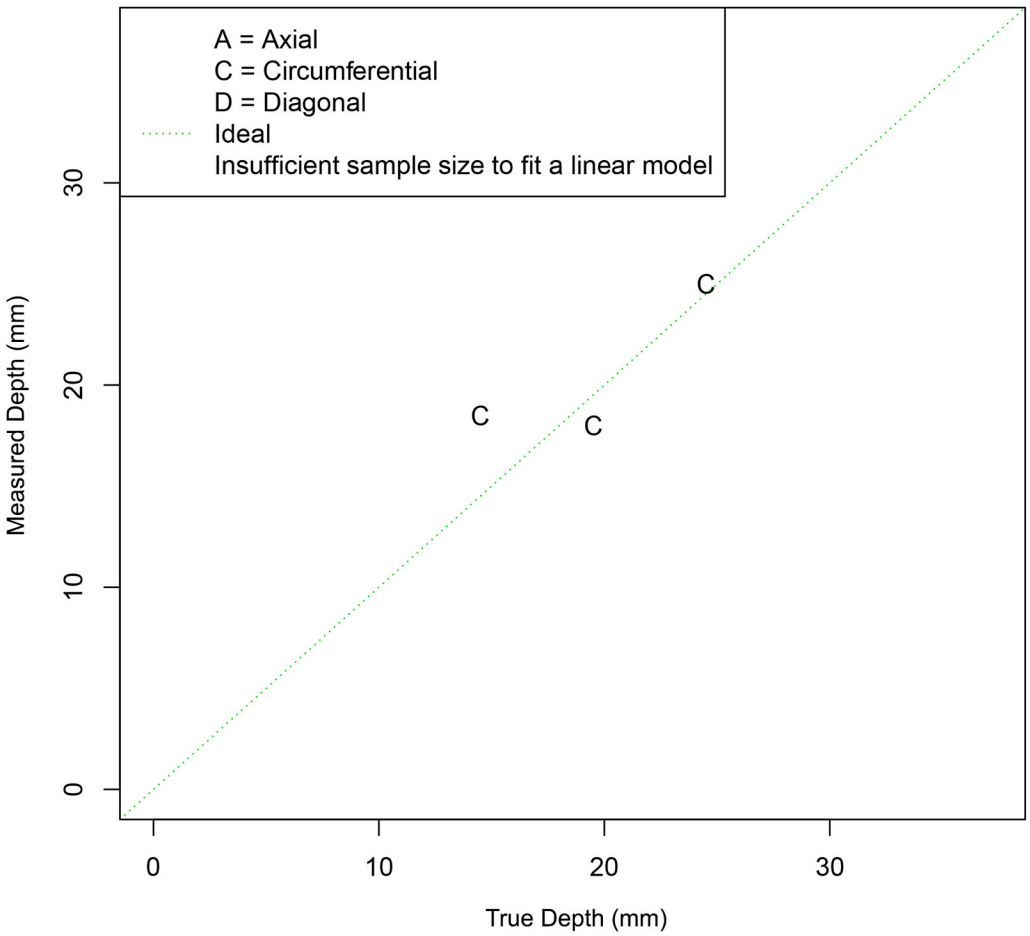

Figure D.4. Depth Sizing Regression Plot for the PA-ATOFD (Surface-Breaking) Technique Employed by Team 29

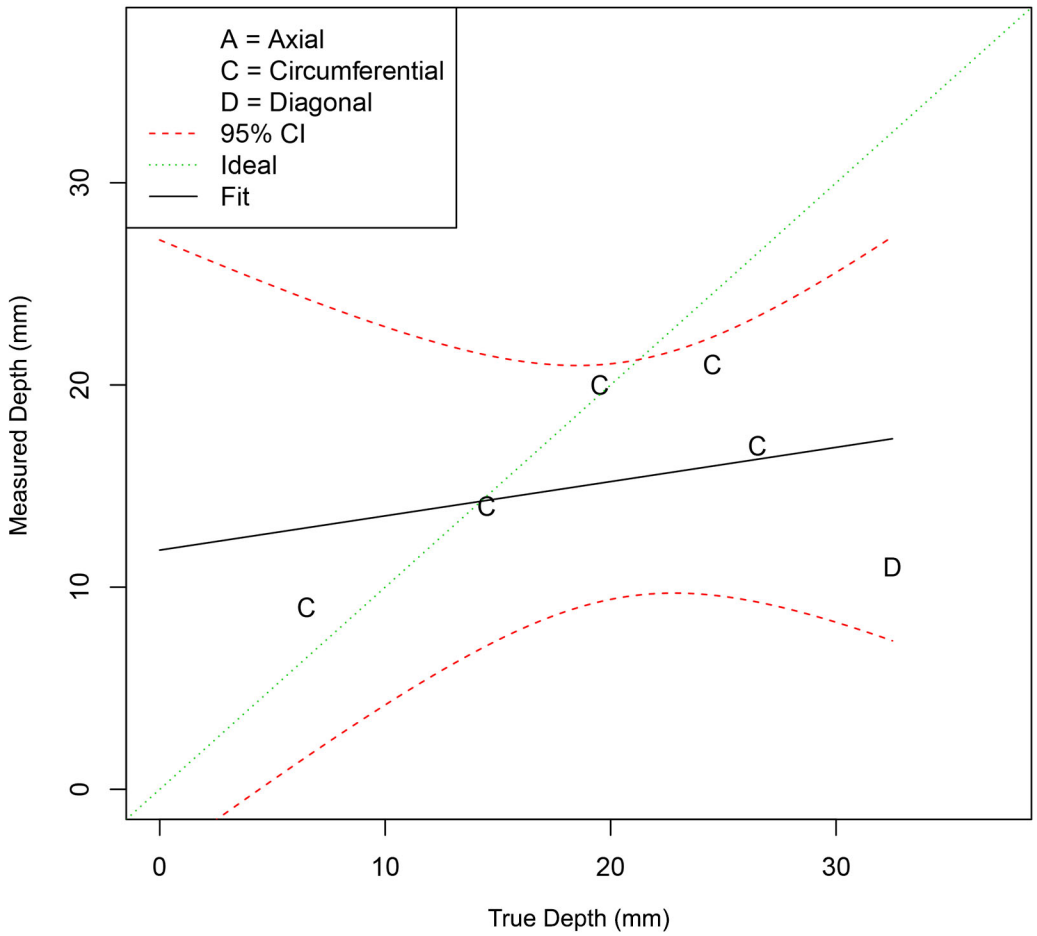

Figure D.5. Depth Sizing Regression Plot for the PA-TP (Interior) Technique Employed by Team 29

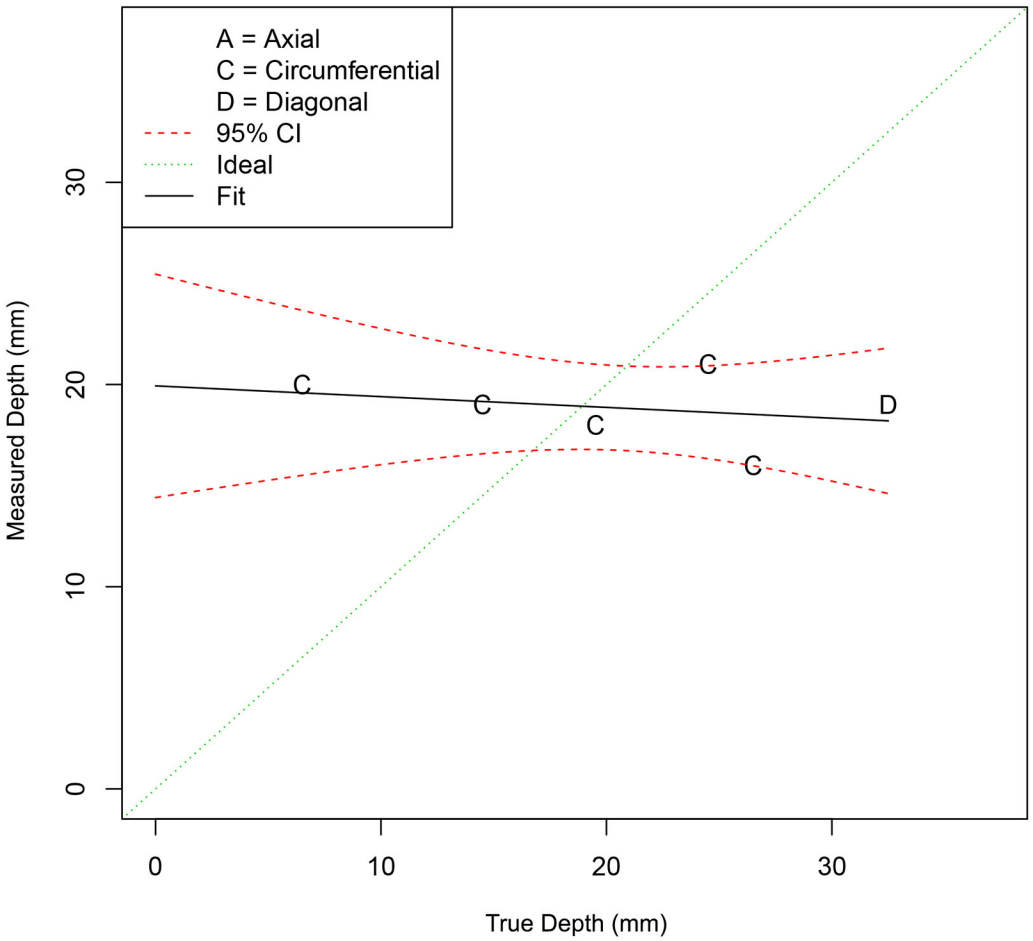

Figure D.6. Depth Sizing Regression Plot for the PA-TP (Surface-Breaking) Technique Employed by Team 29

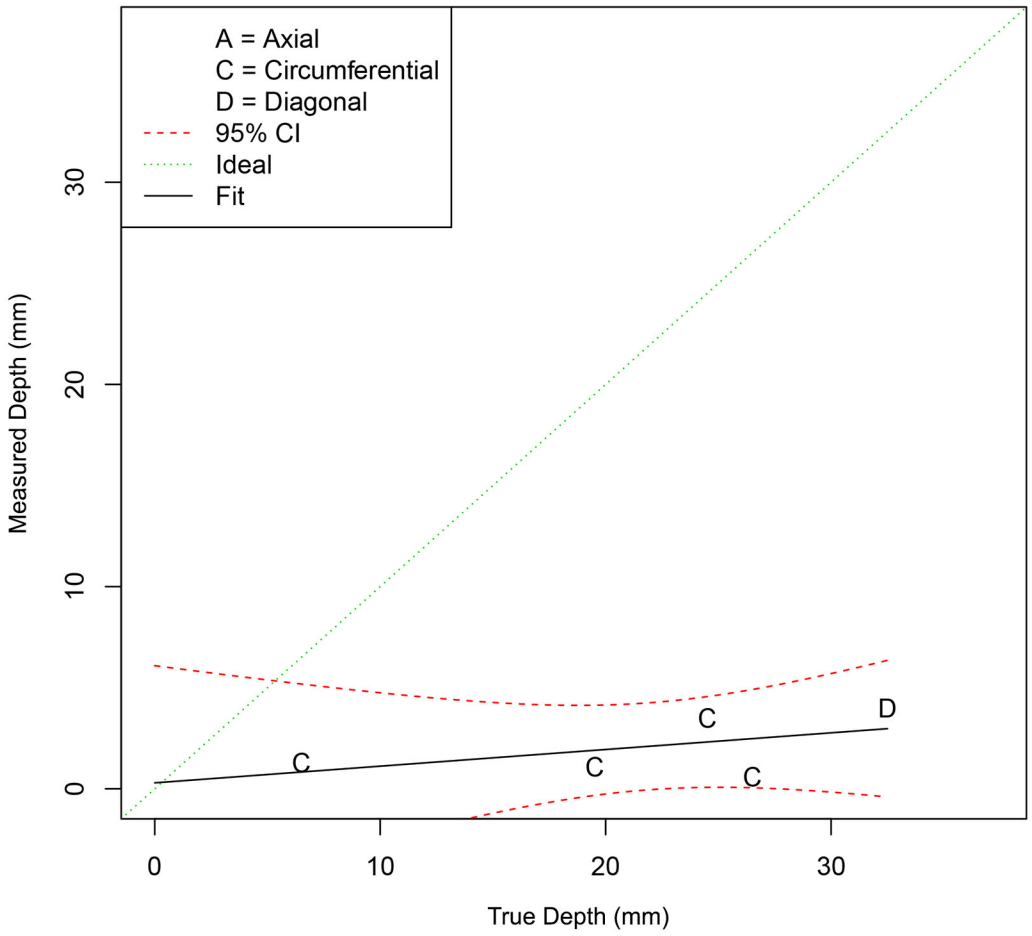

Figure D.7. Depth Sizing Regression Plot for the HHUT Technique Employed by Team 29

D.2 Depth Sizing Regression Plots for Blind Procedures (Established)

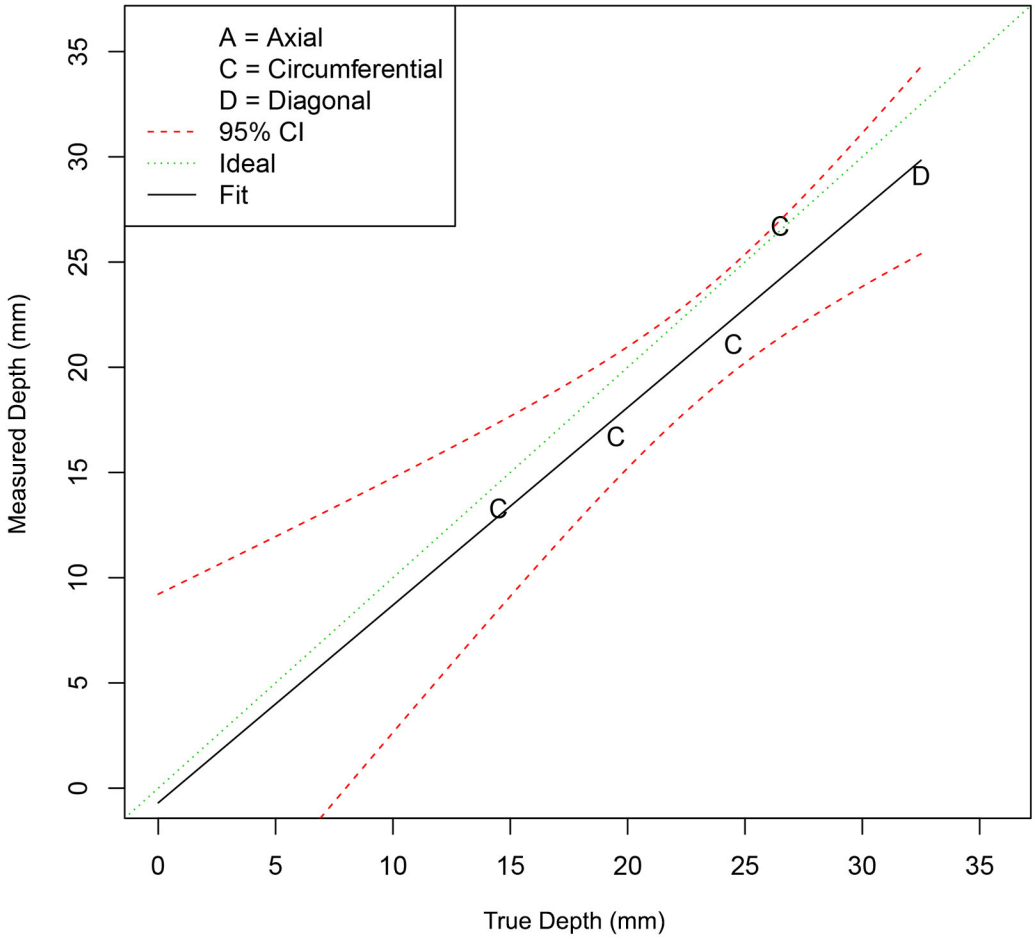

Figure D.8. Depth Sizing Regression Plot for the PAUT Procedure Employed by Team 108

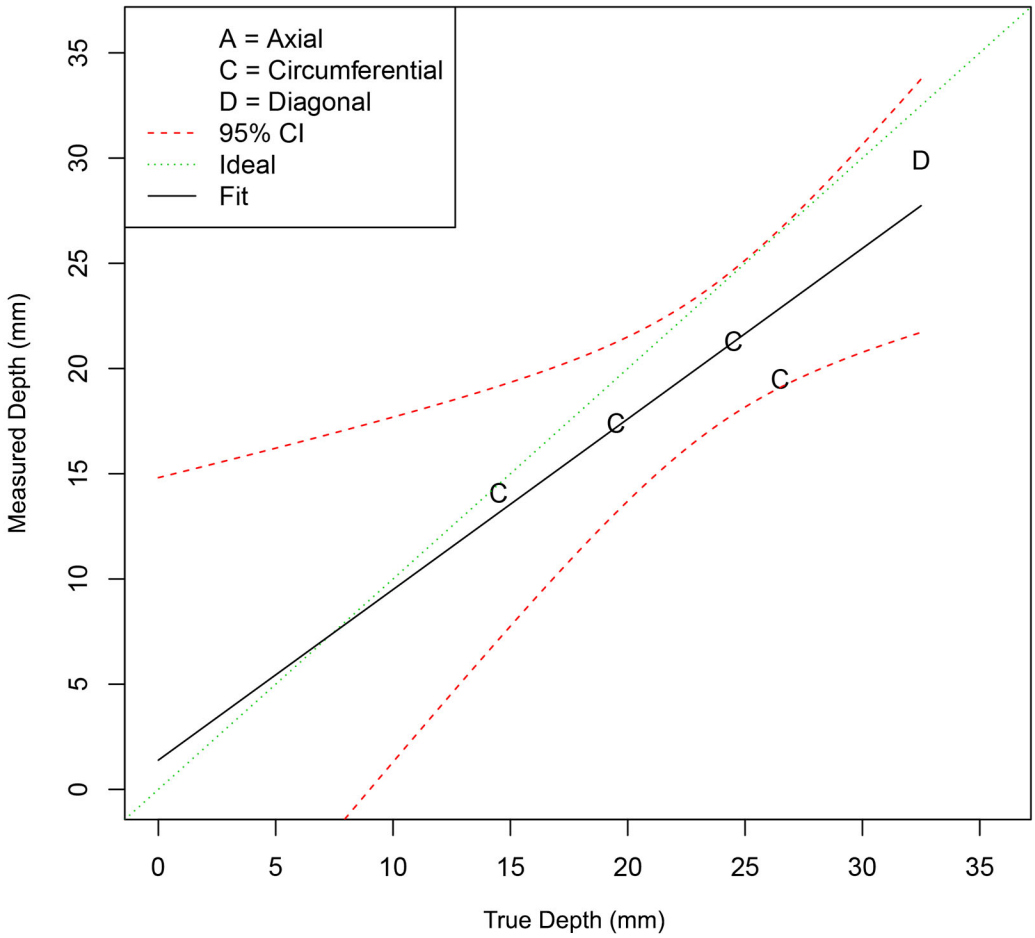

Figure D.9. Depth Sizing Regression Plot for the UT Procedure Employed by Team 108

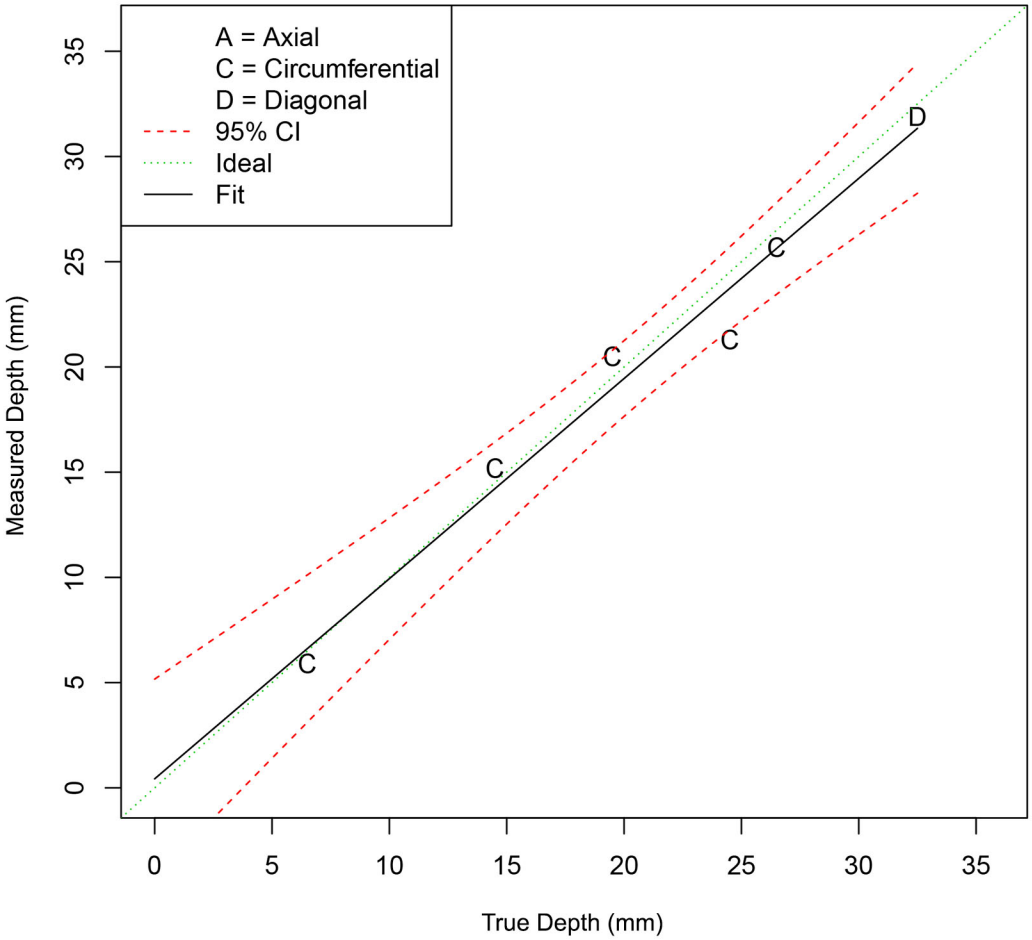

Figure D.10. Depth Sizing Regression Plot for the PAUT Procedure Employed by Team 115

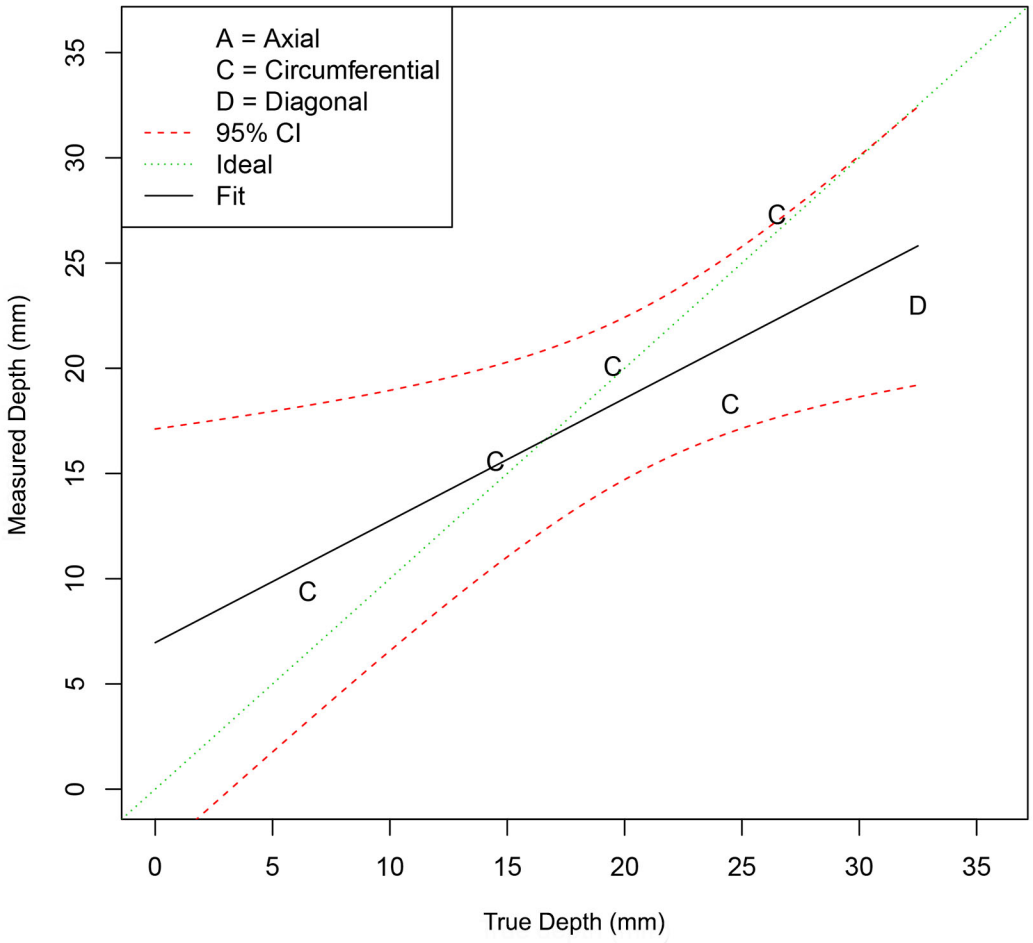

Figure D.11. Depth Sizing Regression Plot for the UT.TOFD Procedure Employed by Team 117

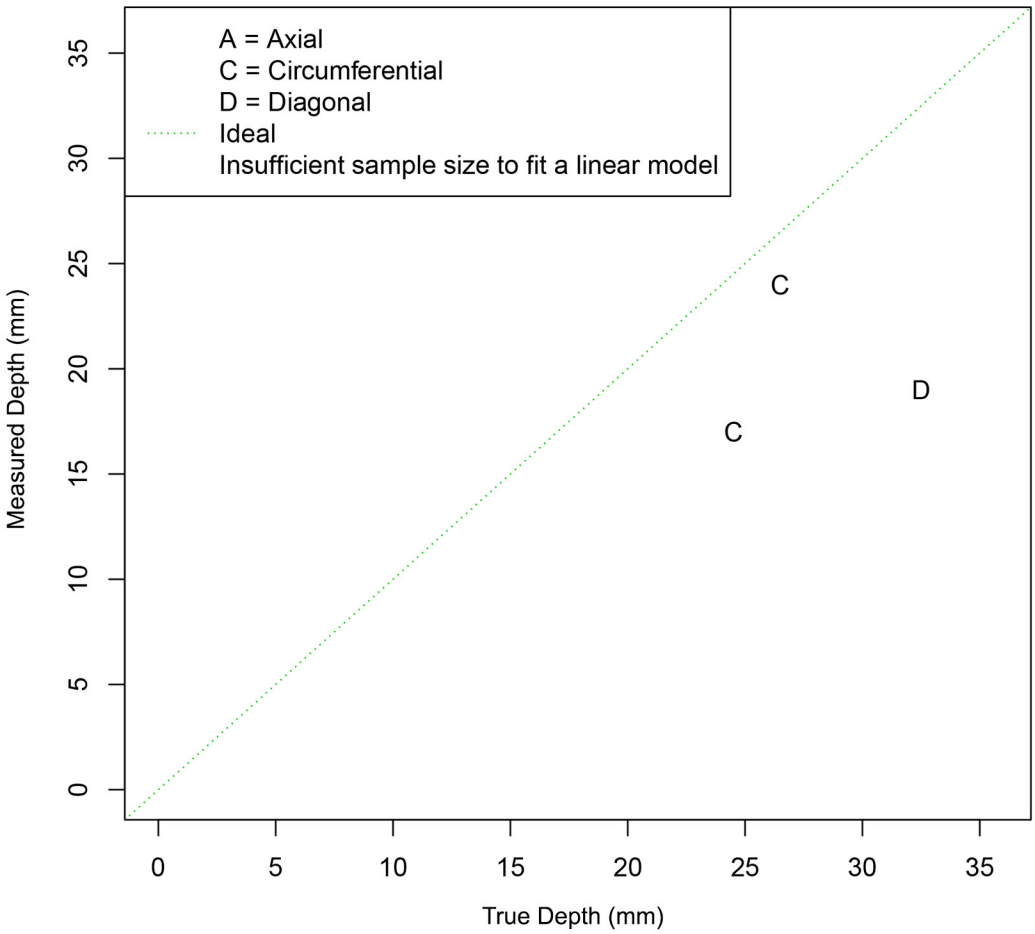

Figure D.12. Depth Sizing Regression Plot for the PAUT Procedure Employed by Team 126

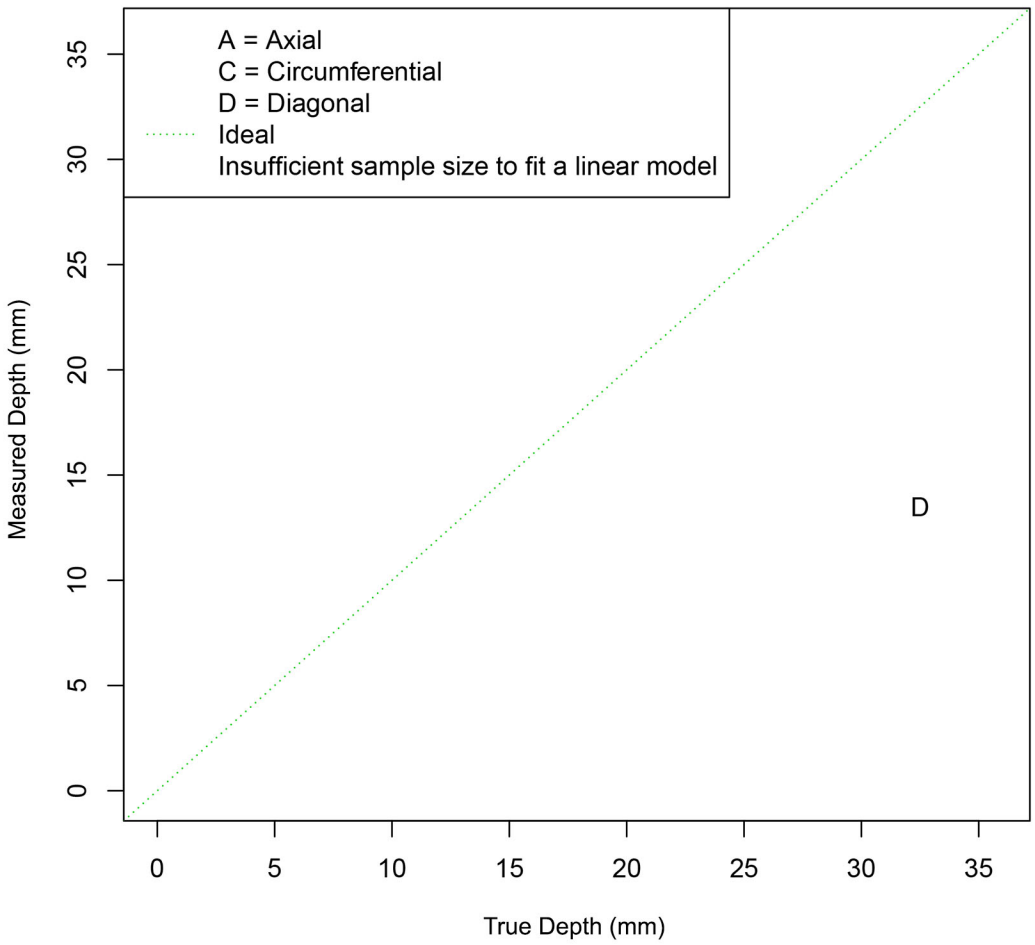

Figure D.13. Depth Sizing Regression Plot for the Conventional UT Procedure Employed by Team 126

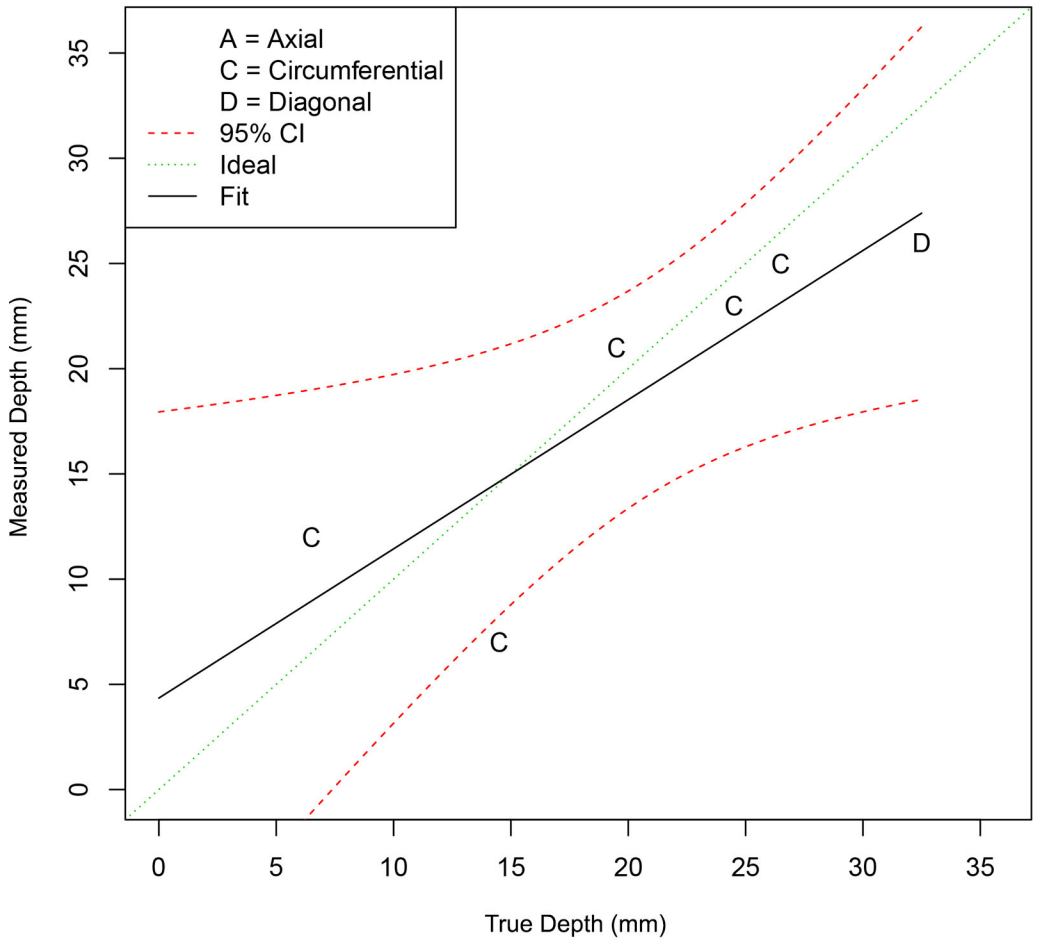

Figure D.14. Depth Sizing Regression Plot for the PAUT Procedure Employed by Team 128

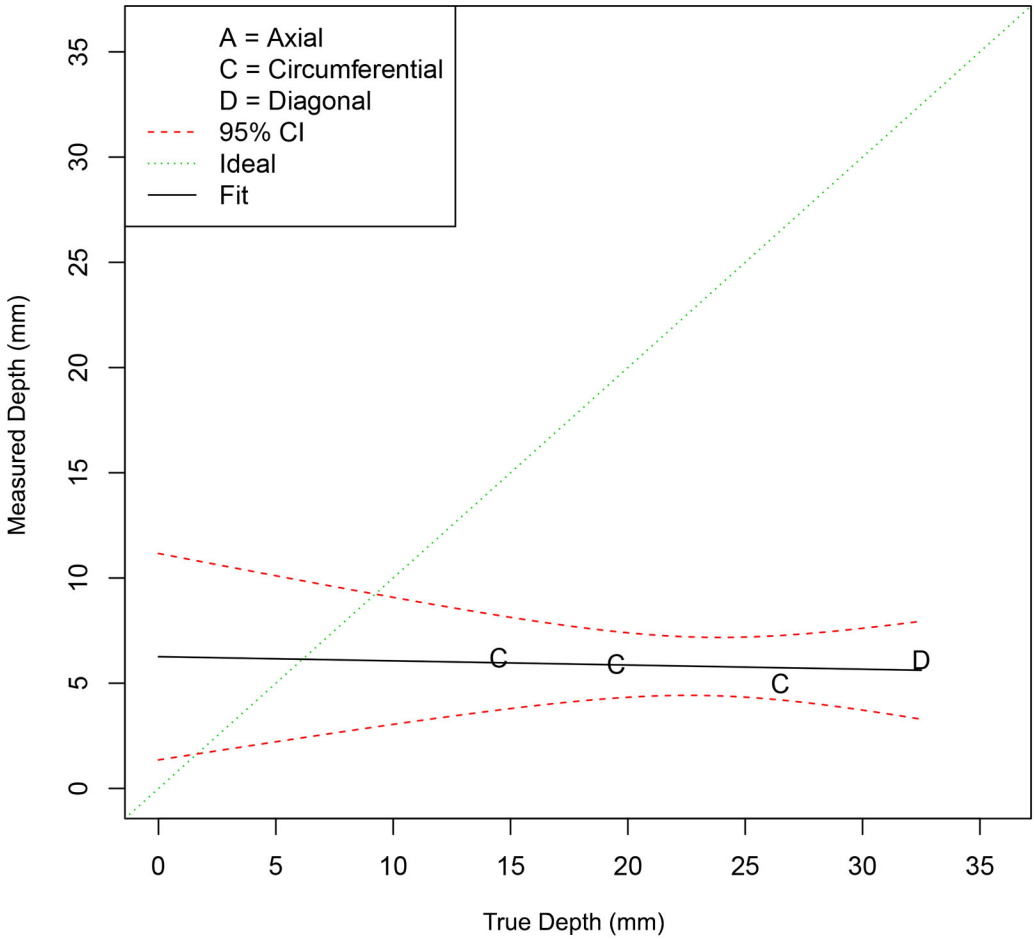

Figure D.15. Depth Sizing Regression Plot for the Conventional UT Procedure Employed by Team 134

Appendix E

Length Sizing Regression Plots

Appendix E

Length Sizing Regression Plots

E.1 Length Sizing Regression Plots for Open Techniques (Emerging)

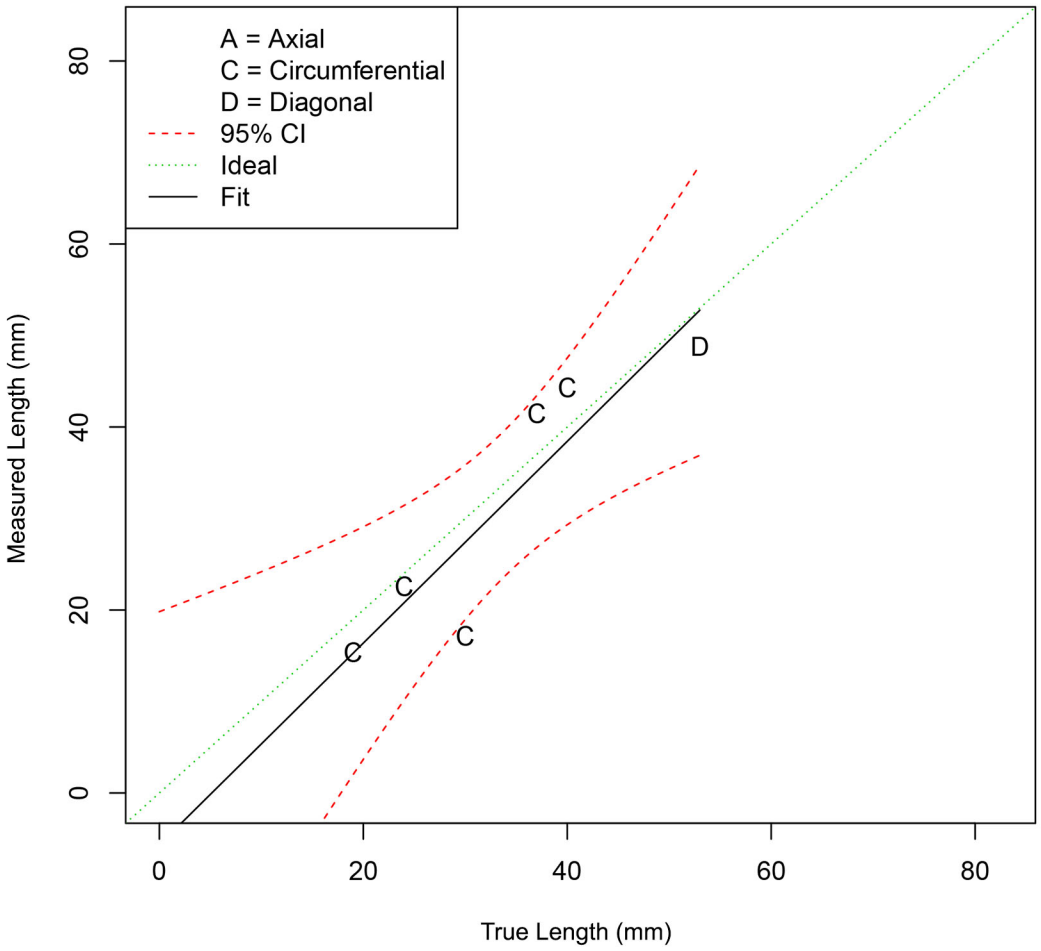

Figure E.1. Length Sizing Regression Plot for the SHPA Technique Employed by Team 6

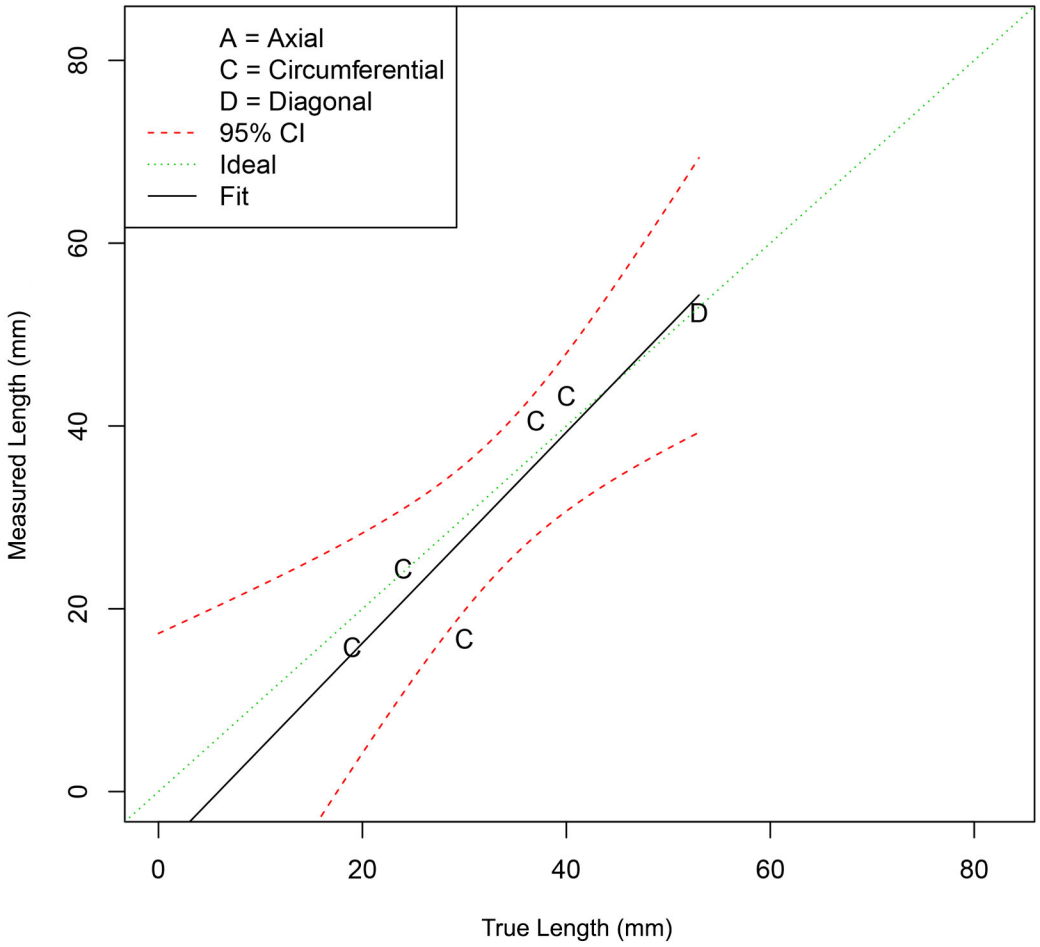

Figure E.2. Length Sizing Regression Plot for the ECT Technique Employed by Team 16

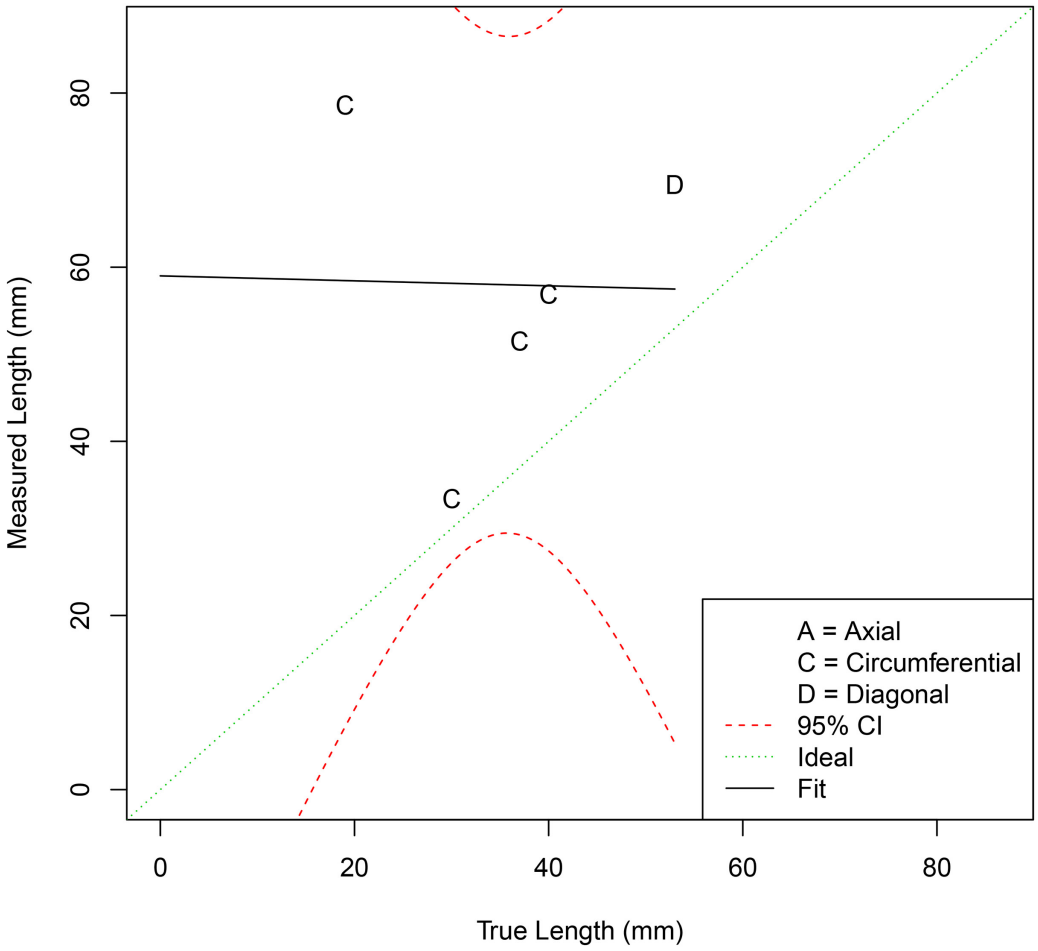

Figure E.3. Length Sizing Regression Plot for the SAFT Technique Employed by Team 17

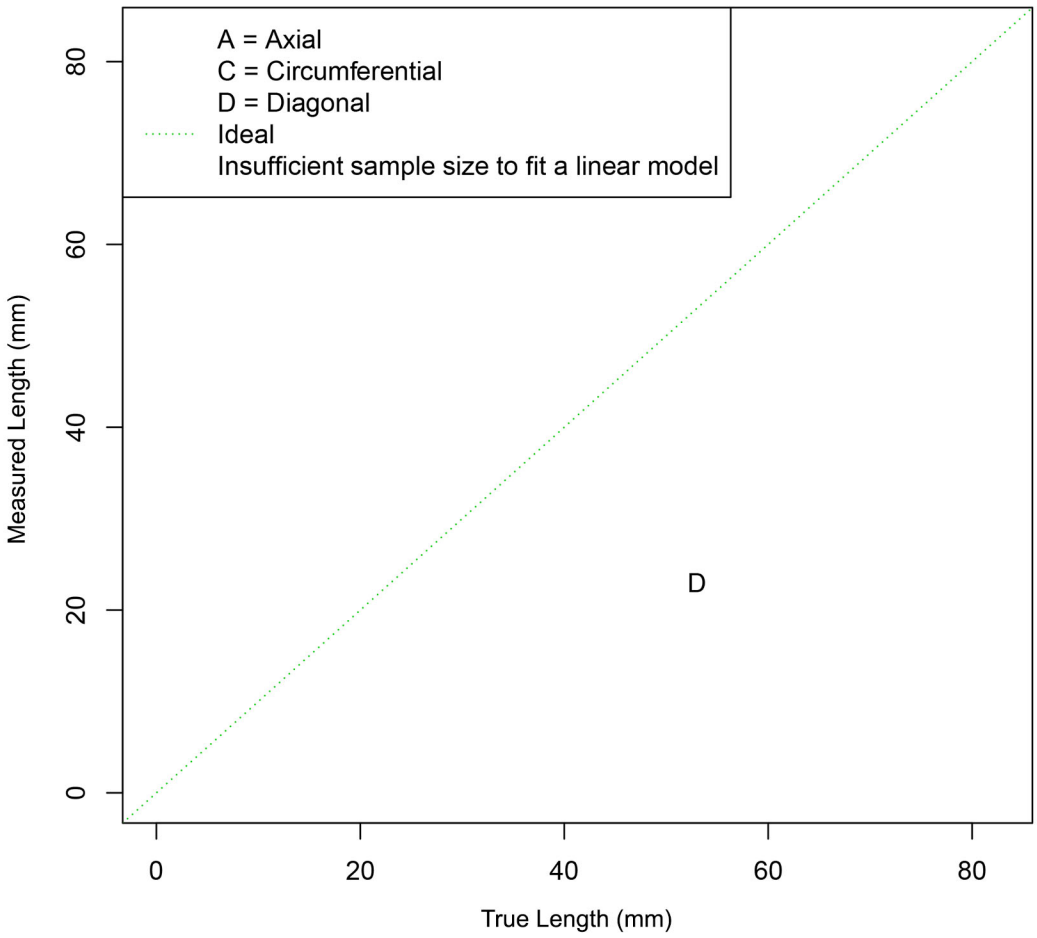

Figure E.4. Length Sizing Regression Plot for the UIRT Technique Employed by Team 20

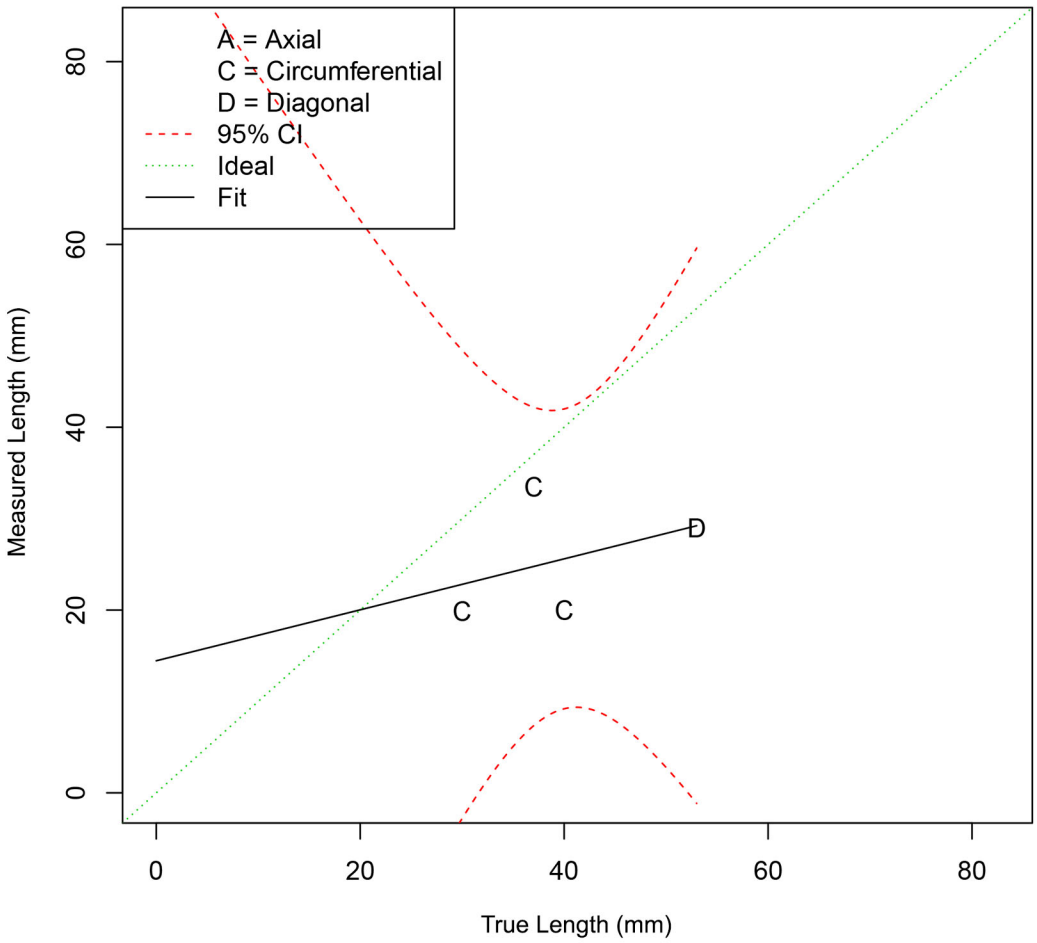

Figure E.5. Length Sizing Regression Plot for the PA-ATOFD (Interior) Technique Employed by Team 29

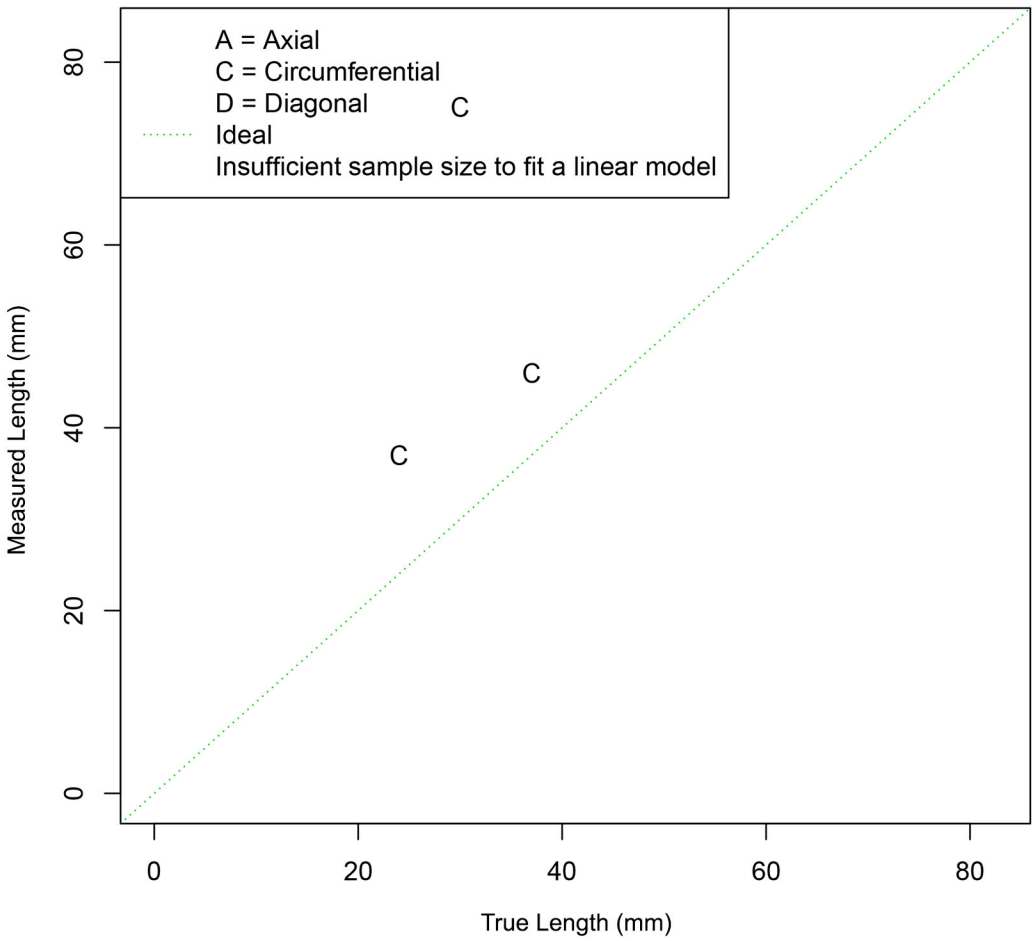

Figure E.6. Length Sizing Regression Plot for the PA-ATOFD (Surface-Breaking) Technique Employed by Team 29

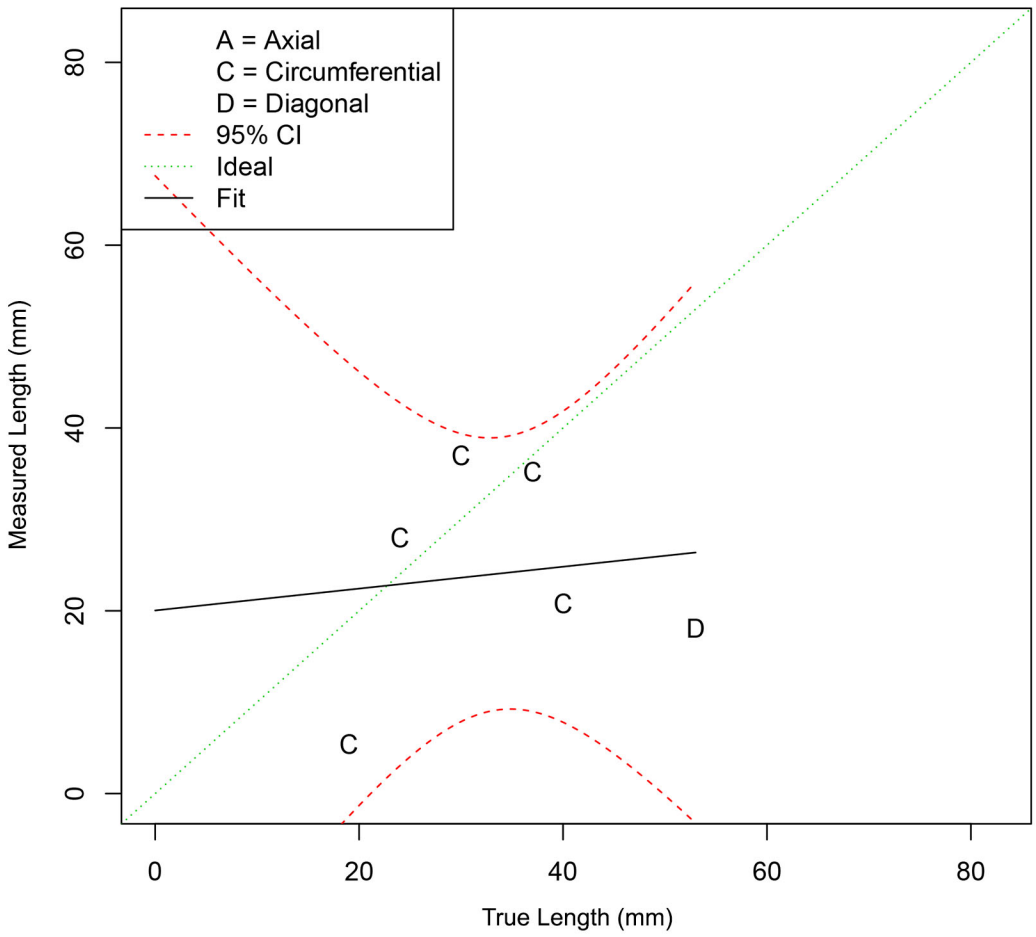

Figure E.7. Length Sizing Regression Plot for the PA-TP (Interior) Technique Employed by Team 29

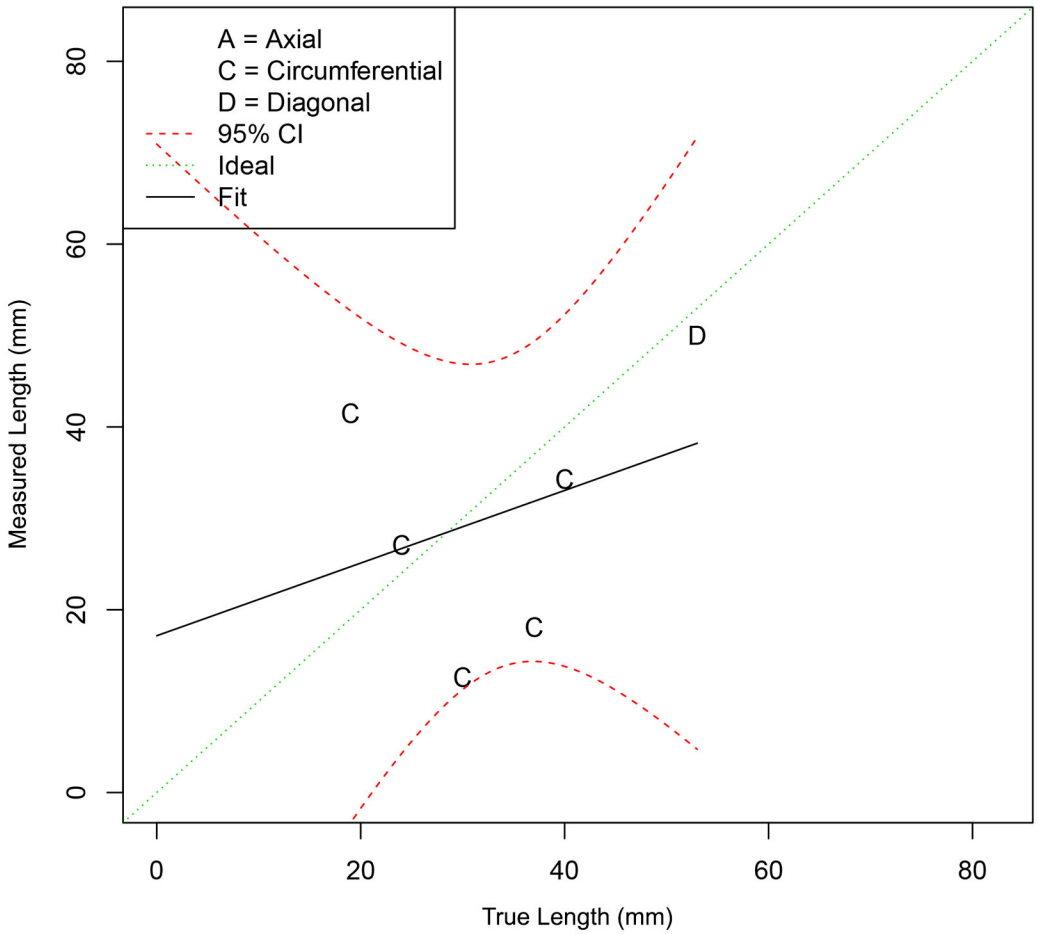

Figure E.8. Length Sizing Regression Plot for the PA-TP (Surface-Breaking) Technique Employed by Team 29

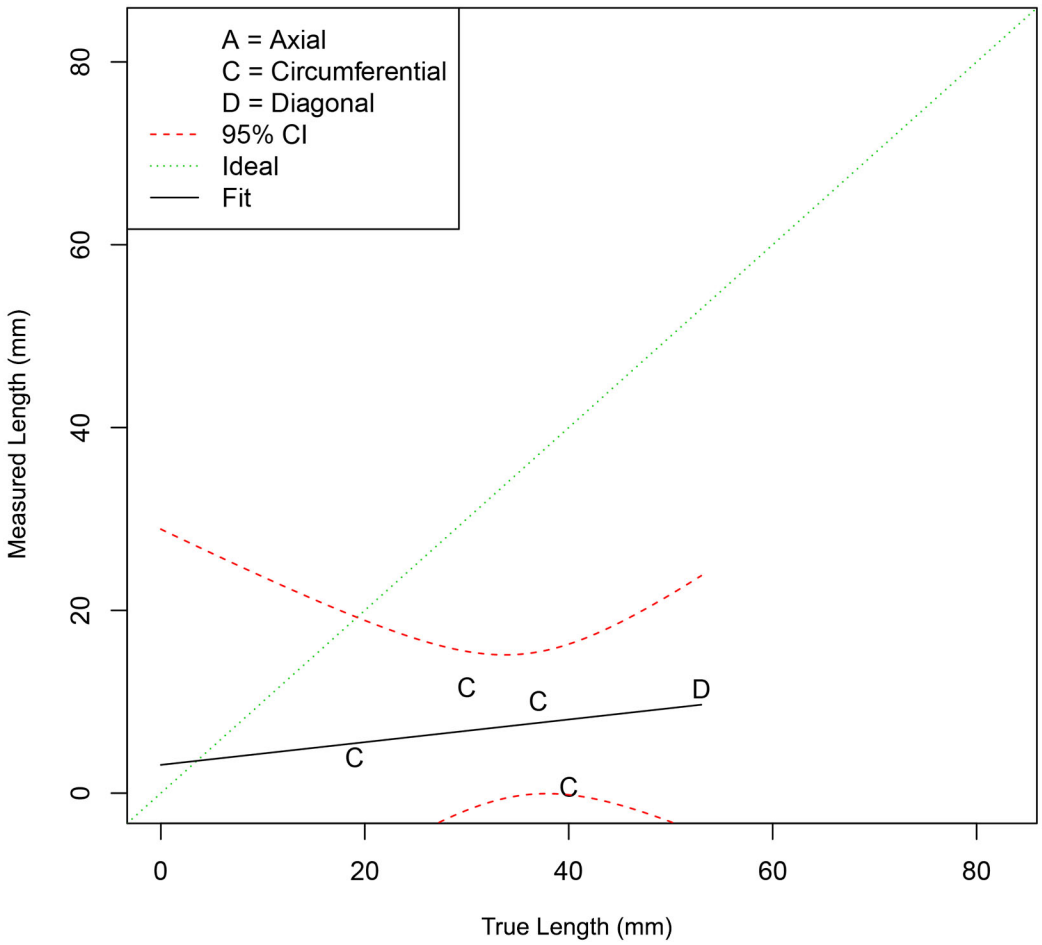

Figure E.9. Length Sizing Regression Plot for the HHUT Technique Employed by Team 29

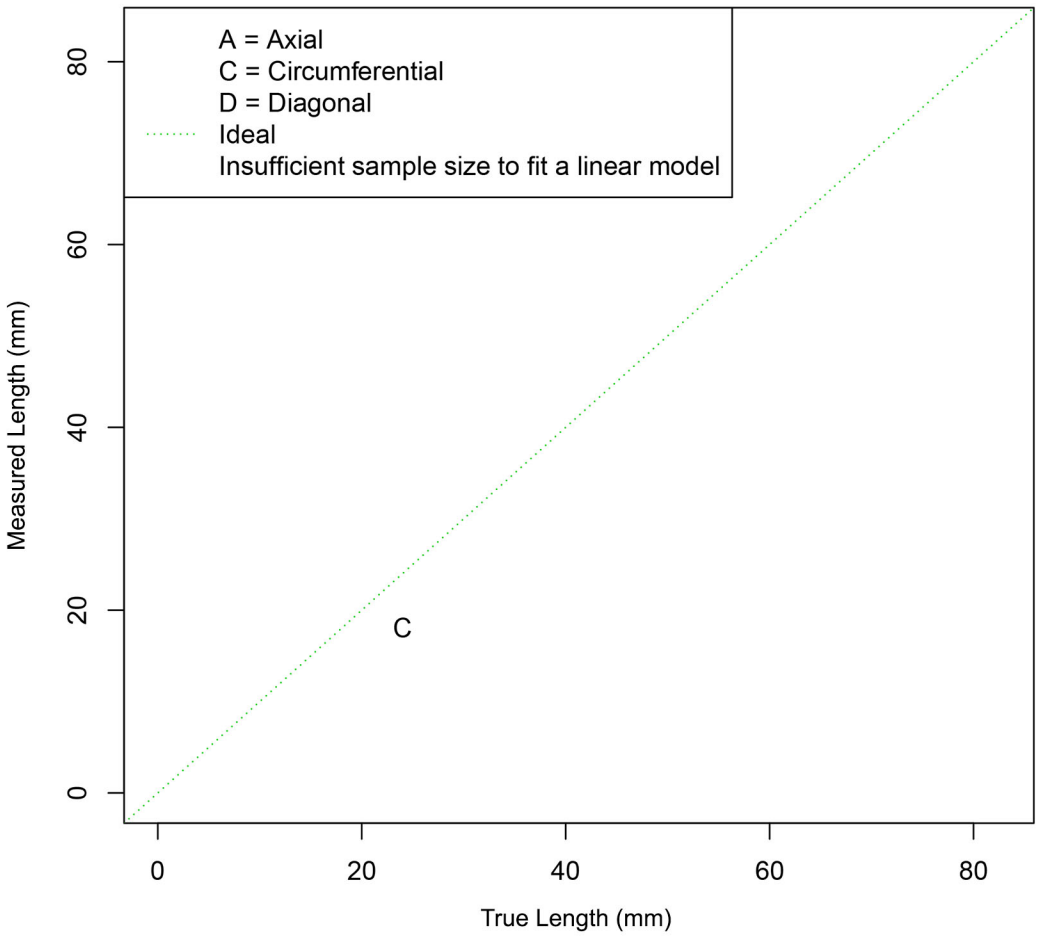

Figure E.10. Length Sizing Regression Plot for the HHUT Technique Employed by Team 30

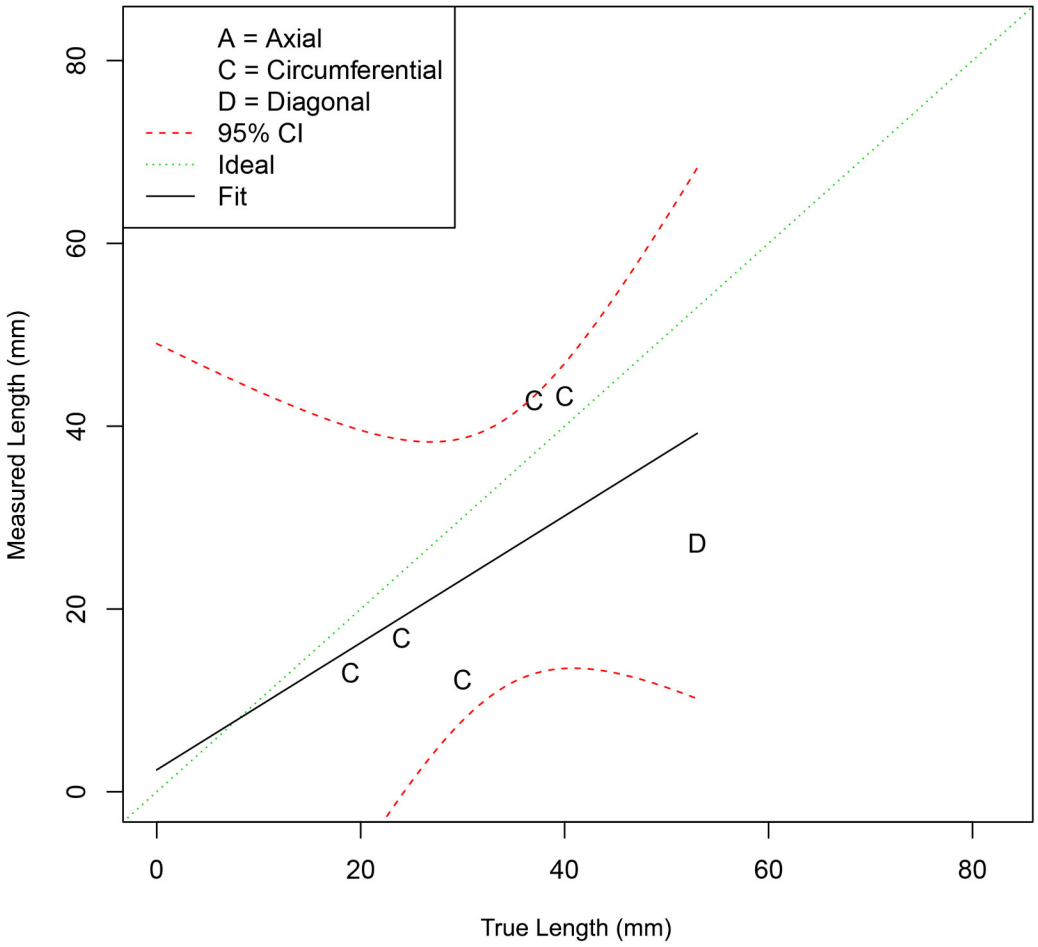

Figure E.11. Length Sizing Regression Plot for the AECT Technique Employed by Team 33

E.2 Length Sizing Regression Plots for Blind Procedures (Established)

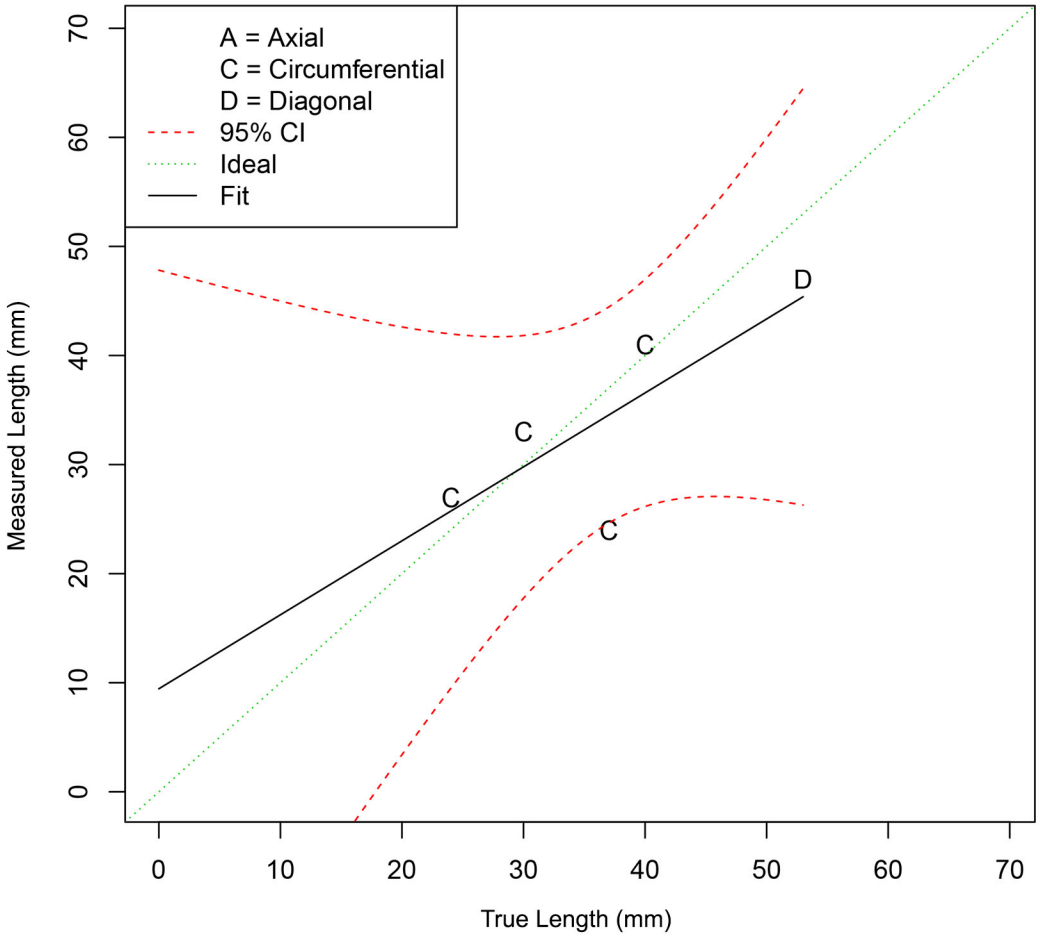

Figure E.12. Length Sizing Regression Plot for the PAUT Procedure Employed by Team 108

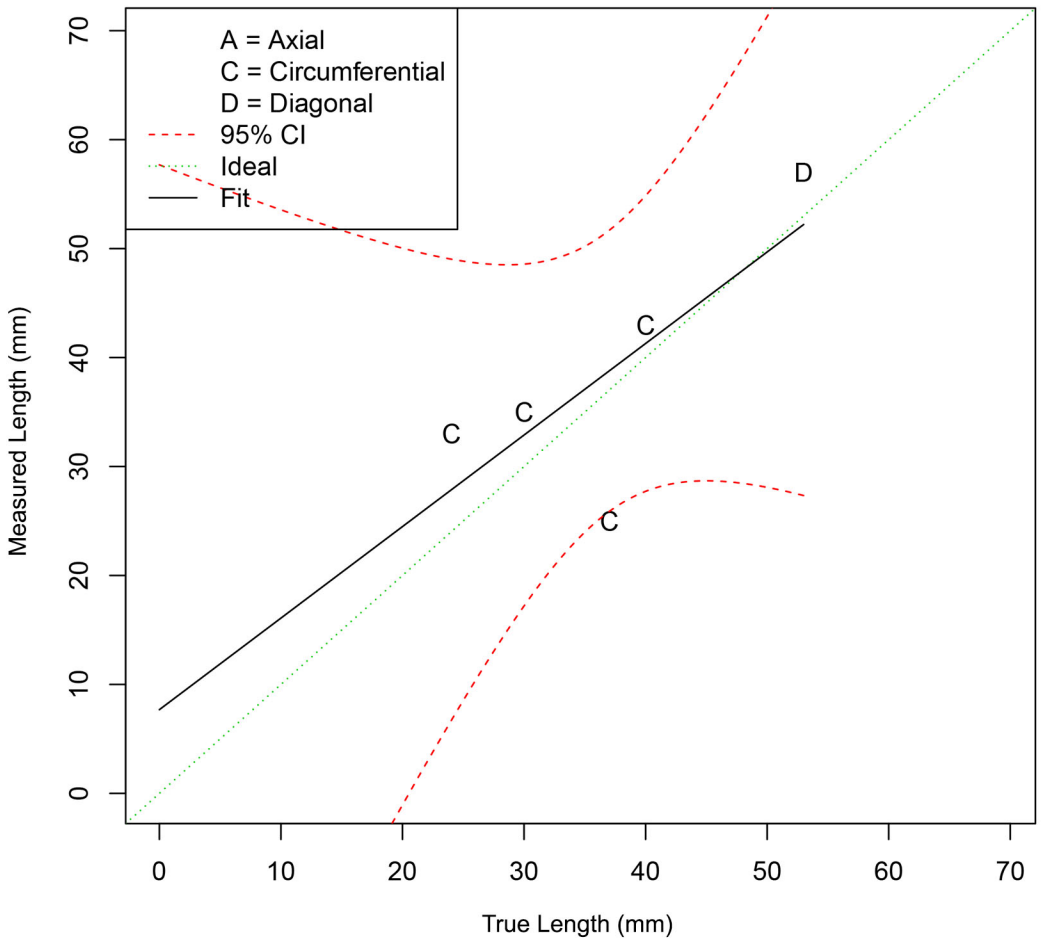

Figure E.13. Length Sizing Regression Plot for the Conventional UT Procedure Employed by Team 108

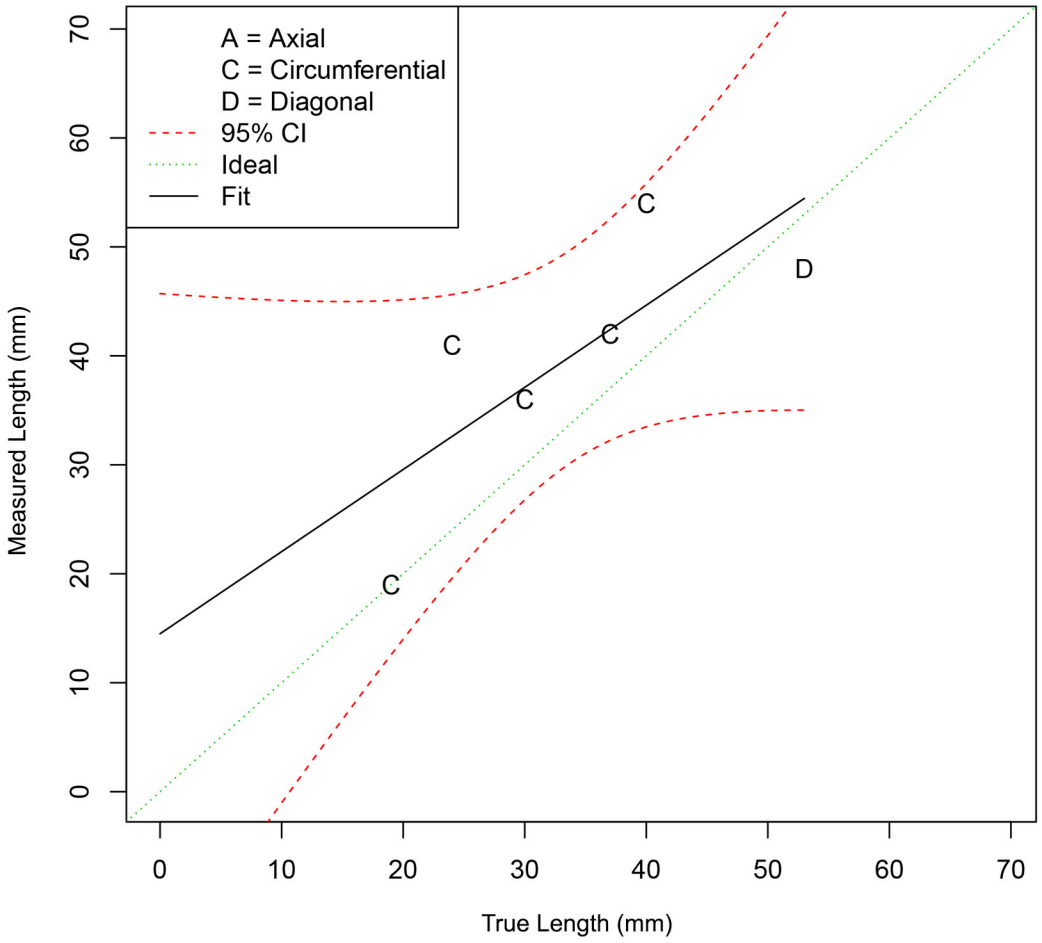

Figure E.14. Length Sizing Regression Plot for the PAUT Procedure Employed by Team 115

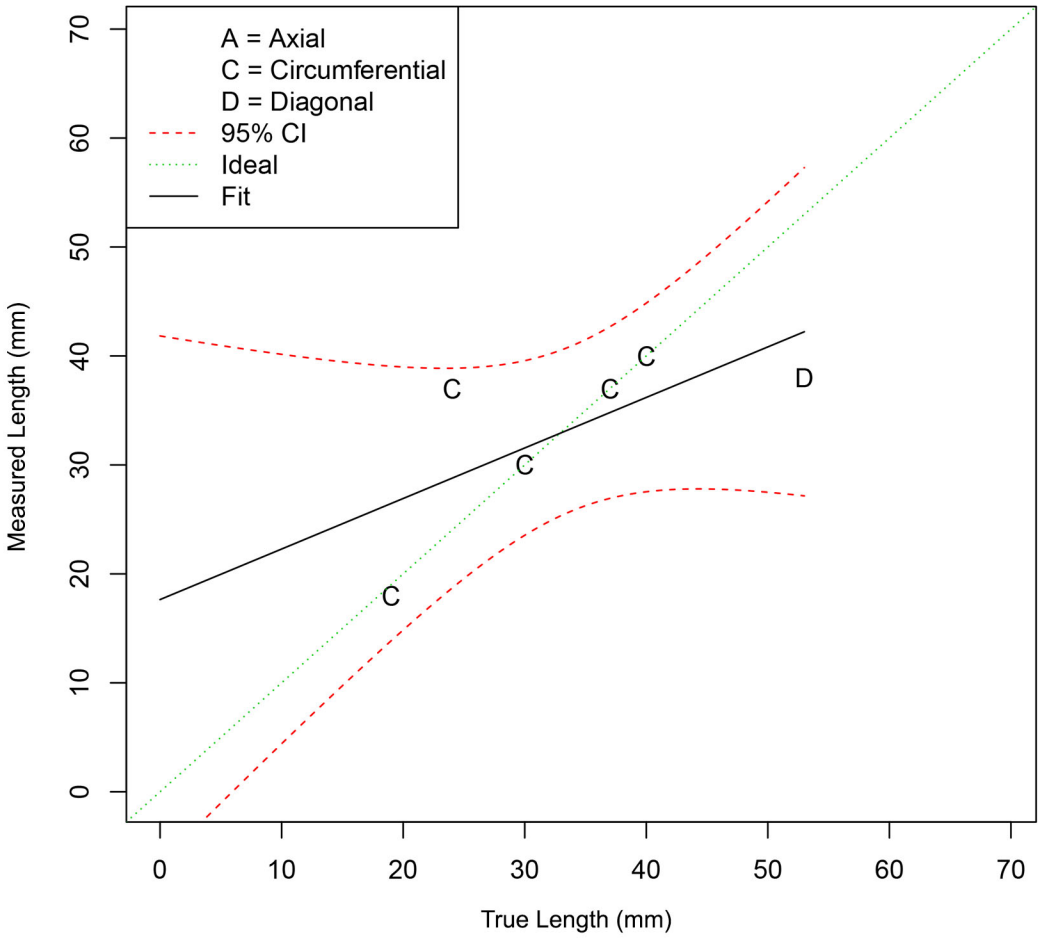

Figure E.15. Length Sizing Regression Plot for the UT.TOFD Procedure Employed by Team 117

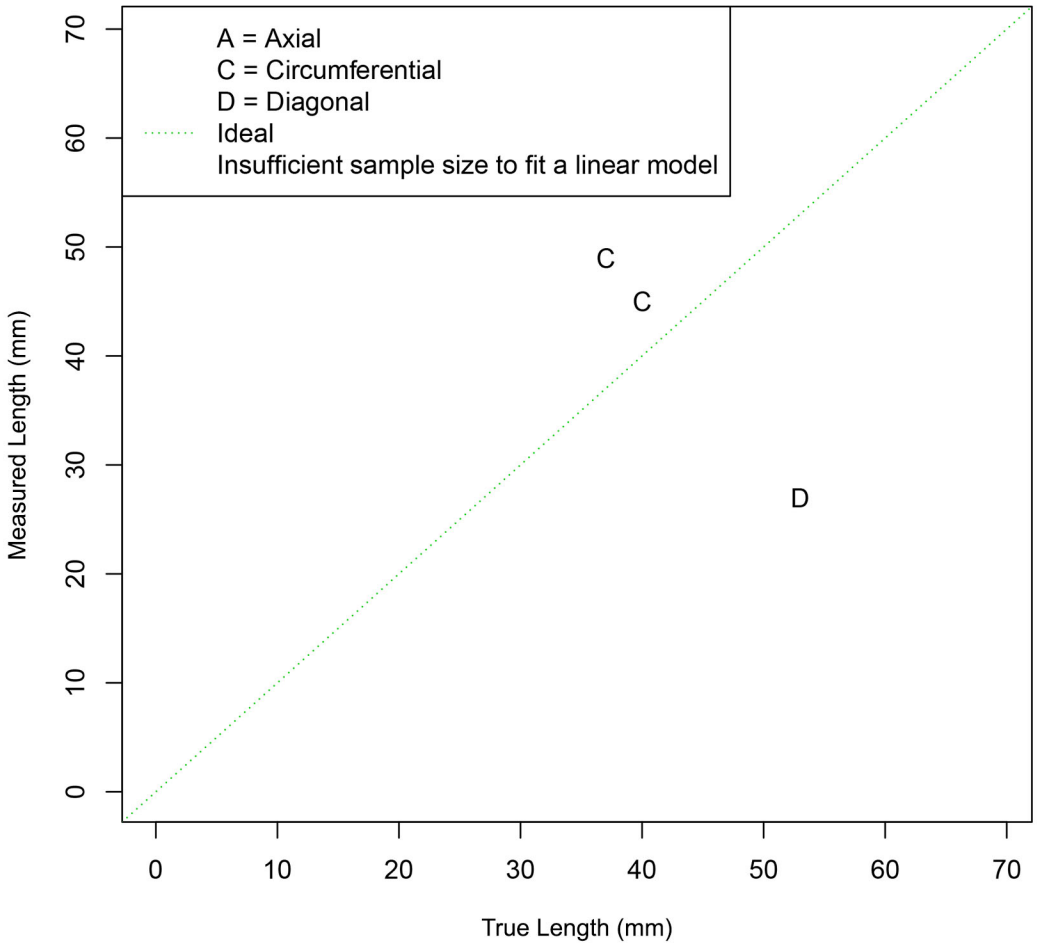

Figure E.16. Length Sizing Regression Plot for the PAUT Procedure Employed by Team 126

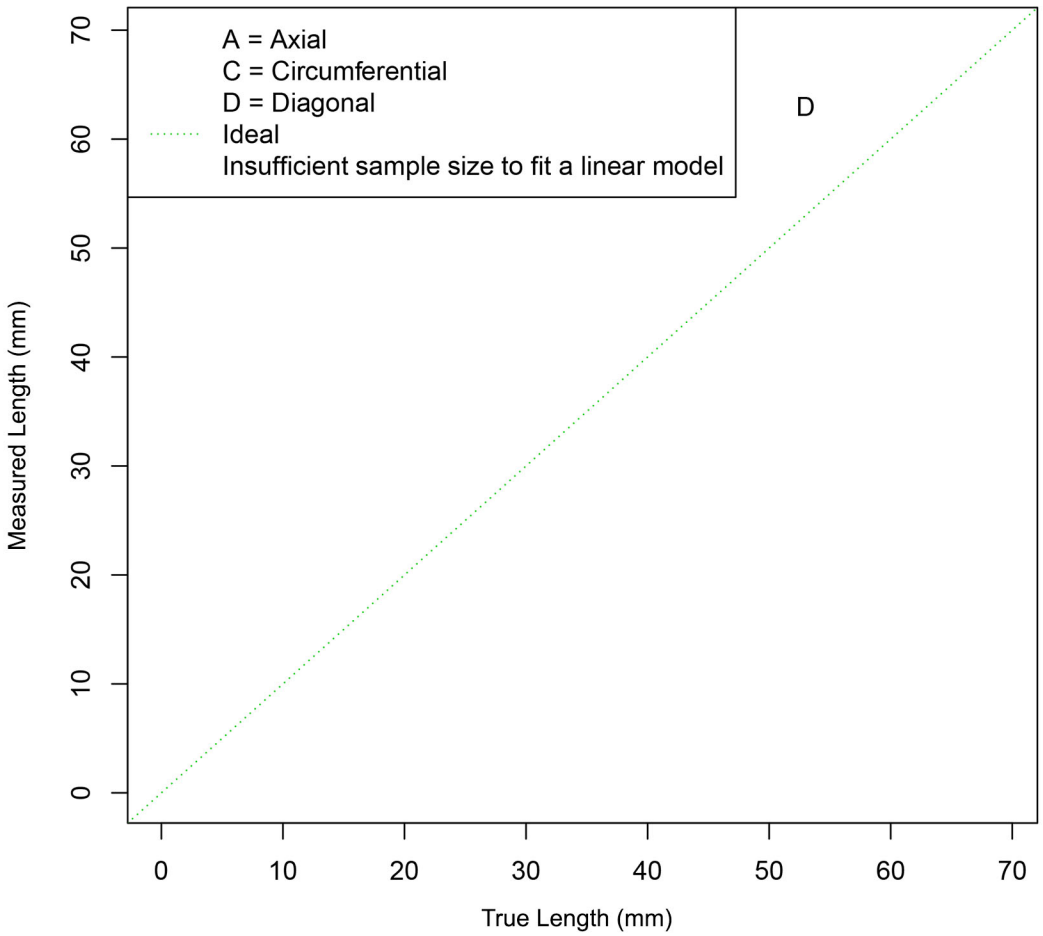

Figure E.17. Length Sizing Regression Plot for the Conventional UT Procedure Employed by Team 126

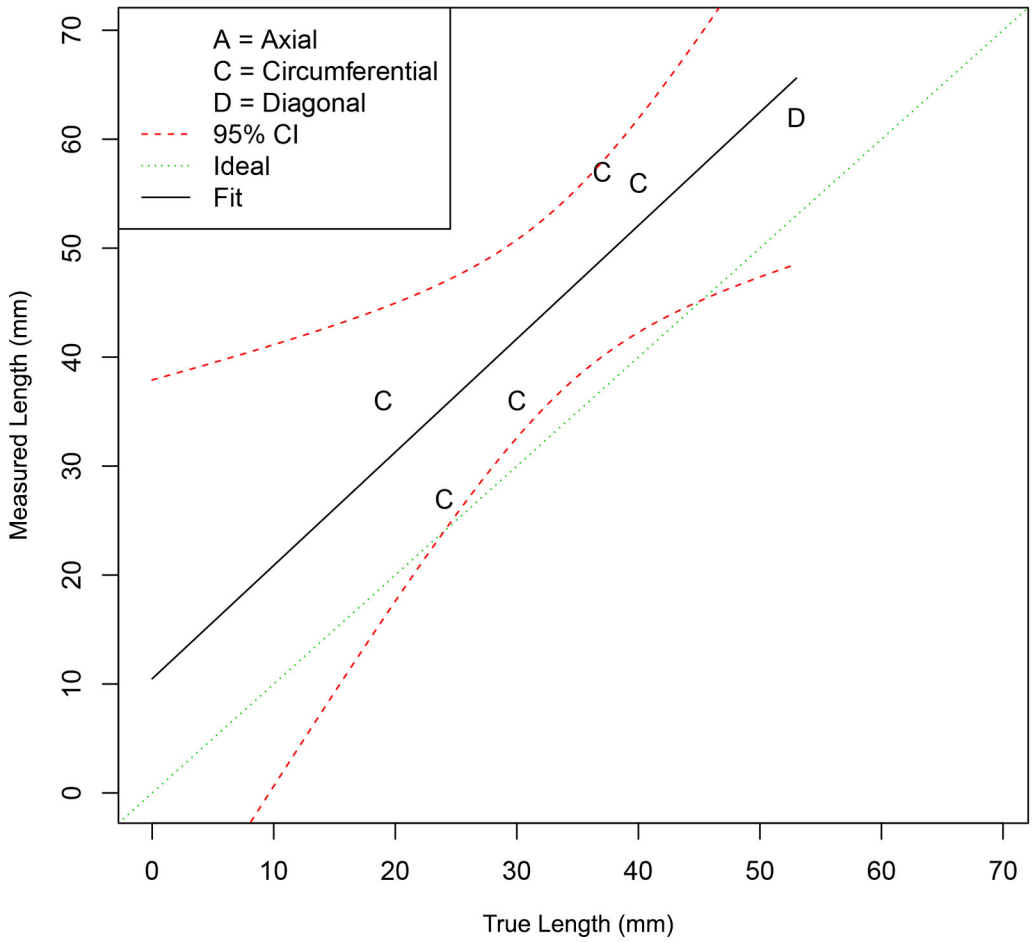

Figure E.18. Length Sizing Regression Plot for the PAUT Procedure Employed by Team 128

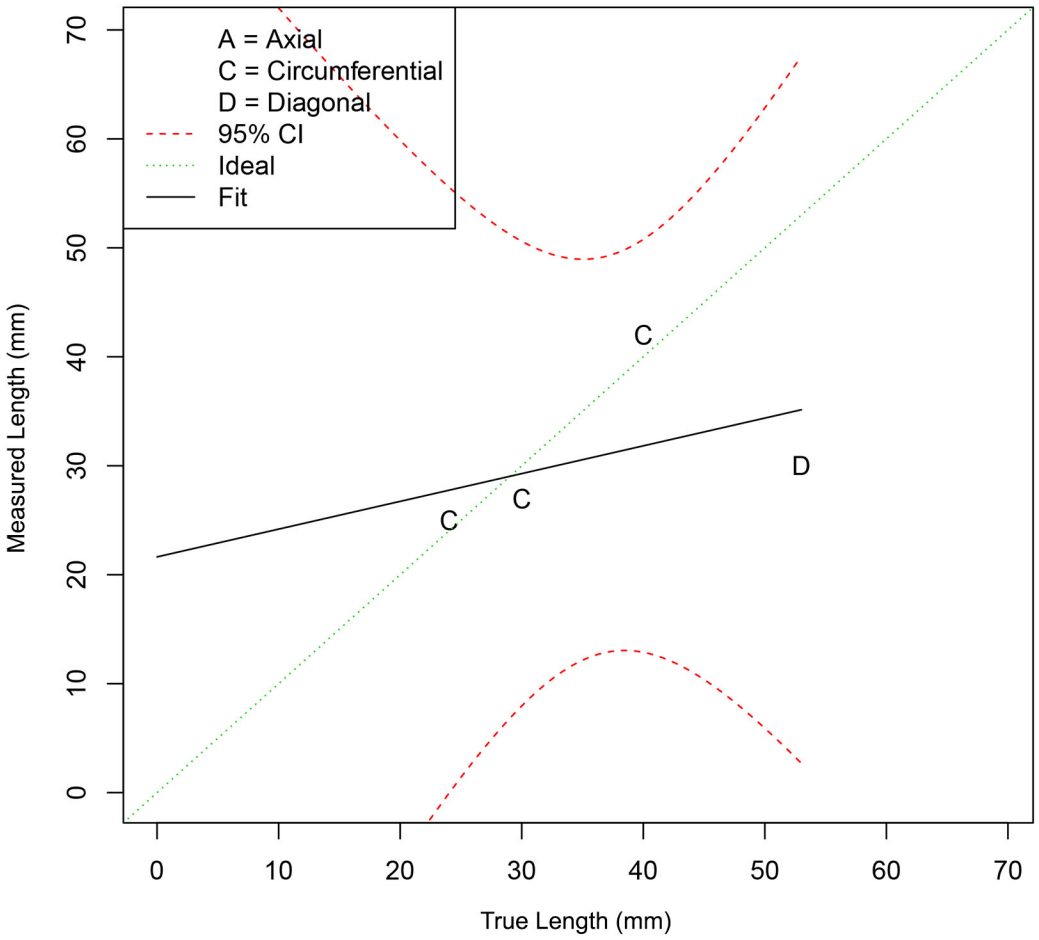

Figure E.19. Length Sizing Regression Plot for the Conventional UT Procedure Employed by Team 134

Pacific Northwest
NATIONAL LABORATORY

Proudly Operated by **Battelle** *Since 1965*

902 Battelle Boulevard
P.O. Box 999
Richland, WA 99352
1-888-375-PNNL (7665)

www.pnnl.gov

Prepared for the U.S. Nuclear Regulatory Commission
under a Related Services Agreement with the U.S. Department of Energy
CONTRACT DE-AC05-76RL01830

U.S. DEPARTMENT OF
ENERGY